HIGH TEMPERATURE SO_2 CHEMISORPTION ON MODEL SYSTEMS

IMPLICATIONS FOR IN-PLUME PROCESSES

PAUL MARTIN AYRIS

SUBMITTED FOR THE DEGREE OF DOCTOR OF PHILOSOPHY

ENVIRONMENT DEPARTMENT, UNIVERSITY OF YORK

SUBMITTED MAY, 2010

For my family.

And for the wizard.

Because of the wonderful things he does.

ABSTRACT

Volcanic volatile species are scavenged by silicate ash during transition through eruption plumes. Scavenging may form S, F and Cl salts and acids on ash surfaces, though the mechanisms and controlling variables remain poorly understood. A limited mechanistic understanding impedes estimation of volcanic volatile budgets and may also prevent assessment of environmental impacts resulting from volatile scavenging. Limited assessment of these impacts may have implications for local communities affected by ashfall onto vegetation, soils and into water bodies, and ashfall from very large eruptions may have global impacts. Through experimental techniques, this study examined SO_2 scavenging mechanisms on silicate ash surfaces. SO_2 uptake experiments were conducted on model Ca-aluminosilicate xerogels and on glasses with chemical compositions of common ash types. The materials were characterised using bulk and surface-sensitive techniques to gain insight into the mechanisms of scavenging and the reaction products formed. SO_2 chemisorption onto glass surfaces may occur on non-bridging oxygens of network modifying cations (Ca), forming sulphate salts ($CaSO_4$) and initiates diffusion mechanisms which resupplies the surface with Ca. The chemisorption-diffusion mechanism may be most efficient at high temperature, and may become significant after a few minutes of SO_2 exposure. The proposed scavenging mechanism may occur during the eruption within the high temperature volcanic conduit and in the core of the plume. High temperature SO_2 scavenging could deposit the soluble S salts inferred to exist on ash and may dictate its surface chemistry for later reactions during transport through the plume and dispersion in the atmosphere and/or environment. It is not yet possible to quantify this mechanism or compare it to other scavenging mechanisms (aqueous acid condensation, high temperature salt condensation), and so future studies should attempt to constrain all volatile scavenging mechanisms occurring on ash surfaces, with particular focus on high temperatures, even in the subterranean environment.

TABLE OF CONTENTS

LIST OF FIGURES

CHAPTER 1. INTRODUCTION

CHAPTER 2. ENVIRONMENTAL EFFECTS OF SILICATE ASH EMISSION

CHAPTER 3. EXPERIMENTAL AND ANALYTICAL METHODOLOGY

CHAPTER 4. SO_2 CHEMISORPTION ON SYNTHETIC MODEL ASH SYSTEMS

CHAPTER 5. SO_2 CHEMISORPTION ON GLASS POWDERS. PART I – RATIONALE, METHODOLOGY AND RESULTS

CHAPTER 6. SO_2 ADSORPTION EXPERIMENTS ON VOLCANIC GLASS POWDERS. PART II – THE MECHANISMS OF SO_2 ADSORPTION

CHAPTER 7. SO_2 ADSORPTION EXPERIMENTS ON VOLCANIC GLASS. PART III – IMPLICATIONS FOR IN-PLUME PROCESSES

APPENDIX ONE.

...

APPENDIX TWO.

LIST OF TABLES

CHAPTER 1. INTRODUCTION

CHAPTER 2. ENVIRONMENTAL EFFECTS OF SILICATE ASH EMISSION

CHAPTER 3. EXPERIMENTAL AND ANALYTICAL METHODOLOGY

CHAPTER 4. SO_2 CHEMISORPTION ON SYNTHETIC MODEL ASH SYSTEMS

CHAPTER 5. SO_2 CHEMISORPTION ON GLASS POWDERS. PART I – RATIONALE, METHODOLOGY AND RESULTS

CHAPTER 6. SO_2 ADSORPTION EXPERIMENTS ON VOLCANIC GLASS POWDERS. PART II – THE MECHANISMS OF SO_2 ADSORPTION

CHAPTER 7. SO_2 ADSORPTION EXPERIMENTS ON VOLCANIC GLASS. PART III – IMPLICATIONS FOR IN-PLUME PROCESSES

...

APPENDIX ONE

LIST OF SYMBOLS USED

μ	Dynamic viscosity of air	$kg\ m^{-1}\ s$
A	Surface area	m^2
a_s	Specific surface area	$m^2\ g^{-1}$
C	Concentration of non-specific element	*As specified*
C_{BET}	Brunaeur-Emmett-Teller constant	*Unitless*
C_p	Specific heat capacity	$J\ kg^{-1}\ K^{-1}$
d	Interatomic distance	*Distance units*
D	Diffusion coefficient	$cm^2\ s^{-1}$
E_a	Activation energy	$kJ\ mol^{-1}$
E_b	Binding energy	*eV*
E_c	Energy to escape a surface	*eV*
$E_{k,l,m,f}$	Energy to remove core and valence electrons	*eV*
g	Gravity	$m^2\ s^{-1}$
I	Intensity	$J\ m^{-2}\ s^{-1}$
I_0	Initial intensity	$J\ m^{-2}\ s^{-1}$
k	Boltzmann Constant	$m^2\ kg\ s^{-2}\ K^{-1}$
k_c	Rate constant of chemisorption	*Unitless*
k_d	Distribution coefficient	*Unitless*
K_E	Kinetic energy	*eV*
l	Path length	*Distance units*
$_{leachate}$	Suffix indicating concentration in leachate solution	*As specified*
N	Number of molecules	*Unitless*
P	Pressure	*Pa*
p_d	Particle diameter	*Distance units*
P_{svp}	Saturation vapour pressure	*Pa*
R	Ideal gas constant	$J\ K^{-1}\ mol^{-1}$
R_g	Submerged specific gravity	*unitless*
R_c	Rate of chemisorption	*unitless*
$S_{erupted}$	Sulphur generated by a volcanic eruption	*Conceptual*
$S_{exsolved}$	Sulphur exsolved from magma	*Conceptual*
S_{magma}	Sulphur dissolved in magma	*Conceptual*

S_{plume}	Sulphur in the eruption plume	***Conceptual***
$S_{scavenged}$	Sulphur scavenged from the eruption plume	***Conceptual***
T	Temperature	***°C***
t	Transmissivity	***Unitless***
T_g	Glass transition temperature	***°C***
$_{total}$	Suffix indicating a measure of total concentration	***As specified***
V	Volume of adsorbate gas	cc^3
V_m	Volume of adsorbate gas to form a monolayer	cc^3
w	Settling velocity	$m\ s^{-1}$
x	Distance	***Distance units***
θ	Bragg Angle	***°, Rad***
λ	Wavelength	***nm***
ν	Kinematic viscosity of water	$m^2\ s^{-1}$
ρ	Particle density	$kg\ m^{-3}$
ρ_{air}	Atmospheric density	$kg\ m^{-3}$
ρ_{gel}	Density of xerogel	***cc g-1***
ρ_{sk}	Density of the lattice	***cc g-1***
Σ	Molar absorption coefficient	***unitless***
τ_a	Atmospheric residence time	***Time units***
τ_s	Soil/sediment residence time	***Time units***
τ_v	Vegetation residence time	***Time units***
τ_w	Water column residence time	***Time units***
Φ	Porosity	$cc\ g^{-1}$
Φ_d	Average pore diameter	***Distance units***
Ω	Work function of X-ray photoelectron spectrometer	***eV***

LIST OF ABBREVIATIONS USED

AOGCM	Atmosphere-ocean general circulation model
0-100	Aluminosilicate xerogel experiments
AT-V	Atmosphere-variable experiments
BO	Bridging oxygen
BET	Brunaeur-Emmett-Teller
50-N	Ca-doped aluminosilicate xerogel experiments
DCT	Dacite
DSC	Differential scanning calorimeter
DTA	Differential thermal analysis
DRIFTS	Diffuse Infrared Fourier Transform Spectroscopy
EDX	Energy-dispersive X-ray spectroscopy
erfc	Complementary error function
FTIR	Fourier transform infrared spectrometer
FWHM	Full width at half maxima
IMFP	Inelastic mean free path
ICP-OES	Intercoupled Plasma Optical Emission Spectroscopy
MFC	Mass flow controller
NBO	Non-bridging oxygen
OP-FTIR	Open path fourier transform infrared spectroscopy
PHN	Phonolite
PAH	Polyaromatic hydrocarbons
PCB	Polychlorinated biphenyls
RHY	Rhyolite
SEM	Scanning electron microscope
SCCM	Standard cubic centimetres per minute
TP-V	Temperature-variable experiments
TPH	Tephrite
TEOS	Tetra-ethoxysilane
TGA	Thermogravimetric analysis
TI-V	Time-variable experiment
XRF	X-ray fluorescence spectroscopy

XPS	X-ray photoelectron spectroscopy
XRD	X-ray powder diffraction spectroscopy

FOREWORD

There is an extensive list of people who committed time and resources in support of this study. I would like to thank my supervisors, Dr. Pierre Delmelle in the Environment Department, and Professor Adam Lee and Dr. Karen Wilson at the School of Chemistry in Cardiff for their support. I would also like to gratefully acknowledge the aide and support of Dr. Nic Carslaw, in her role as chair of the Thesis Advisory Panel. I would also like to thank my external examiner, Dr. Marie Edmonds, for helpful and constructive criticisms during the viva defence.

I would also like to acknowledge the help provided by staff and co-workers in the many departments I have worked in over the past three years. Special thanks go to Rebecca Sutton for her patient tuition, and to Dr. Simon Hackett, Lee Dingwall, Janine Montero and the other Ph.D students in the Department of Chemistry in York for being always ready to answer questions or help when required. Those who donated services, resources and effort to this project out of generosity or a belief in the merits of the work are also owed a special debt of thanks. The invaluable support provided by Professor Don Dingwell at the Department of Earth and Environmental Science at Ludwig-Maximilians Universität München is greatly appreciated. The instruction, assistance and resources provided during work at that facility by Dr. Kai Hess, Dr. Werner Ertel-Ingrisch, Dr. Oliver Spieler, Yan Lavallee, Dr. Daniele Giordano and Dr. Ulrich Küppers are gratefully acknowledged. Thanks are also given to those who have performed happily performed external analysis; the late Dr. Tim Brewer at the University of Leicester; Dr. Leon Van Der Berg at the University of York; Dr. Alex Walton and Dr. Mike Ward at the University of Leeds; Dr. Dominique Richards at LMU; and Dr. Hugh Tuffen at the University of Lancaster.

Finally, I must also thank my family and friends for moral support, admonitions and occasional alcoholic interludes over the past three years, and Harry Snapper Organs of Q Division for apprehending Doug and Dinsdale Piranha. Without the efforts of all of the above, this study could not have been completed, and Spiny Norman would still be asleep in a disused aircraft hangar in Luton Airport.

Dinsdale?

AUTHOR'S DECLARATION

I, the undersigned, hereby assert that the data, interpretations and conclusions presented within this thesis are original and were produced by either by myself, or in the case of analytical techniques conducted at facilities other than the University of York, University of Leeds and the Ludwig-Maximilians Universität München, at my request. Selected highlights from Chapter 2, 5 and 6 have been presented at the American Geophysical Union Fall Meeting, 2009, and the European Geosciences Union General Assembly, 2010 (Appendix 2).

Name ..... Date .....

CHAPTER ONE

INTRODUCTION

CHAPTER ONE. INTRODUCTION

1.1. OVERVIEW

This study investigated sulphur dioxide (SO_2) scavenging by silicate ash particle surfaces within a volcanic eruption plume. The scavenging of volcanic volatile species such as SO_2, but also hydrofluoric acid (HF) and hydrochloric acid (HCl), upon the surfaces of silicate ash particles is known to emplace weakly bound soluble and insoluble salts on those surfaces. Halide salts, specifically F compounds, have previously been identified (Delmelle *et al.* 2007). Soluble chloride (Cl) and sulphur (S) salts have been inferred to exist from analysis of the solutions produced by aqueous leaching of the ash (e.g. Hinkley and Smith 1982). These salts are not only a mechanism by which volcanic volatiles are removed from the plume, but their removal from ash surfaces upon deposition may also have environmental consequences.

The ash particles coated with soluble S and halide salts sedimenting from the plume are a sink for volatile species otherwise to be dispersed in the atmosphere. By acting as a sink, scavenging of S and halide species by ash may potentially mitigate any regional (e.g. Highwood and Stevenson 2003) or perhaps global atmospheric impacts (e.g. Jones *et al.* 2005) associated with their emission. During the eruption of Laki in Iceland in 1783, a mist of sulphate aerosol shrouded much of northern Europe (Highwood and Stevenson 2003), causing thousands of deaths by respiratory illness across the continent. Scavenging of S species by ash may have removed a significant fraction from the atmosphere in proximity to the volcano, which could have prevented the impacts from being more serious than those already experienced.

Ash deposition may also act as a source of readily soluble nutrients (Frogner *et al.* 2001), toxic metals (Mcknight *et al.* 1981) and acids (Le Guern *et al.* 1980) into aquatic and terrestrial environments. These have potential for both beneficial and detrimental effects in the environment. Ash deposition around some volcanoes has been reported to bring fertilising impacts where nutrients provided by ash leaching were previously scarce (Cronin et al. 1998) In the aftermath of the Pinatubo eruption in 1991, for example, ferrous sulphate salts on ash surfaces deposited into iron-limiting ocean waters were hypothesised to have fertilising effects on phytoplankton (Frogner *et al.* 2001). The resultant carbon drawdown from atmosphere to ocean after increased primary productivity was estimated to be over 1.6 Pg (Frogner *et al.* 2001). The effects

may also be directly detrimental, as leaching of acids onto vulnerable fruits and planets may cause acid damage, devastating crops and agriculture in affected communities (Le Guern et al. 1980). The formation of these products on the ash surface may also change the physico-chemical properties of the volcanic eruption plume by dictating future scavenging mechanisms. The scavenging of volatiles by ash surfaces is therefore a subject which concerns not only the physical volcanogist, but also the communities and ecosystems living beneath the ash cloud or otherwise affected by the gas emissions.

To gain a mechanistic insight into volatile scavenging, experimental techniques and methodologies were used to investigate SO_2 scavenging by ash particles through a series of laboratory studies on synthetic model systems. Previous authors (Óskarsson 1980; Rose 1977; Taylor and Stoiber 1973) have put forward several hypotheses by which volatile species are scavenged. The range of possible controlling variables include ash and plume composition, mixing ratios, and environmental effects (Witham *et al.* 2005). Up until this study, these hypothesised variables remained speculative and poorly understood, mainly due to the small number of limited studies which have been previously conducted. The limitations of existing studies are in part a result of a reliance on analysis of the soluble compounds and acids leached from ash surfaces on contact with water or acid. Leachate analysis can identify and quantify the many elements (primarily Na, Ca, Mg, S, Cl; Witham *et al.* 2005) which may be removed from the ash (e.g. Hinkley and Smith 1982), but does not provide any insight into how, where or under what conditions within the eruption plume those salts were emplaced.

This study elected to better constrain the mechanisms of SO_2 chemisorption onto ash particle surfaces. Whilst other proposed mechanisms of scavenging are condensation processes and so are comparatively well understood, chemisorption by ash, simply by its nature, has a number of potential variables, including both compositional and temperature dependences. If determined, improved knowledge of these dependences could ultimately permit the uptake of volatile gases by adsorption on ash to be predicted and modelled. This has benefits not only for efforts to resolve volatile gas budgets and to better understand the volcanic system as a whole, but also in potentially providing advanced warning and pre-emptive guidance on potential chemical impacts which may be devastating to vulnerable communities. This study has therefore sought to determine the compositional and temperature dependence of SO_2 scavenging by ash, and in doing so, has provided a new level of insight into volatile scavenging within the eruption plume.

1.2. VOLCANIC ACTIVITY AND ITS PRODUCTS

Before considering volatile species scavenging on particle surfaces, it is necessary to consider the variables which lead to contact between the silicate ash phase and the volatile volcanic gas phase. Since the largest mixtures of ash and gas are generated within the heart of large explosive eruptions, this study will generally discuss volatile scavenging in context with such phenomena.

1.2.1 OVERVIEW OF A VOLCANIC ERUPTION

To consider volatile scavenging by ash within the heart of a volcanic eruption, the latter must be defined. Volcanic eruptions are essentially fluxes of energy and matter from the Earth's interior to the Earth's surface (Sigurdsson 2000), where the energy flux is derived from both the heat and explosive energy released and the matter flux is derived from molten silicate rock, or magma, or from the volatile species (H_2O, CO_2, SO_2, HF, HCl etc.; Delmelle and Stix, 2000) initially dissolved within that magma.

Volcanic eruptions are generated where a body of molten rock and exsolved volatile species rises buoyantly towards the Earth's surface through the surrounding rock, and ultimately breach the surface at a weak point, or volcanic vent (Sparks *et al.* 1997). The molten rock and volatile species may then be emitted as either an outpouring of molten rock or as explosive or effusive eruptions, which generate high speed (100-600 m s^{-1}) (Sparks *et al.* 1997), high temperature jets of volatiles and pyroclastic materials. The latter are fragments of molten rock and other solid matter, which then rise into the atmosphere under their own momentum and buoyancy (Carey and Bursik 2000). Once the momentum of the gas and particle jet has been expended, gravitational settling of pyroclastic ejecta may occur, removing the largest and heaviest particles first whilst the smaller and lighter particles may remain entrained within the buoyant gas plume. The gas-particle mixture rises as a turbulent, convecting plume until expansion, cooling and entrainment of atmospheric air brings the plume into density equilibrium with its surroundings (Fig. 1.1) (Sparks *et al.* 1997). Once at equilibrium, at the 'height of neutral buoyancy', the plume spreads laterally (Fig. 1.1) to form an eruption cloud which may then be diluted and dispersed, continuing as a cold volcanic cloud within the atmosphere for days, or even weeks after the eruption (Rose *et al.* 2000).

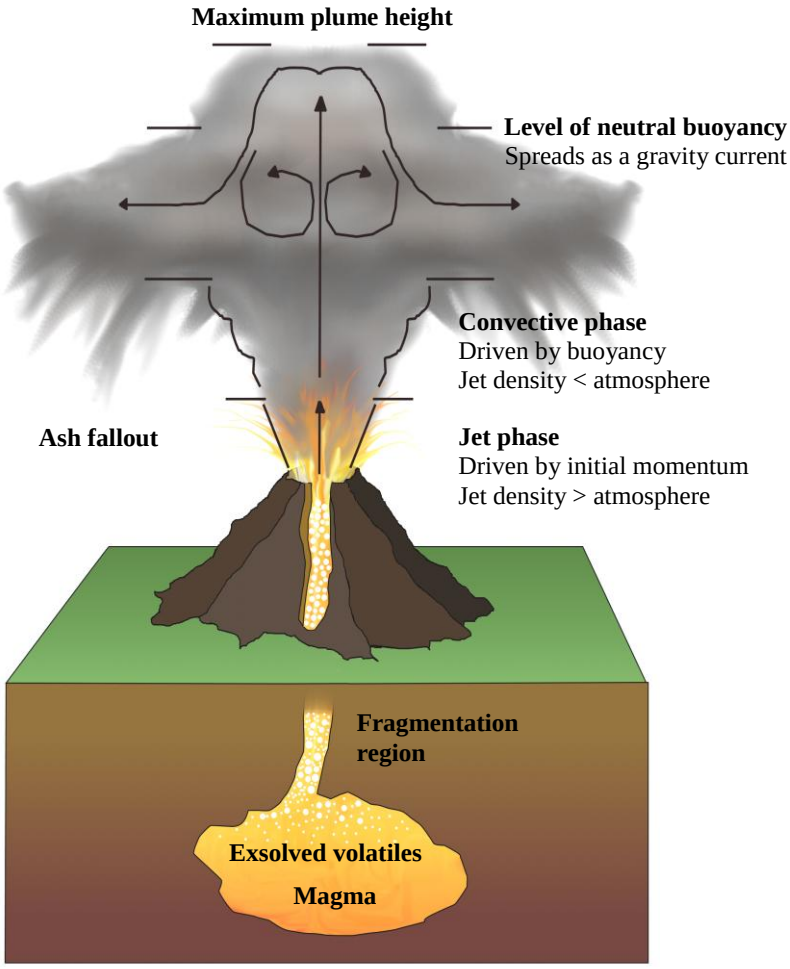

Fig. 1.1 *Stages of a volcanic eruption plume after fragmentation in the subsurface environment and emission from the volcanic vent, based on image in Carey and Bursik (2000).*

Explosive eruptions generate large quantities of silicate ash particles, which are considered to be any silicate particle with a particle diameter (p_d) of less than 2 mm (Heiken and Wohletz 1992), and therefore the mechanisms driving these eruptions are of great interest to this study. Explosive eruptions are initiated by violent exsolution of the dissolved volatile species from the magma, which sends a buoyant mass of gas up the volcanic conduit, entraining fragments of magma, crystalline material and lithic rock eroded from the conduit walls. The most explosive eruptions generate the greatest mass of fine ash due to the greater energy of fragmentation in these eruptions (Zimanowski *et al.* 2003). High energy fragmentation occurs where volatile content is high, but where the growth of gas bubbles (*vesicles*) formed within the magma is impeded by high viscosity. Magma viscosity is dictated by its chemical composition (Mysen and Richet 2005), which may be considered on a general basis by the total-alkali silica system which is used to classify magma and volcanic rocks (Fig. 1.2).

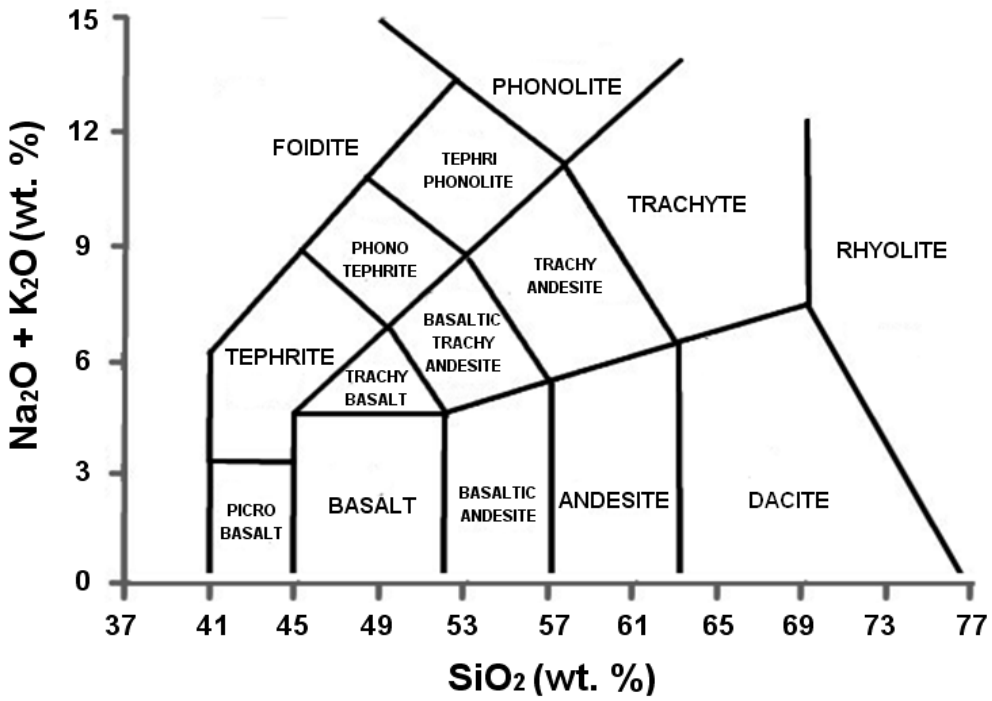

Fig. 1.2 *The total-alkali silica classification system, as used in classifying igneous and pyroclastic rocks (Le Maitre et al. 2002).*

In general, the SiO_2 content of a melt, commonly between 40-80 wt. %, increases as the content of CaO, MgO and Fe_2O_3 with each commonly contributing <10 wt.% to the magma (Rogers and Hawkesworth 2000). The Na_2O, K_2O (<10 wt.%) and Al_2O_3 (10-20 wt. %) content are independent of SiO_2 content (Rogers and Hawkesworth 2000). Considering melt composition in more detail, there may also be dissolved volatiles such as H_2O, CO_2 and SO_2, and crystalline phases including biotite, muscovite, montmorillonite, quartz, cristobalite, plagioclase, hematite and many others (Cashman et al. 2000; Davis et al. 1981). Magma viscosity is increased by the presence of crystalline phases and the strongly bonded aluminosilicate network, and is decreased by the presence of the alkali and alkaline earth cations and dissolved volatiles within the melt (Spera 2000).The variation in viscosity with varying magma chemical composition has direct implications not only for the explosivity of the eruption but also the silicate ash particles generated by that eruption, controlling particle chemical composition but also controlling particle bulk and surface physical properties.

1.2.2. ASH PARTICLES: PHYSICAL AND CHEMICAL PROPERTIES

This study focuses on the scavenging of volatile species on particle surfaces and therefore, the physical (i.e. texture, morphology) and chemical (i.e. surface composition) properties of the particles and the mechanisms which may control these properties are of great importance. Although silicate ash particles may be derived from a number of mechanisms (magma fragmentation, explosive water-magma interaction, magma shearing, particle abrasion or conduit wall erosion; Heiken, 1972), in the largest explosive eruptions, those particles generated by the fragmentation of magma may predominate.

Particles of silicate ash generated by magma fragmentation may have the bulk chemical composition of that magma, including any crystalline components embedded within the melt at the time of fragmentation. At the surfaces of silicate ash particles generated by magma fragmentation, a thin glass coating has been observed to cover crystals at the particle surface (Heiken and Wohletz 1992), so ash particle surfaces could be largely glassy, unless later abrasion or fracture exposes fresh crystals. Although silicate ash particle surfaces may be comprised of the same constituent elements as the source magma and bulk ash particle (Delmelle *et al.* 2007), the chemical composition of the initial surface remains unknown. It may be possible that different fragmentation energies and modes of particle generation may create different surface compositions. These surface compositions could be produced by the varying strengths of different chemical bonds in the glass network in response to stress and strain forces (Scholze 1990). Different glass surface compositions may also be produced by alterations from exposure to heat, abrasion and aqueous or acid alterations (Dunken 1982), all of which may occur before deposition into receiving environments.

In addition to directly controlling ash bulk chemical composition and being a major influence on surface chemical composition, magma chemical composition may also directly control ash particle bulk physical properties such as bulk density (ρ) and optical properties. Within the eruption plume, particle aggregation may create low ρ ash particle clusters (200 kg m^{-3}), but the ρ of single silicate particles may be of the order of 700 kg m^{-3} up to 3300 kg m^{-3} (Shipley and Sarna-Wojciki, 1983). The ρ of silicate ash depends upon the atomic masses of the ions within the glass or crystalline components, but generally decreases with increasing Si content and increasing vesicularity (Shipley and Sarna-Wojciki 1983). The chemical composition and crystallinity of the melt also

dictates particle refractive and reflective properties, which produce the colourings observed in natural ash samples. A low-Si, high-Fe basaltic glass absorbs visible light, so being typically darker than the high Si, low-Fe glass, which reflect and transmit more light (Scholze 1990). Whilst particle colour and ρ have no direct influence on volatile scavenging, ρ and particle diameter (p_d) dictate particle sedimentation rates (Ferguson and Church 2004), controlling the time available for scavenging.

Magma chemical composition directly influences particle chemical composition, which in turn dictates the fore-mentioned ρ, reflective and refractive properties, but may also control particle morphology. Particle morphology may in turn dictate the specific surface area (a_s), being the specific surface area per unit mass of ash particles ($m^2\ g^{-1}$). By its further control on eruption size and mass of ash produced, the magma chemical composition may also dictate the total available surface area produced in the eruption (A). The total available surface area in this case represents the product of a_s and the total mass of ash produced, so representing the size of the silicate surface available for scavenging reactions. In macroporous ash particles (Delmelle *et al.* 2005), a_s may be a product of particle morphology and surface texture, whilst A may be a product of a_s, particle size distribution and the mass of erupted material. The properties influencing a_s and A are therefore the explosivity of the eruption and magma fragmentation, and hence are an indirect product of magma melt composition.

By its effect on melt viscosity, magma chemical composition controls the mechanism of magma fragmentation and eruption explosivity, and hence dictates the total A available for scavenging reactions. In low viscosity, low silica melts, the exsolution of volatile species from solution forms gas bubbles (vesicles) within the melt. The buoyancy and lower densities of the exsolved volatiles and the fluid nature of the melt enables their expansion and percolation to the surface, where they may burst, releasing a spray of melt droplets as the melt surface undergoes ductile deformation and failure (Cashman *et al.* 2000). In contrast, the vesicle walls of silicic melts may behave as immobile constraining walls, inhibiting gas expansion and ascent, and leading to pressurisation of the vesicles (Cashman *et al.* 2000). When the internal pressure of the vesicle exceeds that of the overlying melt, brittle and explosive failure of the viscous magma may result (Cashman *et al.* 2000). Both ductile and brittle fragmentation mechanisms become increasingly efficient and generate greater quantities of smaller particles as the fragmentation energy and eruption explosivity increases (Zimanowski *et al.* 2003), but the surface texture and morphology of the particles may be different. In

the case of fragmentation in fluid melts, the spray of melt droplets may be deformed by aerodynamic forces during rapid quenching, and so may have rounded particle morphologies (i.e. Pele's Hair; Heiken and Wohletz 1992), whilst fragmentation in viscous melts disrupts the near-solid vesicle walls, generating shards of broken vesicle walls with a random, irregular morphology (Cashman *et al.* 2000).

Fragmentation energy increases the amount of small particles which are generated, and by approximating ash particles to simple spheres, it is demonstrated in Fig. 1.3, calculating a_s with equation [1.1] that the former will increase as p_d decreases. It would therefore be expected that the greatest particle a_s would therefore be produced by the largest explosive eruptions, providing the greatest opportunity for extensive volatile scavenging. In any further discussion of the p_d of ash particles, the notation of Durant and Rose (2009) is used, where 'very fine', 'fine' and 'coarse' are used to differentiate between particles with $p_d < 30$ μm, $30 \leq p_d < 1000$ μm and $1000 \leq p_d \leq 2000$ μm respectively.

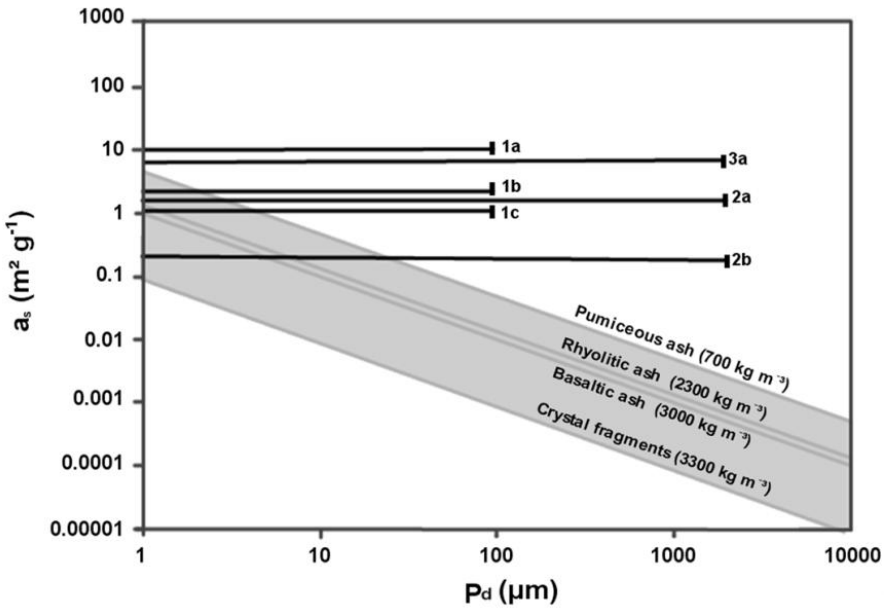

Fig. 1.3 *Relationship between specific surface area (a_s) and particle diameter (p_d) for ash particles, assuming spherical particles with known ρ (Shipley and Sarna-Wojciki 1983). The a_s of hydrothermally altered volcanic ash (1a - Delmelle et al. 2005) a range of selected other volcanic ash samples (Delmelle et al. 2005; 1b - 1c, range from Horwell et al. 2003) and weathered ash from ash explosions and dome collapses at Soufriere Hills during 1999 (2a, 2b, 3a - Horwell et al. 2003) are illustrated. Where size distribution data are available, these are indicated by the length of the bars.*

$$a_s = \frac{6}{p_d \rho} \qquad [1.1]$$

The particle surface texture may also act to increase a_s. Comparison between the calculated a_s in equation [1.1] and the observed a_s of variously sized volcanic ash particles from a number of different eruptions indicates that the spherical approximation underestimates the actual a_s measured by gas porosimetry by an order of magnitude or more (Fig. 1.3). The disparity is attributed to surface texture, particle morphology and particle size distribution. The immediate surfaces of ash particles generated by magma fragmentation may be primarily glassy; although ash can contain extensive bulk crystalline materials, those at the surface have sometimes been observed to be coated with a thin layer of silicate glass (Heiken and Wohletz 1992). After fragmentation, alteration of particle surfaces may increase surface roughness and a_s. The most commonly recorded values for silicate ash particle a_s are generally less than 2 m^2g^{-1}. Where surface deposits are emplaced by hydrothermal alteration or weathering, a_s have been up to 4 times higher, due to the disruption of a smooth surface to make a rougher surface. Comparing a flat surface of known size to one with identical dimensions, but covered with troughs, hills and other surface features, it is clear that the latter will have a higher area within the same unit of space. The above is illustrated in Fig. 1.4, where the complex and highly vesicular surface in Fig 1.4 (a) would be likely to have a higher a_s than the smoother surfaces of the glassy sample in Fig 1.4 (b).

a) 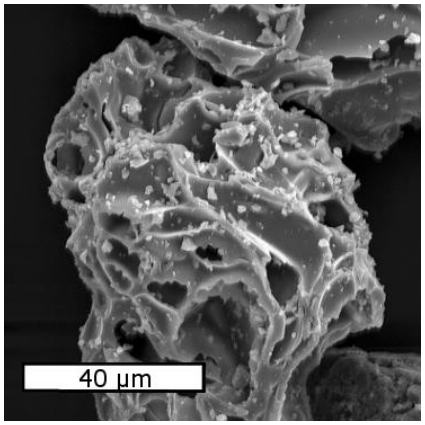

b) 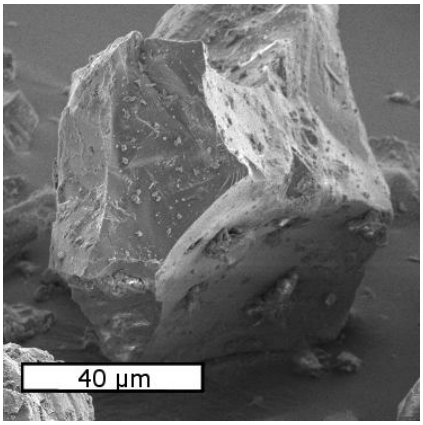

Fig. 1.4 *SEM micrographs - (a) Ash from an eruption at Redoubt on March 22nd, 2009, showing a highly vesicular ash shard with many ruptured gas bubbles. Image courtesy of Pavel Izbekov, Alaska Volcano Observatory. (b) Ash from an eruption at Mt. Etna on August 3rd, 2001, having no obvious vesicularity. Micrograph (b) was taken on a FEI Nova 200 Nanolab Field FEGSEM at the University of Leeds.*

The highest a_s ever reported is 8 m^2 g^{-1} by Delmelle *et al.* (2005), this was attributed to ash which had extensive surface deposits of anhydrite ($CaSO_4$) and clay minerals deposited by hydrothermal alteration. Similarly, the weathered pyroclastic ejecta making up the lava dome at Soufriere Hills was reported to have a_s of 6.4 m^2 g^{-1}, whilst those from explosive eruptions at the same volcano were reported to be between 1.2 – 3.4 m^2g^{-1} (Horwell *et al.* 2003). High a_s ash may therefore be a product of weathering and hydrothermal alterations, whilst particles generated by magma fragmentation might be expected to have a lower a_s, more in keeping with the previously cited 2 m^2g^{-1} value.

1.2.3. VOLATILES IN THE ERUPTION PLUME

Volatile species are derived from the gases emitted either from passive degassing or during an actual eruption. Passive degassing occurs constantly in volcanically active regions, as gases released by magma or from hydrothermal systems percolate to the surface and escape into the atmosphere (Delmelle and Stix 2000). Gases emitted during an eruption can be derived from exsolution during fragmentation, or from the release of any vapour or volatilised fluid phases which were pre-existing within the volcanic conduit or magma chamber (Shinohara 2008).

Volatiles released from magma by exsolution are ultimately a product of the chemical properties of that magma and the environment in which it resides. Volatile species dissolve into the silicate melt, but can reach saturation, after which any further volatiles will form gas bubbles in the magma. The solubility of volatiles in magma decreases in the order HF > HCl ≈ H_2O > S species > CO_2 (Delmelle and Stix 2000). Since volatile solubility is dictated by chemical composition, temperature and pressure (Mysen and Richet 2005), different gas compositions may therefore be yielded as a magma ascends, cools or incorporates material which alters its composition. For example, CO_2 has the lowest solubility of the fore-mentioned species, and so is the first volatile species to reach saturation in response to a decrease in pressure or temperature. As such, magma degassing occurring at depth is generally higher in volatiles with low solubility, i.e. S species, CO_2 than those at shallower depths. This concept was illustrated by the study of gas emissions at Stromboli in 2005 (Burton *et al.* 2007). Passive degassing in the crater was found to produces gases with 18.5 mol. % more H_2O than and 19.5 mol. % less CO_2 than those produced by explosions driven by gas slugs rising from depth. After exsolution, the concentration and speciation of volatiles may be

altered by changes in pressure, temperature and in redox conditions (Heald *et al.* 1963) or by interaction with groundwater or hydrothermal systems en route to the surface (Delmelle and Stix 2000).

In compiling existing estimates and measurements of volcanic gas compositions, Stoiber (1995) calculated that in an average year, the global flux of volcanic gases to the atmosphere contained 94.9 mol. % H_2O, 3.5 mol. % CO_2, 0.9 mol. % SO_2, 0.5 mol. % HCl and <0.1 mol. % HF (Table 1.1). In light of the previous discussion, it should not be surprising that even in examining only a few studies of passive gas emissions (Table 1.1) that around this 'average' composition, there can be significant variation.

Table 1.1 *The average annual gas composition (1) as estimated by Stoiber (1995) and a compilation of selected volcanic gas compositions determined by varying techniques, including OP-FTI[2,3,4] and direct sampling of fumaroles and condensates[5,6]. Data are compiled from 2) Edmonds et al. (2005), 3) Allard et al. (2005), 4) Burton et al.(2007), 5) from selected data presented in review by Francis et al. (2000) in review, 6)Taran et al. (2001).*

Volcano	Source	Volcanic gas composition (mol. %)				
		H_2O	CO_2	SO_2	HCl	HF
Annual average annual[1]	**Compiled**	**94.9**	**3.5**	**0.9**	**0.5**	**< 0.1**
Kilauea[2]	Lava lake	75.0-85.0	0.1-3.0	10.0-13.0	0.3-0.6	0.5
Mt. Etna[3]	Fountain	92-96	3.7-7.3	0.4-1	< 0.1	< 0.1
Stromboli[4]	Crater	82.9	13.6	1.7	1.7	
Stromboli[4]	Explosion	64.4	33.1	1.8	0.33	
Unzen[5]	Fumaroles	95.5-96.8	1.5-2.7	0.4-0.5	0.26	
Mt. St. Helens[5]	Fumaroles	91.6-98.6	0.9-6.9	<0.1 - 0.2	< 0.1	< 0.1
Nevado Del Ruiz[5]	Crater	96.8-92.4	2.2-5.2	0.4-0.5	< 0.1	
Soufriere Hills[5]	Lava dome	90.3	4.3	0.8	3.6	
Colima[6]	Fumaroles	89.2-98.6	0.82-9.3	0.2-2.8	0.1-0.5	< 0.1

The most dramatic divergences from the purported average are the compositions of the three primary constituents, H_2O, CO_2 and SO_2. H_2O concentrations are subject to extensive range, with the lowest recorded value being 64 mol. %, over 30 mol. % lower than the 'average' value (Burton *et al.* 2007). CO_2 concentrations are likewise variable, and whilst the average concentration is 3.5 mol. %, the highest and lowest concentrations for CO_2 are 33 and 0.1 mol. % respectively. SO_2 concentrations recorded are generally around the 1 mol. %, but data from Kilauea demonstrates that it is possible for SO_2 emissions to be more than ten times higher (Edmonds *et al.* 2005). It should

also be noted that there are likely to be differences between eruption plume compositions and those which are passively degassed by the same volcano. It is not presently possible to determine explosive eruption plume gas compositions at the point of emission because the high ash content of the plume makes spectroscopic analysis impossible. This is in part because high volumes of ash interfere with spectroscopy techniques, and also because scavenging of volatiles by ash before spectroscopy can be brought to bear may remove a significant fraction of volatiles before their presence can be identified.

1.3. THESIS RATIONALE

1.3.1. RATIONALE FOR STUDY OF SO_2

This study investigated the mechanisms by which SO_2 molecules are scavenged by silicate ash surfaces during their transition through the eruption plume. Such scavenging reactions are considered to be an important component of in-plume chemistry. Based upon comparison of pre-eruptive melt S concentrations and the mass of S extracted from ash during aqueous leaching, Rose (1977) estimated that ash particles could be a sink for up to 35% of SO_2 within the plume. Similar values have been found by later authors via similar methodologies (de Moor et al. 2005; Varekamp et al. 1984). The potential for such removal of SO_2 from the gas phase onto particle surfaces is noteworthy because it represents a significant sink for volcanic fluxes emitted to the atmosphere, and hence a mitigating influence on atmospheric impacts of gas release. In addition, limited understanding of scavenging of SO_2 and other S species by ash also impedes efforts to resolve eruption plume gas compositions, and as a consequence, the volcanic volatile S budget. These topics are treated in further detail in the following sections.

1.3.1.1. MITIGATION OF SO_2 ATMOSPHERIC IMPACT BY ASH SCAVENGING

The environmental impacts associated with SO_2 emission to the atmosphere are derived from the conversion of SO_2 and other S species to aqueous sulphate aerosols (H_2SO_4). The volatile S species initially exsolved from the magma and emitted by the eruption are hydrogen sulphide (H_2S, SO_2, Delmelle and Stix, 2000) and trace amounts (ppt) of SO_3 (Heald *et al.* 1963). Within the atmosphere, H_2S may be oxidised to SO_2 within a few days of the eruption (Textor *et al.* 2004) and SO_2 is oxidised to form H_2SO_4 aerosols (Baird 2000; Bluth *et al.* 1997). Conversion of SO_2 to H_2SO_4 aerosols may occur via the reaction in equation [1.2] (Bluth *et al.* 1997) in the gas phase, and by the reaction in equation [1.3] (Baird 2000) when SO_2 in the gas phase is dissolved into suspended water droplets. H_2SO_4 aerosols with p_d of 0.1-1.0 μm are able to effectively absorb, backscatter and reflect inbound solar radiation (Self 2006). Volcanic H_2SO_4 aerosol may therefore disrupt the global climate, cooling the troposphere, and warming the stratosphere provided that the aerosols are in sufficient abundance and with optimal particle size distribution.

$$SO_2(g) + OH(g) + 3H_2O(g) \leftrightarrow H_2SO_4(l) + HO_2(g) \quad [1.2]$$

$$SO_2(g) + H_2O(l) \leftrightarrow H_2SO_3(l) \quad [1.3]$$

Scavenging of SO_2 from the atmosphere by various mechanisms may therefore mitigate the possible atmospheric effects of sulphate aerosol generation from SO_2 release. Such mitigating effects may be particularly important where the largest eruptions (>1 km^3 magma erupted, Newhall and Self, 1982) may release the largest quantities of SO_2 and may result in distinct climatic impacts. These single, infrequent eruptions may emit much larger amounts of SO_2 into the stratosphere than calculations based on the average annual SO_2 flux would indicate. Current estimates of volcanic SO_2 budgets indicate that in an average year, approximately 9.7 Mt of SO_2 are emitted by passively degassing volcanism, whilst only approximately 1Mt of SO_2 is erupted explosively (Shinohara 2008). In contrast to this, the 1991 eruption of Mt. Pinatubo produced 19 Mt of SO_2 (McCormick *et al.* 1995). This is essentially double what is estimated to be emitted on average in a year, released in a 9 hour eruption. The SO_2 and H_2SO_4 aerosols released by the eruption of Mt. Pinatubo in 1991 resulted in a 0.1°C decrease in global mean temperatures in the year following the eruption (McCormick *et al.* 1995). The temperature deviation resulting from the eruption of Mt. Pinatubo may be only of limited impact, but in the case of larger eruptions, more prolonged and larger deviations to the global temperatures may result.

Large-scale eruptions are confined to the geologic past, and as such, the potential extent and impacts of these eruptions must be inferred from limited data. Emissions of S from very large explosive eruptions (erupting in excess of 100 km^3 of magma, Newhall and Self 1982) have been estimated from studies of eruption products and paleoproxies such as ice cores (Oppenheimer 2002; Rampino and Self 1982). The Toba eruption, 74000 years ago (74 ka) is one such example, with estimates of S emissions ranging from the equivalent of 66 Mt of SO_2, determined by experimental petrology, 1000-3200 Mt of SO_2, determined from ice core data, and 6600 Mt of SO_2, determined by petrological estimates (Oppenheimer 2002 and references therein). It has been suggested that eruptions releasing such large quantities of SO_2 or other S species could have catastrophic impacts on the global climate. In modeling a 6000 Mt input of SO_2 to the atmosphere within an atmosphere-ocean global climate model, Jones *et al.* (2005) predicted a global cooling of 10°C immediately after the eruption, and prolonged temperature decreases of 0.5-3°C in the following fifty years. The impacts of such

cooling would be considerable; Rampino and Ambrose (2000) described the impacts occurring from the predicted 5°C cooling after the eruption of the Toba supervolcano as being a global ecological disaster, causing total destruction of tropical ecosystems and causing heavy damage to those at higher latitude. The eruption of Toba has also been hypothesised to be the cause of the recorded decrease in human population down to possibly less than 10,000 individuals (Rampino and Ambrose 2000).

In any of the above volcanic eruptions, the removal mechanisms for SO_2 and H_2SO_4 aerosols may occur via different mechanisms within the troposphere and stratosphere and in the eruption plume. In the troposphere, global impacts resulting from SO_2 emissions are negligible due to fast acting wet and dry depositional scavenging, with an *e-folding* time (the time taken to decrease by a factor of *e*) on the order of hours or days (Rodríguez *et al.* 2008). Scavenging may occur to a greater extent in more humid, warmer air where wet depositional mechanisms may be more efficient. Once within the stratosphere, however, where wet deposition is impeded and dry deposition does not occur, SO_2 oxidation may proceed via slower, gas-phase reactions (Bekki 1994). In the eruption plume, the water vapour rich environment may scavenge gases by the precipitation of water vapour as hydrometeors or may be scavenged by ashfall. In a non-steady state, non-hydrostatic numerical model (ATHAM), for a plume reaching a height of 17 km within 5 minutes of the eruption, Textor *et al.* (2003) found that after 90 minutes of scavenging by hydrometeors, more than 99% of the SO_2 erupted remained within the plume. In contrast, where hydrometeors were frozen or ice nuclei otherwise formed, as much as 20% of the SO_2 erupted was scavenged onto the ice particles. Scavenging by ash particle surfaces, on the other hand, has been hypothesised to remove up to 40% of the SO_2 from the eruption plume (Rose 1977; Varekamp *et al.* 1984), and although the mechanisms and variables controlling that scavenging remain unknown, scavenging by ash therefore represents a potentially major, if not the primary in-plume SO_2 scavenging mechanism.

1.3.1.2. THE ROLE OF SO_2 SCAVENGING IN VOLCANIC S BUDGETS

The unknown mechanisms and variables which may affect the scavenging of SO_2 and other volatile species by silicate ash surfaces directly limit the quantification of volcanic S budgets, which has implications not only for study of current eruptions, but also for studies considering the volatile emissions and the potential environmental impacts associated with the large historic supervolcanic eruptions previously discussed.

Quantifying present-day volcanic S budgets, summarised in equation [1.4] can be attempted via analysis of melt inclusions, pockets of undegassed magma captured by crystals. Such mechanisms do not consider the presence of any pre-existing exsolved S as a fluid or vapour phase within the magma chamber (Scaillet et al. 1998). Pre-existing exsolved volatiles enables a larger release of S than could be contained in the mass of magma erupted, particularly in more silicic melts (Shinohara 2008). The so-called 'excess volatile degassing' phenomena has been proposed to be a product of one of several possible mechanisms. These mechanisms include the sinking of dense, degassed magma by convection, leaving a low density vapour rich phase at the top of the magma chamber or by the degassing of an unerupted magma at greater depth within the magma chamber and the percolation of the exsolved volatiles to the melt surface (Shinohara 2008). Excess S degassing has been identified in the eruptions of El Chichón, Mexico, 1982 (Luhr 1990) and at Mt. Pinatubo (Wallace and Gerlach 1994), and has also been hypothesised to explain the 1-2 order of magnitude disparity between the experimental petrography estimates for SO_2 emissions from the Toba supereruption and the estimates from ice core data for the time (Oppenheimer 2002).

$$S_{magma} + S_{exsolved} = S_{erupted} = S_{plume} +_{(?)} S_{scavenging} \qquad [1.4]$$

To determine the total mass of S erupted ($S_{erupted}$) requires that both dissolved and exsolved within the magma chamber be constrained. It is also possible to estimate $S_{erupted}$ by constraining the total S within the plume (S_{plume}). Since there is no direct way to determine $S_{exsolved}$, it is instead estimated by comparing S_{magma} to S_{plume}. This calculation is however complicated by the difficulties in constraining how much S has been scavenged from the plume by the time the S_{plume} reading is taken. This includes considering S washed out by rainfall, or, appropriate to this study, scavenged by ash. If scavenging occurs extensively before the first measurement, than comparisons of S_{magma} and S_{plume} may underpredict the total mass of S exsolved. Since there is at present no

knowledge of how, to what extent and when within the eruption plume SO_2 is scavenged by ash, as the most prevalent form of in-plume scavenging, it is therefore not known whether S_{plume} estimates have been derived correctly. For this reason, the contribution of $S_{scavenging}$ in equation [1.4] is marked with a $+_{(?)}$ indicator . In order to both validate the existing models for the volcanic S budget and then to apply such knowledge for the prediction of the hazards of future eruptions further study of the scavenging of SO_2 by ash is necessary.

1.3.1.3. MECHANISMS OF VOLATILE SCAVENGING BY ASH

There are currently three hypotheses which have been proposed to result in SO_2 scavenging by ash particle surfaces throughout the volcanic eruption plume and atmosphere. These mechanisms may depend on specific combinations of in-plume variables and environmental conditions. One of the proposed mechanisms emplaces aqueous acids from the aerosol phase via condensation or via the dissolution of volcanic volatiles from the vapour phase into an existing aqueous layer (Rose 1977). Another of the proposed mechanisms deposits soluble and insoluble compounds via the precipitation of gas condensates and sublimates onto exposed particle surfaces (Taylor and Stoiber 1973). The final mechanism proposed is that which is investigated in the course of this study, whereby the volatile species undergo direct chemical reaction (chemisorption) or physical adhesion (physisorption) onto the exposed silicate ash particle surfaces (Óskarsson 1980). The three hypothesised mechanisms were combined by Óskarsson (1980) to form a three stage conceptual model (Fig. 1.5) which has been repeatedly cited since that study (Hinkley and Smith 1982; Witham *et al.* 2005), though the aqueous phase and aerosol scavenging model has been more repeatedly invoked (Edmonds *et al.* 2003; Oppenheimer *et al.* 1998; Rose 1977).

Based on leachate analysis, previous authors (Rose 1977) have proposed that scavenging of aqueous aerosols and the dissolution of volatiles into aqueous layers existing on particle surfaces may be the primary mode of volatile scavenging. Aqueous aerosol scavenging may precipitate salts on the ash particle by leaching cations from the ash surface (Rose 1977), which then form the soluble salts as the aqueous layer evaporates (e.g. Gilbert and Lane 1994). Such a mechanism may occur only below the temperature at which the aqueous acids condense, below 338°C for H_2SO_4 and below 100°C for the halogen species (Óskarsson 1980). A low temperature aqueous phase scavenging mechanism was proposed to explain the observed dependence of leachate

concentration on particle a_s up to intermediate distances from the plume, and the decrease in leachate concentrations relative to a_s with increasing distance thereafter (Rose 1977). The observed trend was attributed to the increased evolution of aqueous aerosols with distance from the vent coupled with the decreasing chance of collision due to particle sedimentation and plume dilution (Rose 1977). Interpretations of SO_2 scavenging mechanisms from leachate analysis should however be treated with caution, as the S leached from the ash may be partially derived from mechanisms other than aqueous acid condensation, and those mechanisms occurring at high in-plume temperatures may also have shaped the reactivity of the ash surface to lower temperature scavenging mechanisms. In any study of volatile scavenging by silicate ash particle surfaces, it is therefore necessary to first study the high temperature mechanisms within the core of the eruption plume.

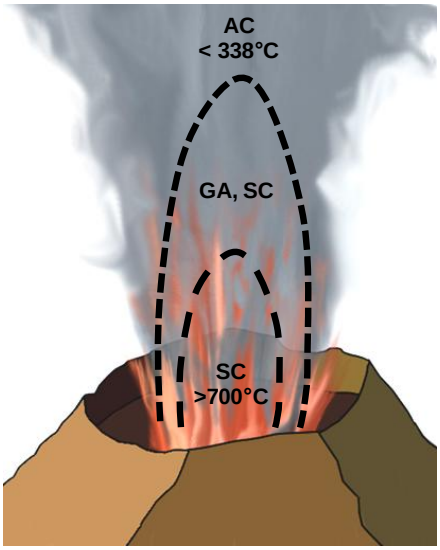

Fig. 1.5 *Cartoon illustrating the combined conceptual model of Óskarsson (1980), showing high temperature deposition of aerosols salts condensing from the vapour phase (SC), a region of gas adsorption and salt condensation (GA, SC), and a low temperature aqueous acid condensation region (AC).*

The high temperature scavenging mechanisms may include the condensation of volatile salts, as first proposed by Taylor and Stoiber (1973) from the study of rock encrustations and condensates found around high temperature fumaroles and on lava surfaces. Thermodynamic modelling and studies of fumarole gas emissions at temperatures up to 900°C show that a diverse range of minerals may be deposited or precipitated onto rock surfaces and quartz glass sampling tubes as the gas phase cools. These minerals may include Na, K, Cl and S as halite (NaCl), sylvite (KCl) and a range

of metal sulphate and sulphide salts (Bernard and Le Guern 1986; Churakov *et al.* 2000). The exact phases deposited are likely to depend on gas composition, fugacity and temperature, whilst the concentrations emplaced may depend on the temperature, pressure and exposed surface area available for gas condensates to be formed upon. It may therefore be possible to model the salt-condensation mechanism through use of thermodynamic calculations, but that would require knowledge of the exact volatile content of gas emissions from explosive eruptions, rather than by reference to those of passively degassed magma via fumarole studies.

Finally, and of greatest interest to this study, SO_2 and other volatiles may be removed from the plume by direct interaction with the ash surface. This was a mechanism first proposed by Óskarsson (1980), after experimental studies on HF-H_2O adsorption by a basaltic ash sample. Unfortunately, knowledge of the variables and mechanisms which may dictate scavenging of SO_2 and other volatiles by adsorption on ash surfaces remains limited. There have been a small number of experimental studies which have investigated volatile scavenging by adsorption on ashes, but these are limited in number and in scope. Further to these studies, some possible insights may be studies in systems which share some key similarities. The available data and existing hypotheses are outlined in the following section.

1.3.1.4. SO_2 SCAVENGING BY ADSORPTION ON ASH PARTICLE SURFACES

There have only been two studies, one published and one unpublished, which have directly investigated scavenging of volatiles by ash surfaces, and then only on a limited basis. Óskarsson (1980) observed that 1 ml of boiling HF-H_2O fumes washed over a basaltic ash sample formed $CaSiF_6$ and CaF_2 on particle surfaces at temperatures up to 1100°C, but beyond identifying the reaction products formed, no further effort to determine the mechanisms driving adsorption was made. The unpublished study (Gu, 1996 referred to in Gu *et al.* 1999) was conducted under equilibrium conditions in a sealed bag containing 400 ppm_v of SO_2 and a sample of dacitic ash at room temperature. Concentrations of SO_2 used in this experiment were not relevant to atmospheric conditions. In both of the above studies, no effort was made to study the effect of volatile adsorption on different ash types. Although interpretations of gas scavenging mechanisms on ash surfaces would be hampered by the unknown in-plume reaction history of those surfaces, even the most basic insight would have represented a significant advancement in the existing knowledge of the time.

More recently, studies on experimental glass materials have offered substantially more insight into the scavenging mechanisms. Experimental glasses with compositions of commonly erupted melts have been used in two recent studies, both of which were based on the same experimental work. Andesite, dacite, rhyolite and silicate glasses were exposed to a static SO_2 atmosphere at a pressure of 100 KPa at 20°C for 24 hours. It was found that the S scavenged by adsorption in this time period was between 20-25 μmol m^{-2} (Schmauß-Schreiner 2007), apparently occurring to greatest extent in the rhyolite glass. Across all glasses, it was found that between 15-74% of the S adsorbed was irreversibly bound to the surface but no effort to identify the reaction products was made. In a later S K-edge micro-XANES (μXANES) study of the glass materials, it was found that surface S concentrations which remained adsorbed during ultra-high vacuum (UHV) exposure were 0.1% for the pure silica glass and 0.4-1.0% for the others (Farges *et al.* 2009). This was attributed to adsorption occurring at alkali and alkaline earth network modifying sites, stabilising the adsorbed SO_2 (Farges *et al.* 2009). It was therefore proposed that irreversible SO_2 adsorption in isolated alkali and alkaline-earth bearing glass regions of ash surfaces could provide micro-sites for scavenging.

Such a proposed mechanism is a significant advancement on the earlier work of Óskarsson (1980), but still offers limited insight into possible high temperature scavenging mechanisms. It remains unknown which of the alkali and alkaline earth cations may react with SO_2 or other scavengeable volatiles within the eruption plume. Reference to industrial studies on soda-lime silicate glasses may suggest that Na would be expected to be the primary reacting cation. SO_2 gases are commonly used in so-called 'fining' processes, where SO_2 adsorption is used to extract Na from the glass, forming an sulphate deposit which is easily removed (Volf 1984). This mechanism, by which the resistance of the glass to aqueous leaching is improved, has been demonstrated to be increasingly efficient with increasing temperature. At 366°C, under a 1% SO_2, 2% H_2O atmosphere, air atmosphere, Na-Ca-silicate glasses formed 7 g m^{-2} of Na_2SO_4 over the course of an hour. In contrast, the same experiment conducted at 800°C emplaced more than 200 g m^{-2} of Na_2SO_4 (Douglas and Isard 1949). Although these studies may point to Na as a primary reactive cation at the glass surface, in light of the studies on natural ash by Óskarsson (1980), reactivity of Ca can also not be discounted. In the HF-H_2O experiments, Óskarsson showed that for one basaltic ash, Ca-F compounds were the primary reaction products at all temperatures. Furthermore, in coal-fired power stations and industrial furnaces, Ca-based, rather than Na-based sorbents are chosen for

desulphurisation reactions, which are known to scavenge SO_2 with greatest efficiency at 800-1000°C (Nowok *et al.* 1995). Since neither of the above systems are ideal analogues for the array of complex Na, Ca, Fe, K and Mg bearing aluminosilicate melts from which ash materials are derived, nor for the eruption plume atmosphere, it is not presently possible to provide any further discussion of the likely mechanisms and possible products formed by the adsorption reaction.

1.4. SELECTING EXPERIMENTAL VARIABLES

Of the mechanisms of volatile scavenging outlined in the previous section, it was decided to study the mechanism of SO_2 adsorption onto ash surfaces. This mechanism represents arguably the largest remaining significant area of uncertainty in our understanding of volatile scavenging processes by ash. This is not to say that the other mechanisms are well defined and or constrained, but they are at least recognised as condensation processes. In principal, with an improved understanding of in-plume physical and chemical composition, it is likely that these mechanisms could be successfully modelled. Similar hypothetical modelling efforts investigating the adsorption of SO_2 and other volatiles by ash surfaces would be significantly impeded in contrast. As described above, there is limited understanding of the mechanisms and controlling variables, and it is only in the past twelve months that alkali and alkaline earth metals have been identified as being key to low temperature SO_2 adsorption by ash surfaces. The question of what mechanisms and variables could drive adsorption within the higher temperature eruption plume itself remains to be answered.

In order to investigate possible mechanisms driving SO_2 adsorption within the plume, it was decided to investigate SO_2 adsorption through a series of laboratory scale experiments. The experimental protocol developed model systems designed to investigate the effects of ash chemical composition on adsorption of SO_2 from a gas stream in a furnace operating at temperatures up to 800°C. The post-experiment surfaces of the model ash systems were characterised using modern bulk and surface sensitive analytical techniques to identify the reaction products formed and the effect of SO_2 adsorption on the composition and structure of the glass surface itself.

1.4.1. ADSORPTION

In order to investigate the variables which may control SO_2 adsorption, it is therefore necessary to first consider those variables which dictate all adsorption processes.

1.4.1.1. PRINCIPLES OF ADSORPTION

Adsorption of volatile species may proceed via either the physical adhesion of an adsorbate species (i.e. SO_2) to an adsorbent surface (i.e. silicate ash) via physisorption or through the chemical reaction of the adsorbate with the adsorbent

surface, being chemisorption. Physisorption occurs by weak *Van der Waals* forces, where the negative electron charge of the adsorbent surface may result in a slight attractive force holding the adsorbate molecule to the adsorbent surface, although adsorbate-adsorbate interactions may also occur, depositing multiple layers of volatile species (Erbil 2006). Physisorption is a low energy process which does not bind adsorbate molecules to a specific surface site, instead enabling them to freely diffuse around the sample surface, and decreases with increasing temperatures until the energy imparted by the surrounding environment exceeds the energy requirement to remove the weakly bound molecule from the surface. In the case of SO_2, the critical temperature at which SO_2 is no longer physisorbed is 157°C (Schenk and Steudel 1968). On the other hand, chemisorption is a chemical bonding which only occurs at specific sites on the sample surface, rather than on both the adsorbent surface and adsorbate molecules as in physisorption (Erbil 2006). In the case of SO_2, chemisorption may occur on Lewis acid and Lewis base sites, with SO_2 acting as a Lewis base in the case of the former and a Lewis acid in the case of the latter. A Lewis acid and base pair exchange electrons between each other; the Lewis acid accepts the electrons from the Lewis base. In the case of SO_2 adsorption, S can act as a Lewis acid, accepting a electron from an oxide site, or the O component of SO_2 can act as a lewis base, accepting electrons from exposed cation sites. Chemisorption of SO_2 directly onto cations in this manner is thought to be of limited significance and chemisorptions on Lewis base sites is expected to predominate (Ziolek *et al.* 1996). Chemisorption can occur at any temperature, but requires activation energy to form the initial surface bond, thus chemisorption generally increases with increasing temperature until there is sufficient energy to break the bond formed via chemisorption (Erbil 2006).

The variables controlling chemisorption can be considered as relating to one of two components, firstly, in the act of the collision between the adsorbate molecule and the surface, a factor common to both physisorption and chemisorption, and secondly, in its chemical reaction with that surface. The collision rate of gas molecules per unit area is given by equation [1.5], where N is the number of gas molecules, P is the partial pressure of the gas, m is the molecular mass of the gas, k is the Boltzmann constant, T is the temperature and the presence of the 2π constant indicates the assumption of a spherical gas molecule (McCash 2001).

$$\frac{dN}{dt} = \frac{P}{\sqrt{2\pi mkT}} \qquad [1.5]$$

The chemisorption of a gas molecule onto a particle surface may be described by the rate constant of the reaction, which is dependent on activation energy to initiate the reaction between the gas molecule and surface site. This activation energy increases exponentially with increasing temperature, so that the rate constant of chemisorption (k_c) may be described by equation [1.6], where dN/dt is the number of collisions, E_a is the activation.energy, and R is the ideal gas equation (McCash 2001).

$$k_c = \frac{dN}{dt} e^{\left(\frac{-Ea}{RT}\right)} \qquad [1.6]$$

The rate of chemisorption of an adsorbate species of known pressure, temperature and quantity onto any surface may therefore be given by the combination of equation [1.5] and [1.6] to give equation [1.7]. Equation [1.7] is a combination of the two, where the first component dictates the chance of collision at known pressure and mass of gas under a specified temperature. The second component of the equation describes chemisorption onto the number of exposed surface sites, depending on the activation energy and temperature (McCash 2001).

$$k_{ads} = \left[\frac{P}{\sqrt{2\pi mkT}}\right](1-\theta)e^{\frac{-Ea}{RT}} \qquad [1.7]$$

1.4.1.2. SIGNIFICANCE OF ADSORPTION IN SO_2 SCAVENGING

Equation [1.5] to [1.7] can be used to illustrate the key variables governing SO_2 scavenging by chemisorption onto the ash surface, and so may be used to identify the key variables which it is necessary to investigate in this study. The key variables which can be inferred to dictate the mass of SO_2 adsorbed onto ash surfaces from equations [1.5] to [1.7] are therefore; the exposure time, which dictates the amount of time within the plume for adsorption to occur; the in-plume SO_2 concentration and pressure, which may dictate the rate of collision between SO_2 molecules and the silicate ash surface; the plume temperature, providing activation energy for chemisorption at the surface after collision; and the number of available sites on the ash particle surface for adsorption reaction.

The variables controlling chance collision between molecules of the volatile species and adsorbing silicate ash surfaces within the eruption plume were described in equation [1.5] to [1.7] as being dependent on the pressure, temperature and ejected mass of the scavengeable volatile species. Considering the eruption plume, the mass of silicate ash particles suspended within the plume may also dictate the chance of collision by controlling the total available area (*A*) upon which adsorption occurs. Eruption plume factors dictating the chance of collision between the volatile species and the silicate ash surface may therefore depend on both magmatic and in-plume properties, in a complex series of interactions between the turbulent convection of the plume, the entrainment of atmospheric air and particle sedimentation (Wilson *et al.* 1978), in addition to the respective mass and chemical composition of the volatile species. At the present time, the sophisticated plume models required to investigate the physical interactions between volatile species and silicate ash particles within the eruption plume are not available, and so this study cannot investigate this component of the scavenging mechanism.

The variables affecting the adsorption of the gas molecule upon collision with adsorption sites, whether Lewis acid or Lewis base sites, are the number of sites on the silicate ash particle surface, the activation energies of the specific sites and the temperature at which chemisorption occurs [1.6]. The chemical composition of the ash surface is assumed to be similar to that of the bulk ash particle, but the structure of that surface and the SO_2 chemisorption sites available as a result of that structure remain unknown. Silicate ash particles which have been recovered after an eruption cannot be studied in SO_2 adsorption experiments, as the chemisorption sites which may exist upon the particle surface may have been filled or modified by in-plume transition and deposition into receiving environments. To study the mechanisms of SO_2 chemisorption on ash surfaces, this study used simple model systems to explore the effects of chemical composition on SO_2 chemisorption and reaction product formation.

From equations [1.5] to [1.7], the temperature of the eruption plume is also hypothesised to be a major controlling variable, and this is consistent with the observations from the studies of commercial glasses and flue gas sorbents. The temperature of the plume provides the activation energy required for adsorption of SO_2, and therefore, with increasing temperature, the amount of available activation energy increases exponentially, and hence the mass of chemisorption should increase (McCash 2001). The influence of temperature on scavenging of volatiles within the eruption

plume is however fundamentally coupled to the duration of time which the volatile species and silicate particles spend in contact at that temperature.

The in-plume exposure times to high temperatures are likely to be brief. The initial temperature of an eruption may vary between 700°C for high silica magmas and 1200°C for low silica magmas (Sparks *et al.* 1997), but rapid cooling of the plume to atmospheric temperatures may occur. The main engines of heat loss from volcanic eruptions are either via the rapid loss of large pyroclasts from the eruption or via the entrainment of air into the turbulent plume. Air entrainment results in a transfer of heat from the eruption plume to the atmosphere, and so a decrease in the temperature of the former (Wilson *et al.* 1978). In large explosive eruptions with abundant fine ash and a lower overall content of coarse pyroclasts, the loss of heat from large pyroclast sedimentation may be limited, and air entrainment may be the principle engine of heat loss (Wilson *et al.* 1978). Cooling times associated with air entrainment remain unknown, but from the one dimensional model of Mastin (2007), and assuming that all particles with $p_d < 100$ μm are in thermal equilibrium with the plume (Woods and Bursik 1991), it may be estimated that ash particles may cool from 800°C to 500°C within 1-10 seconds.

Based on the likely coupled effect of temperature and exposure time, this study investigated both variables in the course of its experiments on SO_2 adsorption in order to determine whether even a brief high temperature exposure can deposit the masses of S observed in leachate solutions, and hence whether high temperature adsorption should be considered a key component of volatile scavenging mechanisms.

1.5. RESEARCH QUESTIONS AND PROJECT SCOPE

In the course of this thesis, there were considered to be two distinct objectives. The first objective, that which was the focus of the experimental research, was to determine the variables and mechanisms controlling SO_2 adsorption on silicate ash surfaces within the eruption plume. The variables investigated specifically through the experimental research were the effect of chemical composition, of temperature and of exposure time. These research questions are summarised as follows;

1. What is the effect of surface chemical composition on the mechanisms and reaction products formed by SO_2 adsorption on volcanic ash surfaces?

2. What is the effect of temperature on the mechanisms and reaction products formed by SO_2 adsorption on volcanic ash surfaces?

3. What is the effect on exposure time on the mechanisms and reaction products formed by SO_2 adsorption on volcanic ash surfaces?

In constraining or better defining the role of these variables, and hence in meeting the specific objectives outlined above, a broader overall objective was to be achieved. This study sought to improve upon the existing knowledge of in-plume scavenging by deploying model analytical techniques and taking advantage of advances in research in related fields since the scavenging of volatile species by ash was first recognised. The overall objective of this study is therefore to improve the existing conceptual model of volatile scavenging by ash within the eruption plume. By revising or expanding upon the existing research, particularly with respect to the influence of temperature, exposure time and composition, this study further hopes to identify the volcanic settings where scavenging may occur to greatest extent. Such identification would have implications not only in constraining volcanic S budgets in more detail, but also in determining the impact of volcanic S on local, regional or global ecosystems.

1.6. THESIS OUTLINE

This study presents a discussion of the importance and implications of volatile scavenging by silicate ash particle surfaces for physical volcanologists and for those affected by volcanic ashfall or volatile emissions to the atmosphere. In Chapter 2, the environmental implications associated with volatile scavenging onto particle surfaces in comparison to those of the physical and chemical hazards associated with the effect of the mass of ash deposited are discussed. Following the environmental discussion, the sequence of experiments which comprise this study's efforts to gain mechanistic insight into SO_2 adsorption on silicate ash surfaces are introduced. The experimental protocols, methodologies and analytical techniques used in all experiments throughout this study are presented in Chapter 3. Chapter 4 presents the results of an experiment which attempted to synthesise simple binary and ternary aluminosilicate and calcium aluminosilicate systems via low temperature wet-chemical techniques, to explore a new method for the study of SO_2 adsorption over a range of eruption plume temperatures. The results and conclusions of Chapter 4 did not support the continued use of such synthetic systems. Therefore, Chapters 5 and 6 present the rationale, results and interpretation of a series of SO_2 adsorption experiments carried out on glasses with compositions of commonly erupted volcanic ash, under varying temperature, exposure time and atmospheres of different chemical composition. The interpretations, volcanic implications and recommendations for further study based on the findings of Chapters 5 and 6 are presented in Chapter 7, which concludes the thesis.

CHAPTER TWO

ENVIRONMENTAL EFFECTS OF VOLCANIC ASH EMISSION

CHAPTER TWO. ENVIRONMENTAL EFFECTS OF ASH EMISSION

2.1. INTRODUCTION

Silicate ash emission and deposition in the aftermath of a volcanic eruption is the most widespread of the visible impacts associated with a volcanic eruption. Ash may be emitted into the atmosphere, sometimes remaining entrained for days or even weeks (Lamb, 1970) before deposition and may be dispersed over 1000's km^2 (Rose *et al.* 2001). After emission, ash may be heavily deposited in proximity to the vent, but in the largest eruptions, thinner, fine grained ash deposits may be found at distances over 1000 km from the vent (Thorarinsson 1979). Due to the global distribution of volcanoes and due to the widespread dispersion of ash into the atmosphere, there may not be a single ecosystem on the planet, including surface waters of fresh water and marine environments, wetlands, forests, pastures, croplands and snowpacks, which will not experience ashfall at some point in its history, and a range of potential physical and chemical impacts may result from such an event.

The environmental impacts associated with ash emission and deposition may be partially a result of the flux of solid particles of varying density, surface texture, colour and morphology (Heiken and Wohletz 1992) to the atmosphere and receiving environments. The catastrophic damage associated with burial of ecosystems beneath metres of ash in proximity to the volcano is well known (e.g. Eggler 1948), but a more complex array of environmental responses, including changes to local albedo and temperature (Jones *et al.* 2005; Mass and Robock 1982), changes to soil-water regimes (Diaz *et al.* 2005; Tejedor *et al.* 2003) and physical alterations to surrounding geomorphology (Hayes *et al.* 2002) may also occur. Ash emission and deposition is also of environmental concern because via the ash particle surface, a pulse of S and halide salts and acids (e.g. Hinkley and Smith 1982) may be quickly released shortly after deposition, whilst on a more long term basis, a gradual release of the major, minor and trace elements commonly found in crustal or mantle rock may occur via dissolution reactions (e.g. Barker *et al.* 2000). The release of acids, salts and the elements derived from ash dissolution may result in a range of impacts in receiving environments, including alterations to soil, water and atmospheric chemistry, physical and chemical impacts on vegetation such as acid and salt damage (Cook *et al.* 1981) and potentially

fertilising or toxic impacts (Duggen *et al.* 2007; Frogner *et al.* 2001; Mcknight *et al.* 1981) from bioavailable element release into soils and surface waters. The potential consequences resulting from the environmental impacts of ashfall are not just confined to the biota within the afflicted ecosystem, but cause secondary impacts on dependent communities, which may in turn have local, regional or even global scale repercussions.

Although a range of physical and chemical effects associated with ashfall have been proposed, there is limited knowledge of the eruptive and environmental properties which dictate the extent, range, severity and any interrelation between these physical and chemical impacts. Accordingly, there is also limited knowledge of what mitigating or remedial techniques should be deployed to different communities in the aftermath of a volcanic eruption. Existing studies are primarily based on post-eruption observations and studies (e.g. Cook *et al.* 1981; Le Guern *et al.* 1980), and a small number of experimental studies have also been conducted (e.g. Cronin *et al.* 1997; Dahlgren *et al.* 1999; Sneva 1982). With the exception of review articles which focused on the impacts in the specific areas of the Pacific North West immediately surrounding Mt. St. Helens after the 1980 eruption (Dale *et al.* 2005; Lee 1996) and a recent review of ocean fertilisation by ashfall (Duggen *et al.* 2010) no previous study has provided a comprehensive review of the environmental impacts associated with sufficient detail to guide the focus of future research over the potential impacts proposed. This review chapter therefore examines the range of physical and chemical effects in atmospheric, terrestrial and aquatic ecosystems which may occur in the aftermath of ash emission and deposition. The existing research into the impacts of ashfall from studies dating as far back as 1914 are integrated with modern understanding of both volcanic ash and the interactions occurring in afflicted ecosystems in this chapter, with the intent to highlight the environmental impacts which may be of greatest concern to both the volcanologist and to the communities which live beneath the ash cloud.

2.2. ENVIRONMENTAL SIGNIFICANCE OF THE VOLCANIC ASH SURFACE

It has long been established that in-plume reactions lead to the formation of soluble salt deposits on the surfaces of ash particles (Witham *et al.* 2005 and references therein). The salts formed are derived from volcanic halide (mainly HCl, HF) and sulphur gas species (mainly SO_2, H_2S). The physical presence of these soluble salts on the ash surface has been determined by atomic force microscopy (Delmelle *et al.* 2007), but apart from $CaSO_4$ (Gilbert and Lane 1994), the nature of the specific salts formed has not been determined.

When immersed in water, ash releases soluble material which can contain more than 50 different chemical elements (Table 2.1, Table 2.2), with Ca, Cl, Na and S usually being the most abundant (Witham *et al.* 2005). It has been shown that the soluble elements are quickly released in the first minutes of exposure, and may be accompanied by a decrease in the leaching solution pH. The rate of extraction decreases rapidly after this point, being approximately constant after 2-4 hours (Frogner *et al.* 2001; Jones and Gislason 2008). In laboratory conditions or in the environment, concentrations in leachate are enhanced by acidic conditions (Hinkley *et al.* 1982) or by decreased water to ash ratios. The leachate solution may contain elements derived from (i) soluble surface salts and acids (i.e. NaCl, $CaSO_4$, H_2SO_4) adsorbed onto the ash surface and (ii) leaching of the silicate and non-silicate components of the ash surface. There is no way to determine the individual contributions of the above components in solution, but the initial pulse of dissolved material is generally attributed to the dissolution of the soluble surface salts and the dilution of any aqueous acids on the ash surface.

With the exception of the sulphur and halide species, which originate from gas-scavenging reactions within the plume, the material leached from the ash may represent at most, only a few percent of the element in the bulk ash. Ash from the 1980 Mt. St. Helens eruption leached in a 1:14 ash: deionised water ratio for a 4-hour period removed up to 6% of the major cations (Hinkley and Smith 1982). It is, however, the rate of extraction which is significant. In a 30 minute extraction in pH 4 conditions, the amount of Si which was leached from ash from the 2000 Hekla, Iceland, eruption (Frogner *et al.* 2001) would require 300 years to be generated by pure dissolution

(Wolff-Boenisch *et al.* 2004). This rapid release of soluble material on initial contact between ash and water is of environmental concern as the pulse may be a source of acute environmental impacts which could not be provided by a slower release of material from ash weathering and dissolution.

Table 2.1 *Maximum, median and minimum concentration of extracted major elements from ash samples (μg g^{-1}) compiled from 28 ash leachate data sets (Armienta et al. 2002; Armienta et al. 1998; Cronin et al. 1998; Hinkley and Smith 1982; Jones and Gislason 2008; Luhr et al. 1984; Óskarsson 1980; Risacher and Alonso 2001; Taylor and Stoiber 1973). The qualifiers 'good', 'moderate' and 'poor' are an arbitrary value to indicate the quality of the data relative to the number of samples. 'Poor' is considered any element where the total number of data points is less than 5, 'moderate' is between 5 and 10, and 'good' is any in excess of 10..*

Element	Water soluble ash component (μg g^{-1})			
	Maximum	Median	Minimum	Data quality
Al	909	20	3	Good
Ca	22160	530	24	Good
Cl	11160	550	53	Moderate
F	3135	23	2	Good
Fe	606	2	<1	Good
K	790	45	4	Good
Mg	2278	70	4	Good
Mn	144	10	<1	Good
N	274	28	<1	Good
Na	2560	322	30	Good
P	66	2	<1	Moderate
S	7680	255	5	Moderate
Si	390	18	6	Good

Table 2.2 *Maximum, median and minimum concentration of extracted minor elements from ash samples (μg g^{-1}) compiled from 28 ash leachate data sets (Armienta et al. 2002; Armienta et al. 1998; Cronin et al. 1998; Hinkley and Smith 1982; Jones and Gislason 2008; Luhr et al. 1984; Óskarsson 1980; Risacher and Alonso 2001; Taylor and Stoiber 1973). The qualifiers 'good', 'moderate' and 'poor' are an arbitrary value to indicate the quality of the data relative to the number of samples. 'Poor' is considered any element where the total number of data points is less than 5, 'moderate' is between 5 and 10, and 'good' is any in excess of 10..*

Element	Water soluble ash component (μg g^{-1})			
	Maximum	Median	Minimum	Data quality
As	0.1	0.1	<0.1	Moderate
B	9.4	2.9	0.4	Moderate
Ba	4.8	1.1	0.1	Moderate
Br	7.2	2.4	0.5	Moderate
Cd	0.3	0.1	<0.1	Poor
Co	1.3	0.2	<0.1	Good
Cr	0.5	0.1	<0.1	Good
Cu	50.0	0.3	0.1	Good
La	<0.1	<0.1	<0.1	Poor
Li	1.2	0.2	0.1	Moderate
Mo	0.2	0.2	0.1	Poor
Ni	1.5	0.3	0.1	Good
Pb	<0.1	<0.1	<0.1	Poor
Sb	<0.1	<0.1	<0.1	Poor
Se	0.2	0.1	0.1	Moderate
Sn	0.1	0.1	0.1	Moderate
Sr	35.0	5.4	0.9	Good
Ti	18.7	0.4	0.2	Poor
Tl	<0.1	<0.1	<0.1	Poor
V	0.3	0.1	<0.1	Moderate
Y	<0.1	<0.1	<0.1	Poor
Zn	18.0	2.6	0.2	Good

2.3. ASH RESIDENCE TIME IN RECEIVING ENVIRONMENTS

The residence times of ash in the atmosphere (τ_a), on vegetation surfaces (τ_v), on soil surfaces (τ_s) and within the water column (τ_w) partly dictate the magnitude of the effects that ash may have on each environmental medium.

2.3.1. RESIDENCE TIME IN THE ATMOSPHERE

The residence time of ash in the atmosphere (τ_a) is governed by its settling velocity and how far it has to fall through the atmosphere before deposition. Particle settling rate through the atmosphere is described by turbulent or laminar flow equations, depending on p_d, ρ_a and the drag effects induced by the morphology of the particle (Bonadonna *et al.* 1998). Assuming that ash particles are spherical and neglecting the drag effects, the settling velocities of ash particles can be calculated using equations [2.1] and [2.2] for laminar flow regimes and transitional laminar-turbulent flow regimes respectively, where ρ_{air} and μ are the density and viscosity of air respectively (Bonadonna *et al.* 1998).

$$w = \frac{g{p_d}^2(\rho_a - \rho_{air})}{18\mu} \qquad [2.1]$$

$$w = p_d\left(\frac{4{\rho_a}^2 g^2}{225\mu\rho_{air}}\right)^{\frac{1}{3}} \qquad [2.2]$$

The approximation to a spherical particle underestimates particle a_s, which implies that with a larger surface area for drag effects, actual settling velocities may be much slower than those calculated. With this caveat, Fig. 2.1 illustrates that for low density particles such as pumiceous ash (200 kg m^{-3}) and ash aggregates (1200 kg m^{-3}) (Shipley and Sarna-Wojciki 1983) fine ash may take up to a week to fall from a height of 30 km, whilst very fine ash may weeks, months or even years. As illustrated in Fig. 2.2, the mass of ash in the atmosphere decreases rapidly with time. From infrared satellite imagery, meteorological information and ash deposition data from the 1992 eruptions of Mount Spurr, Alaska in 1992, Rose et al (2002) estimated that after 24 hours, less than 3% of the initial erupted ash mass remains airborne.

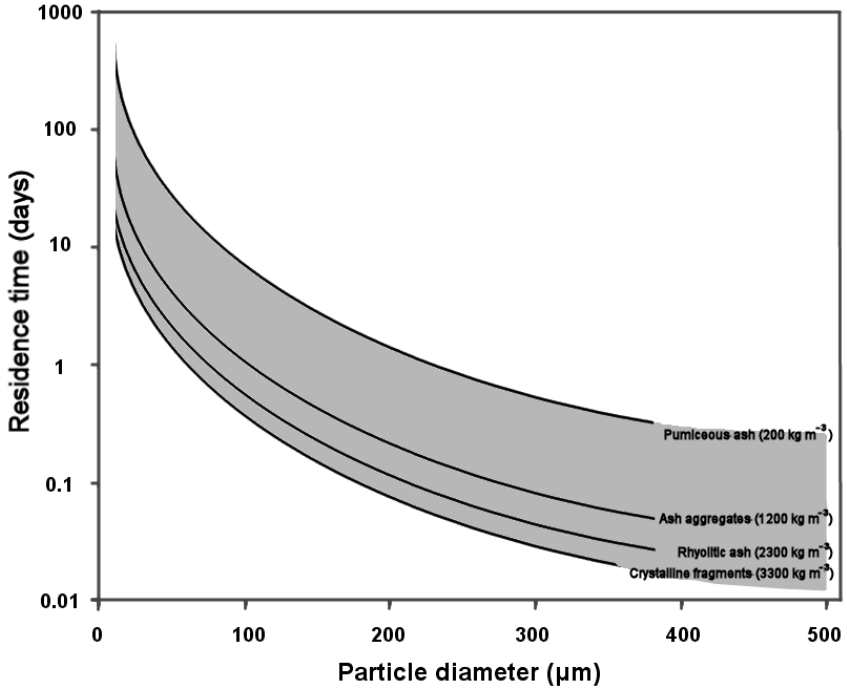

Fig. 2.1 *The relationship between p_d and τ_a, calculated from equation [2.2] for spherical ash particles with known densities (Shipley and Sarna-Wojciki 1983) assuming an injection height of 30 km. Particles above 500 µm fall in turbulent and laminar-turbulent transitional flow regimes and are not shown due to their very short residence times.*

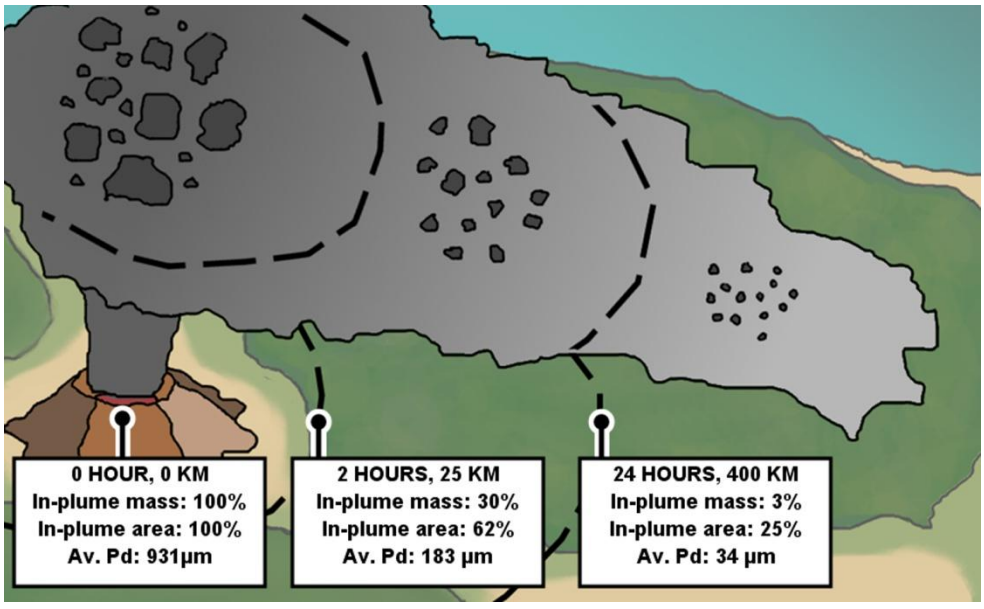

Fig. 2.2 *Cartoon diagram showing the estimated total available area (A) remaining in an eruption plume after 0, 2 and 24 hours, calculated using the mass loss rates and particle size ranges from the three stage conceptual models of volcanic plume/cloud evolution by Rose et al. (2001). Particles are assumed to be spherical with a_s calculated via equation [2.2], with ρ_a of 2500 kg m^{-3} consistent with dacitic ash, an ash type commonly erupted explosively.*

2.3.2. RESIDENCE TIME ON VEGETATION

Before reaching the Earth's surface, ash may be intercepted by canopy foliage (Fig. 2.3, Fig. 2.4), understorey vegation in forested regions, or by grasses, herbage and crops in pastures or plains. Ash retention by vegetation may instigate leaf damage but may also delay the release of ash into the surface environment by acting as a temporary reservoir. In general, the interception of particles with p_d >10 μm by any surface, including vegetation, occurs via impaction (Smith and Staskawicz 1977). Retention is controlled by a number of additional physical variables, many of which are plant-specific. Retention after impaction is enhanced by favourable leaf or branch architecture. In studies of London Plane trees (*Platanus aceriolia*) exposed to urban road dust over a growing season, particles in the 5-50 μm range were found to be most prevalent on exposed, windward twig surfaces and at the base of leaf blades. Accumulation at leaf bases was driven by water erosion as particles were washed from the leaf via the central vein (Smith and Staskawicz 1977). A similar phenomenon is observed in volcanic ash in Fig. 2.3 and Fig. 2.4.

Fig. 2.3 *Ash on leaf surfaces after an eruption in 2009 at Volcano Dukuno in Halmahera, Indonesia. Ash deposits on the exposed leaf surfaces show signs of cementing or crusting, and the accumulation of thick deposits on exposed leaf stems can also be observed. Photography by Martin Rietze, 2009, reproduced by kind permission of the author.*

Surface roughness plays an important role in particle retention, as it mitigates the erosive impacts of wind and water. Cook *et al.* (1981) showed that leaf trichomes on pubescent (hair covered surfaces) leaves and fruits favoured ash retention. In contrast, smooth, waxy leaves are less prone to holding particles at the surface (Smith and

Staskawicz 1977). In the event of heavy deposition, the overloading of the surface may result in its structural failure, and in the case of vegetation, this may result in early abscission of fruit, leaves and branches (Cook *et al.* 1981), which may shorten the residence time of ash on vegetation surfaces and deliver into terrestrial systems. +

Fig. 2.4 *Ash deposits on coniferous needles after the eruption of Mt. St. Helens. Ash has been removed from the exposed needles, but is retained along the central core of the branch where foliage is densely packed and sheltered from wind erosion. Photograph courtesy of Lyn Topinka, United States Geological Survey.*

Wind and water erosion remove ash from vegetation surfaces, but no estimates for the residence time of ash on vegetation (τ_v) are available. Studies of simulated nuclear fallout on vegetation may be used for comparison. After a single application of dry quartz particles, grasses were found to have longer particle retention times than those for trees. In studies of ^{137}Cs-tagged quartz particles (44-88 μm) intercepted by common grasses, deposit retention was 50%, 25% and 12.5% after 4, 37 and 81 days, respectively, likely due to the reduced impact of wind erosion close to the ground (Peters and Witherspoon 1972). In experiments with quartz particles (88-175 μm), oak and pine trees lost 91% and 10%, respectively, of the initial deposits (48 g m^{-2}) after 1 hour under 11-20 km hr^{-1} wind (Witherspoon and Taylor 1969). After one week, oak and pine trees had shed more than 99% of the deposited material; the primary loss mechanism was thought to be water erosion (Witherspoon and Taylor 1969).

Wetting of ash during and/or after deposition may increase retention times on vegetation by cementing the ash deposit into a solid and persistent crust. The cementing reaction occurs when calcium dissolved from surface salts forms calcium hydroxide. Calcium hydroxide then reacts with the vitreous silica component of the ash to form Ca-silicates which can bind neighbouring particles together (Hossain 2004). Dissolved Ca in meteoric waters may trigger cementing in pozzolanic materials (Barker 2007), whilst the dissolution of Ca-based surface salts may also have cementing properties. The cemented ash forms a crust, described as being 'almost like a cement pavement'(Anderson 1908), which has been observed on the surfaces of ash-covered coniferous vegetation, surviving for months after the eruption of Mt. St. Helens (Seymour *et al.* 1983). The delayed release of ash retained on vegetation may mitigate the immediate consequences of ashfall on soil and other environments, but longer retention times may also lead to damaging impacts long after the eruption has ceased. Strong storms in the year following the eruption of Volcan Hudson in 1991 resuspended tree-borne ash deposits, causing secondary damage to recovering agriculture (Inbar *et al.* 1995).

2.3.3. RESIDENCE TIME ON SOIL AND SNOW

Left uneroded, deposits on terrestrial surfaces (i.e. soil and snow) are compacted and eventually cemented by rainfall. If vegetation is not completely buried under ash, the ash deposit may also become stabilized by organic matter (e.g. Lynch and Elliot 1983). Ultimately, it may be incorporated in sediment, soil or snow to form part of the soil profile or snow stratigraphy. In contrast, where erosive forces operate, the residence time of ash deposits on soil may be limited.

Wind-driven saltation is a well-established process responsible for 50-80% of all soil erosion. Saltation bounces particles (p_d ~ 100-500 μm) short distances along the soil surface (Lyles 1988) and may similarly be a dominant mechanism for ash erosion. In Iceland, Arnalds *et al.* (2001) observed through wind tunnel experiments that wind speeds less than 2 km hr^{-1} were able to move coarse, porous ash deposits (p_d > 1000 μm). Resuspension of very fine ash and fine ash with p_d < 100 μm requires higher wind speeds. Under 11 km hr^{-1} winds, erosion of Mt. St. Helens ash deposits in Eastern Washington increased concentrations of submicron particles above ambient values at 0.4-2 km above ground but particles with p_d >1 μm did not exceed ambient atmospheric concentrations for the region (Hobbs *et al.* 1983). Above 11 km hr^{-1}, transport of ash

particles up to 2 km into the atmosphere was observed after erosion of ash deposits in Eastern Washington following the 1980 eruption of Mt. St. Helens (Hobbs *et al.* 1983). Stronger winds (25-36 km hr^{-1}) winds raised atmospheric concentrations of these particles an order of magnitude above the ambient atmospheric concentration (Hobbs *et al.* 1983). In extreme cases, such resuspension may create a new ashfall event even months after the initial eruption. In the year after the eruption of Volcan Hudson, Chile, in 1991, dry conditions, high winds (mean windspeed 33 km h^{-1}) and a series of major windstorm events (10 days with maximum wind speeds of 60-96 km h^{-1})[1] remobilised and resuspended ash, depositing it over cleared sites and recovering agriculture (Inbar *et al.* 1995).

Such extreme erosion is less likely in wetter climates as cementing and wetting of the deposit increases the threshold velocity for wind erosion. In addition, where vegetation cover exceeds 30%, in general, wind erosion does not occur (Pye 2009 and references therein). Erosion in these circumstances is water driven, which on terrestrial surfaces proceeds via sheet, rill, or gully erosion. Sheet erosion removes ash uniformly on low angle slopes whilst rill and gully erosion, scouring channels into ash deposits on steeper slopes (Fig. 2.5), removing more material but along paths of least resistance (El-Swaify *et al.* 1982).

Fig. 2.5 *Steep slopes encourage formation of rill erosion channels which combine and feed into gully channels eroding ash deposits on Rift Valley escarpements west of Ol Doinyo Lengai. Photo courtesy: Tom Pfeiffer / www.volcanodiscovery.com.*

[1] Meteorological information for the year 1991-1992 accessed at TuTiempo.net, for stations at Perito Moreno aerodrome, within the 100 mm ash isopach of the Volcan Hudson eruption.

For four months after the eruption of Miyakejima volcano, Japan, in 2000, extreme gully erosion due to high rainfall scoured through 1 m ash deposits on its flanks, carving channels into the underlying terrain which reached depths of 2-15 m (Tagata *et al.* 2005). Rill erosion at Miyakejima occurred at an estimated rate of 74 mm yr^{-1} (Tagata *et al.* 2005) whilst on ash-covered hillslopes after the eruption of Mt. St. Helens, rill erosion rates were, on average, 26 mm yr^{-1} (Collins *et al.* 1983). Two years after the eruption, rill and sheet erosion had dramatically decreased, the former by more than 24 mm yr^{-1} and almost 85% of the ash deposited remained intact as a result of cementing and channel stabilisation (Collins and Dunne 1986; Collins and Dunne 1988; Collins *et al.* 1983). Renewed erosion of the deposits at these sites may be triggered by mass movement or extreme rainfall events. In vegetated areas, erosion is limited by the time taken for deposit stabilisation to occur, which may be on the order of months to years, but as with wind erosion, most extreme water erosion occurs where deposits are dry and unconsolidated.

The residence time of ash on snow is considered separately to erosion on soils as it is controlled by melting of snow rather than by rainfall. Snowfall may quickly bury ash layers (Fig. 2.6), leading to their integration into the snow and ice stratigraphy. Where snowfall over the ash layer is infrequent and ash remains on the snow surface for prolonged periods, melting may lead to ash aggregation and small scale creeping and where melting is more extreme, small scale debris flows (Manville *et al.* 2000). These processes are exacerbated where ash is dark coloured, absorbing more solar radiation and transferring more heat to the snow layer beneath, although where deposits are more than 20 mm thick, poor thermal conduction through the ash layer prevents this heat transfer (Manville *et al.* 2000). Ultimately, the duration of these effects is determined by the rate of snow accumulation and its melting. In areas where snow cover is perennial, melting completely during the seasonal thaw, ash is remobilised and delivered back into terrestrial environments as a slurry of ash and meltwater (Antos and Zobel 2005). The residence times of such deposits may be a few months at the most.

Fig. 2.6 *Ash deposits from the eruption of Redoubt volcano, Alaska on March 22nd and 23rd, 2009. This photo was taken on March 31st, seven or eight days after the eruption, and the initial ashfall deposit is already several cm beneath the snowpack. Image courtesy of Kristi Wallace, Alaskan Volcano Observatory and the University of Alaska Fairbanks, Geophysical Institute.*

2.3.4. RESIDENCE TIME IN LAKES, RIVERS AND OCEANS

The residence time of an ash particle in the water columns of lakes, rivers and oceans is determined by its settling velocity. Particle settling velocities in water are controlled by the same properties as in air, p_d and ρ_a, and is limited by drag effects resulting from the particle morphology and are calculated by equation [2.3];

$$w = \frac{R_g g p_d^{\,2}}{C_1 v + \sqrt{0.75 C_2 R_g g p_d^{\,3}}} \qquad [2.3]$$

where R_g is the submerged specific gravity, C_1 and C_2 are dimensionless drag coefficients (20; 1), v is the kinematic viscosity of water and all other terms are as previously defined (Ferguson and Church 2004). Dense, crystalline ash particles (p_d, 2 mm) may have rapid settling velocities, taking minutes to sink through a 100 m water column (Fig. 2.7). Such particles may reach the deep ocean floor in hours. In contrast, very fine ash particles, especially those with low density, may take over an hour to fall 100 m (Fig. 2.7) and may take weeks to reach the sea bed. Particle aggregation may act as a rapid delivery mechanism for small ash particles into aquatic sediments as the aggregate falls faster than the individual particles composing it (Wiesner *et al.* 1995).

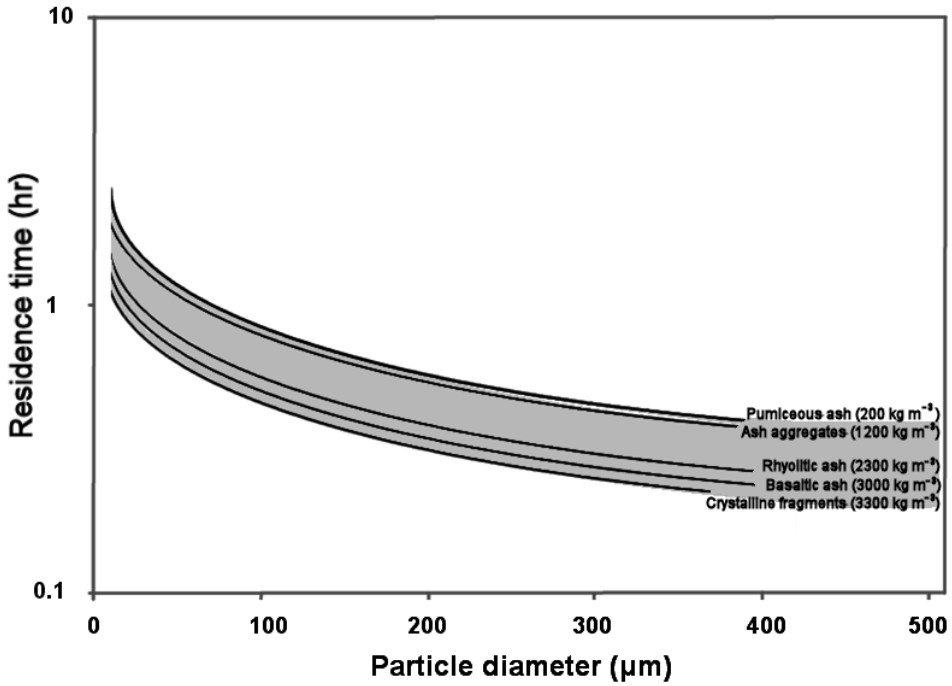

Fig. 2.7 *The relationship between p_d and τ_w calculated by equation [2.3] for spherical ash particles with known densities in a water column with a depth of 100 m (Shipley and Sarna-Wojciki 1983). Particles with p_d < 500 µm fall in turbulent and laminar-turbulent transitional flow regimes and are not shown as their residence times are indistinguishable from those at 500 µm at the scale shown.*

The previous paragraphs discussed particle sedimentation prior to deposition as a measure of water column residence time, but in flowing systems such as rivers, erosion of the ash from the river sediments may resuspend particles after the initial ashfall event. Gordon *et al.* (2004) stated that particles with p_d >63 µm are likely to be transported along the river bed as bedload, via saltation, and are deposited when the river velocity drops below the critical threshold. At Big Creek, Idaho, ash from the Mt. St. Helens eruption in 1980 was reported to collect in 'pools and slack water' (Frenzel 1983). Without burial, erosion events may remobilise deposits; although different in nature to ash deposits, pyroclastic and mudflow deposits in the watersheds surrounding Mt. St. Helens were remobilised by above-average rainfall events, with a single one-in-two-year discharge mobilising 50% of the annual sediment load in the space of a day (Major and Yamakoshi 2004). Therefore, ash deposits may be a constant component of the river system, moving from one low-flow zone to the next with each extreme erosion event.

Particles of sediment with p_d < 63 µm may remain in suspension indefinitely (Gordon *et al.* 2004), as they have a low threshold velocity for suspension. At the Cour

d'Alene river, 250 miles east of Mt. St. Helens, the region received between 5 and 17 mm of ashfall from the 1980 eruption, at least 80% comprised of ash with p_d < 63 µm (Lee 1996; Smith *et al.* 1983). Despite this heavy deposition of fine and very fine ash, river beds were reported to be almost completely ash free (Skille *et al.* 1983), and ash with p_d < 63 µm was similarly absent from Big Creek, Idaho by the end of 1980 (Frenzel 1983). Lateral transport of ashfall is likely to rapidly remove fine ash particles along the water course to be deposited in coastal or lake environments in a short space of time. As fine and very fine particles are suspended along the entire river, these may build up in terminal water bodies, and thus lakes and low flow rivers may develop thicker ash deposits due to accumulation than those found in the surrounding area due to deposition.

2.4. IMPACT OF ASH PHYSICAL AND CHEMICAL PROPERTIES IN THE ENVIRONMENT

The potential physical and chemical impacts of ashfall, in the short term and with particular reference to the post-eruption ash surface, are discussed below in atmosphere, on vegetation surfaces, on soil surfaces and on deposition into waters.

2.4.1. IMPACTS IN THE ATMOSPHERE

Volcanic ash emission and transition through the atmosphere might be argued to be of little significance, as within 24 hours, less than 3% of the erupted mass may remain in suspension (Rose *et al.* 2001). Using the assumption that all ash particles are spherical and the mass loadings, depositions rates and particle size distribution from the conceptual mode of volcanic cloud development by Rose *et al.* (2001), it can be calculated that 25% of the total available surface area generated in the eruption remains aloft in the same time frame (Fig. 2.2). As previously discussed, the spherical approximation underestimates a_s and may therefore underestimate the total available area. If it assumed that an eruption produces 1 km^3 of ash with an a_s of 2 m^2g^{-1}, after 24 hours, the volcanic ash from a single eruption has *A* between 20-240% of the total surface area generated annually by Saharan dust storms. These calculations depend on the values of a_s and mass loading used for the dust storms, which vary between 2.2-5.1 m^2g^{-1} and 260-760 Mt a^{-1} respectively (Goudie and Middleton 2001; Michel *et al.* 2003). Therefore, although the mass loading of ash which remains in suspension may be only a small fraction of that produced in an eruption, this still represents a significant surface area which may be available for reaction between ash surfaces and atmospheric consituents, in a similar manner to those of mineral dust (Usher *et al.* 2003). However, whilst the atmospheric interactions of mineral dust have been extensively studied, the effects of fine and very fine volcanic ash on the atmospheric chemistry are unknown.

The potential for volcanic ash to affect the physical properties of the atmosphere during transport is linked to the quantity, size distribution and colouring of the ash material. A direct effect of ash particles in the atmosphere is to increase optical depth, and thus reduce visibility. Ash suspended in the atmosphere may reflect solar and terrestrial radiation; solar radiation reflection is most pronounced during daylight, whilst terrestrial radiation reflection is most pronounced during night, inducing a warming effect between ground and plume. For example, in Idaho and Montana, Mass and

Robock (1982) reported local air cooling by up to 8°C during daylight hours and a similar magnitude warming effect at night beneath the ash plume produced by the 1980 eruption of Mt. St. Helens. The authors attributed these effects to the presence of ash with p_d between 25 and 500 μm. The duration and intensity of the cooling/warming depend on the concentration and residence time of ash in the volcanic cloud. In general, the effects are short-lived because the bulk mass of the erupted ash is quickly deposited after a few hours or days. When very fine and fine ash is injected into the stratosphere, scattering of inbound solar radiation also may occur. However, the physical presence of volcanic ash has little enduring impact on climate because it settles out of the stratosphere rapidly. Even where large quantities of very fine ash remain in suspension, most of the negative radiative forcing is produced by stratospheric injection of volcanic sulphate aerosols (McCormick *et al.* 1995).

Volcanic ash colours produce ash with different absorptive and reflective properties. Albedo describes the reflectivity of particles on a scale of 0 to 1, 0 being total absorbance and 1 being total reflectance. According to Jones *et al.* (2007), a basaltic ash deposit has an albedo of 0.1–0.2 whilst the albedo of the Bishop Tuff, a pale glassy rhyolite ash deposit, was reported to be 0.6 to 0.8 (Fig. 2.8). Using a coupled atmosphere-ocean general circulation model (AOGCM), Jones *et al.* (2007) predicted that the large ash deposit (~1000 km^3 over the continental United States) from the Yellowstone caldera induced a prolonged local cooling of 5°C in areas of heaviest ashfall as a result of increased land albedo (Fig. 2.9). As a consequence, the temperature gradient between land and ocean may have been altered, possibly affecting atmospheric circulation and forming deep low pressure systems in the North Pacific. This was predicted to raise the frequency and intensity of storm systems on a regional scale and caused 1°C warming and cooling in the Northern Hemisphere in winter and summer, respectively (Fig. 2.9). Jones *et al.* (2007) suggested that the local or regional impacts on climate as a result of large-scale ash deposits may last for several years or even decades, although the local cooling effects will diminish over these timeframes as deposits are eroded and revegetated. Despite the scale of ash deposition and long local duration of cooling effects, the impact of volcanic aerosols may be more significant, as even fifty years after the eruption of similar magnitude to that of Toba, modeling via an AOGCM indicated that a prolonged aerosol induced global temperature decrease of 0.3°C still existed (Jones *et al.* 2005).

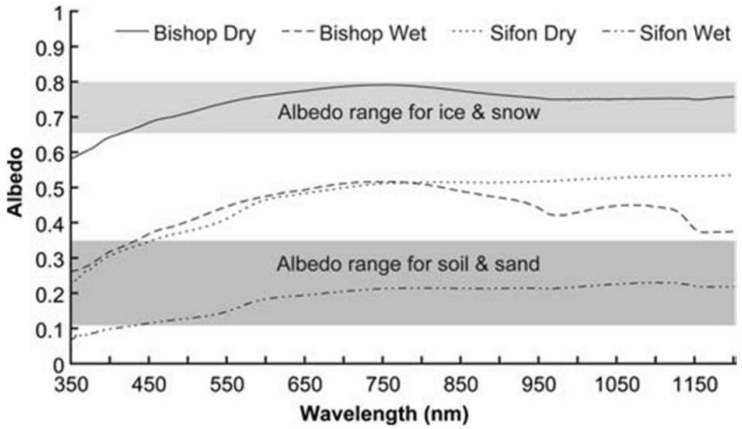

Fig. 2.8 *Albedo ranges of soil, ice and snow, and ash from the Bishop Tuff supereruption, USA, and ignimbrite ash from the Sifon supereruption in Chile, under dry and saturated conditions (Jones et al. 2007).*

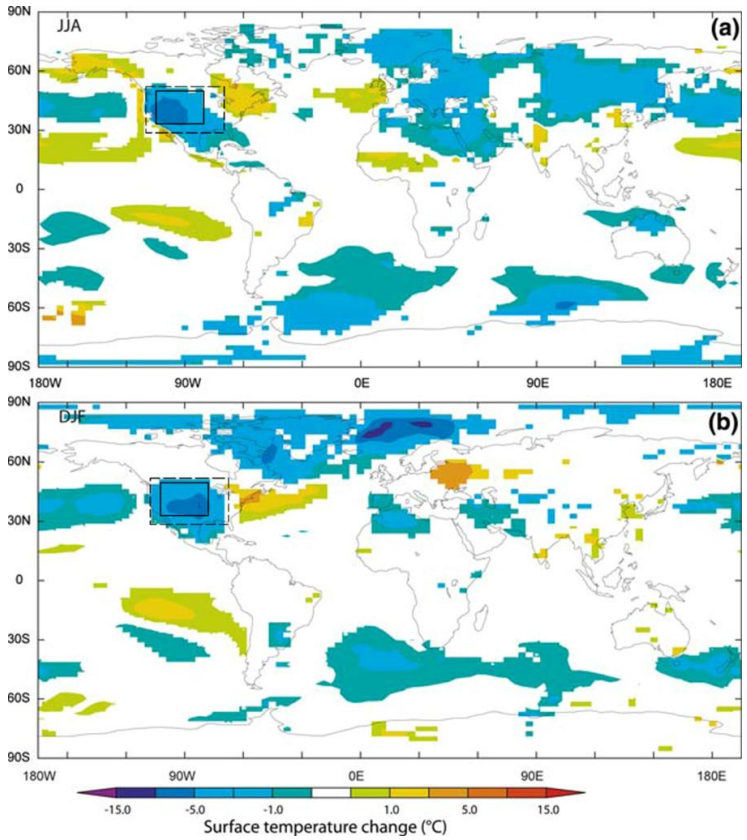

Fig. 2.9 *Temperature deviations in June, July and August (A) and December, January, February (B) from the AOGCM model of Jones et al. (2007) after a 6000 Gt SO_2 injection over North America. Within the solid black line, total ash coverage gives albedo equal to that of the ash and destroys all vegetation. All areas within the dashed line were assumed to have 50% vegetation destruction and albedo equal to the mean of the ash and soil. Local cooling of up to 5 degrees exists within the region of total destruction and ash coverage (modified after Jones et al. 2007).*

There may be potential for volcanic ash to act reactive surfaces for heterogeneous atmospheric reactions in a similar manner to atmospheric mineral dust (Dentener *et al.* 1996; Usher *et al.* 2003 and references therein). The uptake of gas species on ash can also alter the physical and optical properties and the overall ability of ash to act as cloud condensation and ice nuclei. Volcanic ash is assumed for this discussion to have a_s of 1 m^2g^{-1} but the actual reactivity of the ash surface in comparison to mineral dust surface is not known. Even if ash reactivity was found to be significantly lower than that of mineral dust, this lower reactivity might be compensated by the sheer magnitude of ash emission. Mather *et al.* (2003) estimated that tropospheric ash loadings after a very large volcanic eruption could be temporarily increased to 100,000 to 1,000,000 Tg, which would constitute a total area at least 20 times that emitted by dust emissions from the Sahara on an annular basis (calculated from Goudie and Middleton 2001; Michel *et al.* 2003).

Heterogeneous reactions on airborne volcanic ash have not been examined in detail in prior studies. Preliminary insights into how ash may react with atmospheric compounds may be tentatively drawn from existing studies on desert mineral dust. The mean chemical composition of this material reflects that of crustal rock (Usher *et al.* 2003) equivalent to a dacitic composition (Fig. 1.2). However, in contrast to volcanic ash, the mineralogy of desert dust is not dominated by silicate glass but by minerals, including illites, micas, quartz, clays and calcite (Usher *et al.* 2003). Desert dust can also have a_s values which can be up to one order of magnitude larger than those measured for ash particles with similar grain size due to its entirely crystalline character (Michel *et al.* 2003). Some of the salient findings in relation to the heterogeneous chemistry of desert mineral dust in the atmosphere are outlined below; for further details the reader is referred to Usher *et al.* (2003).

The reversible adsorption of SO_2 on mineral dust is thought to involve active metal oxide (*MeO*) surface sites with hydroxyl groups via the reaction in Eq. [2.4] (Ullerstam *et al.* 2002).

$$\{MeO-OH\}+SO_2 \rightarrow \{MeOOH-SO_2\} \qquad [2.4]$$

An oxidant, for example ozone (O_3), is needed to convert the adsorbed SO_2 into sulphate (Ullerstam *et al.* 2002; Usher *et al.* 2003). Mineral dust also is able to take up other atmospheric sulphur compounds, such as the aerosols of sulphuric acid and

ammonium sulphate (Usher *et al.* 2003). The adsorption of O_3 on mineral dust is not well understood, but may be primarily governed by the presence of inorganic and organic coatings on the particles (Usher *et al.* 2003). The reactions and uptake kinetics of mineral dust with nitrogen species, including nitric acid (HNO_3) and nitrogen dioxide (NO_2) are enhanced by water adsorbed on the particle (Goodman *et al.* 2001; Goodman *et al.* 1999). Further, it was shown by these authors that the uptake of NO_2 on a hydrated mineral surface was accompanied by the production of nitrous acid (HONO), an important hydroxyl radical precursor. Finally, volatile and semivolatile organic compounds found in the troposphere are often associated with mineral dust particles.

Metal oxide-type sites also occur at the surface of the silicate glass and mineral components of volcanic ash, and thus may serve as reactive sites for atmospheric SO_2 uptake. One unpublished laboratory study (Gu, 1996 referred to in Gu *et al.* 1999) suggested the potential for natural volcanic ash to adsorb SO_2 at relatively low temperatures (20°C), although the concentration used (400 ppm_v) was not relevant to the atmospheric conditions. Based on water vapour adsorption isotherm experiments (30°C), Delmelle *et al.* (2005) estimated that in the relative humidity range (20-90% RH) typical of most of the troposphere, multilayer adsorption of water can occur on volcanic ash. This implies that, similar to mineral dust, the ash material provides surfaces where heterogeneous nitrogen chemistry can take place.

There is tangible evidence for scavenging of atmospheric organic compounds by volcanic ash. Lamparski *et al.* (1990) analysed ash samples collected at various distances from Mt. St. Helens following the eruption of 1980. Measurable and increased levels of dioxins and polychlorinated biphenyls (PCB) were detected in the ash as it passed from rural to urban environments. Recently, Stracquadanio *et al.* (2003) reported non-negligible concentrations of anthropogenic polycyclic aromatic hydrocarbon (PAHs) in fresh ash deposited by the 2001 and 2002 eruptions of Mt. Etna, Italy. The daily downward fluxes of PAHs were estimated to be an order of magnitude larger than those reported for Great Lakes sites affected by anthropogenic emissions (Muto *et al.* 1994).

The heterogeneous reactions which may take place on volcanic ash particles during transport in the atmosphere could involve silicate surfaces but also the salt substrates adsorbed onto the surface of ash. This may be particularly relevant in the case

where NaCl is associated with the ash, since the interaction of alkali halide salts with atmospheric trace gases often leads to halogen release (Rossi 2003).

2.4.2. IMPACTS ON VEGETATION SURFACES

The first studies detailing the impact of ash fall on natural vegetation were conducted in the regions devastated by the eruptions in 1912 and 1947-1949 of Mt Katmai, Alaska and El Parícutin, Mexico, respectively (Eggler 1948; Griggs 1915). In recent years, much of current knowledge is drawn from the numerous investigations conducted in the aftermath of the 1980 eruption of Mt. St Helens (Antos and Zobel 2005 and references therein; see Cook *et al.* 1981). This eruption also created opportunities to examine vegetation and ecosystem recovery in areas affected by ash fall. This topic is not treated here, but the interested reader is referred to Dale *et al.* (2005) and references therein.

Vegetation in areas affected by heavy ash fall may not survive. Observations made at Parícutin and Ksudach volcanoes suggest that total destruction occurs when the thickness of the ash deposit is greater than approximately 1-1.5 m (Eggler 1948; Grishin *et al.* 1996). In such circumstances, the weight of the ash deposited onto the tree canopy exceeds the mechanical resistance of the stem and/or large branches, resulting in breakage (Fig. 2.10).

Fig. 2.10 *Broken and fallen branches after ashfall from eruptions at the Soufriere Hills volcano on the island of Montserrat, on 12th and 13th of July, 2003. Photograph by Victor James, 2003, reproduced by kind permission of the author.*

Trees, shrubs, herbs and mosses shorter than the ash depth are buried and usually succumb. The data of Antos and Zobel (1985 a, b) indicated that in temperate vegetated regions where the ash is ~150 mm deep, most herb species failed to recover.

At Mt. St. Helens, steppe and understory cryptogams, which include mosses, lichens and algae on the soil surface, died when covered by more than 20 mm of ash, whilst lichens did not survive beneath even thinner deposits (Antos and Zobel 1985; Harris *et al.* 1987). Cryptogams were the communities most affected by the Mt. St. Helens ash in terms of abundance and species composition, an observation also made following the 1912 eruption of Katmai (Griggs 1919). Burial by even a thin layer of ash becomes more severe as cementing and crusting of the deposit occurs, inhibiting reemergence and hence recovery. At Mt. St. Helens, woody plants flattened beneath a snowpack at the time of ash fall suffered more from burial than in other areas with similar ash depths but devoid of snow (Antos and Zobel 1982). In general, areas where vegetation was totally devastated by ash fall can recover rapidly with the emergence of a new distribution of plant communities (Dale *et al.* 2005 and references therein).

Plants buried by ash may survive if the deposit is not too thick (Fig. 2.11). For example, Eggler (1948) noted that a variety of herbaceous and shrub species, as well as pine trees, did not succumb to ash deposits in excess of ~750 mm (Table IV in Eggler 1948). At Mt. St. Helens, ash deposits less than 40 – 45 mm thick did not affect most herb and shrub species (Antos and Zobel 1985). After visiting Katmai in 1913, Griggs (1915) suggested that penetrating the ash deposit may be key to survival of buried plants. Recovering herbage at Mt. St. Helens and since, at other volcanoes, was observed to be focused around cracks and erosion channels in the compacted and cemented deposit (Fig. 2.11) as these areas were offered paths of least resistant for emergent vegetation (Antos and Zobel 2005). Plants may however develop various survival solutions in response to burial (c.f. Antos and Zobel 1985; Kent *et al.* 2001); the survival of an individual may be strongly dictated by its ability to undergo a morphological transformation (Mack 1981). Some plants are able to endure long periods of burial; certain buried plants in the ashfall zone at Mt. St. Helens survived for eight consecutive seasons (Zobel and Antos 1992). Recent field experiments suggest that *Sphagnum* moss is able to grow through 60 mm of ash by sending very thin shoots to the ash surface (Hotes *et al.* 2004). The plant's phenological stage is also an important factor (Antos and Zobel 1985; Antos and Zobel 1987; Zobel and Antos 1987). For example, a Liliacea, (*Veratrum viride*), proved to be highly vulnerable to falling ash whilst mature, but coped particularly well with burial of its perennating organs (i.e., the parts of the plant that survives from year to year to begin the new growth of a plant) by much deeper ash. In the case of peat vegetation, the timing of

ashfall may also be important as a stronger effect was noticed when the ash was applied at the beginning of the growing season rather than at the end (Hotes *et al.* 2004).

Fig. 2.11 *Ash deposits from the early 2006 eruptions of Mt. Augustine. The pre-eruption vegetation is clearly shown in a layer beneath the ash deposit, whilst emergent vegetation is shown protruding through the deposit. Of particular interest is the focusing of new growth along a crack in the deposit. Image courtesy of Christina Neal, Alaskan Volcano Observatory and the University of Alaska Fairbanks, Geophysical Institute*

Plants which do not succumb to an ash deposition event may suffer from a range of direct and indirect physical and physiological effects, even in the case of comparatively minor ash fall. These are governed not only by the ash deposition intensity but also by the morphology and phenology of the plant species affected. Visual inspection in the weeks following the 1980 Mt. St. Helens eruption of the vegetation in a large area east of the volcano revealed three broad categories of plant damages: (i) mechanical overloading, breakage (particularly where ash is wetted) and other direct physical damage, (ii) physiological changes such as decreased plant growth and (iii) damage on leaves in the forms of necrotic lesion, chlorotic spots and other signs of chemical damage.

Using controlled experiments, Black and Mack (1984) concluded that the high percentage of premature leaf abscission observed in a deciduous tree (*Populus*) two weeks after the 18 May 1980 ashfall from Mt. St. Helens was a delayed response to wounding of the leaves by the wind-blown ash. Localised death of leaf tissues occurred due to the abrasiveness of volcanic ash to plant material, a property of volcanic ash also

quoted elsewhere (Cook *et al.* 1981; Griggs 1919; Worcester 1912). As noticed in the area impacted by ash fall from the 1982 eruption of El Chichón, Mexico, coriaceous leaves may be less susceptible to mechanical damage than other leaves (Burnham 1993).

Thermal damage was observed to be a significant source of damage to pre-eruption foliage exposed to ashfall from Mt. St. Helens. However, the source of this thermal damage was not the blast or the heat of the eruption, but rather ashfall itself. Seymour *et al.* (1983) observed that the extent of needle damage in fir-trees (*Abies*) was positively correlated with the amount of ash deposited on the foliage and argued that the damage seen reflected a lethal increase in needle temperatures. This effect was related to a change in the leaf geometry brought about by the ash coating which inhibited heat exchange with the atmosphere and resulted in catastrophic heating beneath ash deposits.

Ash deposited on plant foliage and ground is thought to reduce photosynthesis, which impacts not only on pre-eruption foliage but also on the growth of post-eruption foliage (Hinckley *et al.* 1984). Initially, foliage photosynthetic surfaces are reduced due to the mechanical damage and foliage abscission induced by the ash deposit (Mack 1981; Seymour *et al.* 1983). Remaining vegetation covered by ashfall may see decreases in photosynthesis due to the reduced radiative flux. An ash deposit on pine foliage in excess of 10 g m^{-2} was shown to reduce the quantity of radiation reaching needles by up to 98% (Hinckley *et al.* 1984), whilst almost complete suppression of photosynthesis was quoted for apple leaves coated with 1 mm of ashfall (Cook *et al.* 1981). The very fine (< 2 μm) ash particles may clog the leaf stomates (Fig. 2.12), impeding gas exchange, although this may be a rare occurrence (Hinckley *et al.* 1984; Kennedy 1980). Photosynthesis reduction is regarded as a key factor for explaining the decline in tree radial growth associated with heavy ash deposition (Biondi *et al.* 2003; Eggler 1967; Hinckley *et al.* 1984; Yamaguchi and Hoblitt 1995), and although other factors may also impact upon plant photosynthesis (i.e. soil oxygen exchange impeded by ash deposition Hinckley *et al.* 1984), ash retention on foliage is an important factor in photosynthetic reduction.

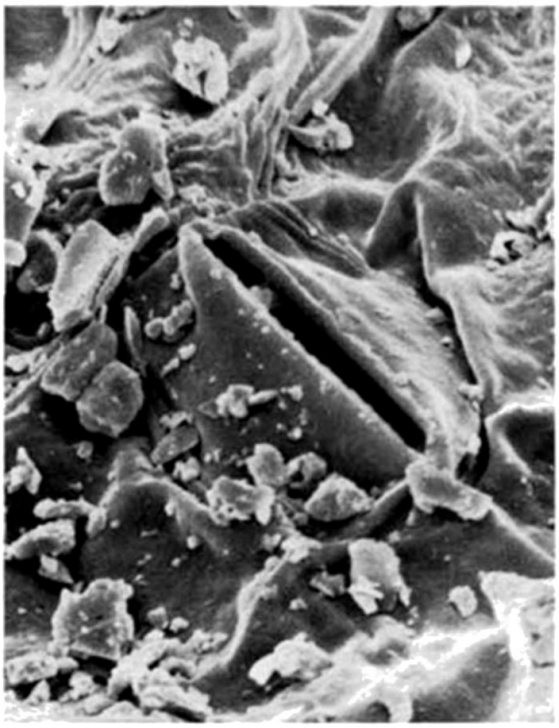

Fig. 2.12 *Ash from the 1980 Mt. St. Helens eruption inside the stomata of an apple leaf, modified after Kennedy (1980).*

Whilst the physical action of ash on plants has been described on a number of occasions, the possibility that ash releases chemical compounds that cause injuries to leaf tissues has been evoked but rarely observed (Black and Mack 1986; Kent *et al.* 2001; Thorarinsson 1979). Despite extensive study, no chemical damage could be identified on ash covered coniferous needles around Mt. St. Helens (Seymour *et al.* 1983). Miller (1966) reported that the ash of the 1963-64 eruption of Irazu, Costa Rica, carried 'sufficient quantities of sulphuric acid …to burn the foliage', and that this resulted in reduced plant growth. The ash generated by the 1976-77 phreatic eruption of La Soufrière in Guadeloupe was held responsible for the necrotic lesions which appeared on banana skins after a rainfall event, rendering the entire crop unmarketable (Le Guern *et al.* 1980). The ash from this eruption contained hydrothermal pyrite (FeS_2), which produced sulphuric acid (H_2SO_4) upon water-mediated oxidation. The prime examples of leaf damage are both from eruptions where aqueous acids were formed or already existed on ash surfaces, and it may be these aqueous acids which are of greatest importance to vegetation surfaces.

The presence of ash-derived acids on foliage may affect the protective surface structures (cuticles) of the leaves, which constitute an important barrier to leaf water and nutrient losses losses (Percy and Baker 1988; Percy and Baker 1990; Shepherd and Wynne Griffiths 2006). Foliage with damaged cuticles are more vulnerable to drought and dessication, which may cause leaf necrosis. The presence of acids on the leaf surface and any damage to leaf cuticular waxes may also increase leaf exudation, i.e., leaching of key plant nutrients such as Ca and Mg (Adams and Hutchinson 1987). The severity of foliage damage from acidic ash leachate is likely to depend on the concentration of acid released, which is controlled not only by ash composition and eruptive history, but also on the quantity of environmental water available to dilute ash-derived acids. Thus, the effect of morning dew on acid release by the ash and subsequent leaf/fruit damage may be larger than that of heavy rainfall. Foliage damage by acids may also be dependent on plant species. For example, acid mist experiments (< pH 3) have been observed to cause necrosis and chlorosis in broadleaf and fruit surfaces but coniferous needles appear to be more resistant (Haines *et al.* 1985).

A variety of water-soluble sulphate and halide salt compounds are known to be associated with the surface of volcanic ash. The presence of these salts may cause injuries to fruits. This was suspected to be the case for blueberries which received a wet ashfall during the 1980 eruption of Mt. St. Helens (Cook *et al.* 1981). The nature of the salt compounds which may responsible for such damage is not known but it has been shown that excess chloride on plant surfaces results in salt burn (Rosen and Eliason 2005); fluoride is another likely candidate (Weinstein and Davison 2004).

Uptake of various elements leached from the ash or deposited with the ash from the plume has been hypothesised to occur. Martin *et al.* (2009) argued that the dominant source of the spatial and temporal variability in the concentrations of As, Cd, Cu, Mo, Tl and Zn in sweet chestnut leaves (*Castanea sativa*) on the flanks of Mt. Etna, Sicily in July 2007 was via deposition of volcanic plume material, including ash. However, the main route (foliage vs. roots) through which these elements are uptaken by chestnut tree was not identified, and large uncertainties remain concerning the role of soil composition heterogeneity and biological processing in explaining the observed variability. The data of Siegel and Siegel (1982) also suggested leaf uptake, as above-normal Hg contents measured in horsetail (*Equisetum arvense*) foliage in areas beneath the plume of the Mt. St. Helens eruption did not necessarily correlate with elevated Hg contents in the soil.

Leaf uptake of nutrients can be beneficial in sufficient quantities, foliar fertilisation being an accepted agricultural practice requiring lower concentrations of nutrients than ground level applications. It is however also possible for excess delivery of nutrients to lead to detrimental effects, particularly for Fe, Cu, Mn and Zn (Rosen and Eliason 2005). Concentrations of Cu, Mn and Zn in ash leachate are generally low and by reference to Table 2.3, it can be seen that extremely thick ash deposits more likely to result in abscission or total burial of the plant are necessary for beneficial nutrient inputs (Fig. 2.14 to Fig. 2.13). These values are calculated using the median values, and reference to Table 2.1 and Table 2.2 demonstrate that although low values of elements may be more common, rare eruptions can be major sources of these elements (i.e. Fe). Even in such cases, the significance of foliar fertilisation by ash deposits is limited by the timescale of nutrient uptake; leaf surface uptake requires hours to days to take place (Scherbatskoy and Tyree 1990), whilst ash leachate is likely to be quickly lost from leaf surfaces by runoff, and retention of leachate water under ash deposits may lead to fungal growth and disease (Antos and Zobel 2005).

Ash leachate washed from vegetation or input directly into the soil may trigger physiological response in the plant root system. Plants optimize root growth into lateral rooting to reach nutrient microsites, particularly in low nutrient soils (Forde and Lorenzo 2001). Patchy application of nutrients may trigger increased root growth rates; less than a day after P application, a tussock grass species (*Agropyron esertorum*) increased root growth rates by 30% (Jackson and Caldwell 1989). Although even a thick deposit of ash cannot emplace equivalent quantities of P, it may be that in barren ash, stress from low nutrient surroundings might make smaller nutrient pulses significant. By initiating lateral rooting, leachate pulses could be important in stabilising the ash deposit and initiating recovery, although this may be highly dependent on individual plant response and the local environment.

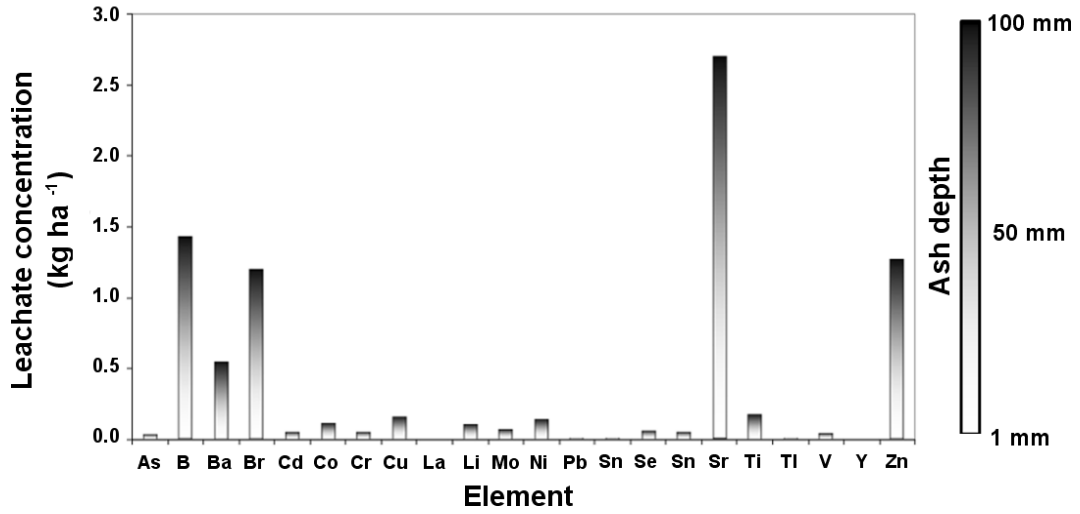

Fig. 2.13 *Input to soil by leaching of minor elements as per median values in Table 2.2, assuming ash depths of 1 to 100 mm (shading of bar) with deposit densities of 1600 kg m^{-3}, that of uncompacted ash (Shipley and Sarna-Wojciki 1983) and displaying inputs in agriculturally relevant units (kg ha^{-1}).*

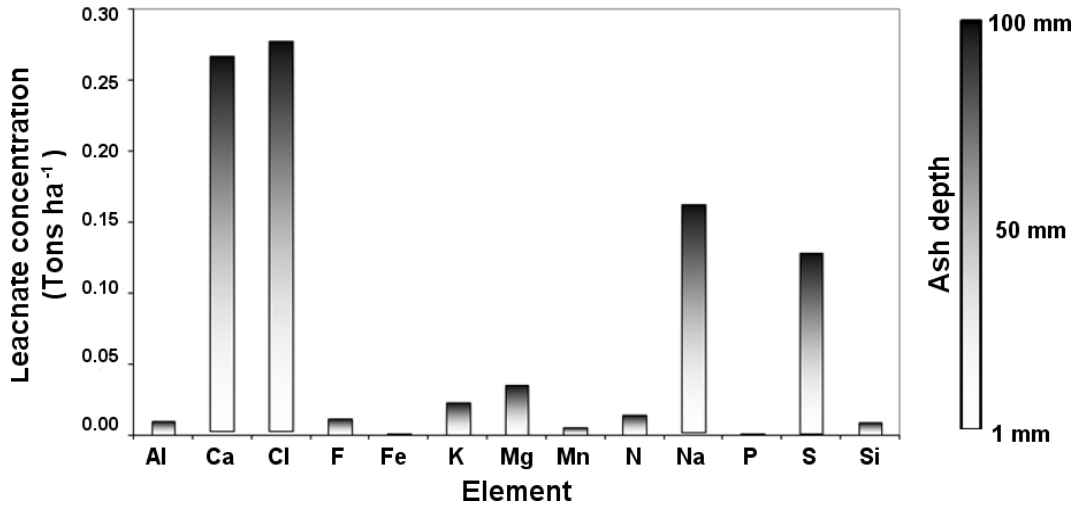

Fig. 2.14 *Input to soil by leaching of major elements as per median values in Table 2.1, assuming ash depths of 1 to 100 mm (shading of bar) with deposit densities of 1600 kg m^{-3}, that of uncompacted ash (Shipley and Sarna-Wojciki 1983) and displaying inputs in agriculturally relevant units (Tons ha^{-1}).*

Some authors postulated that deposition of a thick layer of ash has a major influence on the hydrology of peatlands. Edwards *et al.* (2004) and Giles (1999) inferred drier peat surfaces due to formation of a crust of tephra. In contrast, Crowley *et al.* (1994) concluded that wetness of peat surfaces and water ponding increased due to sealing of surface pores by ash. Hotes *et al.* (2004) simulated ash deposition on wetlands vegetation and did not observe crust development. Alteration of peatland hydrology following ash deposition may also be a secondary effect linked to burial and destruction of the peat vegetation.

Table 2.3 *Recommended fertiliser application rates for a range of fruit and vegetable crops to attain viable agricultural yields where the selected element is present in low quantities in the soil. Data derived from advice for farmers in Minnesota (a) in Rosen and Eliason (2005) and from general advice to commercial and domestic growers in (b) Swiader (2002.*

Element	Dose (kg ha^{-1})	Notes
Ca	1011 a	Fruit and vegetable crops in low (0 - 150 ppm) Ca soil
Cu	51 a	Fruit and vegetable crops in low (0 - 2.5 ppm) Cu soil
Fe	10 - 25 b	In event of Fe deficiency in plants
K	77 - 153 a	Vegetable crops in low (0 - 40 ppm) soil
Mg	506 a	Fruit and vegetable crops in low (0 - 49 ppm) soil
Mn	20 - 75 a	Fruit and vegetable crops in pH > 5.8 soil
Mo	1 - 2 a	In event of Mo deficiency in plants
N	303 - 909 a	Vegatable crops in low (< 3.1 %) organic matter soil
P	32 - 85 a	Fruit and vegetable crops in low (0 - 10 ppm) P soil
S	506 a	Fruit and vegetable crops in low (0 - 6 ppm) S soil
Zn	10 - 50 a	Fruit and vegetable crops in low (0 - 0.5 ppm) Zn soil

2.4.3. IMPACTS ON SOILS

The biggest effect of ash on soil is to form a new substrate. If the ash is thick enough, development of a new soil profile may take place (e.g., Shoji *et al.* 1993 and references therein). Soil formation is dependent on factors such as climate, parent material, time, surface relief and effects of organisms. In cold, humid climates with an average annual temperature of 10°C, the rate of weathering of volcanic ash to a volcanic andisol may be on the order of 1200 years; in warmer climates, this rate may be doubled, particularly where low silica volcanic ash is deposited, whilst where conditions

are dry and colder than 10°C, the rate of weathering of volcanic ash to form volcanic soils may be significantly longer than the 1200 year estimate (Shoji *et al.* 2003).

Where the ash layer is thinner, it may alter the physical, chemical and biological properties of the underlying soil, although the effects may be temporary and may decrease in severity as the ash is eroded or incorporated into the soil. A direct result of covering the soil surface with ash is to change the soil albedo, which may in turn alter the soil's thermal profile. Soil albedo varies from 0.1 for dark coloured soil surfaces, to 0.5 for light coloured soil surfaces (Dubos 2006), and Cook *et al.* (1981) estimated that soils covered with the light-coloured dacite ash from Mount St. Helens reflected 2 to 3 times more incoming radiation than ash-free soils. Similarly, Black and Mack (1986) measured a twofold increase in soil albedo (from 0.14 to 0.29) following artificial application (up to 70 mm) of this ash material. Increasing soil albedo typically decreases net radiation, which in turn affects soil temperature. Soil temperatures measured beneath a few centimeters of undisturbed ash were up to 10°C lower than those in soils not covered by ash (Black and Mack 1986; Cook *et al.* 1981). It was also noticed that the increase in reflected incoming radiation from the soil raised the temperature of the overlying canopy due to interception of reflected radiation by the foliage (Fuchs *et al.* 1976). Finally, deposition of ash onto snow-covered soil reduces the albedo of the snow-soil surface (Warren 1982). However, this effect is of short duration because the ash layer may be soon covered with new snow.

The presence of ash on soil also may dramatically alter the water flow through the soil by modifying evaporation. A layer of ash may act as a mulch, retarding evaporation from the soil surface (Fig. 2.15), thus keeping the soil wet during rainless periods. The mulching effect of ash was evoked by Cook *et al.* (1981) to explain in part the above-average autumn wheat production in eastern Washington following the 1980 eruption of Mount St. Helens. In addition, farmers in Lanzarote, Spain, have traditionally used layers of basaltic tephra to successfully improve water conservation under arid conditions. Tejedor *et al.* (2003) and Diaz *et al.* (2005) demonstrated experimentally that this practice reduces soil water evaporation substantially. For soils covered with high-albedo ash, evaporation may also be further impeded due to development of low soil temperature. Finally, the ash erupted in 1980 by Mt. St. Helens was shown to have a high capacity to retain water (Goldin 1982) and thus, the addition of ash may contribute to reduce evaporation.

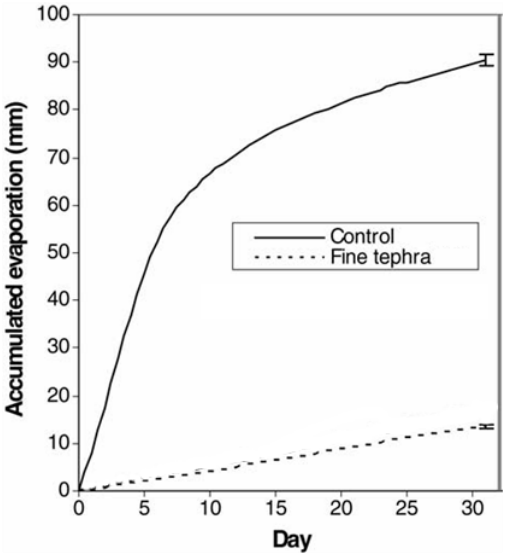

Fig. 2.15 *The influence of a 5 cm deposit of coarse ash (p_d 1 – 2 mm) on soil evaporation relative to an unamended control plot during and at the end of a thirty day period. Modified after Diaz et al. (2005)*

A layer of ash on soil may also alter water infiltration. Cook *et al.* (1981) indicated that the ash from the 1980 Mt. St. Helens eruption had a lower permeability for water than the soil, thus causing a reduction in the rate of water infiltration. The authors argued that the ash layer lacks continuous porosity due to clogging by the fine, angular ash particles of the larger pores formed around the coarser ash grains. A reduced rate of infiltration may delay the entry of rain, snowmelt and irrigation water into soil, thus increasing runoff. Disruption of the hydrology of the region may ensue if a vast catchment area is covered by ash. In contrast, enhanced water infiltration has been observed when the ash deposit has undergone successive wetting and drying, which forms cracks in the impermeable crust, allowing water infiltration. Measurements made after the 1980 Mount St. Helens eruption revealed that the infiltration rate for the ash crust was 18 times higher than for the underlying soil (Goldin 1982).

In a detailed experimental study on the effects of the fine-textured Mount St. Helens ash on the steppe environment of south-central Washington, USA, Black and Mack (1986) concluded that the initial positive mulching effect of ash on soil moisture was rapidly annihilated by the decreased infiltration through the ash-capped soil, and the increased use of water by Sagebrush (*Artemisia tridentate*) shrubs, which were subject to a higher radiation load from the ash-covered soil surface. The response to ash was a marked decline (up to 40%) in soil moisture which persisted 17 months after

treatment. In this case, the major barrier to infiltration was not considered to be the ash itself, but the buried vegetation litter and cryptogame crust.

Some authors postulated that deposition of a thick layer of ash has a major influence on the hydrology of peatlands. Edwards *et al.* (2004) and Giles (1999) inferred drier peat surfaces due to formation a crust of tephra. In contrast, Crowley *et al.* (1994) concluded that wetness of peat surfaces and water ponding increased due to sealing by the ash of surface pores. Hotes *et al.* (2004) simulated ash deposition on wetlands vegetation and did not observe crust development. Alteration of peatland hydrology following ash deposition may also be a secondary effect linked to burial and destruction of the peat vegetation.

Whilst an ash layer may disturb the movement of water in and out of the soil, it has also been suggested that it may impact on the aeration requirement of the soil. Elliott *et al.* (1982) tested this idea in a laboratory experiment but did not notice an aeration effect in soil amended with up to 20 wt.% of ash. However, measurements on sites 12 to 21 km of Mt. St. Helens volcano which were covered with 100 to 350 mm of ash revealed lower oxygen levels with increasing ash thickness and moisture, although there was no indication of plant root oxygen stress (Schulte *et al.* 1985). A significant decrease in soil oxygen concentration was also reported in peat soils treated with 30 mm of fine (median grain size 9 µm) ash (Hotes *et al.* 2004).

Ash falling on natural and cultivated land is also often regarded as a route for introducing various chemicals into the soil, possibly affecting the soil nutrient status and hence plant nutrition and growth. Using the leachate data compiled in Table 2.1 and Table 2.2, the nutrient and metal input of ash from leaching is displayed in agriculturally relevant units in Fig. 2.14 and Fig. 2.13 for freshly fallen ash. From comparison to Table 2.3, it can be seen that at the upper limits of the compiled leachate data, approximately 10 mm of ashfall is required to deliver the recommended fertiliser applications for Ca, Fe and S, whilst K, Mg, Mn, P and Zn could be provided in deposits approximately 100 mm thick, although these application rates are plant and soil fertility specific. S has previously been identified as of potential significance to soil fertility and Goldin (1982), Sneva (1982) and Cronin *et al.* (1998) recognized that a few mm of ash is equivalent of several years of S amendment. A direct fertilising effect of ashfall on soil S was demonstrated after the 1995-96 eruptions of Mt. Ruapehu, New Zealand. Cronin *et al.* (1998) measured increases in soil extractable sulphate and in total

S contents in areas where the ash thickness was more than 3 mm. Soil extractable S concentrations increased from 0.07 µmol g^{-1} to 1.60 – 2.03 µmol g^{-1}, whilst no record of the Se content in the soil was measured. Increases in plant contents of both S and Se were recorded, with plant S contents doubling from 0.20-0.25% to 0.4-0.5%, and Se contents increasing from 1 nmol g^{-1} to 6 nmol g^{-1}. These increases were inferred to be associated with fertilising effects. Greenhouse experiments on ryegrass plants (*Lolium perenne L. Cv.*) grown in silica sand conducted under S-limiting conditions showed a statistically significant increase in dry matter yield after amendments with up to 5 mm of ash from the eruption .(Cronin et al. 1998). The ash from the Ruapehu eruption is anomalous, as it was enriched in S (up to 10 g S kg^{-1}) due to incorporation of elemental S when the volcanic eruption disrupted the active magma-hydrothermal system in the crater lake (Christenson 2000). Such a phenomenon is rarely observed in natural ash leachate studies, so such a significant release of sulphate in leaching solutions may be unlikely in most cases. It should be noted that soils found in volcanic regions often belong to the Andosols group, and as such they show a marked retention capacity for fluoride and, to a lesser extent sulphate (Delmelle *et al.* 2003), and thus may become enriched in F and S upon repeated addition of these anions via inputs of ash leachates.

Whilst soluble elements other than S may also be rapidly leached from the ash, soil measurements are lacking to assess how this process modifies the soil chemical properties, including nutrient status. However, field and laboratory observations suggest increased uptake by plants of some elements after natural or artificial application of ash. Based on glasshouse trials, Mahler (1984) concluded that ash treatments had a positive effect on S, P, Mg and Ca uptakes by wheat but increasing amounts of ash did not necessarily led to higher yields, which is likely due to the plant response to the overall nutrient supply; plants in low nutrient environments may be more prone to luxury uptake (accumulating excess nutrient levels), whilst those in high nutrient environments do not require this (Stuart Chapin 1980). The work of Mahler contrasted with an earlier greenhouse study (Cochran *et al.* 1983) which showed no clear effects on N, P and K uptake by swiss chard (*Beta vulgaris*) and barley (*Hordeum vulgare*) amended with ash from Mt. St. Helens of up to 400 g kg^{-1}. After the 1995-96 eruptions of Mt. Ruapehu, Cronin *et al.* (1998) found that S and Se contents of pasture herbage in areas directly exposed to the ash plumes were two and five times higher, respectively, than normal and correlated with thickness of the ash deposit (Fig. 2.16). Moreover, application of the S-rich ash to S-deficient soils planted with ryegrass (*Lolium perenne*) increased S, Ca,

Na, and Se uptake. The plants were also able to take up more P and K but this was due to relief of the soil S deficiency. On the island of Montserrat after the Soufriere Hills eruptions of 2005, Bhat *et al.* (2005) determined that the plant-extractable Fe and Cu reached toxic concentrations in soils due to leaching and dissolution of frequent ashfall deposits by the soil organic acids. The positive correlation inferred between several elements (i.e., B, Cd, Zn, Tl, Cu, Ni and Co) in coirón grass (*Festuca pallescens*) and ash thickness in the region which received more than 2 mm of ash during the May 2008 explosive eruption of Chaitén volcano, southern Chile (Martin *et al.* 2009), may also be indicative of a change in soil chemistry, although absorption through foliage and stem constitutes another route by which plants can take up soluble elements. It should be noted that the effect of an ash layer on the soil physical properties (e.g., temperature, root aeration) may also influence the chemical (nutrient and water uptake) and biological (growth) response of the plants. A rigorous interpretation of increased accumulation of chemical elements in plant foliage would require additional physical and biological measurements.

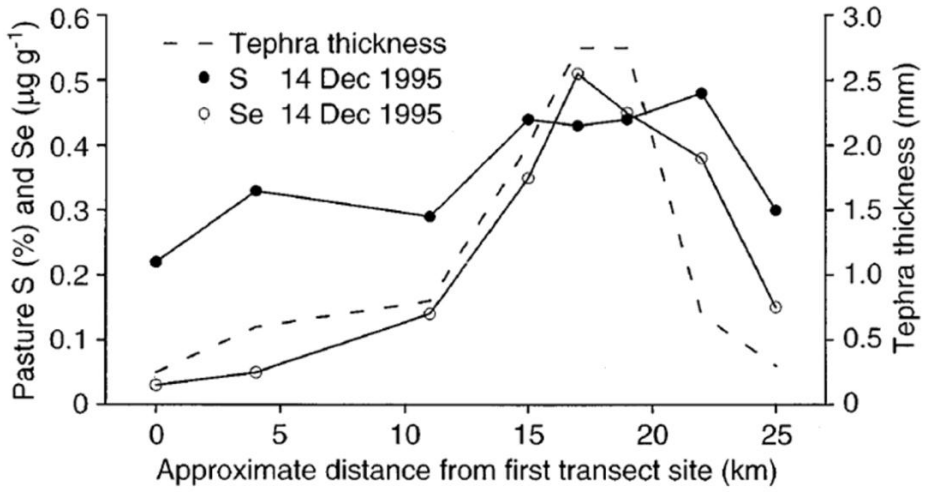

Fig. 2.16 *Concentrations of S and Se in pasture herbage as sampled along a 25 km transect of areas in northern Rangitikei affected by the 14th October 1995 eruption of Ruapehu Pasture herbage S and Se concentrations along a 25 km transect, compared to the ashfall thickness measured in that area (Cronin et al. 1998)*

The contribution of soluble elements delivered by ash to the soil nutrient budget may have the most significant impact in nutrient-poor environments, such as those supporting subtropical rainforests, where any additional input of nutrients to the system is invaluable. The study of Kellman and Hudson (1982) who, in Honduras in 1978, recorded an ash deposition event whilst measuring throughfall fluxes beneath the

canopy of a tropical forest, suggested that infrequent nutrient pulses were an important component of low-fertility subtropical ecosystems. The ash originated from the eruption of Fuego volcano, Guatemala, around 330 km away and was deposited onto the forest canopy. Kellman and Hudson's data indicate that the fluxes of Na, Mg, K and Ca were greater from the ashfall event than any other single nutrient input measured over an 18 month period. Similarly, the ash from a small eruption at Nevado del Ruiz, Columbia in 1987 which was intercepted by wet montane forest canopies provided a nutrient input between 2-3% for SO_4, and 2% of the Cl, Ca and Mg delivered annually in throughfall to the area (Veneklaas 1990). It is important to note that although volcanic ashfall events may provide sporadic nutrient inputs in such cases, such ecosystems are likely to be equally dependent on other infrequent events such as dust storms for their nutrient inputs.

Hotes *et al.* (2004) tested the idea that addition of volcanic ash to nutrient- and mineral-poor peat soil can have a major influence on the soil solution composition, eventually impacting on plant communities and peat accumulation (Wolejko and Ito 1986). They analysed pore water peat soils which were treated with varying ash layer thickness up to 60 mm and ash grain sizes down to a median p_d of 9 µm. Over a period of two years, statistically significant increases in pH, Na, K, SiO_2 and NH_4 were detected in pore waters of the fine and thick ash treatments, respectively. The ash used in these studies was excavated from a dig site and dated from 1739, and so may represent impacts due to ash dissolution or the physical presence of an ash layer over the deposit rather than the immediate post-depositional impacts of ash leaching. In peats, vascular plants may benefit from increased concentrations of the potentially limiting elements N and K, at the cost of *Sphagnum*. The growth of the latter may also be impeded by higher concentrations of dissolved N, Ca and S (Hogg *et al.* 1995; Malmer 1993). Some authors have argued that the chemical changes induced by the entry of ash into peat soils were partly responsible for a shift of the peat plant communities (Wolejko and Ito 1986). However, evidence from the fossil record does not unequivocally support such effect (Giles *et al.* 1999; Hotes *et al.* 2001).

A potential effect of ash fallout on soil functioning is an alteration of methane emissions in peatlands. The chronic deposition of sulphate, from acid rain, has been shown to dramatically reduce the output of CH_4 from natural CH_4-emitting wetlands by altering the microbial ecosystems within them (Dise and Verry 2001; Gauci *et al.* 2008; Gauci *et al.* 2002; Granberg *et al.* 2001) argued that large volcanic eruptions which

increase the oxidised sulphur contents of the troposphere may also induce a similar effect. These authors suggested that the proximity of many peatlands to areas receiving frequent ashfall, whether due to active volcanism nearby or being located under the plume of larger explosive eruptions at greater distance, increased the significance of any volcanogenic sulphate impacts on the receiving wetlands. The same reasoning may be applied to ash material deposited onto peat surfaces as this acts as a discrete source of sulphate upon washing by rain. The most significant release of sulphate from ash on contact with water occurs in the first hour after exposure, particularly on contact with acidic waters (Frogner *et al.* 2001; Hinkley and Smith 1982). Gauci *et al.* (2005) observed that a single large 50 kg ha^{-1} pulse of sulphate was able to suppress methane emissions in peatlands, although the limiting factor to methane suppression above an annual dose of 15 kg ha^{-1} was not the magnitude of the sulphate dose. Although the peatland systems are highly complex, methane suppression from an ashfall event cannot be ruled out, although in proximity to volcanoes, frequent sulphate deposition from passive degassing may be more significant.

Soil acidification from droplets of H_2SO_4 and HCl carried by ash particles (Grattan and Gilbertson 1994) may be a source of concern in affected ecosystems as it can be associated with the permanent loss of the soil exchangeable monovalent cations (Na, K) and divalent cations (Ca, Mg) and with potentially toxic levels of aluminium in the soil solution (Dahlgren 2008). The magnitude of acidification will depend not only on the size of the acid input but also on the long and short-term buffering capacity of the soil. The only direct observation of a decrease in soil pH (up to ~0.5 pH unit) linked to ash addition was made for pasture soils in the months following the 1995-96 activity of Mt. Ruapehu (Cronin *et al.* 1998). The acid production was attributed to oxidation into H_2SO_4 of the hydrothermally-formed elemental S associated with the erupted ash, although as previously stated, this represents an unusual case and should not be expected in other ashfall events (Cronin *et al.* 1998). No inferences were made on whether or not the reduction in soil pH impacted on soil acidification processes. However, both the presence in fresh ash of readily soluble base monovalent and divalent cations (Na, K and Ca, Mg) and the weathering reactions of the ash by the action of adsorbed aqueous acids ameliorate acidity, therefore raising the question of whether acid release from moderate ash deposits is of any real consequence in terms of soil acidification. Perhaps the only soils which may be at risks are peat soils, which lack mineral weathering and so have a weak capacity to buffer acid input (Cresser *et al.*

1993). Acidification in peatlands and other highly vulnerable ecosystems may lead to prolonged effects under a specific combination of conditions; after the 4290 yr BP eruption of Mt. Burney in the Southern Andes, 50- 120 mm thick deposits of ash rich in S (600-700 ppm) were deposited over a steeply sloping wetlands catchment area in a superhumid climate (Kilian *et al.* 2006). The affected region was already acidic and poorly buffered, and once buffering cations were leached, there was insufficient cation replenishment from exterior sources to buffer the acidification. Acidification may have been exacerbated by frequent extreme erosion events which stripped soil and vegetation from the system, further inhibiting cation replenishment (Kilian *et al.* 2006). The duration of acidification was a remarkable 2000 years, which demonstrates that highly sensitive ecosystems may be significantly affected by ashfall for much longer than the short term effects discussed in this paper can account for.

2.4.4. IMPACT IN WATER COLUMNS AND AQUATIC SEDIMENTS

The entry of volcanic ash into water bodies may be responsible for a range of physical, chemical and biological effects in different areas of the water column, but these may all combine to have secondary impacts on the lake systems. At the immediate surface of the water body, the physical consequences of ashfall may result in damage to marine vegetation from the abrasive action of the ash. After the 1912 Novarupta eruption in Alaska, kelp forests were heavily damaged by thick deposits of floating pumices (Rigg 1914). As particles of pumiceous material less than 500 μm will sink almost immediately (Bryan *et al.* 2004), such an effect may be restricted to larger pumice fragments. This phenomenon may only occur in proximity to the volcano so may be of little concern to ashfall, although abrasion to vegetation as particles sink through the water during sustained ashfall remains likely.

It has been hypothesised that the release of nutrients from ash surfaces may result in fertilising effects in aquatic ecosystems. Such potential fertilising effects will be in part a product of the depth to which sunlight may penetrate and any stratification effects which may impede mixing of the water column. Sunlight may penetrate to depths of up to 200 metres in non-turbid waters such as the open ocean (Kaiser *et al.* 2005), but where sediment loads are high, as in estuaries or turbid lakes, penetration may be less than a metre (Grobbelaar 1985). Stratification effects, occurring in response to thermal or salinity gradients in lakes and other small water bodies, may then be a mechanism for retaining nutrients in surface waters (Golterman *et al.* 1975), as mixing

between stratified lake waters is impeded as the stratification becomes more pronounced.

The first inference of increased nutrient uptakes by phytoplankton following ash deposition was made after Novarupta erupted in 1912. Eicher and Rounsefell (1957) attributed the rapid recovery of damaged salmon populations in lakes affected by ash fallout to enhanced phytoplankton mass. Observations made during the 1955 eruption of Mt. Bezyiaminy in Kamchatka confirmed this idea: according to Kurenkov (1966), the addition of 1 Tg of ash to a lake located 80 km northwest of the volcano raised diatom population from 10^4 to 10^6 cells per litre within a year of the eruption, an effect which was sustained for nine years. There is also a report of algal blooms in a eutrophic lake in Montana following an ash deposition event during the 1980 Mt. St. Helens activity (Juday and Keller 1984). This effect was further confirmed by laboratory measurements where the addition of ash to the lake water was shown to increase the concentration of chlorophyll-a, a key component of photosynthesis in phytoplankton. The rapid release of soluble Fe, P and N were held responsible for the fertilisation effects at Mt. Bezyiaminy and in Montana (Juday and Keller 1984; Kurenkov 1966), whilst the later work of Goldman (1960) found that the lakes surveyed by Eicher and Rounsefell (1957) were P- and N-limited (depending on the season), and so might also be susceptible to N addition. Recent laboratory experiments, which showed that together with other soluble elements, Fe, P and N can be leached in appreciable quantities during an eight hour period of contact between ash and deionised water or seawater (Jones and Gislason 2008). Sustained ashfall will maintain a constant supply of unleached ash deposition into surface waters for the duration of the eruption, and thus that initial nutrient fluxes released on first contact with water may be maintained within surface waters at least until ashfall stops. At Novarupta and in Montana after the Mt. St. Helens ashfall, lake specific seasonality and nutrient status were identified as being important variables; if productivity is not limited by the specific nutrients which could be provided by ashfall but rather is inhibited by the lack of a different nutrient, or by lack of sunlight or oxygen, ashfall is unlikely to have a fertilising effect.

Whilst ash deposition may be beneficial for the aqueous biota, it may also have detrimental effects. Toxic responses have been suggested in a number of studies, but have only been definitively identified in one study (Mcknight *et al.* 1981). Toxic metals may include Al, Fe, Mn and Cu. Frogner *et al.* (2006) and Flaathen and Gislason (2007) have demonstrated that phytotoxic Al-F complexes can be formed in ash leachates if

leaching waters are acidic. This may occur during the initial rains after ashfall when aqueous acids on the ash surface may also be mobilised, but a toxic response specifically attributed to Al-F complexes in ash leachates has yet to be identified. At Liberty Lake in eastern Washington after the eruption of Mt. St. Helens in 1980, a 50% decrease in algal population occurred in the first month of the eruption, which coincided with increases in concentrations of Al, Fe, Mn and Cu by factors of 200-1000% (Funk 1980). McKnight *et al.* (1981) conducted bioassay experiments on an A*nabaena* species using ash leachate from Mt. St. Helens. At ash:water ratios of 1:10-1:500, decreases in chlorophyll-a were observed, which were attributed to soluble trace metals or toxic organic compounds. At more dilute concentrations (1:1000), McKnight *et al.* (1981) observed growth rate increases, but these were also accompanied by growth defects, suggesting that even where ashfall may appear to have a fertilising effect, as in the study of Juday and Keller (1984), a physiological toxic response may still occur.

One of the most recent developments in studies dealing with the environmental effects of volcanic eruptions is the idea that large ash deposition events over the open ocean surfaces may induce massive phytoplankton growth, with a concomitant increase in biological drawdown of atmospheric CO_2 and alteration of the ocean biological carbon pump (Sarmiento 1993; Spirakis 1989; Watson 1997). This mechanism could provide a plausible connection between volcanism and climate forcing in the past (Bains *et al.* 2000; Bay *et al.* 2004; Cather *et al.* 2009).

The hypothesis that ash inputs to the open oceans act as fertilisers is supported by several direct and indirect observations. Sarmiento (1993) and Watson (1997) argued that a temporary decrease in global CO_2 concentrations, which began in mid-1991 after the eruption of Mt. Pinatubo and continued into 1992, estimated to be a loss of approximately 1.6 Pg of C, was a product of that eruption. It has been proposed that, similar to mineral dust deposition, heavy ashfall which occurred in the Southern Ocean as a result of that eruption had a fertilising effect on the open ocean. The volcanic element primarily held responsible for this effect is Fe, a micro-nutrient for phytoplankton which is lacking in some parts of the open ocean, i.e, the so-called high-nutrients, low chlorophyll (HNLC) areas. Geochemical experiments in the laboratory confirm the capacity of fresh ash material to readily release nano- to micro-concentrations of soluble Fe, along with other elements, upon contact with seawater (Duggen *et al.* 2007; Frogner *et al.* 2001; Jones and Gislason 2008). Further, bio-incubation tests also indicate a positive response of *Chaetoceros dichaeta*, a diatom

species typically found in Fe-limited Antarctic waters, to ash addition (Duggen *et al.* 2007).

The volcanic and environmental factors governing the amounts of soluble Fe in the ash material deposited over the ocean surfaces are poorly constrained, but mineral dust particles are thought to contain 1-2% soluble Fe on deposition (Meshkhidze *et al.* 2003), and some degree of comparability between these systems and ash systems may be possible. The fluxes of volcanic material to the open ocean are also not known, nor are their temporal and spatial distributions. There is also the possibility that ash releases significant concentrations of soluble species (e.g. Cu) potentially toxic to phytoplankton (Jones and Gislason 2008). Finally, Jones and Gislason (2008) evoked the potential for toxic effects of ash addition to surface oceanic waters due to the generation of transient low pH values. Increased seawater acidity may damage shell and skeletal structures and would encourage migration of biota into deeper waters to escape surface water acidity, which may be fatal due to changes in water pressure (Jones and Gislason 2008). It should be noted that the geochemical experiments which led the authors to speculate on such effects corresponded to very high ash loadings representative of voluminous but rare volcanic eruptions, which may deposit up to one meter of ash in the ocean. Furthermore, the pH decrease of seawater following ash addition was noticed only for ash from the 2001 eruption of Hekla, Iceland.

Chemical effects in the water column may be transient, aside from very fine ash particles in a deep water column. Longer term effects may result from the deposition of ash into marine or lake sediments. Ash in sediments may act as a barrier to nutrient recycling from the buried sediments back into lake or ocean bottom waters (Barker *et al.* 2000; Telford *et al.* 2004); it may inhibit oxygen diffusion into the ash layer and the sediments (Haeckel *et al.* 2001); or it may release soluble elements into lake and bottom waters (Lee 1996 and references therein; Telford *et al.* 2004). These elements may originate from dissolution of the glass, but may also originate from ash leaching, particularly where large ash particles sediment rapidly through a shallow water column, when leaching may not be complete before ash is deposited into sediments or buried by sustained ashfall. Whilst the effects of ash deposition into sediments are felt by marine and lake systems, any impacts on the overlying water column will be most strongly observed in small water bodies, and may be negligible in the global ocean.

Metals and nutrients are delivered to sediments either as inorganic or organic compounds, effectively removing them from the water column unless they are recycled by microbial decomposition or by reduction of oxidized metals to mobile, reduced forms (Bailey 2002). The deposition of an ash layer over the sediments may inhibit nutrient recycling; limiting of P recycling by ash is thought to cause diatom population changes in lakes affected by historic eruptions (Barker *et al.* 2000; Telford *et al.* 2004) and favours populations adapted to low P conditions. Response to ashfall was generally observed at thicknesses above 10 mm (Telford *et al.* 2004) so thinner deposits may not trigger significant response, particularly where a steady supply of nutrients is received from the catchment. In such cases, inhibited nutrient recycling may be inconsequential or of limited duration. In the lakes receiving ashfall (1 – 10's mm) after the eruption of Mt. St. Helens, only one lake was reported to show a decrease in total phosphorus (Funk 1980), but as the lake was in a region which received less than 5 mm of ashfall, inhibited nutrient cycling seems unlikely.

Oxygen exchange between bottom waters and the ash layer and underlying sediments are inhibited by deposits containing smaller ash particles, which have smaller pore sizes and low permeabilities, leading to anoxia in both ash and sediment. Where ash layers contain coarse particles, the random orientation of large interconnected pores may create permeable channels in the deposit, but the likelihood of these channels remaining unblocked decreases as deposit thickness increases. The loss of oxygen in sediments may have direct consequences on benthic environments; in the South China sea, deep sediments underlying ashfall from the 1991 eruption of Mt. Pinatubo were rendered anoxic by a 30 mm overlying ash layer, which caused mass mortality of benthic foraminifera due to suffocation (Haeckel *et al.* 2001). Thinner deposits may have limited impact, as a 15 mm ash layer did not render sediments anoxic until depths of 80-120 mm into the sediment (Haeckel *et al.* 2001), and beneath ash layers less than 10 mm thick, no adverse impact as a result of ashfall was reported in benthic communities in the lakes around Mt. St. Helens (Lee 1996 and references therein).

Where anoxic conditions exist in ash deposit pores, there may be a variety of complex geochemical processes which may mobilise toxic metals into pore waters and bottom waters. Under anoxic conditions, microbial communities may reduce insoluble Mn and Fe to soluble forms and may reduce sulphate to sulphur species such as H_2S (Bailey 2002), which is toxic to biota at concentrations of 2 $\mu g\ l^{-1}$ (Office of Water and Hazardous Materials, 1976). The presence of transition metals may also lead to

precipitation of insoluble sulphide species, which may remove potentially toxic species from solution (Bailey 2002). Metal speciation under anoxic conditions is affected by the pH and chemistry of individual lake or ocean waters, and toxic effects cannot be inferred from sediment (or ash deposit) composition alone (Bailey 2002). If a toxic response is hypothesised to occur, low permeability ash layers may be expected to confine it to sediments whilst a permeable deposit may permit the exchange of pore waters with bottom waters. In both oxic and anoxic bottom waters, this exchange may be a pathway for potentially toxic species to be recycled into the water column.

Ash dissolution in sediments may also have beneficial impacts on lake systems. Si released from ash dissolution can be beneficial to diatom populations under Si-limiting conditions, although Telford *et al.* (2004) found that that even in analysis of multiple ash fall events across sediment cores from the same lake, there was no simple relationship between diatom populations and Si content of ash. Beneficial impacts of ash dissolution may therefore be dependent on a specific combination of circumstances, particularly in the future, as modern lakes are less sensitive to volcanogenic Si input by increased anthropogenic Si inputs (Telford *et al.* 2004).

2.5. CONCLUSION

In considering the environmental effects of ash emission and deposition, this discussion has identified the potential areas where impacts may occur (Fig. 2.17). Some of these are on global scales. The atmosphere and ocean may be the areas where chemical impacts associated with ash particles may have wide ranging effects. Bioavailable Fe release from ash in marine surface waters may result in enhanced primary productivity and increased CO_2 uptake by phytoplankton (Duggen *et al.* 2007; Frogner *et al.* 2001). It is proposed that the vast reactive solid surface area emitted by large explosive eruptions into the atmosphere may be an important catalytic surface for atmospheric chemical interactions (e.g. O_3 destruction). The effect of increased atmospheric and terrestrial albedo from ash particles in suspension may result in climatic effects from the reflection of inbound solar radiation, but it has long been known that the cooling effect of H_2SO_4 aerosols generated from large scale volcanic eruptions may be significant, and could eclipse the chemical impacts of ashfall. The potential for physical and chemical impacts associated with ashfall in large scale volcanism clearly merit further study, but should considered in context with the other impacts of very large explosive eruptions.

It is important not to neglect smaller scale impacts in the face of those which have global repercussions. Impacts occurring at local scales may be devastating to vulnerable communities and on those who depend upon those communities. The small scale effects of ash emission and deposition may include acid and salt damage to vegetation, burial and chemical impacts on soils and alterations to water chemistry and nutrient loadings in lake and river systems. Focusing research on smaller scale impacts of ashfall and the consequences at the local and regional level is a worthwhile task, as with further study, it may be possible that the environmental impacts which may be damaging to vulnerable communities can be mitigated, prepared for and perhaps even prevented.

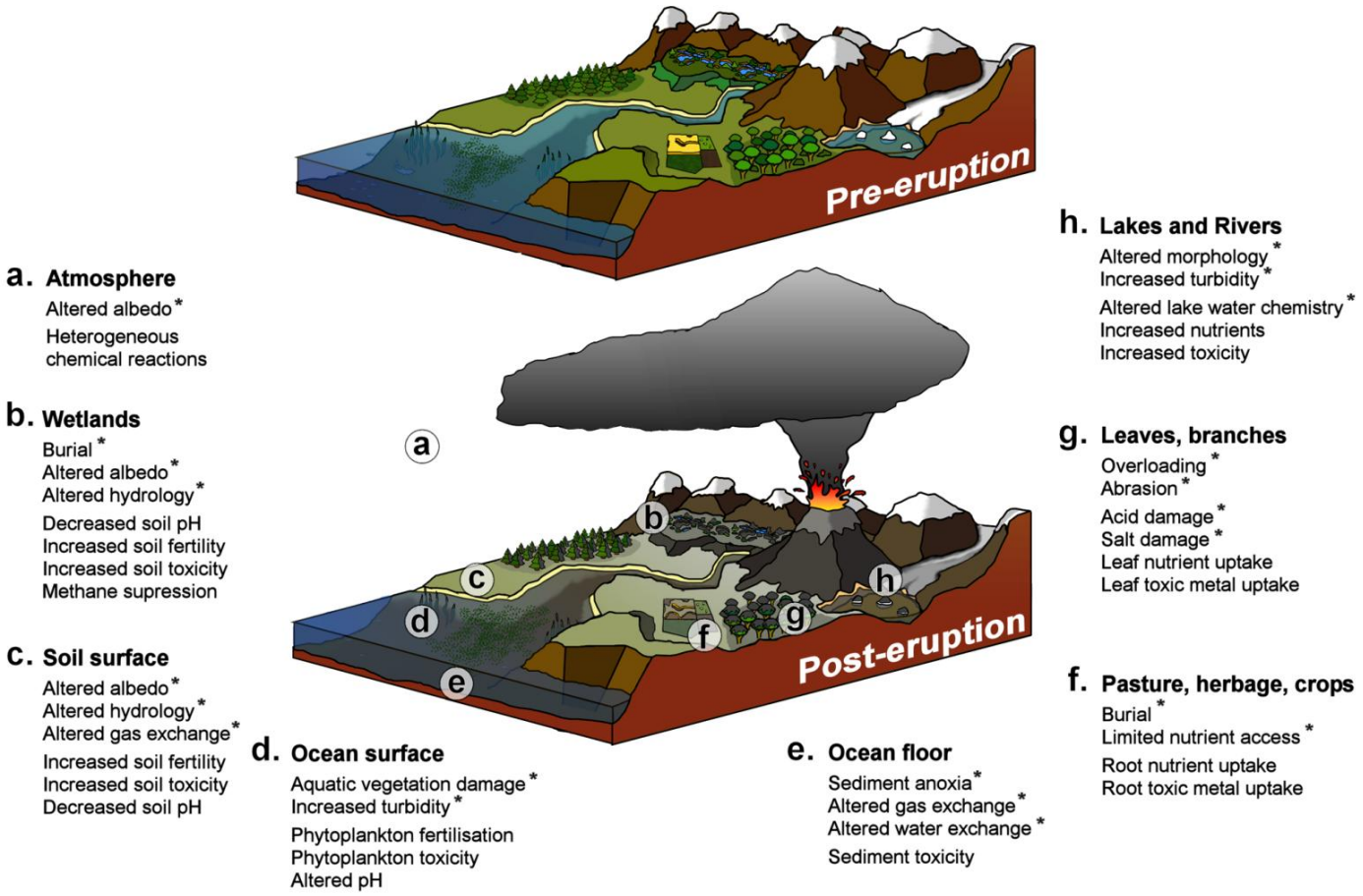

Fig. 2.17 *Cartoon illustrating the range of environmental impacts which may follow a volcanic ashfall event. The most well constrained impacts, whether by available studies from volcanic research or whether due to available information from similar phenomena such as mineral dust, industrial ash or acid deposition, are indicated by an asterix.*

The impacts on vegetation associated with physical ash deposition may be highly damaging without removal, as ash cover on leaves may stunt growth by limiting photosynthesis (Hinckley *et al.* 1984) and may promote fungal growth beneath the ash cover (Cook *et al.* 1981). Rapid removal of ash after an eruption may not be sufficient to prevent chemical damage to the ash surface resulting from acid and salt leaching from the particle surface, unless the deposit is dry. Acid and salts leached from ash on contact with water may damage or spoil foliage, crops and fruits, with clear economic consequences (Le Guern *et al.* 1980) and rendering the affected plant more vulnerable to other stresses (Cook *et al.* 1981; Shepherd and Wynne Griffiths 2006). The potential for acid damage may be particularly high on vegetation surfaces with low tolerance to acids (Adams and Hutchinson 1987) and where the water which leaches the acid is in low volume, i.e. morning dew rather than heavy rain. Further research into ash surface chemistry and the release of acidity from ash surfaces on contact with water is required to determine what conditions may cause damaging acid release. Such experiments would inform vulnerable communities whether resource intensive ash removal before contact with water occurs is merited.

In soil systems, consideration must be given to physical and chemical effects of ashfall. The physical effects are comparatively well constrained, but would benefit from further research to improve existing mitigation and remedial advice. The USGS recommends that ash be incorporated into the soil where the deposit is <50 mm[2]. Incorporation of ash into the soil may impact on soil water budgets, but whether the effect to soil water is beneficial or detrimental to agriculture may depend on particle size distribution, as fine ash may block infiltration pathways and so reduce soil water over time (Black and Mack 1986). The effect of p_d and particle size distribution must therefore be considered before recommending mitigating action. Ash resuspension after an eruption (Inbar *et al.* 1995) should also be considered, as it may create an ash deposit with an entirely different particle size distribution to that deposited elsewhere within the region. With respect to chemical impacts from ashfall events, it is anticipated that a single deposition event may generally be of limited consequence. Chemical impacts may however occur where the ash is unusually enriched in a fertilising nutrient (i.e. P, K, S etc.) or may generate toxic species such as Al-F complexes (Frogner *et al.* 2006) and soluble Fe, Mn or Cu (Bhat *et al.* 2005) which may be bioavailable. Ultimately, the chemical impacts in the soils, may be dictated by the properties of the receptor, for

[2] From http://volcanoes.usgs.gov/ash/agric/index.html, accessed 11th May, 2010

example, fertilising effects may only occur where nutrient limiting conditions exist (e.g. Cronin *et al.* 1998), whilst acidification of soils may occur where buffering base cations are in limited supply (e.g. Kilian *et al.* 2006). Fertilising effects from ashfall in soil may be of limited concern due to ubiquitous usage of chemical fertiliser, whilst acid deposition from anthropogenic or passive degassing sources may be more significant than a transient leachate pulse. Future studies may therefore be best focused on studying any toxic responses from ash leaching, possible via glasshouse and control plot experiments, as used by Cronin *et al.* (1998), Sneva (1982) and others.

Unless physical ash deposition in water bodies results in the significant disruption of the water course by altered bed morphology or sediment loading, the chemical impacts of ash deposition into lake systems may be the greatest source of concern. It may be possible in poorly buffered lake systems for acid release from ash to impact on water pH and hence on water chemistry (Kilian *et al.* 2006), but this remains speculative. Macro- and micro-nutrients leached from ash systems may have a fertilising effect on lake waters, particularly as lakes may receive further ash input from wind and water erosion from the surrounding catchment. Where a pre-existing tendency towards eutrophic conditions exists or where a key nutrient is limiting, due to seasonality or inadequate supply from the catchment, ash deposition may trigger phytoplankton blooms (Juday and Keller 1984). In the study of Juday and Keller (1984), these blooms were accompanied by growth defects, which the authors attributed to toxic effects associated with ash leachate, possibly derived from metals such as Cu, Cd, Mn and Zn (Mcknight *et al.* 1981). Ash fertilisation of surface waters may be of concern if the phytoplankton blooms contain harmful algae, as these may be damaging to public health or livestock using the lake as a drinking source. The lake water chemistry is highly specific to the individual lake and the surrounding catchment, and studies conducted on one lake may not be applicable to those neighbouring it (Lee 1996). Responses to environmental impacts of ashfall on lake systems may therefore have to be precautionary rather than remedial. By studying lakes in areas likely to receive ashfall, modelling catchment inputs and conducting bioassay experiments using representative leachate solutions, the impacts of ashfall on lakes should be considered on a case-by-case basis and could offer specific guidance to local communities with regard to using their local water sources after an ashfall event.

Ultimately, all of the above scenarios would benefit from an improved knowledge of ash surface chemistry and how that chemistry may vary from volcano to volcano, or even from eruption to eruption. The importance of studying volatile scavenging reactions occurring within the eruption plume and in the atmosphere is therefore emphasised by this review chapter. Whilst knowledge of volatile scavenging mechanisms remains limited, experimental studies using solutions which are representative of those leached from ash particles focusing specifically on the local scale environmental impacts are recommended. Exploring the effects of leachate pulses via the application of solutions with similar compositions, without requiring the application of ash, may enable the chemical effects of ashfall to be explored in isolation. Such studies would however require new analytical protocols for leachate, which would include the recording of pH, distance from the vent etc. as per the recommendations of Witham *et al.* (2005), but would also require characterising particle diameter, a_s and particle size distribution in order to better constrain the range of leachate compositions which are commonly generated from erupted ash.

CHAPTER THREE

EXPERIMENTAL AND ANALYTICAL METHODOLOGY

CHAPTER THREE. EXPERIMENTAL AND ANALYTICAL METHODOLOGY

3.1. INTRODUCTION

To study SO_2 chemisorption on model ash systems, this study examined the changes to the bulk and surface properties (chemical composition and structure, reaction products, surface textural properties) in post-experiment model systems compared to those prior to the SO_2 chemisorption experiments. The rationale behind the specific design of the experimental reactor and the range of the variables of temperature, composition and exposure to be studied are discussed in this chapter. This chapter also includes the basic principles, general operating protocols and any specific protocols specific to the range of bulk analysis, surface analysis and leachate analysis techniques used throughout Chapters 4 and 5.

3.2. EXPERIMENTAL METHODOLOGY

3.2.1. EXPERIMENT DESIGN AND METHODOLOGY

To study SO_2 chemisorption on volcanic ash, the experimental reactor design was based on those used in studies of SO_2 physisorption and chemisorption on mineral dust surfaces (Adams *et al.* 2005) with some modifications (Fig. 3.1). To investigate adsorption at eruption plume temperatures, the experimental reactor and protocol were adapted to study the mechanisms of SO_2 chemisorption with respect to the research questions posed in Chapter 1. The general design and operational protocol of the experimental reactor is described below, whilst specific details of sample composition, temperature, exposure time and the experimental atmospheres under investigation are discussed in the following section.

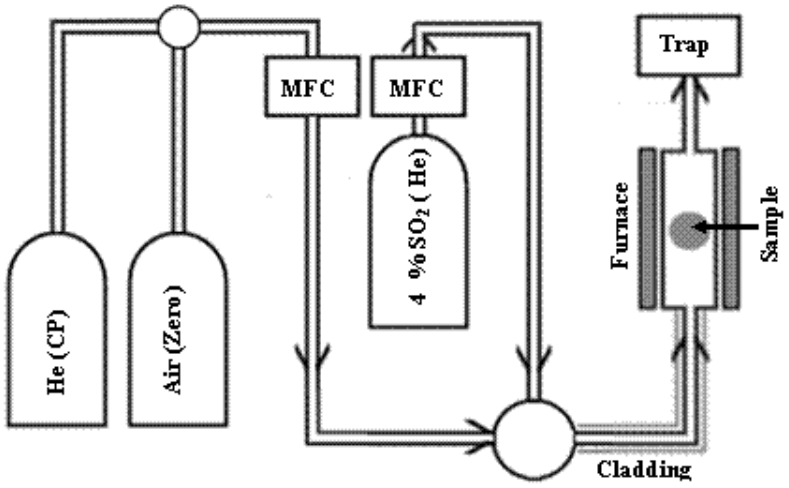

Fig. 3.1 *Experimental reactor schematic, where MFC indicates a mass or manual flow controller regulating the gas streams and furnace atmospheres.*

Model systems representative of selected aspects of the silicate ash systems were inserted into quartz glass flow tubes and held in place by quartz wool plugs. Quartz materials were used for their lack of reactivity to SO_2, except to limited extent at temperatures >800°C. These tubes were positioned within a vertically oriented Carbolite furnace (Fig 3.1) which heated the samples at a ramp rate of 15°C min^{-1} to the specified temperature, and cooled by allowing the furnace and reactor tube to cool via contact with the atmosphere. Heating and cooling within the quartz flow tube tubes was conducted under an inert gas stream of CP grade He at 100 sccm, whilst the SO_2-bearing gas stream was introduced into the quartz flow tube once the furnace had reached the specified temperature for the desired exposure time. All gases were carried

by Teflon feedlines connected to the quartz glass flow tubes by a Teflon valve exterior to the furnace (Fig. 3.1). SO_2-bearing gas streams were regulated by a Hastings 202 digital mass flow controller, whilst carrier gas streams and the inert heating/cooling gas stream were regulated by a manual flow controller. At the end of the experiments, once at a temperature of 200°C, samples were extracted and stored under atmospheric conditions in sealed soda-lime glass vials.

3.2.2. MODEL SYSTEMS FOR STUDY

The effect of the chemical composition of volcanic ash surfaces on SO_2 uptake was explored by means of synthetic aluminosilicate xerogels and multi-component aluminosilicate glasses. For a specific discussion of the rationales behind both of the model systems studied, see Chapter 4 and 5.

3.2.3. EXPERIMENTAL TEMPERATURE RANGE

The experimental temperature range which was explored lies between 25°C and 800°C. Conducting experiments at temperatures of 25-800°C encompasses a range which is likely to be experienced, however briefly, by silicate ash particles within volcanic eruption plumes. Temperatures in excess of 800°C are confined to low Si content magmas, and so may not be appropriate to studies of SO_2 chemisorption on more viscous magmas. Additionally, temperatures in excess of 800°C may threaten the integrity of the quartz reactor tubes by softening and in the case of the multi-component glass model system, may completely melt the sample, fusing it into the reactor tube. The temperature range used in this experiment series, which has the increments of 25, 100, 200, 300, 400, 500, 600, 700 and 800°C, was therefore selected both for scientific and logistical reasons.

3.2.4. EXPERIMENTAL EXPOSURE TIME

The duration over which samples were exposed to experimental atmospheres, excluding cooling and heating time, was 60 minutes in the bulk of experiments conducted in this study. These timescales are longer than the likely in-plume exposure times, as discussed in Chapter 1, but may be used to establish a 'fingerprint' for the reaction products and mechanisms driving SO_2 chemisorption. 'Fingerprinting' can be used to study samples exposed to varying temperatures over much shorter time durations. In Chapter 1, it was hypothesised that the minimum exposure time to the highest temperatures of this study may be on the order of seconds, but that uncertainties

with regard to these estimates remained. A range of time increments was therefore selected for study, including some short time duration experiments, in order to generate a full temporal profile of SO_2 chemisorption at different temperatures. The increments used were 0.5, 1, 2, 5, 10, 20, 40, 60, 120 and 240 min.

3.2.5. EXPERIMENTAL ATMOSPHERE

In this study, SO_2 chemisorption experiments were conducted with a 1 mol. % SO_2 atmosphere carried by either He only or 75 mol. % air in He atmosphere. The rationale for the selection of such a gas composition is two-fold. First and foremost, this study is mechanistic, and is not conducted on a truly 'representative' in-plume atmosphere. This is a necessary restriction, as before any consideration of how much SO_2 may be adsorbed under specific concentrations of in-plume gases, it is first necessary to constrain what the mechanism of adsorption is and what the key variables controlling that adsorption are. Therefore, the choice of SO_2 concentration to be investigated must be of an appropriate order of magnitude, but does not necessarily need to represent a specific plume or eruptive gas atmosphere. In light of the variation in volcanic gas compositions detailed in Chapter 1, it is likely that SO_2 concentrations within the plume do vary, but the average value calculated by Stoiber (1995) may be an appropriate mass of SO_2 which all ash types could experience. Conducting experiments on a rhyolite ash under the very high SO_2 concentrations found at Kilauea may not be appropriate, but a basalt or low-Si ash being exposed to a lower concentration of SO_2 is more likely to occur. Hence, the estimated annual average SO_2 concentration of ~1 mol. % SO_2 is used as the experimental atmosphere in this study. The use of 1 mol. % SO_2 gas mixtures was also required by logistical constraints. At higher concentrations of SO_2/He mixtures, additional safety protocols are required as the mixtures are considered toxic, and also cannot be stored under high cylinder pressure (D. Grocott, pers. comm. 2007), which limits the number of experiments which can be conducted with these specialised and expensive gas mixtures. By using both SO_2/He and SO_2/He/Air systems, it was intended that any variables which are dependent on the presence of O_2 in the atmosphere to occur would be identified. In practice, with the exception of one experiment series in Chapter 4, all experiments in this study were conducted under 1% SO_2/He/Air atmosphere. Additional experiments conducted under He-only and air-only were required to separate any alterations to the sample which may occur due to the effects of heat treatment and the existence of either of the above atmospheres, irrespective of the presence of SO_2.

3.3. ANALYTICAL TECHNIQUES - LEACHING

3.3.1. PRINCIPLES OF AQUEOUS LEACHING

The study of the solutions generated by leaching silicate ash particles in aqueous solutions forms the cornerstone of existing research into volatile scavenging, and was used extensively by this study. Leachate analysis offers valuable insight into the quantities and constituent elements of the soluble salts emplaced by volatile scavenging, but must be combined with additional analytical techniques to gain a more detailed insight into the mechanisms and variables which may drive the volatile scavenging. In this study, leachate analysis was combined with bulk and surface-sensitive techniques to provide mechanistic insight into the SO_2 chemisorption on model ash systems.

'Leaching' is the term used to describe the aqueous extraction of soluble material from silicate ash particles and the model ash systems used in this study, but this is a slight misnomer. The interaction of aqueous solutions with aluminosilicate materials results in the dissolution of soluble surface reaction products (i.e. salts), but also in the direct dissolution of the glass through the disruption of the aluminosilicate network by OH^-, as summarised in equations [3.1] to [3.3] (Scholze 1990). Leaching may also result in the exchange of monovalent and divalent cations in the sample with H^+ ions in solution [3.4]. Leaching of monovalent and divalent cations occurs more rapidly than the dissolution reaction, leaving a surface layer which may be depleted in these cations (Scholze 1990). The depth of the leached layer is dependent on the diffusivity of exchangeable cations, which is affected by the properties of the aluminosilicate network and on the duration of leaching (Paul 1982). The contribution of the dissolution and leaching of the underlying sample surface in addition to the dissolution of soluble surface salts must therefore be considered in interpreting leachate data.

$$\equiv Si - O - Si \equiv + H_2O \quad \rightarrow \quad \equiv Si - OH + HO - Si \equiv \qquad [3.1]$$

$$\equiv Si - O - Si \equiv + OH^- \quad \rightarrow \quad \equiv Si - OH + O^- - Si \equiv \qquad [3.2]$$

$$\equiv Si - O^- + H_2O \quad \rightarrow \quad \equiv Si - OH + OH^- \qquad [3.3]$$

$$\equiv Si - O^- Na^+ + H^+ \quad \rightarrow \quad \equiv \text{Si-OH} + \text{Na}^+ \qquad [3.4]$$

3.3.2. LEACHING PROTOCOL

The leaching methodology of this study used 0.1g of sample in 5 ml of deionised water (1:50 sample:water ratio) under static conditions for a four hour period. At the end of the four hour period, the samples were placed within a centrifuge for 5 minutes to separate sample and liquid, and were filtered through 0.45 μm cellulose-acetate membrane filters. The leachate solutions were then further diluted and stored in polystyrene vials for analysis.

The sample:water ratio used in this study was higher than the most commonly used ash:water ratios in studies of silicate ash particles (Witham *et al.* 2005), which is largely due to the limited quantities of sample material available for use in this research. Since multiple analytical techniques were used in the course of this study, it was desirable to minimise the amount of material lost in destructive analysis such as leaching. Additionally, as exposure times were much longer than in-plume exposure times, it was considered likely that greater concentrations of soluble surface reaction products could be emplaced, and that there may be a risk of saturation of leachate solutions resulting in only partial dissolution of soluble species. Accordingly, a 1:50 sample:water ratio using 0.1 g of sample was used, which ensured that in none of the leaching experiments in this study were the major constituent elements saturated in solution. The four hour leaching time was selected based upon the work of Frogner *et al.* (2001) and Jones and Gislason (2008). The leaching methodology of these authors, despite being a flowing, rather than static system, demonstrated that it may take up to four hours for the concentrations of elements extracted by leaching from silicate ash particles to reach a constant 'baseline' concentration after the initial pulse of soluble elements into solution. Based upon the existing studies, a four hour leaching time was considered to provide time for dissolution of all soluble surface reaction products without resulting in significant dissolution or leaching of the underlying sample surface.

3.3.3. LEACHATE ANALYSIS

Leachate solutions were analysed in-situ for major anions (specifically SO_4^{2-}) on a Dionex 120 Ion Chromatograph, whilst the major elements Ca, K, Mg and Na were analysed on a Shimadzu AA-6300 Atomic Absorption Spectrophotometer by this author. Selected leachate solutions were analysed externally for Fe, Al and Si.

3.3.3.1. LEACHATE ANALYSIS – ION CHROMATOGRAPHY

Ion chromatography (IC) analysis was conducted by this author on a Dionex 120 Ion Chromatograph, using an IonPac AS14 anion exchange column and a Na_2CO_3 / $NaHCO_3$ eluent with concentration 3.5mmol l^{-1} / 1mmol l^{-1} and flow rate 1.1 ml min^{-1}.

IC can be used to determine cations with the appropriate column, this technique was not used in this study and so reference is only made to anion exchange. IC using an anion exchange column relies on the exchange of anions in solution with eluent anions occupying anion exchange sites on the AS14 column. The charge of the sample anions and the strength of the exchange sites dictates the time taken for the sample anions to travel through the column. This is a product of the partition between the mobile (solution) and immobile (column) phases (Fig. 3.2), which is described by the distribution coefficient (k_d) (Small 1989). An anion with low k_d has a low retention time within the column, whilst an anion with a large k_d is strongly partitioned in the immobile phase and takes much longer to pass through the column (Small 1989). The partitioning between the immobile and mobile phases therefore seperates the anions from each other which then enables their respective concentrations to be determined.

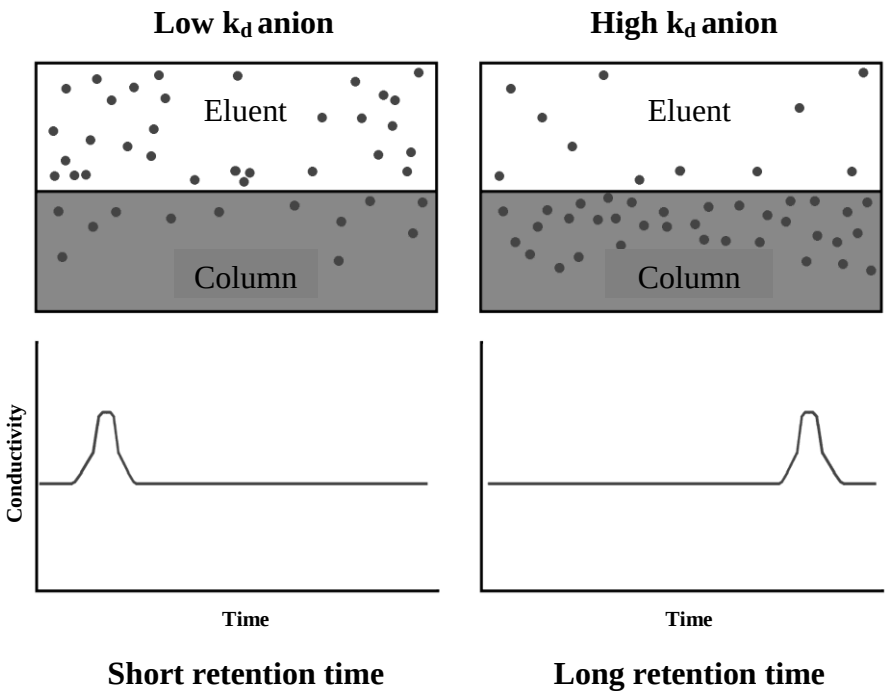

Fig. 3.2 *Conceptual diagram illustrating the partition of a low k_d anion into the mobile phase with an accordingly short retention time within the column, and a high k_d anion partitioned into the immobile phase with a long column retention time.*

Concentration is determined initially from the conductivity of the solution travelling through the column with time. The baseline for conductivity is provided by the conductivity of the carbonate eluent after passage through a column suppressor which exchanges Na cations in the eluent with H^+ forming carbonic acid (H_2CO_3), lowering its conductivity (Small 1989). The anions travelling through the column do not have their conductivity suppressed and so register as peaks on the chromatogram (i.e. Fig. 3.3) appearing at different locations according to the K_d of the individual anion (Small 1989). Through reference to a series of known standards, the area of the conductivity peak can be related to the initial concentration of the specific anion within the sample solution.

Analysis conducted by ion chromatography in the course of this study is considered to be reliable and consistent. Fig 3.4 shows the average peak area returned by analysis of 14 independent sets of calibration standards, and the average error of ±15% demonstrates that standards can be reproduced reliably. The detection limit of these analyses is specific to the analytical method used, specifically with respect to eluent conductivities and chemical composition. In practice, the detection limit for the ion chromatograph was 100 μg l^{-1} due to trace S contamination in the deionised water control.

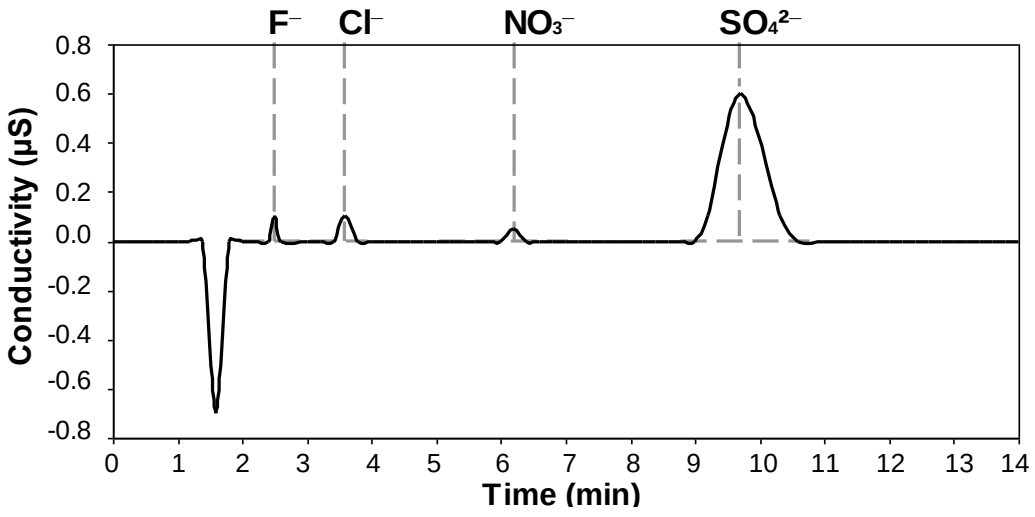

Fig. 3.3 *Replica chromatogram as would be produced by ion chromatography using the method outlined in section 3.3.1. In this diagram, the sample running time and retention times of the major anions as observed during analysis are illustrated.*

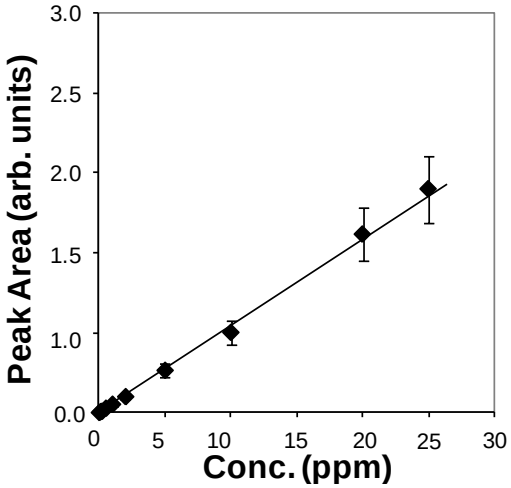

Fig. 3.4 *Average value of calibration standards from 14 independent analytical sessions on the ion chromatograph. Samples have an average error of ±15%, and demonstrate the consistency with which standards can be produced and accurate analysis of leachate solutions can be performed.*

3.3.3.2. LEACHATE ANALYSIS – ATOMIC ABSORPTION SPECTROPHOTOMETRY

Atomic absorption spectrophotometry (AA) was used to identify the major cations in the leachate solution. Leachate analysis for the major cations Ca, Mg, K and Na was conducted by this author on a Shimadzu AA6300 atomic absorption spectrophotometer burning an air-acetylene flame at a temperature of approximately 2125°C.Within the flame, gas molecules may be converted into free atoms in the ground state, which can then be excited by a beam of light with energy corresponding to that required to raise an electron from the ground state to the excited state (Rubeška and Moldan 1971). The decrease in the incident radiation flux as measured after the beam has passed through the flame is related to the concentrations of atoms in the aspirated solution by the Beer-Lambert Law.

The Beer-Lambert law [Eq. 3.5, 3.6] states that the ratio of emerging radiation intensity to the incident intensity (transmissivity, *T*) is described by the molar absorption coefficient (Σ) for the specific element within the species under investigation and the path length (*l*) of the incident radiation (Atkins 2001).

$$T = \log \frac{I}{I_0} \qquad [3.5]$$

$$\frac{I}{I_0} = e^{-\Sigma l} \qquad [3.6]$$

The units of molar absorption coefficient are 1 / (Concentration × Length), and so if the length, absorption and path lengths are known, then the concentration of the absorbing species in the flame may be determined (Atkins 2001). Relating the decrease in incident radiation to the concentration of ground state atoms within the free atom cloud is impeded by various in-flame and aspiration phenomena, but these effects can be negated or reduced by reference to known standards and the addition of various reagents.

During aspiration and evaporation, when dealing with complex solutions, some elements in solutions may condense or form involatile compounds (Fig 3.5) with other elements and so will lower the free atom content of the flame. For Ca and Mg, reactions can occur with elements such as Si, Al and Fe to form involatile compounds which will reduce the number of free atoms available for absorption. Lanthanum chloride can be added which preferentially reacts with the additional elements and prevents the interference effect (Rubeška and Moldan, 1969). Additionally, as indicated by Fig. 3.5, excitation and ionisation may be induced by both the light beam and the flame, but any excitation prior to exposure to the light beam may lower the number of atoms in the ground state prior to the ignition of the lamp (Rubeška and Moldan, 1969). This effect can be mitigated; for K, the addition of $CsCl_2$ to the sample generates free electrons by the conversion of the chloride ion to a free atom, preventing ionisation (Lagalante 1999; Rubeška and Moldan 1971). The use of standards will further mitigate any remaining ionisation effects, and samples should be diluted to fall within the range corresponding to a linear relationship between absorbance and concentration before such effects become pronounced.

The detection limits of atomic absorption flame spectrophotometry for Ca, K, Mg and Na are low, being 1 ppb for Ca and K, 0.2 ppb for Na and 0.1 ppb for Mg. As such, the instrument can be used to detect very low concentrations in dilute solutions (Welz 1985). The standard ranges used in this study were calculated to take advantage of these detection limits, the range over which concentration is linearly proportional to absorbance and knowledge of the likely elements to be extracted from the materials. For Ca, a range between 0.1 and 4 ppm was used; for Na, a range between 0.05 and 1 ppm was used; for K, a range between 0.05 and 0.6 ppm was used and for Mg, a range

between 0.02 and 0.8 ppm was used. Fig 3.6 a-d shows the average absorbance of 5 randomly selected series of calibration standard sets to demonstrate the consistency with which concentrations of major cations can be estimated. Mg and K show greater error than either Ca or Na, but throughout this study, it was found that Na and Ca were the only elements which were present in concentrations of any significance. A marginally lower quality calibration for Mg and K is not therefore considered to be of any consequence.

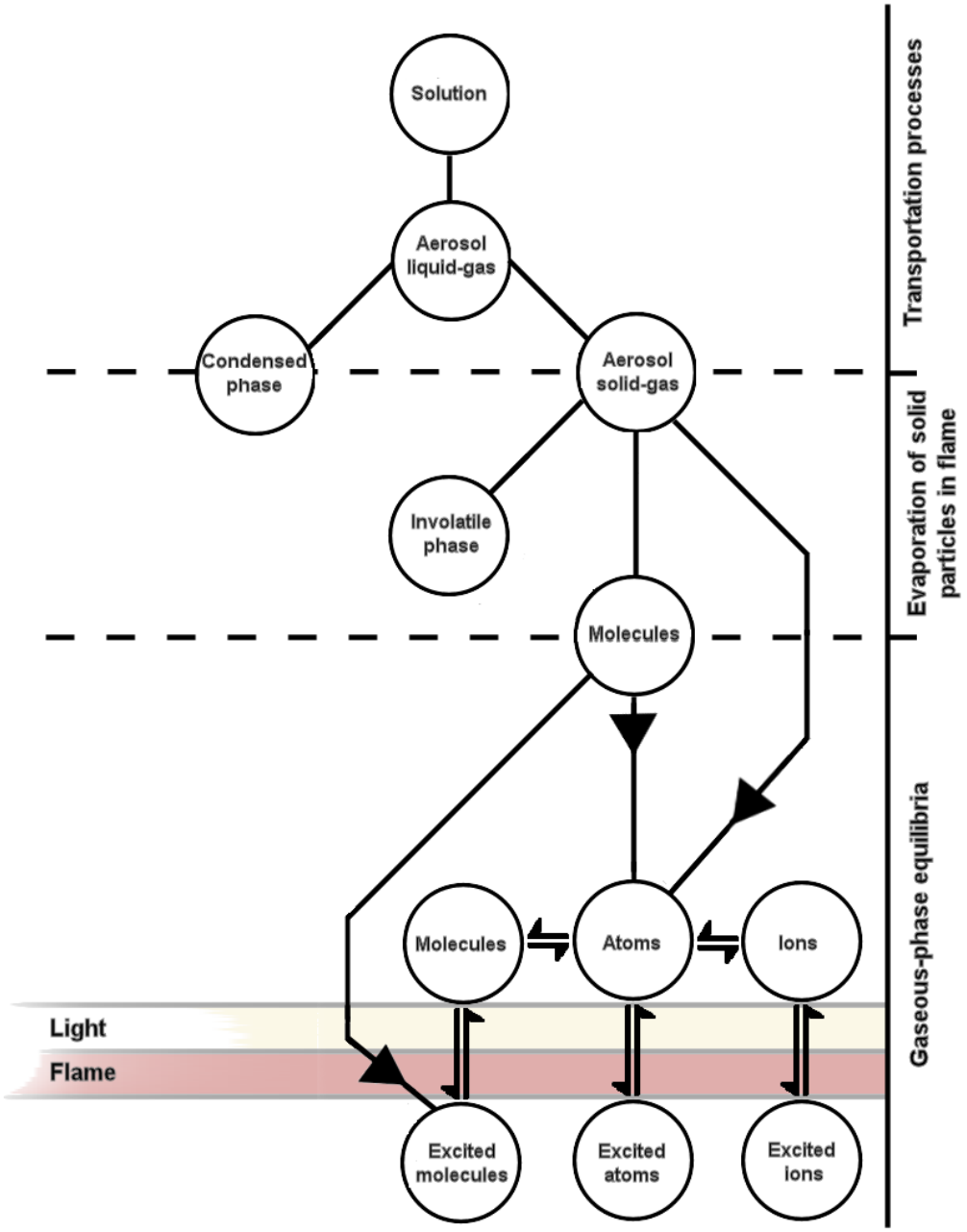

Fig. 3.5 *Physical and chemical processes which occur during aspiration and evaporation of sample solution during atomic absorption. Modified after Rubeška and Moldan (1971).*

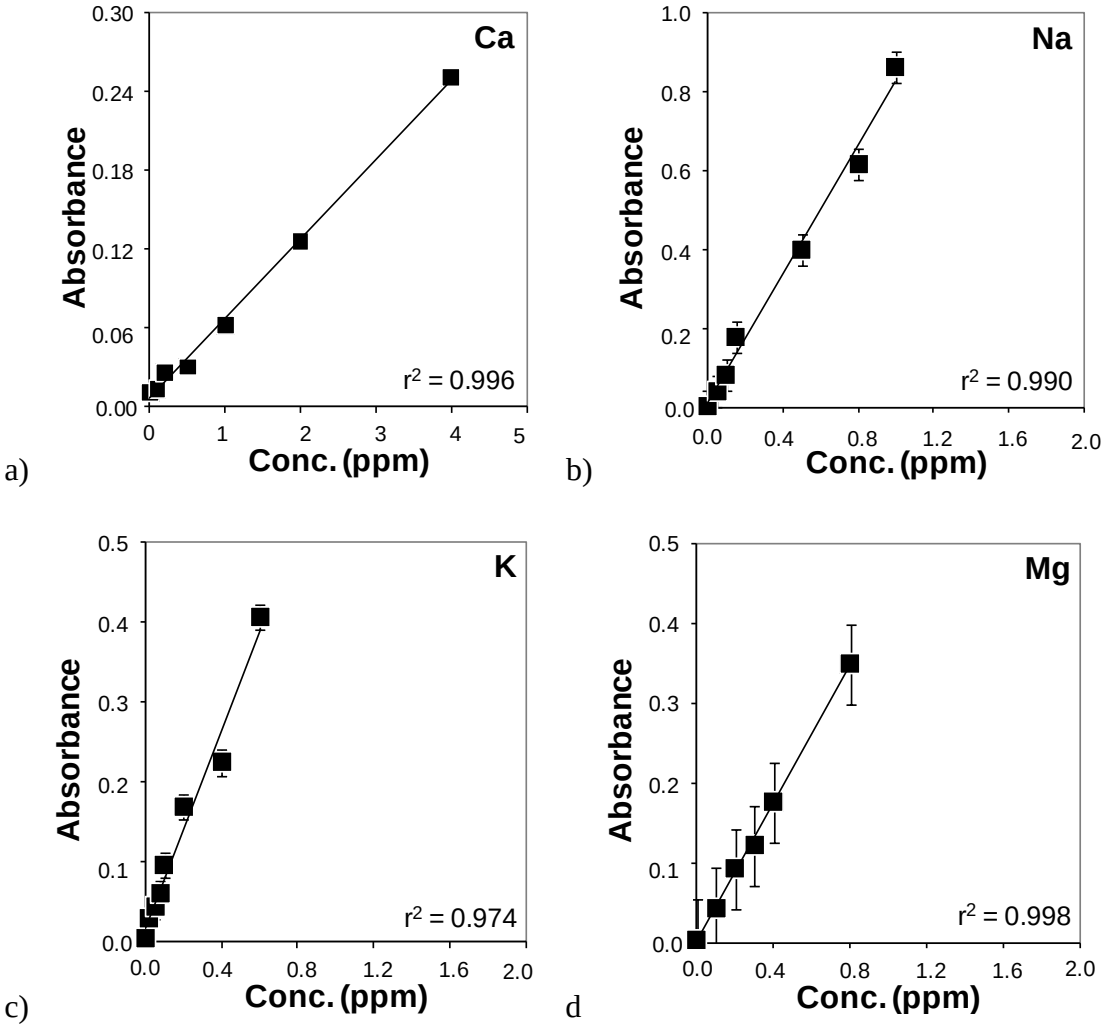

Fig. 3.6 *Average value of calibration standards for the elements Ca (a), Na (b), K (c) and Mg (d) from 5 randomly selected independent analytical sessions on the atomic absorption spectrophotometer. Individual errors vary, with Mg and K showing the highest variation, and Ca being the most consistent with the smallest error.*

3.3.3.3. LEACHATE ANALYSIS – OPTICAL EMISSION SPECTROSCOPY

The other major cations found in volcanic ash and glasses, Fe and Al, were analysed externally by Inductively Coupled Plasma Optical Emission Spectroscopy (ICP-OES) on a Thermo Fisher Iris Intrepid II spectrometer. These were conducted externally, by Dr. Leon Van Derberg at Radboud University Nijmegen. Not all samples were analysed for these elements, a selection of 36 representative samples were despatched for analysis and it was found that concentrations of these cations in acidified leachate solutions was too low to merit further analysis. As this technique was not extensively used, no discussion of its operating principles will be included.

3.4. SURFACE ANALYSIS

3.4.1. X-RAY PHOTOELECTRON SPECTROSCOPY

X-ray photoelectron spectroscopy (XPS) analysis was conducted on a Kratos AXIS HSA XPS facility by this author under supervision, unless otherwise stated. This instrument provides quantitative information on surface compositions for elemental surface concentrations which can be as low as <0.1 wt. % (Kratos 2006), with a Mg source with an energy of 1235.6 eV. Selected samples were analysed by request of this author at the Leeds EPSCR Nanoscience and Nanotechnology Facility, using a VG Escalab 250 instrument with an Al source with an energy of .1486.6 eV.

XPS is a surface sensitive technique used to determine the composition and chemical speciation and bonding environment of a surface through the ejection of electrons from the core orbitals of atoms after collision with an X-ray photon. In XPS, a sample is bombarded with X-ray photons from what is commonly an Al or Mg anode, which have energies of ~1400 eV and ~1200 eV respectively (Rouxhet and Genet 1991). Using photons with a range of energies from 50 eV to 1400 eV permits the probing of the surface of the sample to a depth of < 10 nm. Any photons with energies lower than ~50 eV are likely to have insufficient energy to interact with atomic orbitals and cause photoelectron ejection, having a long inelastic mean free path (Fig. 3.7). Conversely, as the energy of the X-ray photon increases, the chance of interaction increases, but the high energy of the photon permits greater penetration into the sample (Rouxhet and Genet 1991). The limiting factor in the case of high energy X-ray photons is that although the penetration of the photons may be deep, the ejected photoelectron will not be able to escape the surface due to inelastic collisions between the point of emission and the sample surface. The useful depth probed by XPS is therefore approximately 1-6 nm (Stöcker 1996).

At the detector, the kinetic energy (K_E) of the photoelectron is measured, and by calculating the energy difference between the source X-ray photons (hv) and the kinetic energy (K_E) of the photoelectron, XPS can deliver information on the chemical nature of the surface. As illustrated in the equation and diagram in Fig. 3.8, K_E is determined by the detector; hv is the known energy of the X-ray photon; $E_{k,l,m,f}$ are the energies needed to remove a photoelectron from the respective orbital shells; E_C is the work required for the photoelectron to escape the sample surface, particularly where a positive charge has built up (charging); and Ω is the spectrometer-specific energy required to raise a

photoelectron from the sample surface to the detector (Rouxhet and Genet 1991). Binding energies (E_b) are sensitive to the attraction of the positive nucleus, the shielding effect of neighbouring electrons and the presence of neighbouring or bonded atoms which may exert their own influence (Rouxhet and Genet 1991). Determining E_b can therefore give detailed information about surface composition and the chemical state of the atoms within that surface.

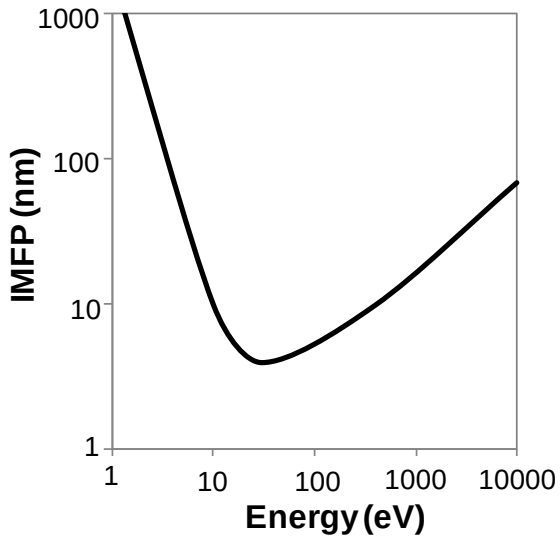

Fig. 3.7 *Conceptual diagram of the relationship between the energy of an X-ray photon and its inelastic mean free path (IMFP), based on the work of Seah and Dench (1979)*

XPS generates spectra which plot intensity peaks of measured electron flux across a range of binding energies (Fig. 3.9). When dealing with high resolution spectra for a single element which may be bonded to other elements, multiple peaks may exist and overlap. Overlapping peaks are interpreted through the manual fitting of representative peaks with properties appropriate to the chemical state of the specific atom. Manual peak fitting is complicated by various phenomena which may alter peak shape or intensity. Various phenomena may decrease the K_E after photoemission, charge the surface and so increase or otherwise alter E_b during photoemission. The relevant phenomena for this study are those which effect E_b, such as doublet separation and multiplet splitting, and those which modify E_c or decrease E_k such as 'shake up' effects, sample charging. These effects are summarised in brief in the following paragraphs.

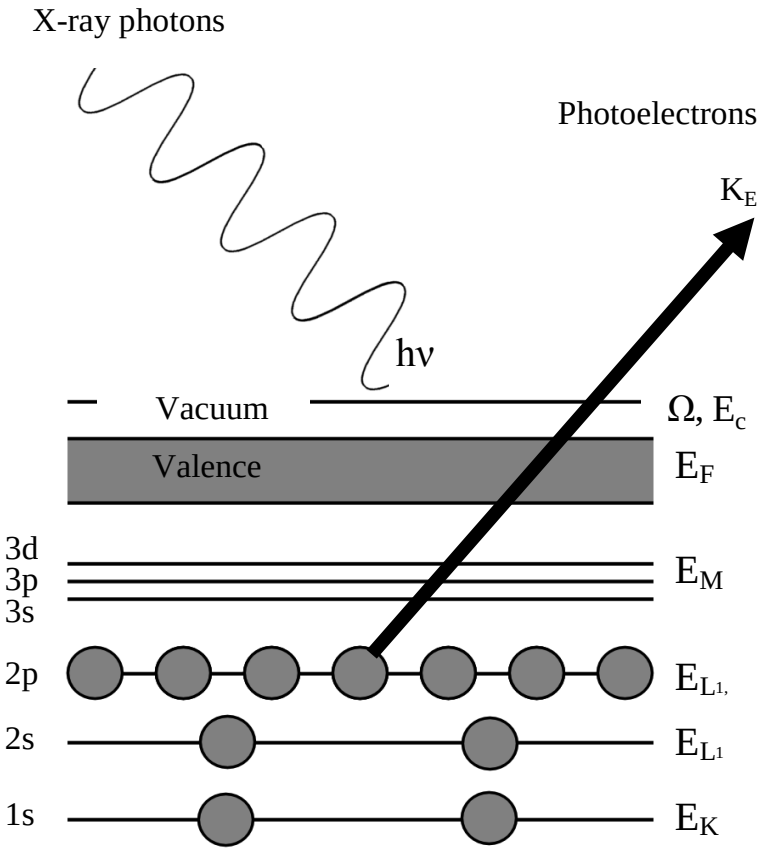

$$E_K = h\nu - E_1 - \Omega - E_c$$

Fig. 3.8 *Principles of XPS, where the kinetic energy of the sample is known and can be used to determine E_K, E_L, E_M and E_F, as the binding energies required to remove an electron from the 1s, 2s, $2_{p,s,d}$ and valence orbitals respectively, via the known quantities hν as the initial energy of the X-ray photon and Ω is the energy required for the photoelectron to escape the sample surface and reach the detector through the spectrometer vacuum chamber (instrument specific) and E_C is any additional work required for the photoelectron to escape the surface due to charging effects.*

When interpreting peaks of core level orbitals (i.e. Si 2p) with paired electrons, two separate peaks are observed. These should not be attributed to separate chemical phenomena, but rather to spin-orbit effects which are compensated by the fitting of two components (i.e. Si ($2p\ ^3/_2$), Si ($2p\ ^1/_2$), Fig. 3.10) with an energy difference accounted for by the spin-orbit coupling of the electron pair (Venezia 2002). Multiplet splitting effects metal atoms with unpaired electrons in a valence shell which may combine with partially filled core shells (Fadley and Shirley 1970). This alters the binding energy of the core shell electrons, which complicates the interpretation of the XPS spectra. This phenomena is most relevant for the Fe (2p) spectra in this study.

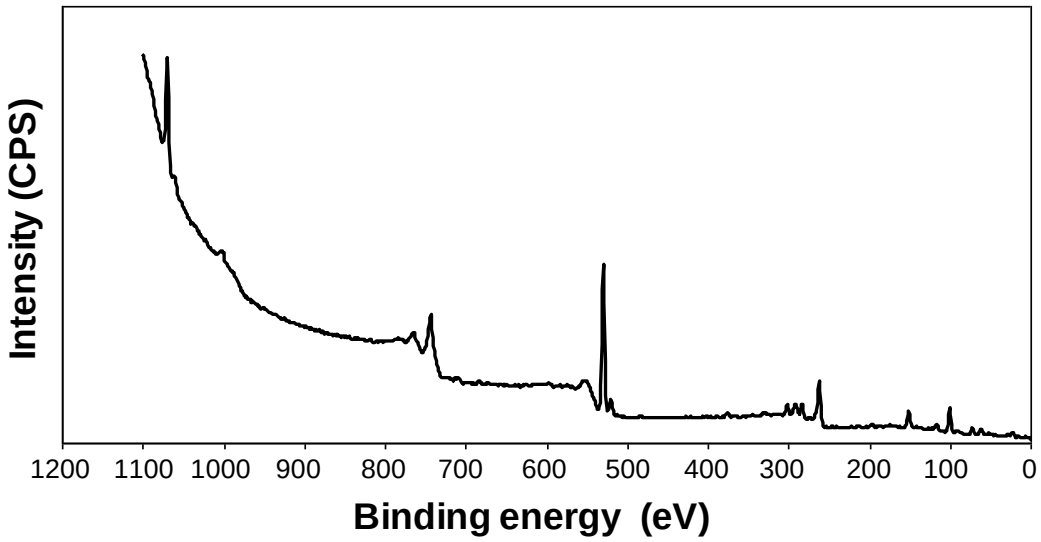

Fig. 3.9 *Example photoelectron spectra generated from analysis of a glass surface for a wide scan across all photon energies performed on a Kratos AXIS HSA XPS facility.*

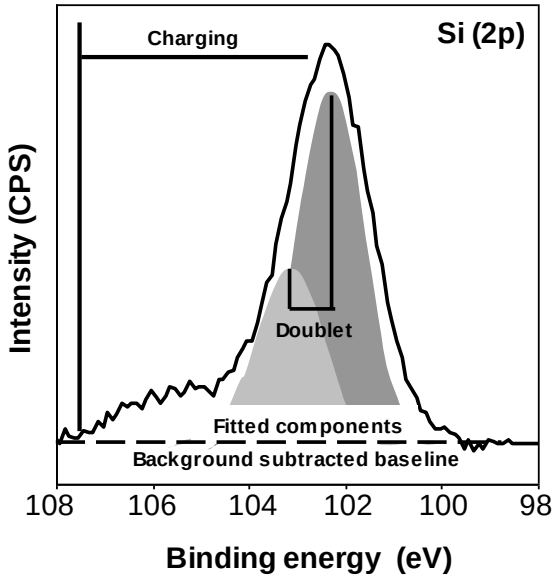

Fig. 3.10 *Sample Si (2p) region of an XPS spectra for the showing the fitted components with an assigned doublet separation due to the nature of the electron configuration in the Si (2p) core shell. The effect of charging, which creates a discernible asymmetry in the peak above the fitted sample baseline, is also indicated.*

Factors influencing E_b indirectly, via decreasing K_E or by altering E_c include 'shake up' or 'shake off' effects and sample charging. 'Shake up' and 'shake off' occur when a photoelectron collides with a higher energy electron during escape, and loses kinetic energy; in 'shake up', this results in a loss of kinetic energy from the sample which may manipulate the equation given in Fig. 3.8 to give higher binding energies

(Stöcker 1996). In ‘shake off’, the higher energy electron may also be ejected, but in either case, this results in a ‘satellite’ peak (Stöcker 1996). These effects occur most strongly in transition metals and rare-earth compounds which have unpaired electrons in their higher orbitals (i.e. Fe) (Rouxhet and Genet 1991). Charging effects occur when a sample is unable to neutralise the positive charge built up as a result of a loss of electrons. This occurs in insulating materials, and electrons must escape an increasingly positive surface which requires more E_c and hence alters K_E. Charging and ‘shake up / off’ effects may result in an asymmetry within a photoelectron intensity peak (Fig. 3.10) (Stöcker 1996), and this should be considered during data interpretation.

XPS data can therefore be used in two specific ways, to determine the relative surface composition and to analyse shifts or changes in the lineshape of the peaks which comprise the XPS spectra. The relative surface composition was determined in CasaXPS version 2.3.9 by the summation of the intensities of the identified peaks of XPS spectra, using instrument and element specific constants to calculate the relative surface composition (atm. %) of all identified elements. To interpret changes in peak lineshape or peak position in the region of the XPS spectra under analysis, manual fitting of representative peaks is required. All manual peak fitting was performed in CasaXPS version 2.3.9, and used a Shirley type baseline and a symmetrical Gaussian-Lorentzian lineshape for non-metallic elements. In interpretation of metallic element spectra, a Doniach-Sunjic profile was applied to generate an asymmetric lineshape to compensate for ‘shake up’ effects. Where available, full width half maxima (FWHM) and doublet separations were assigned using values from existing literature or in the case of post-experiment analysis, by comparison to the initial surface. Appropriate caution and consideration to satellite peaks or charging was used when assigning multiple peaks to the data. Although the quality of the fit to the spectra increases when multiple peaks are used, the relevance of such peak fitting decreases as the number of fitted components increases without an appropriate rationale for such an inclusion. XPS analysis is ultimately a subjective technique, reliant on the individual user’s analysis, interpretation and even aesthetic judgements of baseline positions. It is not therefore possible to assign a value to any imparted error, and XPS analysis should therefore be used alongside alternative data sources for corroboration wherever possible.

3.4.2. NITROGEN ADSORPTION POROSIMETRY

Surface area analysis was conducted by this author on a Quantachrome Nova 600 porosimeter, using N_2 gas as the adsorbate gas.

Determining the specific surface area (a_s) of a sample via gas adsorption determines the number of molecules adsorbed onto the surface, assuming total coverage of one layer of molecules, and assumes that a molecule of gas is spherical (Lowell and Shields 1984). The cross sectional area for nitrogen, for example, is assumed to be 16.2 Å. Nitrogen is often favoured as an adsorbate gas due to its tendency not to be constrained solely to specific adsorption sites, whilst still forming a discrete, organised layer of gas (Lowell and Shields 1984). Monolayer gas adsorption is described by the Langmuir model, which assumes that no adsorbate-adsorbate interactions occur. Where a non porous solid adsorbs gases in multiple, rather than monolayers, the Brunauer, Emmet and Teller (BET) may be more appropriate.

The Brunauer, Emmet and Teller theory (BET) is applicable to non-porous solids where gas adsorption results in the emplacement of multiple layers of adsorbed gas molecules. A layer of adsorbed molecules is not completed before new layers of adsorbed molecules are bound to the underlying layer, which is accounted for by the BET theory, permitting the extrapolation of the number of molecules required to complete a monolayer. The BET equation is given in equation [3.6] (Hiemenz and Rajagopalan 1997) where V and V_m are the volume of the adsorbed gas and the volume of the adsorbed gas required to form a monolayer, P is the experimental pressure, P_0 is the initial pressure and C is the BET constant. For a full derivation of the BET constant, the reader is referred to general surface chemistry textbooks (Hiemenz and Rajagopalan 1997; Lowell and Shields 1984). By varying adsorbing N_2 gas concentrations under varying P/P_0, plotting [3.7], where all terms are as previously defined and P_{svp} is the saturation vapour pressure, against [3.8] produces a linear relationship of which the intercept and the gradient of the line can be used to determine both V_m and C (Hiemenz and Rajagopalan 1997). Hence, the specific surface area of the sample can be determined by converting V_m to the number of molecules, and with the cross sectional area of 16.2 Å, so determine a_s.

$$\frac{V}{V_m} = \frac{C(P/P_0)}{(1-P/P_0)[1+(C-1)P/P_0]} \qquad [3.6]$$

$$\frac{P}{V(P_{svp}-P)} \quad [3.7]$$

$$P/P_{svp} \quad [3.8]$$

The porosity (Φ) and median pore diameter (Φ_d) can also be determined by porosimetry. Porosity is determined by knowing the mass of sample and the volume of N_2 which occupy an empty reaction tube at the saturation vapour pressure. The average pore diameter is determined by complex computations involving the change in the volume of adsorbate with changing pressure (Barrett-Joyner-Halenda method) as the N_2 gas is desorbed, and produces the median pore diameter assuming that pores are geometric cylinders (Goworek 2000).

The error on surface area analysis and on porosity and pore diameter using the NOVA 600 porosimeter was found to be on the order of less than ±1%, ±5% and ±0.5% error respectively (S. Wainright, pers. comm. 2010). Error was minimised by the use of large volume bulbs which could contain higher masses of material, particularly when analysing low surface area volcanic ash and glass materials.

3.4.3. SCANNING ELECTRON MICROSCOPY

Scanning electron microscopy (SEM) was conducted at the Leeds EPSRC Nanoscience and Nanotechnology Facility in the presence of this author. Powder samples for SEM are fixed on carbon tape and were sputtered with Pt-Pd prior to analysis and analysed on a LEO 1530 Gemini FEGSEM. Optical microscopy was conducted with a beam with an electron gun accelerating voltage of 3 keV, whilst localised energy dispersive X-ray detection (spot-EDX) was conducted at 30 keV.

SEM uses an electron beam with photon energies ranging from 0.1 to 50 keV with a beam diameter of <10 up to 100 nm (Reimer 1998), which is swept across the sample and either transmitted, absorbed or scattered. The absorption of electrons can be pronounced, and the depth through which the electron beam can be transmitted is of the order of 1 μm thick (Jones 1987). This transmission is accompanied by some reflection and backscattering, both from the immediate surface and from throughout the 1 μm depth probed by the technique. Electrons from within the surface may escape after interacting with multiple atoms within the sample. These atoms will have lower energies as a result of their impacts than the energy of those which have only undergone

one interaction. There may also be some secondary electrons produced by the transferral of energy from electron beam to electrons in orbitals within the sample, which may result in their ejection; these may be used for compositional analysis of the sample by energy-dispersive X-ray detectors (Jones 1987). The backscattered electrons are recorded by detectors and where topographic variation in the surface of the sample exists, scattering will be focused in some directions and decreased in others, and the variations recorded at these detectors are recorded for each square cell analysed by the SEM (Jones 1987). These can then be assembled to make a raster image of the sample surface, which can have a spatial resolution of the order of <10 nm and the variations recorded at multiple detectors can be used to create an image of the sample surface at a much greater resolution and magnification than those offered by optical microscopes (Jones 1987).

3.4.4. TRANSMISSION ELECTRON MICROSCOPY

After the submission of this thesis, access was gained to the TEM facilities at the Leeds EPRSC Nanoscience and Nanotechnology Facility. Thin sections were extracted from three samples of post-experiment glasses from the study in Chapter 5 by Dr. Mike Ward and analysed by TEM in the presence of this author. As this technique was not extensively used, only a brief discussion of the operating principles of TEM is provided.

In TEM, electrons passing through a thin section may be diffracted (Williams and Barry Carter 2009). The extent to which an electron is diffracted, combined with the overall flux of electrons through the sample can be used to produce a contrast image of the sample. Electrons backscattered from the analysis which have lost energy due to inelastic collisions with surface electrons can also be used to determine surface elemental composition (Williams and Barry Carter 2009). Use of a scanning TEM can then be used to create elemental maps of the thin sections under analysis. This technique offers a much higher spatial resolution (0.2 - 0.3 nm, Williams and Barry Carter 2009) than similar surface analysis using SEM. In the work conducted during this study, a thin section penetrating into the sample surface allowed the use of this technique for depth-profiling the variations in elemental composition in a near surface region of the particles.

3.5. BULK ANALYTICAL TECHNIQUES

3.5.1. X-RAY FLUORESCENCE SPECTROSCOPY

Initial X-ray fluorescence spectroscopy (XRF) analysis of the model ash systems was conducted for the samples in Chapter 5 externally on a PANalytical Axios-Advanced XRF PW4400 spectrometer by the late Dr. Tim Brewer.

X-ray fluorescence spectrometry (XRF) is a bulk analysis secondary emission technique which uses X-ray photons to probe the sample. It is favourable over techniques which probe surfaces using primary excitation via an electron gun, as these cause surface modification, altering the composition of the sample at the point of contact (Bertin 1970). The X-ray photons are generated by two mechanisms; the electron stream from the cathode of the X-ray source impacts on the anode and the deceleration on impact (braking radiation) is emitted as photons with a continuous spectrum of energies (Guiner and Dexter 1963). Photons are also emitted as line radiation after the excitation of electrons in the anode. Excited electrons are ejected and higher energy electrons drop down to fill the vacancy, emitting a photon with specific energy equivalent to the energy difference between the orbitals (Russ 1984). The X-ray photons are then directed to impact with the sample, causing excitation and ejection of electrons. As higher energy electrons fill the vacancies left behind, secondary photons are emitted and are detetected by a scintillation counter (Schlotz and Uhlig 2000). Compensating for secondary X-ray interactions and the scattering of original X-ray photons, the composition of the sample can be determined from the spectra by complex equations which also consider the specific properties of the sample and the XRF spectrometer used (Russ 1984).

The XRF analysis conducted at the University of Leicester were analysed via fusion of 0.1g of sample in 3g of lithium tetraborate flux. This method of analysis conducted at the instrument at Leicester provides a detection limit of 0.01% with a precision better than 0.5% at 100 x the detection limit (Mahler 1984). The analyses in Chapter 4 were conducted by this author using a Horiba Scientific XGT-7000 micro-XRF analyser with a Rh source with maximum voltage of 50 keV. All analyses using this instrument were conducted under full vacuum with a 300 second acquisition time with three measurement points per sample. The heterogeneities within the samples were the limiting factors in the latter analyses, and detection limits associated with this analysis are considered in Chapter 4.

3.5.2. X-RAY POWDER DIFFRACTION

X-ray powder diffraction (XRD) was conducted by this author on a Bruker D8 "Focus" diffractometer using a Cu source with a wavelength of 1.5 angstroms (154 pm).

X-ray photons can be used to probe the crystallographic nature of a sample by the scattering of an incident X-ray by an atom (Buerger 1942). The interaction of X-ray photons with the electrons of an atom results triggers vibrations in the electron which generates an X-ray photon with the same wavelength and frequency as the inbound X-ray. These X-ray photons are emitted across a range of directions and so the X-ray can be considered as being scattered. In a single plane of atoms, the adjacent spherical waves create a series of peaks by constructive interference, and the intensity of these peaks decreases as the difference between the angle of the incident beam and the 'reflected' beam increases (Buerger 1942). When dealing with a crystal lattice, however, these peaks are susceptible to destructive interference from out of phase 'reflections' from underlying layers. There is only one angle where constructive interference occurs, where the path length difference of two parallel X-rays is 1 wavelength (i.e. AB+ BC = $n\lambda$; Fig 3.9). This angle is described by the angle of the inbound X-rays with the sample surface θ and the distance between the lattice planes d, giving the Bragg law [3.9] where λ is the wavelength of the 'reflected' X-ray photon, d is the interatomic spacing and θ is the Bragg angle (Atkins 2001).

$$n\lambda = 2d\sin\theta \qquad [3.9]$$

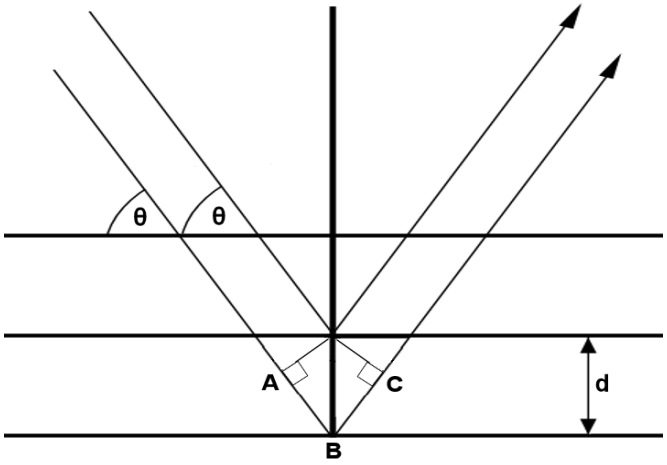

Fig. 3.11 *Conceptual diagram illustrating the reflection of X-rays by lattice planes separated by distance d for X-rays with path length difference of (AB + BC), being equal to nλ, where n is an integer (Atkins 2001).*

When dealing with a mixture of crystalline materials, it is expected that not all crystals will be oriented in the same direction, and assuming random distribution, it would therefore be expected that different crystal faces will be exposed and will generate different diffraction peaks. This essentially creates a diffraction fingerprint common to a single crystal which can be used to identify it in other samples (Jones 1987). Identification is based upon the position of the peaks and the intensity of the peaks; the former can be complicated by the presence of multiple crystallites which may make the separation of individual spectra, and by the constructive interference of overlapping peaks.

Crystalline phases are identified from XRD diffraction patterns by comparison with existing diffraction patterns for known reference standards, which are given in the text when referred to. In interpreting the XRD diffraction patterns of pre-experiment and post-experiment samples, data processing using the BrukerAKS Diffrac^{plus} software enables the subtraction of the baseline spectra of the diffraction pattern, leaving only the discrete crystalline phases. With the exception of XRD analysis conducted on the pre-experiment sample surfaces, all XRD data in the following chapters is presented after baseline subtraction.

3.5.3. TOTAL SULPHUR ANALYSIS

Total sulphur analysis was conducted using a paid service at McGill University, Montreal, Canada on a Perkin-Elmer Aanalyst100 atomic absorption spectrophotometer burning a nitrous oxide flame. In order to digest the aluminosilicate materials and glasses for analysis, a lithium metaborate fusion technique was used at that facility, whereby the sample for analysis is fused into a lithium metaborate glass, which is then dissolved in nitric acid for analysis. As an atomic absorption spectrophotometry technique, detection limits are as previously described in 3.3.3.2.

3.5.4. GLASS TRANSITION TEMPERATURE

To determine glass transition temperatures of the processed glasses, differential scanning calorimetry (DSC) was conducted externally on a Netzsch® DSC 404C Pegasus diffuse scanning calorimeter by Dominique Richards at Ludwig-Maximilians Universität München.

In the course of the following chapters, reference is made to properties of glasses, particularly with respect to the multi-component aluminosilicate glasses used in

Chapter 5. When working at high temperatures, it is necessary to be aware of whether the glass has undergone transition to a liquid melt rather than a frozen solid (Paul 1982), as this may alter the surface and bulk structure of the glass and so alter the number and reactivities of surface sites for SO_2 chemisorption. The transition between glass and liquid occurs at different transition temperatures (T_g) depending on the heating and cooling rate to which the melt or glass is exposed, and so in determining T_g, standardised rates of heating and cooling are used (Bair 1994).

DSC heats a sample within a sample holder at a given temperature rate (10 K min^{-1}) but through use of a heater within the holder, maintains the temperature of the sample in equilibrium with the sample holder. To maintain this equilibrium requires varying energy input to the heater, depending on whether the sample is undergoing an endothermic or exothermic reaction (Bair 1994). The fluctuations in the energy useage of the heater can therefore be related to the thermal behaviour of the sample and can be used to determine the heat capacity (C_p) of the sample (Bair 1994). Determining C_p allows the T_g to be determined, as the transition between glass and liquid is accompanied by an increase or step in the specific heat capacity of the sample without an increase in sample temperature (Bair 1994). T_g readings are taken from the initial deviation from the existing heat capacity gradient (Fig 3.10) or can be estimated by the model of Giordano (2008).

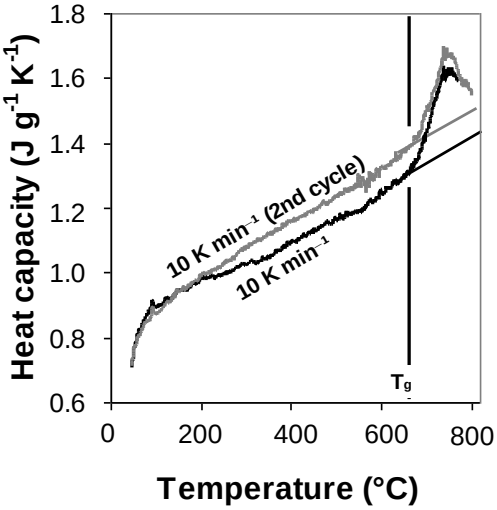

Fig. 3.12 *Sample DSC plot of a glass sample heated at 10 K min^{-1}. Glass transition temperatures (T_g) are determined from the point at which the deviation in heat capacity begins.*

CHAPTER FOUR

SO_2 CHEMISORPTION ON SYNTHETIC MODEL ASH SYSTEMS

CHAPTER FOUR. SO_2 CHEMISORPTION ON SYNTHETIC MODEL ASH SYSTEMS

4.1. INTRODUCTION

4.1.1. OVERVIEW

In Chapter 1, it was hypothesised that the extent of SO_2 chemisorption which could occur on silicate ash particles was dependent on the reactivity and number of sites available for that chemisorption. The objectives of the experimental work presented in this chapter were to determine the validity of a wet chemical, low temperature 'sol-gel' technique in creating aluminosilicate and Ca-doped aluminosilicate materials as model systems for the study of the mechanisms of chemisorption of SO_2 by silicate ash surfaces with respect to Ca, Si and Al.

4.1.2. THE ALUMINOSILICATE GLASS SURFACE

Constraining SO_2 chemisorption on silicate ash surfaces requires more detailed consideration of the specific adsorption sites which exist on that surface. In Chapter 1, the silicate ash particle surfaces as generated by magma fragmentation, which may comprise the majority of ash particles within large explosive eruption plumes, were considered to have surfaces which were entirely glassy (Heiken and Wohletz 1992). The role of crystal phases which exist in magma melts may therefore be of limited importance, but this hypothesis was not investigated further in this study, which considered only the chemisorption occurring on glass particle surfaces.

The aluminosilicate glass surface generated by magma fragmentation during an explosive eruption may originate either from the quenching of a pre-existing melt surface or from the fracture or explosive disruption of a bulk glass. The surface features which may result from generation by fragmentation or rapid quenching may include microcracks, surface crystallites, clusters or aggregates of immiscible phases or ion-diffusion induced alterations to surface composition (Dunken 1982). Surface modification may occur in response to external stimuli such as the addition of heat, abrasive action, or chemical interactions, particularly via adsorption of environmental gases (Dunken 1982). The extent to which such mechanisms may occur within the eruption plume or within the subsurface volcanic conduit or magma chamber prior to fragmentation are not known, but regardless of the mechanism by which the surface is

generated, the glass particle surfaces produced are ultimately derived from the aluminosilicate network which makes up the glass and may therefore have adsorption sites which are a specific result of the network structure.

Volcanic aluminosilicate glass is structured around a network of Si-O tetrahedra (Fig. 4.1), with tetravalent Si coordinated with 4 divalent O anions which are a component of a wider random network of tetrahedral and other structural units with varying bond angle and length and no long range order (Mysen and Richet 2005; Volf 1984). The incorporation of trivalent ($^{3+}$) cations (Al, Fe) into the silicate network may result in the substitution of these cations for the tetravalent ($^{4+}$) Si cation, but the charge deficit produced by their substitution must be compensated by a neighbouring cation in close association (Fig. 4.1) (Mysen and Richet 2005). In aluminosilicate systems, charge compensation roles may be fulfilled by monovalent ($^{1+}$), divalent ($^{2+}$) or in rare cases, even trivalent cations existing within the interstices of the network, although the latter two must compensate for more than one network unit in order to maintain charge balance (Scholze 1990). In natural magmatic melts, charge compensation is entirely fulfilled by the monovalent alkali and divalent alkaline earth metals (Mysen and Richet 2005). Where charge balancing requirements are fulfilled or not required, additional cations can exist in 'network modifying' roles (Fig. 4.2). Network modifying monovalent and divalent cations bond with non-bridging oxygens (NBO), those oxygens which are not connected to two silicate tetrahedral units (Scholze 1990). Network modifying cations may exist as octahedral units (Fig. 4.2), in contrast to the tetrahedral network forming units, and depolymerise the silicate network by disrupting the strong Si-O-Si bond (Mysen and Richet 2005). The relative strengths of the network modifying cations coordinated with NBO increase with their valence, a divalent Ca cation being more strongly bound within the network than monovalent Na, for example (Scholze, 1990). In addition to the cations as network formers and modifiers, it is also possible for different ions to replace the divalent O anion which holds the network together, although this may depend on oxygen fugacity, the physical and chemical solubility of the species in the melt, and the pressure and temperature of the latter (Scholze 1990). These anions may be monovalent, i.e. OH, F, Cl or divalent, i.e. S, SO_3 and CO_3, and may hold a variety of positions within the network, with monovalent anions acting as NBO (Scholze 1990), whilst the integration of the divalent anions may result in polymerisation of the aluminosilicate network (Mysen and Richet 2005).

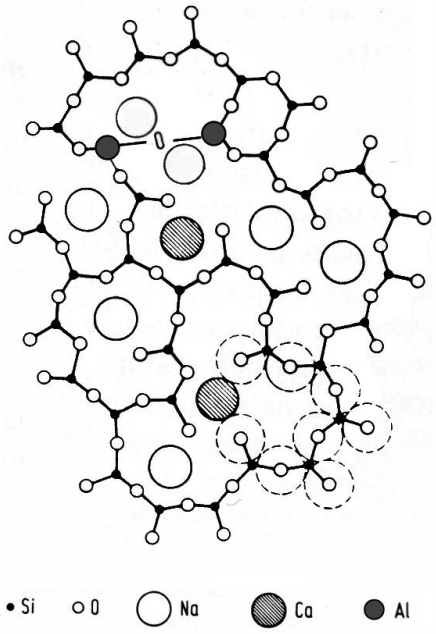

Fig. 4.1 *Two dimensional diagram of the random aluminosilicate network containing monovalent (i.e. Na) and divalent (i.e. Ca) cations in both charge compensating and network modifying roles, the latter creating terminal oxygens (right). The fourth bonds of the tetrahedral network project upward or downward of the plane of the illustration. Modified after Scholze (1990).*

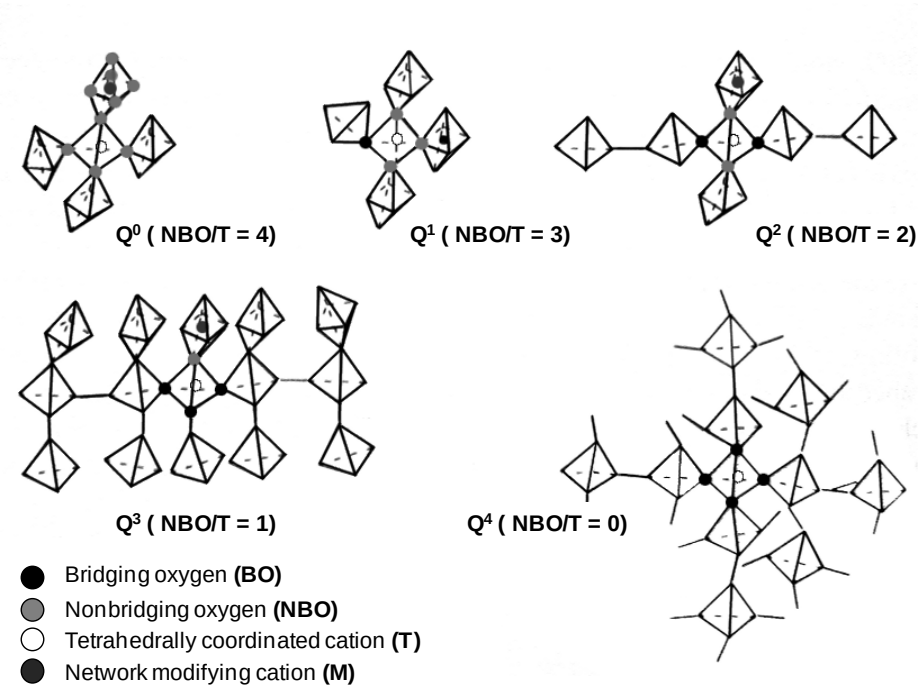

Fig. 4.2 *Schematic representation of the silicate tetrahedra network and the network disruption and octahedral configuration resulting from the insertion of network modifying cations. The short lines at the end of the structure illustrated in Q^4 show the infinite extension of the network. From Mysen and Richet (2005).*

4.1.2. SO_2 CHEMISORPTION ON ASH SURFACES STUDIED THROUGH MODEL SYSTEMS

Volcanic ash and glass materials recovered from eruption sites cannot be used in high temperature SO_2 chemisorption experiments due to their unknown reaction history within the plume or at other times during their history. It is also not possible to use glass particles generated by experimental fragmentation as they cannot be generated in sufficient quantity nor without requiring room-temperature grinding to obtain a desirable size fraction, which destroys the sample surface produced by fragmentation. It is therefore not currently possible to study a system which is entirely representative of the silicate glass particles surfaces as generated within the plume, and model systems with similar chemical composition or surface structure must therefore be used to explore the mechanisms of high temperature SO_2 chemisorption.

To explore the chemisorption of SO_2 and the effect of chemical composition on the reactivity of surface chemisorption sites to SO_2, it was elected to use model aluminosilicate materials generated by a 'sol-gel' method. The 'sol-gel' technique has been used in industry to generate high a_s (100's-1000's m^2g^{-1}, Scholze, 1990) materials with specific chemical compositions without requiring the temperatures required for fusing of the component oxides. The benefits of such systems are apparent; by offering a particle with a_s orders of magnitude larger than that of silicate glass particles, more chemisorption sites per unit mass of sample are provided and it is hence easier to identify and analyse the reaction products formed by SO_2 chemisorption. The 'sol-gel' technique offers further advantages as it offers a low cost method of synthesis which can be used to synthesise aluminosilicate materials with different chemical compositions at the same time and under the same experimental conditions within a laboratory fume cupboard and without requiring a specialised high temperature furnace or its attendant safety precautions.

The surfaces of the aluminosilicate materials produced by the sol-gel method are generated by the precipitation of the gel phase and by room-temperature grinding after the synthesis. The surfaces of the samples may therefore comprise sites for chemisorption produced by the physisorption and chemisorption of environmental gases such as H_2O, CO_2 and O, forming surface hydroxyls and carbonates on NBO and on terminal cations and oxygens associated with defect sites produced by grinding (Dunken, 1982). There are likely to be differences between glass surfaces generated by high temperature fragmentation and the aluminosilicate materials produced by the 'sol-

gel' technique and low temperature grinding, but both have an aluminosilicate network structure and may share common surface sites for SO_2 adsorption. Even after grinding, the surface areas of the model aluminosilicates remain two to three orders of magnitude larger than those of volcanic ash. Any reaction products or other changes in surface composition which may aid in the study of scavenging mechanisms may be much more clearly visible than if natural ash materials were used. SO_2 chemisorption on 'sol-gel' derived aluminosilicates may therefore serve as a simple model system for chemisorption on the surfaces of silicate glass particles generated by fragmentation.

4.1.3. EXPERIMENTAL RATIONALE

The work planned as part of this study was that the major metals (Na, K, Ca, Mg, Fe) common to silicate ash particles would be studied in SO_2 chemisorption experiments as single components of ternary metal-aluminosilicate systems. If the reactivities of the individual surface sites to SO_2 could be quantified, a composite estimate for the chemisorption potential of SO_2 could be derived. Ca was selected as the first cation for investigation based on the chemical compositions of solutions extracted from natural silicate ash particles in 28 studies previously referenced in Table 2.1 and Table 2.2. In leachate data, it is known that Ca is a major element (Witham *et al.* 2005), in the data sets summarised, Ca constituted 34±22 % of all soluble cations in solution. Furthermore, in previous studies, Ca/S ratios in leachate solutions were consistent with the presence of Ca-S compounds. Working on binary aluminosilicates and on ternary Ca-aluminosilicates is therefore a logical starting point for this study, as there is sufficient evidence to indicate that Ca-S compounds may be a major reaction product of volatile scavenging in the eruption plume.

The objectives of this study were two-fold. The first objective was to determine whether a low-temperature sol-gel synthesis method generating high surface area aluminosilicates is appropriate for use in studying SO_2 adsorption on volcanic glass and ultimately ash surfaces. If the wet-chemical technique for sample synthesis was determined to be appropriate, the second objective was to gain insight into the chemisorption sites for SO_2 on the Ca-Al-Si model system which could then give insight into chemisorption sites on silicate ash particle surfaces. Successful fulfilment of both objectives was to serve as the starting point for more detailed study of chemisorption sites on different metal-aluminosilicate systems to explore the range of sites which may exist on silicate ash particle surfaces.

4.2. SAMPLE SYNTHESIS

In this study, aluminosilicates were synthesised via the sol-gel method at room temperature using a solution of solvents and aluminium and silica precursors, aluminium sec-butoxide ($C_{12}H_{27}AlO_3$) and tetraethoxysilane (TEOS) ($(C_2H_5O)_4Si$) (Matsumoto *et al.* 1999) and were doped with calcium nitrate tetrahydrate ($Ca(NO_3)_2$ $4H_2O$).

4.2.1. SOL-GEL TECHNIQUE

The sol-gel method precipitates colloidal particles or clusters of a network of metal oxide polymers from a solution of metal precursors, alcohols and an acid or base catalyst (Paul 1982). The result is a gel comprised of crosslinked metal oxide polymers and molecule chains surrounded by and incorporating a liquid phase (Brinker and Scherer 1985). Metal alkoxides are commonly used as precursors in sol-gel synthesis, as the metal oxide gel produced has low crystallisation tendency (Paul 1982), and hence can produce an amorphous material. The reaction of metal alkoxides in solution to form the metal oxide network occurs via an initial hydrolysis reaction, followed by condensation and removal of the water and alcohol components from the gel phase (Paul 1982).

The hydrolysis and condensation reactions are summarised in simplified form in equations [4.1-4.4], where Me is a metal group (i.e. Al and Si) and R is an alkyl group with $(OR)_x$ indicating the number of initial Me-OR bonds (Paul 1982). The presence of H^+ or OH^- originating from a catalyst, commonly either an acid or base reagent, enhances the hydrolysation of the metal alkoxide [4.1], whilst condensation from the liquid to solid phase [4.2-4] precipitates clusters of the metal oxide network. The polymer clusters may become crosslinked to form a network of interconnected discrete clusters (Fig. 4.3), in the same manner as a series of colloidal particles (Brinker and Scherer 1985)

$$Me(OR)_x + H_2O \leftarrow catalyst \rightarrow Me(OR)_{x-1} + ROH \quad [4.1]$$

$$\equiv Me-OH + HO-Me \equiv \quad \leftrightarrow \quad \equiv Me-O-Me \equiv \quad + \quad H_2O \quad [4.2]$$

$$\equiv Me-OR + HO-Me \equiv \quad \leftrightarrow \quad \equiv Me-O-Me \equiv \quad + \quad ROH \quad [4.3]$$

$$\equiv Me-OR + RO-Me \equiv \quad \leftrightarrow \quad \equiv Me-O-Me \equiv \quad + \quad R_2O \quad [4.4]$$

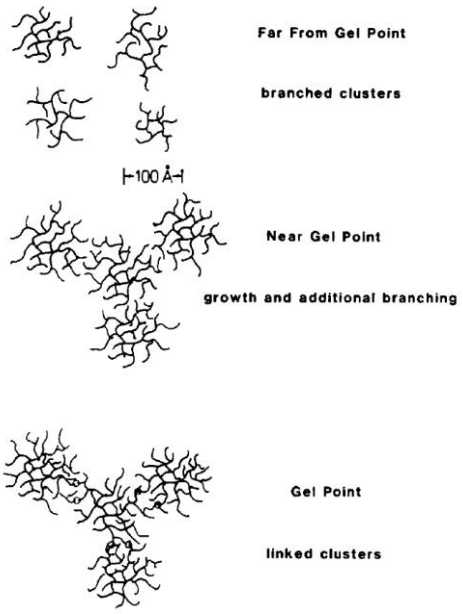

Fig. 4.3 *Schematic representation of the gelation of base catalysed sols (Brinker and Scherer 1985)*

The precipitated gel must be dried to remove the liquid phase surrounding and within the metal oxide network clusters, which is achieved by calcination to evaporate the water vapour and organic compounds. The removal of solution results in the collapse and shrinkage of the cluster network due to the surface tension created by solvent evaporation, until the surface tension is reduced sufficiently for the strength of the network to resist further compaction (Brinker and Scherer 1985). During this period, residual hydroxyl and alkoxy groups coming into contact with each other during collapse may condense and further interconnect the clusters (Brinker and Scherer 1985). The result is a distorted and contracted metal oxide network comprised of interconnected and crosslinked clusters with a high porosity (Φ), and hence a high a_s (Fig. 4.4).

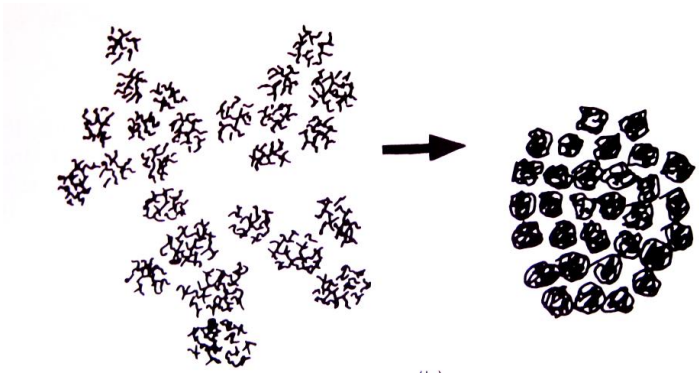

Fig. 4.4 *Schematic representation of the drying of a base catalysed gel to produce a xerogel (Brinker and Scherer 1985).*

4.2.2. SOL-GEL SYNTHESIS AND CA DOPING METHODOLOGY

The method of synthesis used in this study was a modified (K. Wilson, A.F. Lee, pers. comm. 2007) method from Reese *et al.* (1993) and Matsumoto *et al.* (1999) designed to produce amorphous mesoporous aluminosilicates. Ratios of TEOS to aluminium sec-butoxide were calculated from the desired stoichiometric ratios of Si to Al within the end product and the specific quantities of these precursors used are given in Table 4.1. TEOS was dissolved in 750 ml of 2-propanol ($CH_3CHOHCH_3$), which was then added to a solution of 1800 ml of deionised water and 96 ml of 35% aqueous ammonia (NH_3). The aluminium sec butoxide was added to this solution after the TEOS, as the hydrolysation time of TEOS is slow (Paul 1982) and may be overtaken by the hydrolysation of the aluminium precursor, which would precipitate Al-O-Al rather than Si-O-Al. The solution was stirred at a constant rate for 24 hours at room temperature, before the solution was vacuum filtered through Cat. 4 Whatman filter paper, dried at 105°C for 24 hours to remove the aqueous phase and the bulk of the liquid from the gel, and finally calcined at 550°C with a ramp rate of 1°C per minute and a dwell time of 5 hours to remove extraneous solvents. The calcined samples were then powdered with an agate pestle and mortar and stored under atmospheric conditions until use. The materials produced by the above methodology are 'xerogels', as the gelation and drying were not conducted under controlled pressure and temperature.

Table 4.1 *Precursor volumes used in synthesis of pure aluminosilicates in order to produce the estimated total Si and Al concentrations shown (atm. %), assuming 100% efficient reaction of the precursors during synthesis.*

Sample	TEOS (ml)	Al-sec butoxide (ml)	Estimated chemical composition (atm. %)	
			Si	Al
100	180 ± 1.0	0	33.3	0.0
90	168± 1.0	22± 0.5	30.1	3.9
80	150± 1.0	45± 0.5	26.8	7.9
50	93± 0.5	112± 1.0	16.8	19.8
20	30± 0.5	180± 1.0	6.8	31.9
0	0	180± 1.0	0.0	40.0

To dope the aluminosilicate materials with Ca, 3g of the aluminosilicate materials were added to a slurry of 10 ml of deionised water and a specified mass of calcium nitrate tetrahydrate ($Ca(NO_3)_2\ 4H_2O$) in concentrations calculated to dope the surface of the sample with a specific mass of Ca (Table 4.2). The Ca slurry and aluminosilicate materials were stirred for 2 hours at room temperature before being stirred at 50°C for a further five hours to evaporate the water and precipitate the Ca onto the sample surface. After Ca doping, samples were again calcined under the same temperature conditions as in the initial synthesis.

Table 4.2 *Mass of Ca nitrate tetrahydrate doped onto the aluminosilicate materials to give total Ca concentrations as estimated assuming 100% efficient doping.*

Sample	Sample (g)	Dopant (g)	Estimated Ca (atm. %)
50-1	3.0 ± 0.1	0.34 ± 0.01	0.5
50-3	3.0 ± 0.1	0.70 ± 0.01	1
50-5	3.0 ± 0.1	1.10 ± 0.01	3.5
50-7	3.0 ± 0.1	2.39 ± 0.01	6.9

During the SO_2 chemisorption experiments on the Ca-doped aluminosilicates, it was decided to conduct a further experiment on an amorphous Ca-aluminosilicate, synthesised via a one-step rather than two-step process. The methodology used for synthesising the aluminosilicate materials initially was used, but was scaled down by a factor of 5, as the masses of material needed were not on the same scale as the initial aluminosilicates (Table 4.3). At the point at which TEOS was added, $Ca(NO_3)_2\ 4H_2O$ dissolved in 2-propanol was also added. The sample synthesis after this was conducted as previously described in the aluminosilicate synthesis.

Table 4.3 *Volumes of precursors used in synthesis of Ca-aluminosilicates and the estimated Si and Al contents of the aluminosilicates produced, assuming 100% efficient reaction of the precursors during synthesis.*

Sample	TEOS (ml)	Al-sec butoxide (ml)	Calcium nitrate tetrahydrate (g)	Estimated chemical composition (atm. %)		
				Si	Al	Ca
50-12	17.0 ± 1.0	19.0 ± 0.5	35.3 ± 0.1	11.2	12.9	16.1
80-12	32.0 ± 1.0	2.0 ± 0.5	35.3 ± 0.1	21.1	1.3	16.1
95-12	27.0 ± 1.0	8.0 ± 0.5	35.3 ± 0.1	17.8	5.1	16.1

4.3. SAMPLE CHARACTERISATION

The samples synthesised by the sol-gel method for use in SO_2 chemisorption experiments were characterised by bulk and surface-sensitive techniques. In the following sections, the characterisation data of the aluminosilicate samples are presented in section 4.3.1, the characterisation data of the Ca-doped aluminosilicates are presented in section 4.3.2, and the characterisation data of the one-step Ca-aluminosilicate samples are presented in section 4.3.3.

4.3.1. CHARACTERISATION OF ALUMINOSILICATE MATERIALS

In the course of this study, the aluminosilicate materials were referred to via a numerical code. The code refers to the approximate percentage of Si relative to the total Si and Al in the sample, where a pure alumina sample is '0' and a pure silica sample is '100'. Collectively, the aluminosilicate materials are referred to as the '0-100' series, for brevity.

4.3.1.1. TOTAL AL AND SI ANALYSIS

The '0-100' series samples were analysed by XRF (Table 4.4), and were found to have total Al and Si concentrations which were in good agreement (Fig. 4.5) with the estimated values in Table 4.1.

Table 4.4 *Total Si and Al concentration in the '0-100' series determined by XRF. The remainder of the sample chemical composition is assumed to be oxygen. Experimental and analytical error is ±0.5 and ±0.6 atm. % for Si and Al based on the average standard deviation (S.D.) of three replicate analyses on the same sample.*

Sample	Chemical composition (atm. %)	
	Si	Al
100	32.4 ± 0.5	0.5 ± 0.6
90	28.4 ± 0.5	5.9 ± 0.6
80	26.9 ± 0.5	7.7 ± 0.6
50	19.9 ± 0.5	16.1 ± 0.6
20	9.2 ± 0.5	28.9 ± 0.6
0	0.1 ± 0.5	39.9 ± 0.6

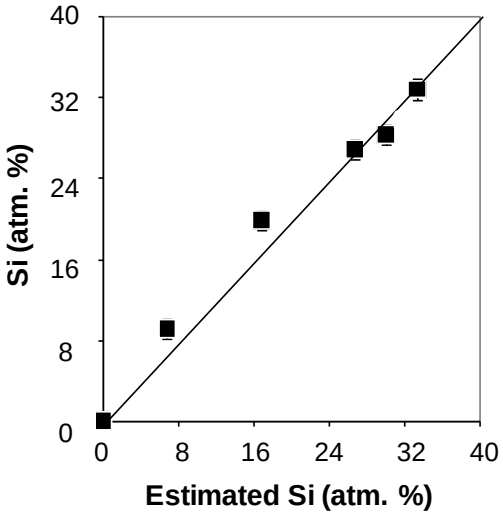

Fig. 4.5 *Comparison of the total Si concentration in the'0-100' series (Table 4.4), determined by XRF, and the estimated total Si concentration in the aluminosilicate materials (Table 4.1). Experimental error is ±0.5 atm. %.*

4.3.1.2. MINERALOGY

The '0-100' series samples were analysed by XRD (Fig. 4.6) and were found to be amorphous, showing no discrete crystalline phases and only showing the broader 'halos' consistent with diffraction through amorphous solids with variable bond angles. The 'halos' identified were attributed to amorphous Si at 25° 2θ (Warren and Biscoe 1937), and amorphous γ-Al_2O_3 at 37, 47 and 60° 2θ (Dwivedi and Gowda 1985). The amorphous γ-Al_2O_3 phase was only present in samples '0' and '20'.

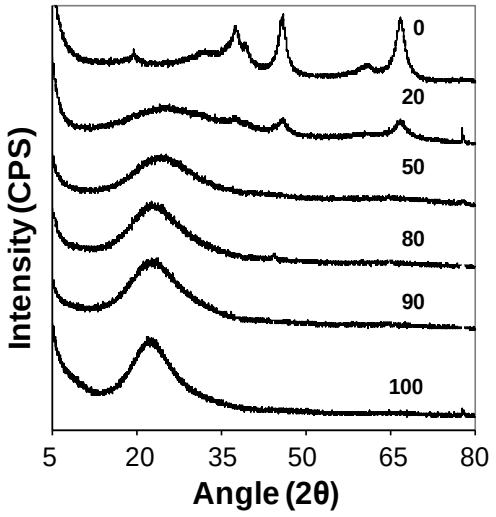

Fig. 4.6 *XRD patterns of the initial pre-experiment '0-100' series samples.*

4.3.1.3. SPECIFIC SURFACE AREA (a_s), POROSITY (Φ) AND PORE SIZE (Φ_d)

The a_s and Φ of the '0-100' series samples were determined via nitrogen adsorption porosimetry (Table 4.2). The '0-100' series samples were found to have high a_s up to 440 m^2g^{-1} and high Φ on the order of 0.69 cc g^{-1} with average pore diameter (Φ_d) being less than 100 Å. a_s, Φ and Φ_d all decreased with increasing Si content (Fig. 4.7), excluding '100', as this sample was synthesised by a modified methodology which required heating to 80°C for 5 hours in order to promote gelation, and hence was not comparable.

Table 4.5 *a_s, Φ and Φ_d of the '0-100' series samples determined by nitrogen adsorption porosimetry. The experimental and instrument error on a_s measurements was found to be ±0.4 m^2 g^{-1}, based on the S.D. of 5 replicate analyses on subsamples of '80', equating to an average error of 0.2%, and the error on Φ and Φ_d is approximately 5% (S. Wainright, pers. comm. 2010).*

Sample	a_s (m^2 g^{-1})	Φ (cc g^{-1})	Φ_d (Å)
100	441.4 ± 0.2%	N/A	N/A
90	143.5 ± 0.2%	0.30 ± 5%	20.9 ± 5%
80	217.1 ± 0.2%	0.41 ± 5%	22.2 ± 5%
50	211.6 ± 0.2%	0.44 ± 5%	22.7 ± 5%
20	244.3 ± 0.2%	0.69 ± 5%	28.8 ± 5%
0	285.9 ± 0.2%	N/A	N/A

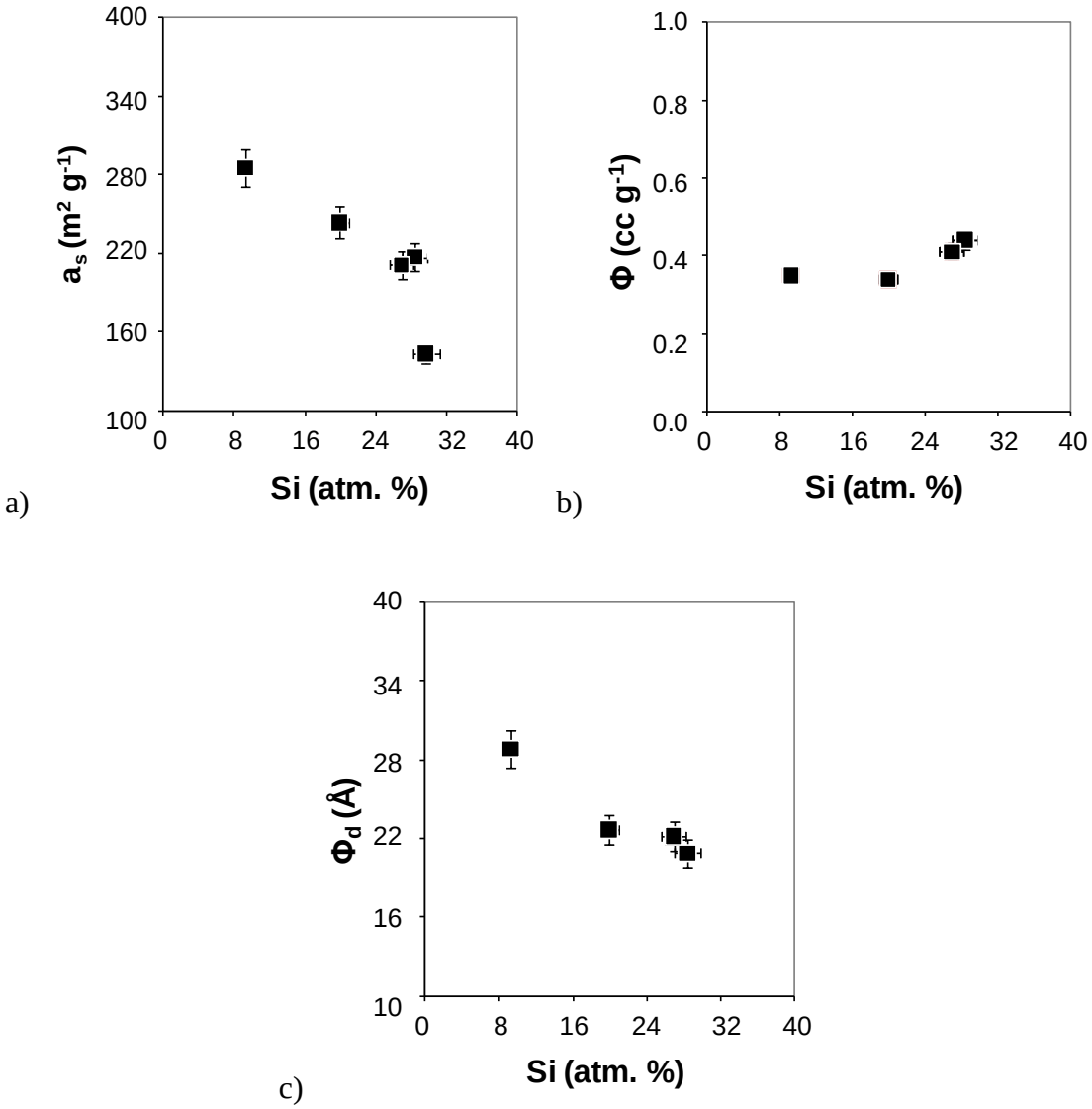

Fig. 4.7 *Comparison of a_s (a), Φ (b) and Φ_d (c) for '0-100' series samples (Table 4.5) with total Si concentration (atm. %) (Table 4.4). Experimental and analytical error is as defined in Table 4.5.*

4.3.1.4. X-RAY PHOTOELECTRON SPECTROSCOPY

The relative surface chemical composition of the '0-100' series samples was determined by XPS. The relative surface composition assuming that the sample contains only Si, Al and O are given in Table 4.6. The relative surface chemical compositions were consistent with those of the bulk chemical composition, although there was a 3% and 9% depletion in Al surface concentrations of the '0' and '20' samples (Fig. 4.8). The Al (2p) and Si (2p) regions of the XPS spectra for the aluminosilicates were interpreted by reference to the samples '0' and '100', these being only comprised of alumina and silica respectively. These spectra were therefore fitted with peaks attributed to Al-O-Al (73.7 eV) and Si-O-Si (103.5 eV) bonds respectively (Fig. 4.9). The Al-O-

Al and Si-O-Si peaks may be fitted to all spectra, but diminish in significance as the Si/Al ratios approach unity, to be replaced by a secondary peak at a higher binding energy for Al and a lower binding energy for Si which represents the Si-O-Al bond which makes up the aluminosilicate network

Table 4.6 *Relative surface chemical composition of the '0-100' series samples, determined by XPS. Based on XPS analysis in Chapter 5, experimental and analytical error is ± 9% error (Table 5.16).*

Sample	Surface composition (atm. %)	
	Si	Al
100	29.9	0.4
90	25.2	4.1
80	24.2	5.2
50	13.7	14.0
20	4.4	24.2
0	0.3	30.0

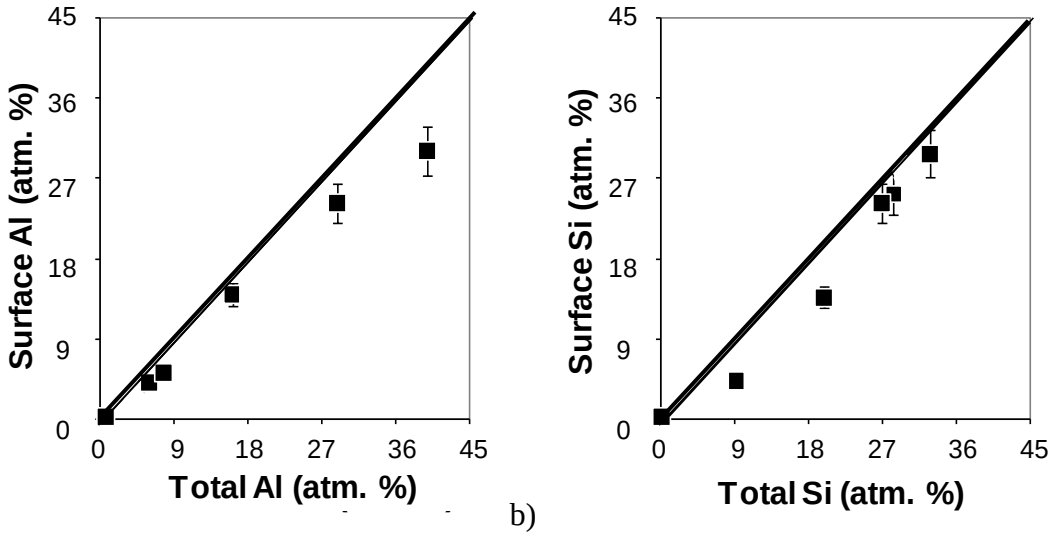

a) b)

Fig. 4.8 *Comparison of surface Al (a) and Si (b) concentrations determined by XPS (Table 4.6) plotted against total Al and Si concentrations for the '0-100' series samples determined by XRF (Table 4.4) compositions of the '0-100' series samples for Al (a) and Si (b).*

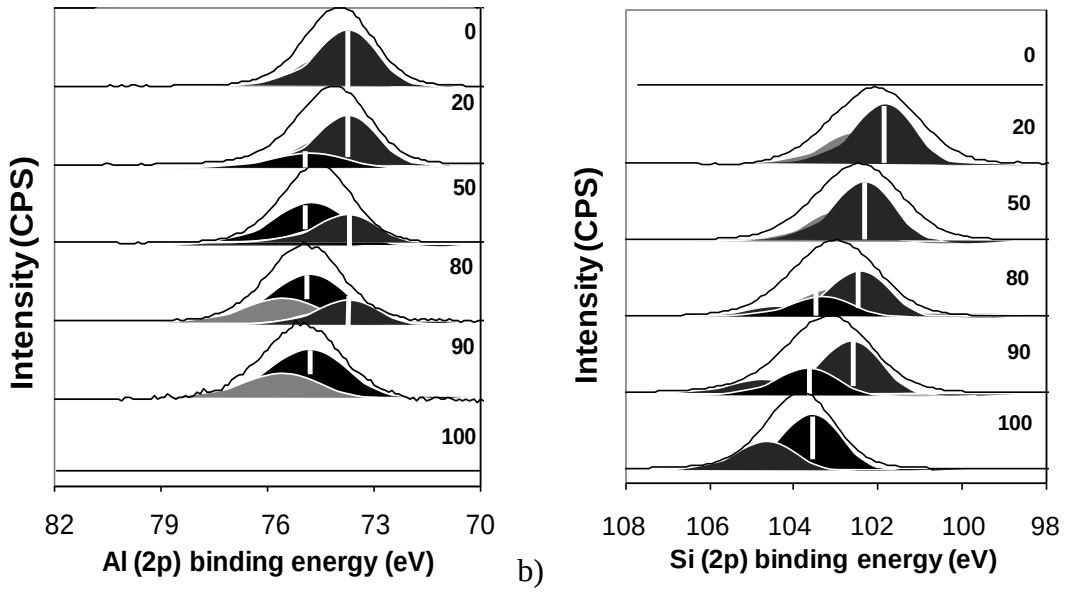

Fig. 4.9 *Al (2p) and Si (2p) regions of the XPS spectra for the '0-100' series samples. The Si (2p) and Al (2p) spectra are fitted with doublet pairs of Gaussian-Lorentzian 30 lineshapes with Doniach-Sunjic asymmetry parameters of 0.005,450 and FWHM of 2.4 eV and 1.7 eV respectively. Al (2p) spectra have been scaled by factors of 84, 169, 1168 and 1845% for the '20', '50','80' and '90' samples to plot them on the same scale as the spectra of the '0' aluminosilicate. Si (2p) spectra have been scaled by factors of 714, 371, 265 and 182% for the '20', '50', '80' and '90' to plot them on the same scale as the spectra of the '100' sample spectra.*

4.3.2. CHARACTERISATION OF CA-DOPED ALUMINOSILICATES

In the course of this study, a simple numeral code was used to describe the Ca-doped aluminosilicate samples. In addition to the aluminosilicate code used to describe the existing aluminosilicate materials, an additional suffix indicating the approximate bulk atomic percentage of Ca doped onto the sample surface was added. A sample with an aluminium to silica ratio of 50/50 and a Ca content of 5 atm. % is therefore '50-5'. Collectively, the Ca-doped samples are referred to as '50-N' series samples, for brevity.

4.3.2.1. TOTAL CA, SI AND AL ANALYSIS

The Ca doping of the aluminosilicate samples was found to have been successful in doping the samples with the desired Ca concentration by XRF analysis (Table 4.2, Fig. 4.10). Experimental and analytical error is ±0.3, 0.4 and 0.5 atm. % for Ca, Si and Al based on the average standard deviation (S.D.) of three replicate analyses on the same sample.

Table 4.7 *Total Ca, Si and Al concentrations in the'50-N' series samples. Experimental and analytical error is ±0.3, ± 0.4 and ±0.5 atm. % for Ca, Si and Al based on the average standard deviation (S.D.) of three replicate analyses of the same sample.*

Sample	Chemical composition (atm. %)		
	Ca	Si	Al
50-1	0.4 ± 0.3	16.7 ± 0.4	19.7 ± 0.5
50-3	0.7 ± 0.3	16.6 ± 0.4	19.5 ± 0.5
50-5	3.7 ± 0.3	15.6 ± 0.4	18.4 ± 0.5
50-7	7.6 ± 0.3	14.3 ± 0.4	16.8 ± 0.5

4.3.2.2.MINERALOGY

The '50-N' series samples were analysed by XRD, but no crystalline phases other than those determined to exist in the '50' aluminosilicate prior to doping were observed (Fig. 4.11).

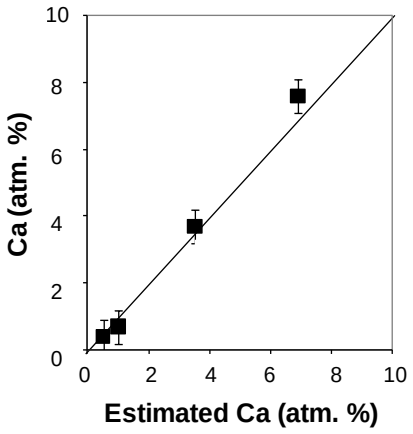

Fig. 4.10 *Total Ca concentration (atm. %) in'50-N' series samples by XRF (Table 4.7) compared to the estimated total Ca concentration (Table 4.2). Experimental and analytical error is ±0.3 atm. %.*

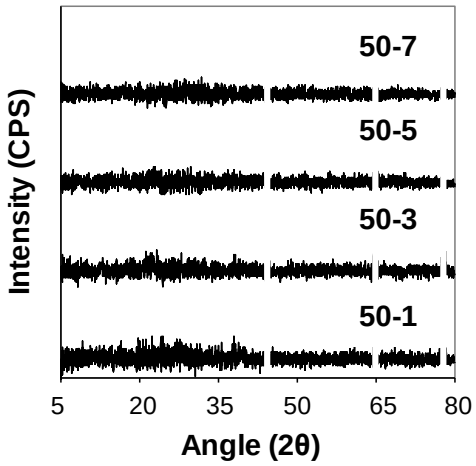

Fig. 4.11 *Baseline subtracted XRD patterns for the '50-N' series samples. Gaps in the data indicate the removal of sharp peaks attributed to the aluminium sample holder.*

4.3.2.3. DIFFUSE INFRARED FOURIER TRANSFORM SPECTROSCOPY (DRIFTS)

DRIFTS analysis was conducted using a 1:10 dilution of the '50-N' series samples in KBr (Fig. 4.12). The only vibration mode identified which was attributed to Ca phases was the v_3 vibration mode of C-O for $CaCO_3$ at 1483 cm^{-1} (Legod *et al.* 2001) which was most pronounced in the highest Ca doped sample and indistinguishable at the lowest Ca doping.

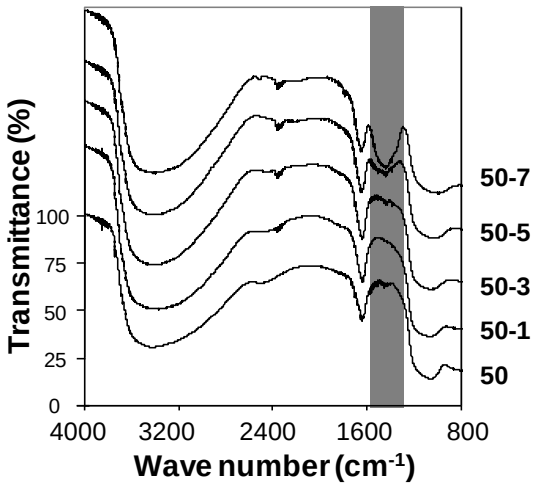

Fig. 4.12 *DRIFTS spectra for the '50-N' series samples and the original '50' source material '50'. The presence of the $CaCO_3$ ν_3 C-O vibration mode is indicated by the grey band (Legod et al. 2001).*

4.3.2.4. SPECIFIC SURFACE AREA (a_s), POROSITY (Φ) AND PORE SIZE (Φ_d)

The a_s, Φ and Φ_d of the '50-N' series samples was determined via nitrogen adsorption porosimetry (Table 4.8). Relative to the initial surface of the '50' aluminosilicate, surface areas showed an initial increase of 39 m^2g^{-1} at '50-1' but decreased rapidly after that point, being 78 m^2g^{-1} lower in the highest Ca doped sample (Fig. 4.13). A similar trend was observed for Φ, which, relative to the undoped '50' material increased by 0.14 cc g^{-1} initially, but decreased by 0.05 cc g^{-1} in the highest Ca-doped sample. Φ_d, was observed to increase relative to the initial average pore size of the undoped material in all samples, but to greatest extent in the 50-7 sample (Fig. 4.13).

Table 4.8 *a_s, Φ and Φ_d of '50-N' series samples determined by nitrogen adsorption porosimetry. The experimental and instrument error on a_s measurements was found to be 0.4 m^2 g^{-1}, based on the S.D. of 5 replicate analyses on subsamples of '80', equating to an average error of 0.2%, and the error on Φ and Φ_d is approximately 5% (S. Wainright, pers. comm. 2010).*

Sample	a_s (m^2 g^{-1})	Φ (cc g^{-1})	Φ_d(Å)
50-1	250.4 ± 0.2%	0.54 ± 5%	33.3 ± 5%
50-3	217.3 ± 0.2%	0.46 ± 5%	28.6 ± 5%
50-5	167.1 ± 0.2%	0.42 ± 5%	40.3 ± 5%
50-7	133.7 ± 0.2%	0.35 ± 5%	49.5 ± 5%

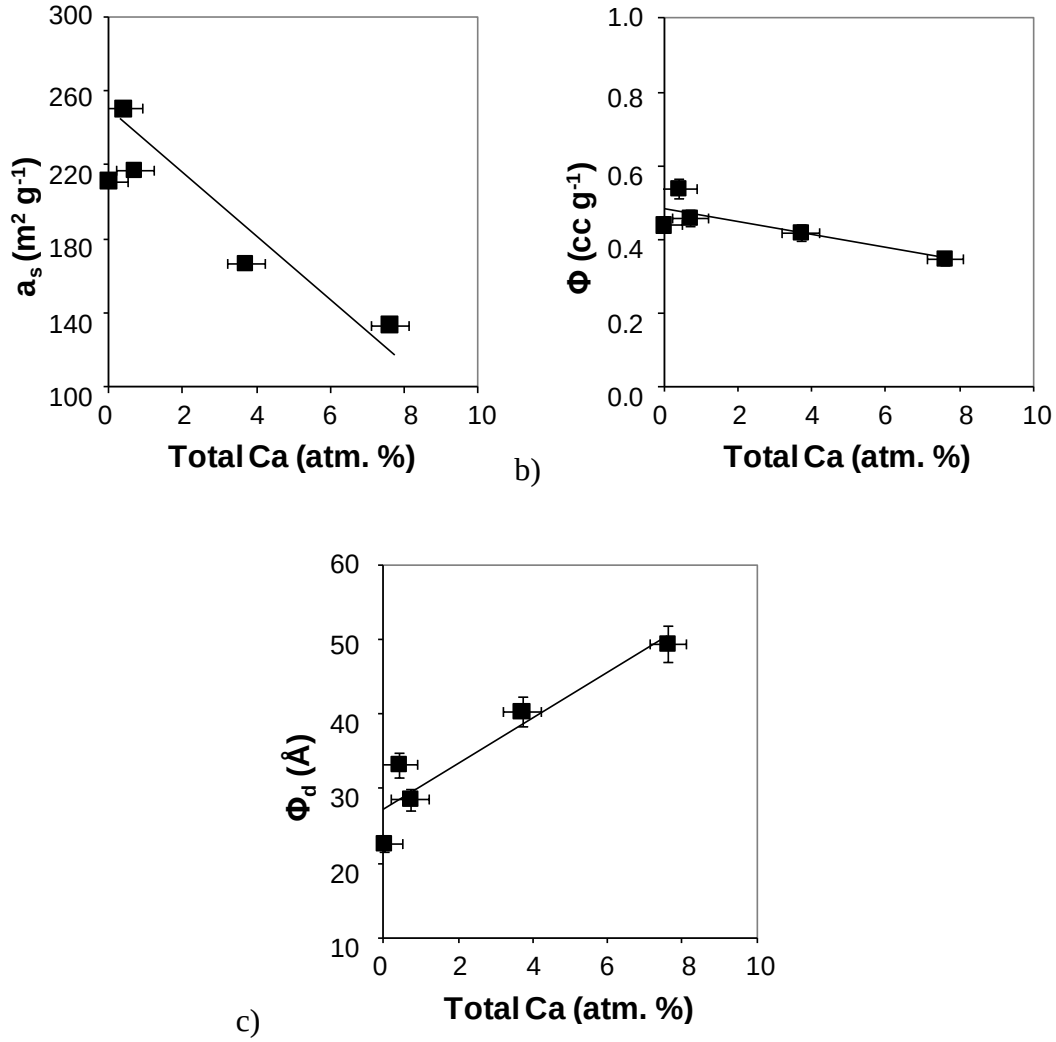

Fig. 4.13 *Comparison of '50-N' series sample a_s (a), Φ (b) and Φ_d (c) (Table 4.8) with total Ca concentration (atm. %) (Table 4.7).*

4.3.2.5. X-RAY PHOTOELECTRON SPECTROSCOPY

The relative surface chemical composition of the '50-N' series samples was determined by XPS (Table 4.9). Comparison of the surface Ca concentration and the total Ca concentration indicated that the two were of similar magnitude, although slightly depleted in the surface by 2 atm. % relative to the bulk at the highest Ca-doping (Fig. 4.14). The Ca ($2p\ ^3/_2$) peak is interpreted to determine the likely phases of Ca existing on the sample surface (Fig. 4.15), and based upon evidence from DRIFTS, a low binding energy component (347 eV) attributed to $CaCO_3$ (Christie *et al.* 1983) was fitted to each spectra, whilst an additional higher binding energy component (348 eV) was also fitted to the spectra.

Table 4.9 *Surface chemical composition of '50-N' series samples as determined by X-ray photoelectron spectroscopy. Surface compositions were normalised to remove adventitious carbon, and oxygen was assumed to be the only other major component of the surface. Combined experimental and analytical errors for XPS are assumed to produce an approximate* ± *9% error (Table 5.16).*

Sample	Surface composition (atm. %)		
	Ca (2p)	Si (2p)	Al (2p)
50-1	0.6	14.4	13.6
50-3	1.4	14.6	13.4
50-5	2.9	15.5	14.5
50-7	5.5	11.9	12.9

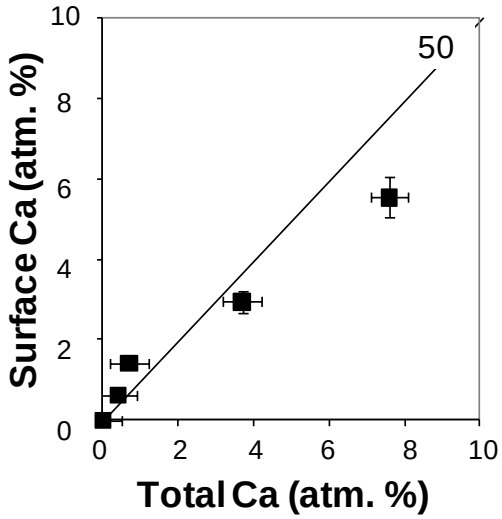

Fig. 4.14 *Comparison of surface Ca concentration for the '50-N' series samples determined by XPS (Table 4.9) compared to the total Ca concentration in the sample, determined by XRF (Table 4.7).*

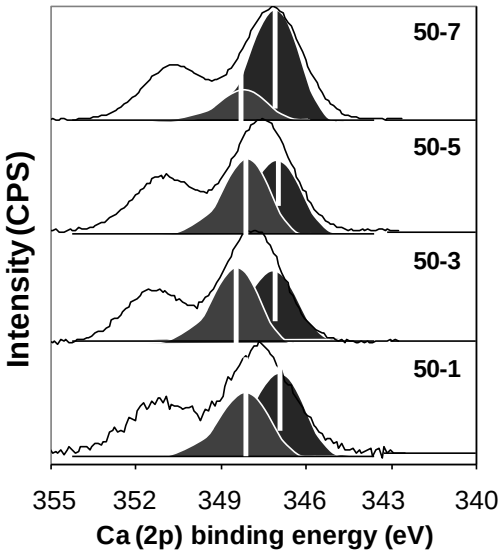

Fig. 4.15 *Ca (2p) region of the XPS spectra of the '50-N' series samples. Spectra are fitted with two Gaussian-Lorentzian 30 lineshapes with Doniach-Sunjic asymmetry parameters of 0.005,450 and FWHM of 2 eV. Spectra were scaled by 39, 30 and 10% for the 50-3, 50-5 and 50-7 samples respectively in order to plot them on the same scale as the spectra of the 50-1 sample.*

4.3.3. CHARACTERISATION OF 'ONE-STEP SYNTHESIS' CA-ALUMINOSILICATES

The one-step synthesis Ca aluminosilicates synthesised for use in this study were referred to by a numerical code similar to that of the Ca-doped aluminosilicates, but for these samples, the prefix number indicates the Si/(Si+Al), i.e. a sample with a 50/50 Si/Al ratio is '50', and the suffix number indicates the bulk Ca content in atm. %. Therefore, a sample with 50/50 Si/Al ratio and 12 atm. % Ca is referred to as '50-12', and collectively, the samples are referred to as the 'Ca-N' series samples.

4.3.3.1. TOTAL CA, SI AND AL ANALYSIS

The total Ca, Si and Al concentrations in the 'Ca-N' series were determined by XRF and are given in Table 4.10, and were consistent with the estimated total Ca, Si and Al concentrations estimated in Table 4.3.

Table 4.10 *Total Al, Si and Ca concentrations in the 'Ca-N' series, determined by XRF. as determined by X-ray fluorescence. Experimental and analytical error is ±0.9. ±0.6 and ±1.7 atm. % for Al, Si and Ca respectively based on the average standard deviation (S.D.) of three replicate analyses of the same sample.*

Sample	Chemical composition (atm. %)		
	Al	Si	Ca
95-12	2.8 ± 0.9	24.8 ± 0.6	9.2 ± 1.7
80-12	3.8 ± 0.9	21.7 ± 0.6	12.6 ± 1.7
50-12	14.0 ± 0.9	13.3 ± 0.6	12.5 ± 1.7

4.3.3.2. MINERALOGY

XRD analysis determined that the 'Ca-N' series were amorphous aluminosilicates, but also showed discrete crystalline phases (Fig. 4.16) which were identified as $CaCO_3$ (Prencipe *et al.* 2004). These crystalline phases occurred to greatest extent in the lowest Si sample, and the height of the $CaCO_3$ peak decreases with increasing Si content.

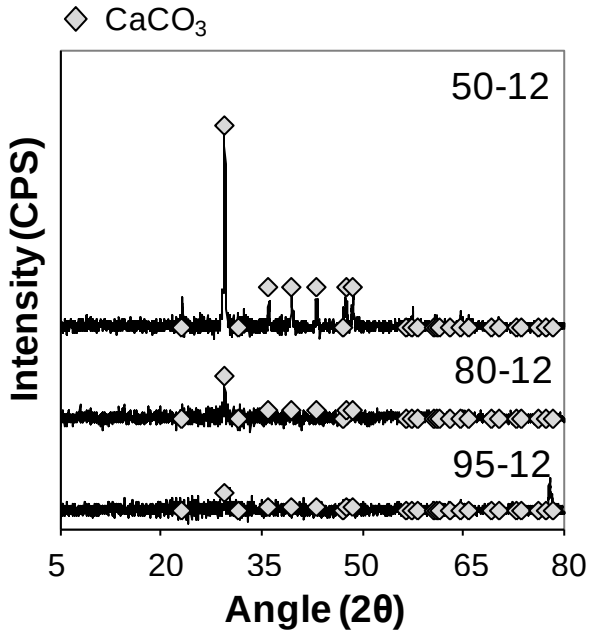

Fig. 4.16 *Baseline-subtracted XRD patterns for the 'Ca-N' series, with the light grey filled diamonds indicating the $CaCO_3$ peak positions and heights (Prencipe et al. 2004).*

4.3.3.3. SPECIFIC SURFACE AREA (a_s), POROSITY (Φ) AND PORE SIZE (Φ_d)

The a_s, Φ and Φ_d of the 'Ca-N' series samples was determined by nitrogen adsorption porosimetry. It was determined that a_s varied widely across the three samples, ranging from 70.9 m^2g^{-1} to 14 m^2g^{-1} with increasing Si content (Table 4.11). Both Φ and Φ_d showed a similar decrease with increasing Si content.

Table 4.11 *Specific surface area (a_s), porosity (Φ) and average pore size (Φ_d) of 'Ca-N' series samples as determined by nitrogen porosimetry. The experimental and instrument error on a_s measurements was found to be 0.4 m^2 g^{-1}, based on the S.D. of 5 replicate analyses on subsamples of '80', equating to an average error of 0.2%, and the error on Φ and Φ_d is approximately 5% (S. Wainright, pers. comm. 2010).*

Sample	a_s (m^2 g^{-1})	Φ (cc g^{-1})	Φ_d (Å)
50-12	70.9 ± 0.2%	0.35 ± 5%	202 ± 5%
80-12	44.7 ± 0.2%	0.18 ± 5%	167 ± 5%
95-12	14.7 ± 0.2%	0.04 ± 5%	95 ± 5%

4.4. RESULTS OF SO_2 CHEMISORPTION EXPERIMENTS

In all of the SO_2 chemisorption experiments on the synthesised sol-gel samples, approximately 0.4 g of the sample was exposed to adsorption experiments at 300°C, 500°C and 800°C for 60 minutes. The results of the SO_2 chemisorption experiments on the '0-100' series samples are presented in section 4.4.1, the results of the SO_2 chemisorption experiments on the '50-N' series samples in section 4.4.2, and the results of analysis on the 'Ca-N' series samples from a series of experiments conducted at temperatures of 300,400, 500, 600, 700 and 800°C for 60 minutes are presented in section 4.4.3.

4.4.1. SO_2 CHEMISORPTION ON ALUMINOSILICATE SAMPLES

SO_2 adsorption experiments under 1% SO_2/He atmosphere were conducted for the aluminosilicate samples '0', '20', '50', '80' and '100'.

4.4.1.1. TOTAL S ANALYSIS

The total S concentration in the '0-100' series samples after exposure to 1% SO_2/He are given in Table 4.12. Total S concentrations in any samples other than the '0' and '20' aluminosilicates were negligible, as all total S concentrations in the samples are low enough that calculating one standard deviation for the replicate values made these data indistinguishable from zero.

Table 4.12 *Total S (S_{total}) analysis determined by XRF for the '0-100' series samples exposed to 1% SO_2/He at 300°C, 500°C and 800°C. Experimental and analytical error is ±0.2 atm. % based on three replicate analyses of the same sample by XRF.*

Temperature (°C)	Sample	S (atm. %)
300	**0**	1.3 ± 0.2
	20	0.4 ± 0.2
	50	0.1 ± 0.2
	80	0.0 ± 0.2
	100	0.0 ± 0.2
500	**0**	0.7 ± 0.2
	20	0.2 ± 0.2
	50	0.2 ± 0.2
	80	0.0 ± 0.2
	100	0.0 ± 0.2
800	**0**	0.4 ± 0.2
	20	0.1 ± 0.2
	50	0.0 ± 0.2
	80	0.0 ± 0.2
	100	0.1 ± 0.2

4.4.1.2. LEACHATE ANALYSIS

Soluble S concentrations extracted from the '0-100' series samples by leaching are displayed in Table 4.13, and were found to be consistently low, being less than 4 nmol m^{-2}.

Table 4.13 *Soluble S ($S_{leachate}$) extracted from aqueous leaching of the '0-100' series samples exposed to 1% SO_2/He for 60 minutes at 300°C, 500°C and 800°C, normalised to sample a_s (Table 4.5). Replicate analyses were not conducted, but based on the analyses in Chapter 5 (Table 5.11), an error of ±15% was considered appropriate.*

Temperature (°C)	Sample	$S_{leachate}$ (nmol m^{-2})
300	**0**	4
	20	<1
	50	<1
	80	<1
	100	<1
500	**0**	<1
	20	<1
	50	<1
	80	<1
	100	<1
800	**0**	<1
	20	2
	50	<1
	80	<1
	100	<1

4.4.1.3. MINERALOGY

XRD did not identify any S compounds on the‘0-100’ series samples (Fig. 4.17).

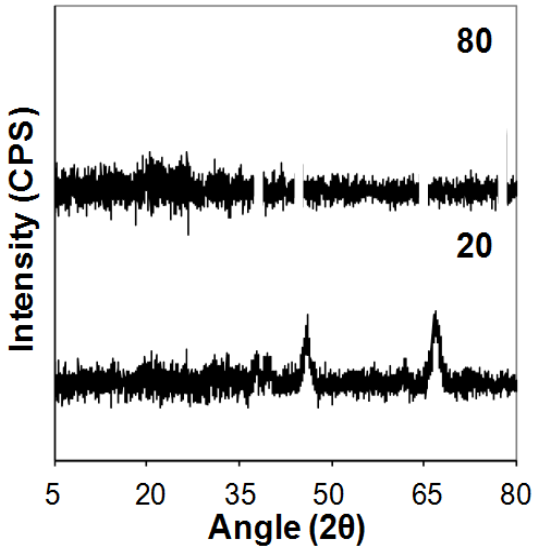

Fig. 4.17 *Baseline subtracted XRD patterns for samples ‘80’ and ‘20’ exposed to 1% SO_2/He at 500°C for 60 minutes.*

4.4.1.4. X-RAY PHOTOELECTRON SPECTROSCOPY

Selected ‘0-100’ series samples were analysed by XPS. All compositions were analysed from experiments conducted at 500°C (Table 4.14), and the aluminosilicate sample ‘20’ was analysed by XPS after exposure to 300, 500 and 800°C (Table 4.14). For all samples at 500°C, surface S concentrations were not detected in any sample apart from the ‘0’ and ‘20’ aluminosilicates, which had surface S concentrations of 0.6 and 0.2 atm. % respectively. The S (2p) region of the XPS spectra for ‘0’ and ‘20’ aluminosilicates are shown in Fig. 4.18. In the ‘20’ aluminosilicate analysed by XPS over all three temperatures, it was observed that surface S concentrations were 0.3, 0.2 and 0.2 atm. % for 300°C, 500°C and 800°C. The S (2p) region of the XPS spectra for ‘20’ aluminosilicate at all three temperatures are shown in Fig. 4.19.

Table 4.14 *Relative surface chemical composition (atm. %) for the '0-100' series samples exposed to 1% SO_2/He atmospheres at 500°C as determined by XPS. Experimental and analytical error is ±9%.*

Sample	Surface composition (atm. %)		
	Al (2p)	S (2p)	Si (2p)
0	31.1	0.6	0.0
20	25.3	0.2	5.0
50	14.9	0.0	15.5
80	4.8	0.0	26.1
90	4.2	0.0	26.6
100	0.0	0.0	29.4

Table 4.15 *Relative surface chemical composition (atm. %) for the synthetic aluminosilicate '20' exposed to 1% SO_2/He atmospheres at 300, 500 and 800°C as determined by XPS. Experimental error is ±9%.*

Sample	Surface composition (atm. %)			
	Al (2p)	O (1s)	S (2p)	Si (2p)
300	25.6	65.2	0.3	3.3
500	24.6	67.7	0.2	2.6
800	28.4	64.5	0.2	2.0

Based upon comparison to an $Al_2(SO_4)_3$ standard (Fig. 4.20) analysed by XPS, the S (2p) spectra was fitted with two components, one representing the aluminium sulphate phase which has an S ($2p\ ^3/_2$) peak position of approximately 169.6 eV, and a lower binding energy component at 167.9 eV which may be attributed to surface aluminium sulphite species (Smirnov *et al.* 2003). The same peak fitting was applied to the aluminosilicate sample '20' and the fitted peaks attributed to both aluminium sulphate and sulphite were able to describe the S (2p) spectra at all temperatures for this sample (Fig. 4.19).

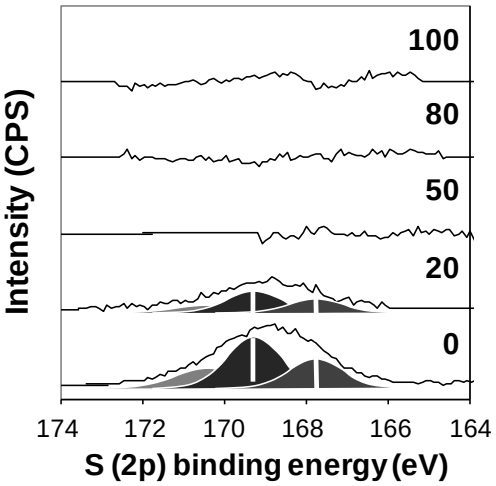

Fig. 4.18 *S (2p) region of the XPS spectra of '0-100' series samples exposed to 1% SO_2/He at 500°C for 60 minutes. Only '20' and '0' show* sulphur *peaks, and these are fitted with two sets of doublet pair of Gaussian-Lorentzian 30 lineshapes with FWHM of 1.9 eV. Spectra have not been scaled.*

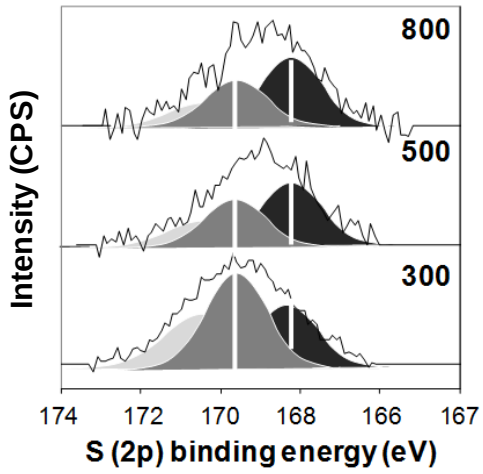

Fig. 4.19 *S (2p) region of the XPS spectra of aluminosilicate sample '20' exposed to 1% SO_2/He at 300°C, 500°C and 800°C for 60 minutes. Spectra are fitted with two sets of doublet pairs of Gaussian-Lorentzian 30 lineshapes with FWHM of 1.9 eV. Spectra are scaled by 491 and 203% for the samples exposed to 800°C and 500°C respectively in order to be plotted at the same scale as the spectra of the sample exposed to 300°C.*

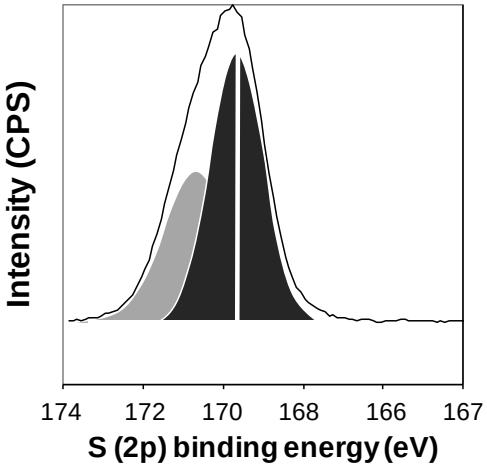

Fig. 4.20 *S (2p) region of the XPS spectra of $Al_2(SO_4)_3$ fitted with a doublet pair of Gaussian-Lorentzian 30 lineshapes with FWHM of 1.6 eV.*

4.4.2. SO_2 CHEMISORPTION EXPERIMENTS ON CA-DOPED ALUMINOSILICATES

SO_2 adsorption experiments under 1% SO_2/He atmosphere at 300°C, 500°C and 800°C were conducted for all '50-N' series samples, and these data are presented below.

4.4.2.1. TOTAL S ANALYSIS

The total S concentration of the post-experiment '50-N' series samples are given in Table 4.16. The total S content increased with increasing Ca doping for all samples, and were consistently lowest in the samples exposed to 800°C, whilst under 300°C and 500°C, total S contents varied.

4.4.2.2. MINERALOGY

Selected samples of the '50-N' series samples were analysed by XRD. The '50-7' Ca doped aluminosilicates from experiments conducted at 300°C, 500°C and 800°C were analysed and the crystalline phases identified from the baseline-subtracted diffraction patterns were those of anhydrite ($CaSO_4$) at 500°C and 800°C, and bassanite ($CaSO_4$. ½ H_2O) at 300°C (Fig. 4.21). Analysis was also conducted on sample '50-1' at 500°C (Fig. 4.22), in order to explore the behaviour of both the highest and lowest Ca-doped experiments, but no crystalline phases were identified in the '50-1' sample.

Table 4.16 *Total S concentration of the '50-N' series samples exposed to 1% SO_2/He/air at 300°C, 500°C and 800°C, as determined by XRF. Experimental and analytical error is ±0.5, ±0.4, ±0.1 and ±0.3 atm. % for Al, Si, S and Ca respectively, based on three replicate analyses of the same sample.*

Temperature (°C)	Sample	Chemical composition (atm. %)			
		Al (± 0.5)	Si (± 0.4)	S (± 0.1)	Ca (± 0.3)
	50	21.2	27.9	0.1	0.1
	50-1	15.0	20.0	0.1	1.1
	50-3	14.3	19.7	0.2	2.2
	50-5	13.7	18.0	0.6	4.8
300	**50-7**	12.9	15.9	2.1	5.8
	50	21.7	27.4	0.2	0.1
	50-1	16.4	18.7	0.4	0.5
	50-3	15.0	19.5	0.1	1.7
	50-5	14.2	18.6	0.2	3.8
500	**50-7**	12.5	15.4	2.4	6.5
	50	21.6	27.5	0.0	0.1
	50-1	15.7	19.8	0.1	0.6
	50-3	15.7	19.0	0.1	1.7
	50-5	14.8	18.4	0.2	3.4
800	**50-7**	12.9	18.2	0.5	5.6

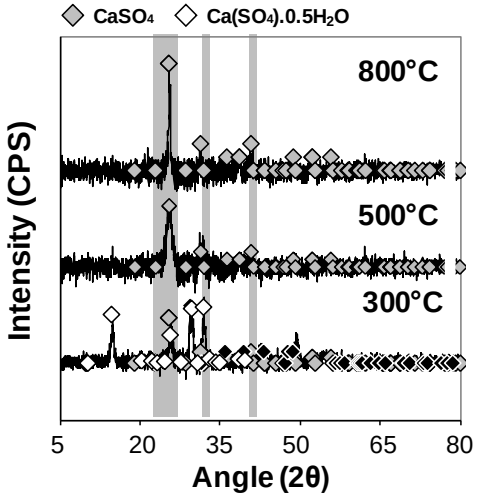

Fig. 4.21 *Baseline subtracted XRD patterns for '50-7' calcium doped aluminosilicates exposed to 1% SO_2/He/air at 300°C, 500°C and 800°. The filled diamonds indicate the diffraction pattern for $CaSO_4$ (anhydrite) (Wasastjerna 1927) and for $Ca(SO_4).0.5(H_2O)$ (bassanite)(Weiss and Braeu 2009).*

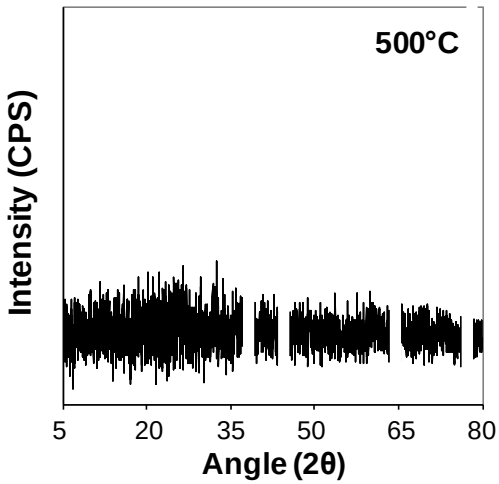

FIG. 4.22 *Baseline subtracted XRD pattern for '50-1' calcium doped aluminosilicates exposed to 1% SO_2/He/air at 500°C for 60 minutes.*

4.4.2.3. DIFFUSE INFRARED FOURIER TRANSFORM SPECTROSCOPY (DRIFTS)

DRIFTS was conducted on sample '50-7' for all samples exposed to 1% SO_2/He/Air at 300, 500 and 800°C (Fig. 4.23), but the only significant feature identified was the decrease in size of the $CaCO_3$ ν_3 vibration previously identified in the pre-exposure samples at 1500 cm^{-1} (Legod *et al.* 2001).

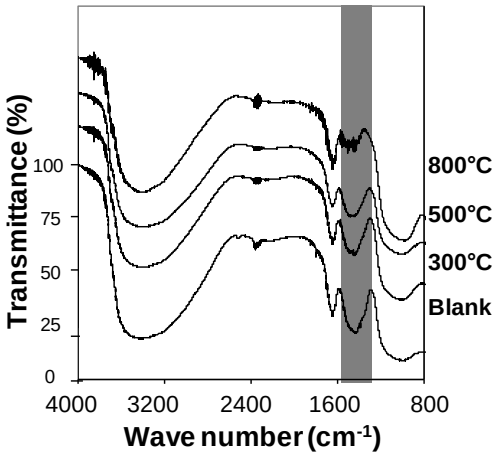

Fig. 4.23 *DRIFTS spectra for Ca-doped aluminosilicate '50-7' exposed to 1% SO_2/He/Air at 300, 500 and 800°C for 60 minutes. The presence of the $CaCO_3$ v_3 vibration is indicated by the grey band (Legod et al. 2001).*

4.4.2.4. LEACHATE ANALYSIS

The '50-N' series samples were leached and the solutions extracted from the samples by leaching were analysed for S by IC (Table 4.17), and normalised to sample a_s (Table 4.8).

4.4.2.5. SPECIFIC SURFACE AREA (a_s), POROSITY (Φ) AND PORE SIZE (Φ_d)

Selected samples were analysed by nitrogen adsorption porosimetry and the a_s, Φ and Φ_d were determined for the 50-7 sample exposed to 1% SO_2/He/Air at all experimental temperatures (Table 4.18). The greatest surface area decreases were observed at 300°C and 500°C being 31 and 35 m^2g^{-1} respectively. In all cases there was a decrease in Φ and in the 300°C and 800°C experiments, an increase in Φ_d was observed.

Table 4.17 *Soluble S ($S_{leachate}$) extracted from aqueous leaching of the '50-N' series samples exposed to 1% SO_2/He/Air for 60 minutes at 300°C, 500°C and 800°C, normalised to sample a_s (Table 4.8). Replicate analyses were not conducted, but based on the analyses in Chapter 5 (Table 5.11), an error of ±15% was considered appropriate.*

Temperature (°C)	Sample	$S_{leachate}$ (µmol m^{-2})
300	**50**	0.30
	50-1	0.30
	50-3	0.32
	50-5	0.50
	50-7	0.20
500	**50**	0.30
	50-1	0.11
	50-3	0.00
	50-5	0.94
	50-7	0.57
800	**50**	0.51
	50-1	0.55
	50-3	0.43
	50-5	0.17
	50-7	0.94

Table 4.18 *a_s, Φ and Φ_d of '50-N' series samples exposed to 1% SO_2/He/Air at 300°C, 500°C and 800°C, determined by nitrogen adsorption porosimetry. The experimental and instrument error on a_s measurements was found to be 0.4 m^2 g^{-1}, based on the S.D. of 5 replicate analyses on subsamples of '80', equating to an average error of 0.2%, and the error on Φ and Φ_d is approximately 5% (S. Wainright, pers. comm. 2010).*

Temperature (°C)	a_s (m^2 g^{-1})	Φ (cc g^{-1})	Φ_d (A)
Initial	133.7 ± 0.2%	0.35 ± 5%	49 ± 5%
300	105.1 ± 0.2%	0.25 ± 5%	64 ± 5%
500	97.2 ± 0.2%	0.23 ± 5%	46 ± 5%
800	111.9 ± 0.2%	0.30 ± 5%	65 ± 5%

4.4.2.6. X-RAY PHOTOELECTRON SPECTROSCOPY

The '50-N' series samples sulphated at all temperatures under 300°C, 500°C and 800°C in 1% SO_2/He/air atmospheres were analysed by XPS. The relative surface chemical compositions of the analysed samples are given in Table 4.19. The S (2p) (Fig. 4.24) and Ca (2p) (Fig 4.25) regions of the XPS spectra of the samples were interpreted to provide further insight into the reaction products formed.

Identifiable S (2p) peaks were present in all samples analysed by XPS, but not at all experimental temperatures (Fig. 4.24), even though the relative surface chemical compositions indicated the presence of very low (0.1 atm. %) concentrations of surface S (Table 4.19). In the '50-1' sample, peaks attributable to S were only observed at 300°C and 500°C, and only at 300°C in the '50-3' sample. The binding energies of the S ($2p\ ^3/_2$) peak are 169 eV in the '50-5' sample at 500°C and 800° and at all temperatures in the '50-7' sample.

Table 4.19 *Relative surface chemical composition of '50-N' series samples exposed to 1% SO_2/He/air at 300°C, 500°C and 800°C, as determined by XPS. Based on XPS analysis in Chapter 5, experimental and analytical error is ± 9% error (Table 5.16).*

Temperature (°C)	Sample	Surface composition (atm. %)				
		Si (2p)	Al (2p)	C (1s)	S (2p)	Ca (2p)
300	**50-1**	11.3	13.0	4.3	0.2	1.3
	50-3	13.4	13.4	4.1	0.1	1.6
	50-5	11.5	11.9	4.8	0.2	2.6
	50-7	12.0	11.1	5.0	0.7	4.1
500	**50-1**	13.3	11.3	2.2	0.2	0.5
	50-3	13.5	12.7	2.7	0.0	1.3
	50-5	11.7	12.6	3.4	0.2	2.4
	50-7	10.5	10.8	10.2	1.0	3.7
800	**50-1**	15.3	15.5	3.2	0.1	0.4
	50-3	13.0	13.0	1.1	0.1	1.3
	50-5	12.0	13.3	5.0	0.1	2.4
	50-7	10.4	12.9	4.3	0.9	4.8

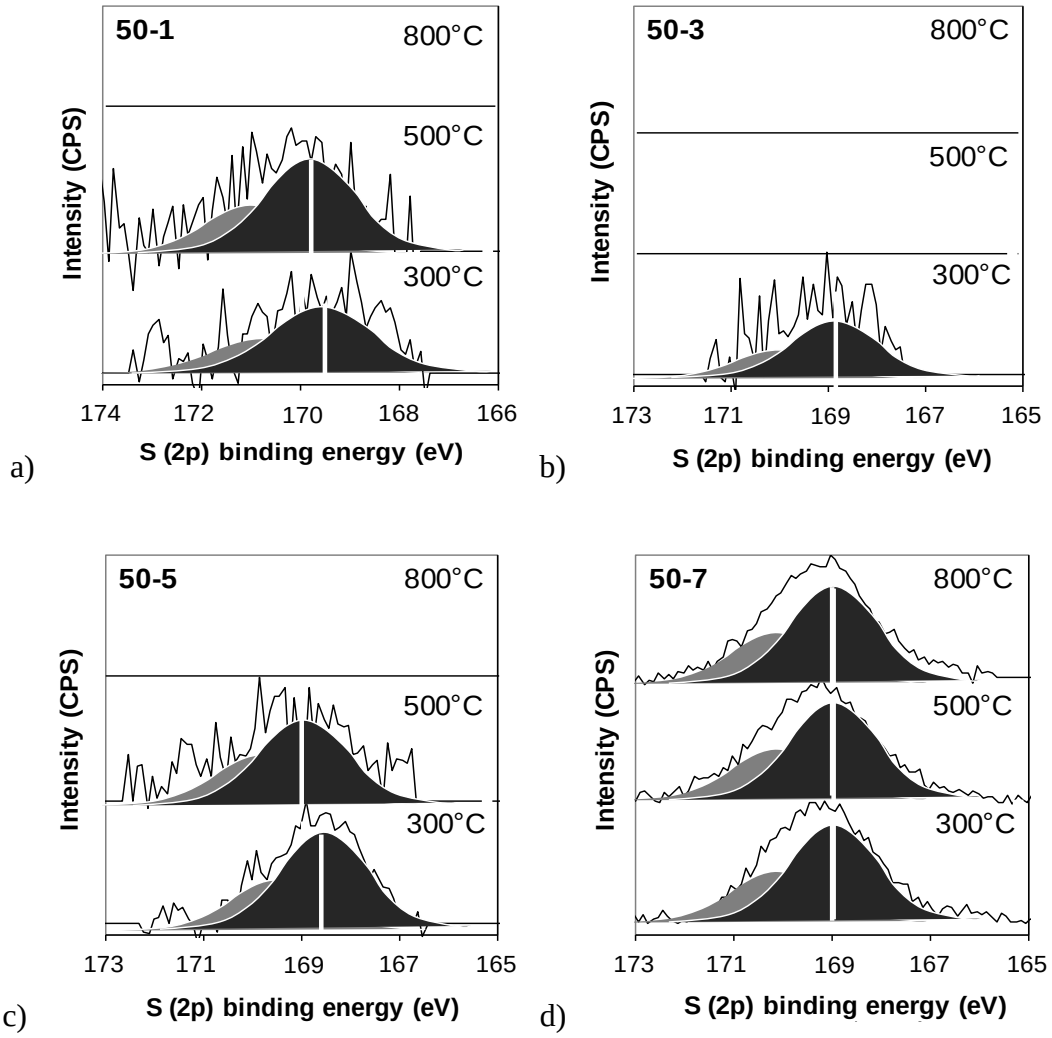

Fig. 4.24 *S (2p) XPS spectra of the '50-N' series samples exposed to 1% SO_2/He/Air at 300°C, 500°C and 800°C, fitted with a doublet pair of Gaussian-Lorentzian 30 lineshapes and FWHM of 1.6eV. Spectra for each of the above diagrams have been scaled by factors of 180% for the 50-1 sample exposed to 500°C to be plotted on the same scale as the spectra from the sample exposed to 300°C. No scaling was required for 50-3. Scaling factors of 231% and 190%, and 125% and 101% applied to the spectra of 50-5 and 50-7 for the 500°C and 800°C samples to plot them on the same scale as the spectra of the samples exposed to 300°C.*

Based on literature values, this peak was attributed to anhydrite ($CaSO_4$) (Christie *et al.* 1983). In the '50-3' and '50-5' samples at 300°C, S ($2p_{3/2}$) peak binding energies were 168.4 eV, which was attributed to $CaSO_3$. In sample '50-1', S ($2p^3/_2$) binding energies are 169.3 eV at 300°C and 169.9 eV at 500°C. The Ca ($2p^3/_2$) spectra was fitted with two components at 347 eV and 348 eV (Fig. 4.25 - Fig. 4.28), which were previously ascribed to $CaCO_3$ and a possible Ca-aluminosilicate phase respectively. It was observed in Fig. 4.25 to Fig. 4.28 that in all samples and all temperatures, the contribution of the low binding energy Ca ($2p^3/_2$) was decreased in all

samples by up to 30% in the '50-1' and '50-15' samples, and up to 15% in the other two samples.

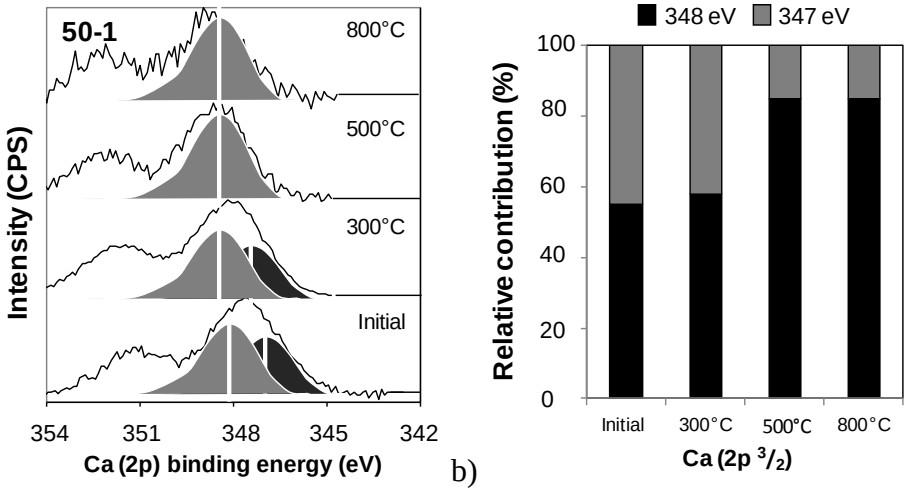

Fig. 4.25 *Ca (2p $^3/_2$) region of the 50-1 Ca-doped aluminosilicate exposed to 1% SO_2/He/Air at 300°C, 500°C and 800°C. The spectra are described by two Gaussian-Lorentzian 30 lineshapes with Doniach-Sunjic asymmetry parameters of 0.005,450 and FWHM of 2.2 eV. The relative contributions of the fitted components are illustrated in (b). Spectra have been scaled to 26, 110 and 252% for the Ca-doped aluminosilicate exposed to 300°C, 500°C and 800°C to be plotted on the same scale as the spectra of the initial material.*

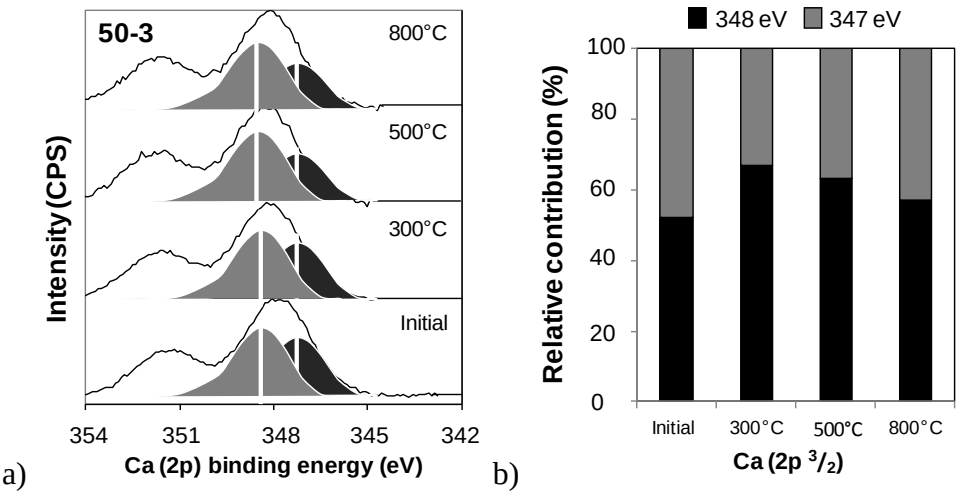

Fig. 4.26 *Ca (2p $^3/_2$) region of the 50-3 Ca-doped aluminosilicate exposed to 1% SO_2/He/Air at 300°C, 500°C and 800°C. The spectra are described by two Gaussian-Lorentzian 30 lineshapes with Doniach-Sunjic asymmetry parameters of 0.005,450 and FWHM of 2.2 eV. The relative contributions of the fitted components are illustrated in (b). Spectra have been scaled to 47, 90 and 102% for the Ca-doped aluminosilicate exposed to 300°C, 500°C and 800°C to be plotted on the same scale as the spectra of the initial material.*

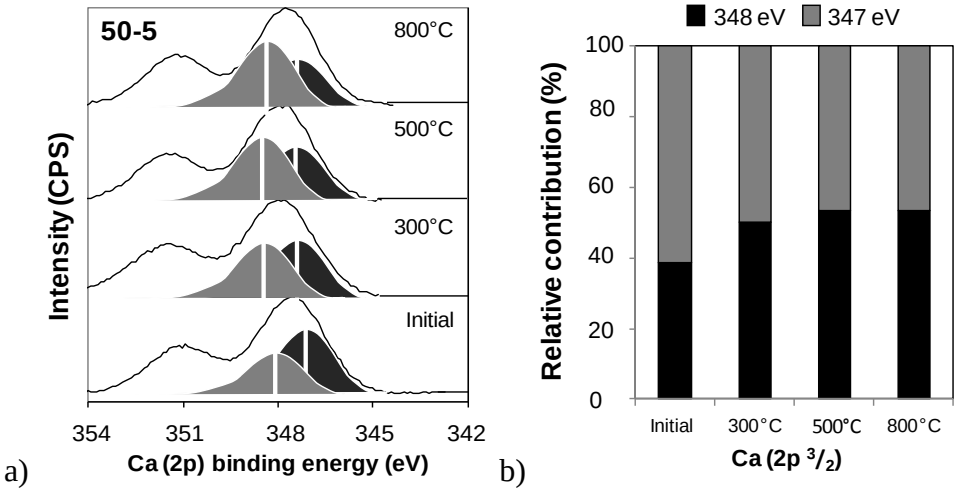

Fig. 4.27 *Ca (2p $^{3}/_{2}$) region of the 50-5 Ca-doped aluminosilicate exposed to 1% SO_2/He/Air at 300°C, 500°C and 800°C. The spectra are described by two Gaussian-Lorentzian 30 lineshapes with Doniach-Sunjic asymmetry parameters of 0.005,450 and FWHM of 2.2 eV. The relative contributions of the fitted components are illustrated in (b). Spectra have been scaled to 43, 45 and 67% for the Ca-doped aluminosilicate exposed to 300°C, 500°C and 800°C to be plotted on the same scale as the spectra of the initial material.*

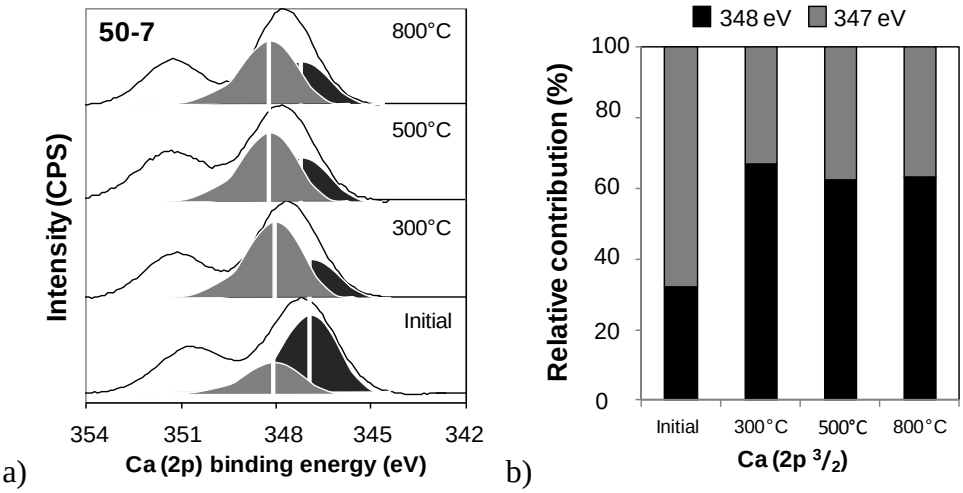

Fig. 4.28 *Ca (2p $^{3}/_{2}$) region of the 50-7 Ca-doped aluminosilicate exposed to 1% SO_2/He/Air at 300°C, 500°C and 800°C. The spectra are described by two Gaussian-Lorentzian 30 lineshapes with Doniach-Sunjic asymmetry parameters of 0.005,450 and FWHM of 2.2 eV. The relative contributions of the fitted components are illustrated in (b). Spectra have been scaled to 87, 171 and 73% for the Ca-doped aluminosilicate exposed to 300°C, 500°C and 800°C to be plotted on the same scale as the spectra of the initial material.*

4.5. SO_2 CHEMISORPTION ON ALUMINOSILICATE SAMPLES

In considering the results of the SO_2 chemisorption experiments and the data produced by analysis, it is first necessary to discuss the structure of the samples as inferred from the existing literature and from the characterisation data in section 4.3.1.

4.5.1. DETERMINING THE XEROGEL MACROSTRUCTURE

The xerogel materials produced by synthesis were amorphous (Fig. 4.6) aluminosilicate, aluminate and silicate networks, based upon XRD and XPS. The presence of both Si-O-Si and Si-O-Al bonds where Si/Al ratios were greater than unity was inferred from XPS analysis, and Al-O-Al and Si-O-Al bonds were inferred where Si/Al ratios are less than unity. If the network structure of the network is dependent upon the valence of the dominant network forming cation, then in the '0' and '20', the network structure may be primarily trivalent rather than tetravalent.

The porous '0-100' series xerogels had high a_s, up to 440 $m^2g^{-1}$and Φ of up to 0.67 cc g^{-1}, (Table 4.5), but also showed a small Φ_d on the order of < 10 nm (100Å) in size, may have a specific macrostructure, the arrangement of the aluminosilicate polymers within the particle itself. Base catalysed sol-gel systems such as those used in this study, create aluminosilicate networks which are precipitated as discrete clusters aggregated together without amalgamation (Brinker and Scherer 1985). The xerogel macrostructure may therefore be approximated by the assumption of colloidal spherical particles packed together to form the gel (Brinker and Scherer 1985). Sample a_s and Φ can be combined with sample bulk density (ρ_{gel}) via equations [4.5] and [4.6] estimate the approximate size (p_d) and density (ρ_{sk}) of the colloids or clusters which make up the xerogel, assuming that they are perfectly spherical (Brinker and Scherer 1985). ρ_{gel} data was only available by coincidence for the '50' sample, giving an estimated colloid size of 41 nm (410 Å) and a skeletal density, that of the aluminosilicate network, of 0.69 cc g^{-1}. The observed skeletal density, much lower than that observed in an aluminosilicate glass (2-3 cc g^{-1}, Chapter 2 and references therein), is indicative of clusters of randomly branched polymer chains of aluminosilicate networks (Brinker and Scherer 1985) rather than a dense interconnected network. A branching structure would contain high Φ but small Φ_d due to void spaces between branches, consistent with the Φ_d observed (< 10 nm, 100Å) in the aluminosilicate xerogels of this study.

$$a_s p_d = \frac{6000}{\rho_{sk}} \qquad [4.5]$$

$$\phi = \frac{1}{\rho_{gel}} - \frac{1}{\rho_{sk}} \qquad [4.6]$$

4.5.2. REACTION PRODUCTS FORMED BY SO_2 CHEMISORPTION

The SO_2 chemisorption experiments on the '0-100 series samples have been identified as aluminium sulphate ($Al_2(SO_4)_3$) and aluminium sulphite ($Al_2SO_3)_3$ by XPS (Fig. 4.18), but this has only been confirmed by reference to an $Al_2(SO_4)_3$ standard (Fig. 4.20) rather than verified by another analytical technique. XRD showed no identifiable crystalline phases and leachate S was very low, when normalised to sample surface area being less than 4 nmol m^{-2}, representing less than 1% of the total S identified by bulk analysis techniques (Table 4.20). As leachate solutions contain negligible S, no further reference to these data is included.

4.5.3. COMPOSITIONAL DEPENDENCE ON SO_2 CHEMISORPTION

The formation of $Al_2(SO_4)_3$ and $Al_2(SO_3)_3$ was hypothesised to occur as a result of SO_2 chemisorption on the aluminium component of the network. From reference to Table 4.20, it is apparent that although there are trace amounts of S on the sample surface at higher Si/Al ratios, that chemisorption occurs to greatest extent in the '0' and '20' samples, being between 110% and 610% larger than the highest S concentrations in the higher Si content xerogels. These samples have large Al-O-Al components which remain identifiable, albeit with substantially limited significance in XPS spectra even in sample '80' (Fig. 4.9). The continued presence of Al-O-Al, even in the highest Si containing samples may be a result of the faster hydrolysation of the Al sec-butoxide precursor relative to TEOS (Scholze, 1990), which may result in its faster precipitation into the gel phase, creating discrete 'pockets' of aluminate network amongst the aluminosilicate network. Given the trace SO_2 adsorption inferred on the higher Si content samples and the substantial adsorption at lower Si content samples, it was hypothesised that all chemisorption in these samples occurs on the isolated aluminate network surfaces, and therefore that the aluminosilicate network is essentially of limited reactivity to SO_2.

Table 4.20 *S_{total} concentration on '0-100 series sample surfaces assuming that all S identified by total S analysis (Table 4.12) is deposited on the sample surface (a_s, Table 4.5), compared to the soluble S extracted from leaching of the samples.*

		S (nmol m^{-2})	
Temperature (°C)	**Sample**	**Total**	**Leachate**
300	**0**	1460	4
	20	470	<1
	50	90	<1
	80	240	<1
	100	n/d	<1
500	**0**	800	<1
	20	280	<1
	50	250	<1
	80	90	<1
	100	20	<1
800	**0**	500	<1
	20	180	2
	50	10	<1
	80	40	<1
	100	140	<1

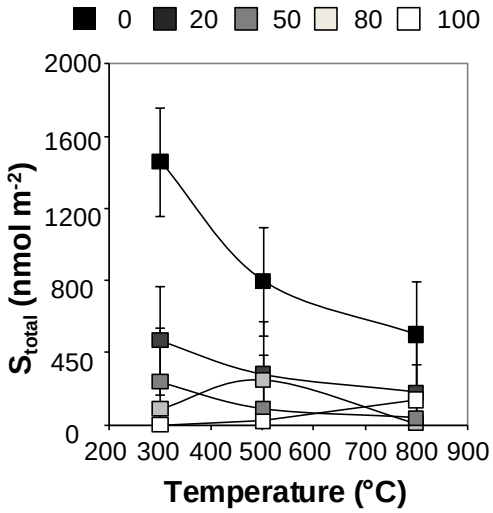

Fig. 4.29 *Total S concentration of the '0-100 series samples normalised per m^2 of sample a_s for the aluminosilicates exposed to 1% SO_2/He. Experimental and analytical error is calculated as being 300 nmol m^{-2}.*

4.5.4. TEMPERATURE DEPENDENCE ON SO_2 CHEMISORPTION

The $Al_2(SO_4)_3$ and $Al_2(SO_3)_3$ compounds was identified at all experimental temperatures for the '20' sample analysed by XPS (Table 4.14, Fig. 4.19), but these phases are fully decomposed in an He-atmosphere at 680°C and decomposition begins at 320°C (Hegedues and Fukker 1956). The formation of $Al_2(SO_4)_3$ apparently above its decomposition temperature was attributed to residual gases trapped within pores which have undergone collapse (sintering) or have been otherwise sealed during high temperature exposure. During cooling, trapped SO_2 gases may then be chemisorbed onto the aluminate network adsorption sites to form the observed S compounds, particularly as the cooling time from 800°C to 200°C was of a similar duration to that of the initial chemisorption experiment. The potential for post-experiment SO_2 chemisorption limits the ability of this study to consider the effect of temperature on chemisorption but reference to Fig. 4.29 demonstrates that uptake for '0' and '20' does show highest total S content at 300°C. The high total S at 300°C for '0' and '20' is likely a result of rapid chemisorption on surface sites proceeding more rapidly than at any higher temperature due to the lack of decomposition effects. It has been demonstrated by these observations that the presence of pores within the xerogel and their collapse may be an important component of the SO_2 chemisorption mechanisms on the aluminosilicate xerogel.

4.6. SO_2 CHEMISORPTION ON CA-DOPED ALUMINOSILICATES

4.6.1. IDENTIFYING CA PHASES ON THE ALUMINOSILICATE SURFACES

In considering the results of the SO_2 chemisorption experiments and the data produced by analysis, it is first necessary to discuss the phases of Ca doped onto the sample surface and their location on or within the sample surface, based on the characterisation data in section 4.3.2.

The initial material prior to doping was the '50' aluminosilicate xerogel described in the previous section. Ca may be deposited over the pore walls in a number of possible forms. At the lowest Ca doping, it was inferred from a slight increase in surface area and porosity that Ca may be integrated into the aluminosilicate network (Table 4.8). The divalent Ca cation has a much larger ionic radius (100 pm) than Al (53 pm), Si (40 pm) (Chang 1994), and the insertion of the larger cation into the network may disrupt or distort the network structure sufficiently to increase the microporosity of the network itself, hence increasing surface area and average pore size. At higher Ca dopings, the hypothesised phenomena would still occur, but Ca may also be deposited over that surface to form crystalline Ca phases on pore walls which would decrease the available volume within them and decrease the overall surface area. This is consistent with the decreases in surface area and porosity observed, but the average pore size of the Ca-doped samples was observed to increase. The increase in Φ_d was attributed to the blocking of smaller pores by Ca doping, which would actually serve to increase the average pore size by preventing N_2 access to the smallest pores during porosimetry.

The phases of Ca doped onto the sample surface, either integrated into the aluminosilicate network or deposited over it as discrete crystalline Ca phases were difficult to determine due to the lack of discrete peaks attributable to such phases by X-ray diffraction (Fig. 4.11). It has been possible by reference to the DRIFTS spectra to identify $CaCO_3$ (Legod *et al.* 2001), particularly in the highest doped samples (Fig. 4.12), whilst the additional possible phases which may exist could include CaO, $Ca(OH)_2$, calcium silicate, aluminate or aluminosilicate compounds, but there was no evidence of these compounds by any technique deployed. XPS spectra for the Ca ($2p^{3}/_{2}$) peak can be fitted with two components (Fig. 4.15), the lower binding energy component was attributed to $CaCO_3$ but as the binding energies of CaO, $Ca(OH)_2$, $Ca_3Al_2O_6$ and $CaSiO_3$ also fall within the range of binding energies covered by $CaCO_3$, this interpretation is not certain (Ball *et al.* 1987; Sugama *et al.* 1989; Van Doveren and

Verhoeven 1980; Wagner *et al.* 1982). The broad (2 eV) peak at 348 eV was attributed to the presence of Ca in charge compensating positions within the aluminosilicate network, as similar binding energies are reported for a microporous, crystalline calcium-aluminosilicate zeolite (Barr 1983), which is consistent with the hypothesised integration of Ca into the aluminosilicate sample surface and it has already been hypothesised that Ca is integrated into the aluminosilicate surface. This hypothesis is further supported by the observed decrease in the relative contribution of the higher binding energy peak as Ca doping increases (Fig. 4.15), consistent with deposition of crystalline Ca phases over the Ca integrated into the aluminosilicate surface.

4.6.2. REACTION PRODUCTS FORMED BY SO_2 CHEMISORPTION

The reaction products of SO_2 chemisorption on the '50-N' series samples have been hypothesised to be anhydrite ($CaSO_4$) at 800-500°C and bassanite ($CaSO_4.½H_2O$) at 300°C in sample '50-15' (Fig. 4.21). The S (2p) peak for '50-15' samples at all temperatures occurred at 168.9 eV and was therefore inferred to indicate the presence of anhydrite (Fig. 4.24), being consistent with binding energies observed by previous authors (Christie *et al.* 1983). The hypothesised peak attributed to $CaSO_4$ is also identified in sample '50-5' at 500°C, whilst at 300°C in sample '50-5' and '50-3', a slightly lower binding energy component at approximately 168.6 eV is identified (Fig. 4.24). The decrease in binding energy may be due to a difference in the form of the Ca-S reaction product beneath the immediate sample surface, as in pure $CaSO_4$, the binding energy of the S (2p) peak was 0.4 eV higher than a layer of $CaSO_4$ formed by oxidation of $CaSO_3$, with a $CaSO_3$ deposit beneath that oxidized layer (Baltrusaitis *et al.* 2007), but the exact chemical composition of such a sub-surface layer is not known. The behaviour of the lowest Ca doped sample has an S (2p) binding energy which is almost 1 eV higher than those of the other samples at 500°C (Fig. 4.18, Fig. 4.20). The observed binding energy was consistent with the previously observed binding energies for $Al_2(SO_4)_3$ in the aluminosilicate samples, but it is not possible to determine whether Al-S compounds may be deposited by any other experimental technique.

4.6.3. COMPOSITIONAL TREND IN SO_2 CHEMISORPTION

The compositional trend in SO_2 adsorption observed with increasing Ca doping is displayed in Fig. 4.30a, and shows an exponential increase in SO_2 uptake as Ca doping increases for all samples. By reference to the observed reaction products, this compositional trend may be explained. At the lowest doping, '50-1', it was inferred

from the XPS data that an alternative S compound other than CaSO4 or $CaSO_4.½H_2O$ may be formed by SO_2 chemisorption, possibly an Al-S compound. The lack of apparent Ca-S compounds in this sample was attributed to the likely dispersal of the Ca as charge compensating units on the aluminosilicate surface rather than as discrete crystalline Ca phases. Charge compensating Ca may be fully coordinated with the aluminosilicate network and may therefore expose no basic oxide sites for SO_2 chemisorption reactions. The apparent formation of Al-S compounds in this sample may be an indicator of SO_2 chemisorption onto the existing aluminate network clusters, as it was previously demonstrated that the aluminosilicate network is unreactive to SO_2, the apparent enhanced S uptake relative to the undoped material may be due to the increased a_s and Φ of the sample, as this may have increased the number of accessible chemisorption sites for SO_2 on the sample.

If Ca in the aluminosilicate network presents no chemisorption sites for SO_2, then SO_2 adsorption should occur solely on the crystalline phases deposited on the sample surface. By XPS, the reactive sites to SO_2 may therefore be those represented by the low binding energy component fitted to the Ca (2p 3/2) spectra at 347 eV. If the total S concentration of the samples normalised to a_s is compared to the relative surface Ca concentration which is represented by the 347 eV peak (Table 4.21), and if it is considered that in sample '50-1' that chemisorption of SO_2 does not occur on Ca sites, the exponential trend observed in SO_2 uptake compared to total Ca concentration is replaced by linear relationships with r^2 values of 0.97 and above (Fig. 4.30b).

Table 4.21 *Relative contribution of the identified Ca-aluminosilicate and other Ca phases in the initial surfaces of the '50-N' series samples, based on the Ca (2p $^3/_2$) peaks in Fig. 4.15.*

Sample	Total Ca (atm. %)	Ca-aluminosilicate		Other	
		Peak contribution	Atm. %	Peak contribution	Atm. %
50-1	**0.62**	77%	**0.47**	33%	**0.15**
50-2	**1.40**	49%	**0.68**	51%	**0.72**
50-3	**2.94**	49%	**1.44**	51%	**1.50**
50-4	**5.53**	33%	**1.82**	77%	**3.71**

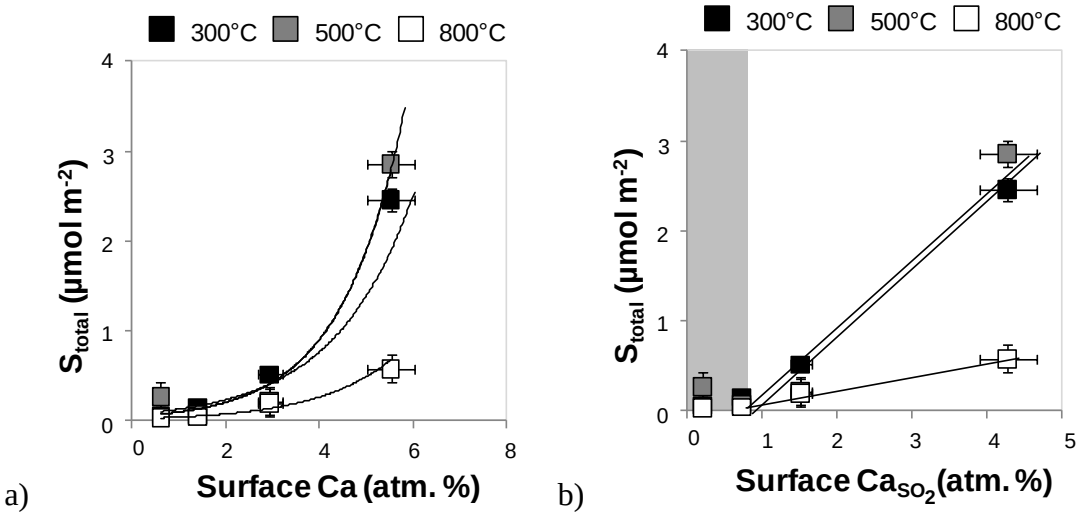

Fig. 4.30 *Comparative plot of total S normalised to sample a_s against (a) the initial relative surface Ca concentration measured by XPS and (b) the modified relative surface Ca concentration attributed to the presence of discrete Ca phases on the sample surface (Table 4.21). The grey area indicates that the '50-1' sample is disregarded in this consideration. The linear trendlines in (b) have r^2 >0.97.*

4.6.4. TEMPERATURE TREND IN SO_2 CHEMISORPTION

The trends in adsorption of S/Ca ratios at higher Ca dopings (Fig. 4.31) may be explained by reference to the SO_2 chemisorption of the Ca crystalline phases on the sample surface and to the collapse and shrinkage of samples under the effects of high temperature exposure, whilst SO_2 chemisorption at the lowest Ca-doping is hypothesised to result in Al-S compound formation.

In Ca-doped samples other than '50-1', low temperature SO_2 chemisorption may occur rapidly on exposed surface sites, namely those of Ca carbonates, hydroxides and oxides on the sample surface via reactions [4.7-4.9] (Krammer *et al.* 1997) to create $CaSO_3$ or $CaSO_3.{}^1/_2H_2O$, which may then be oxidised to the anhydrite and bassanite phases identified by XRD.

$$CaO_{(s)} + SO_{2(g)} \leftrightarrow CaSO_{3(s)} \qquad [4.7]$$

$$Ca(OH)_{2(s)} + SO_{2(g)} \leftrightarrow CaSO_3 \cdot \frac{1}{2}H_2O_{(s)} + \frac{1}{2}H_2O_{(g)} \qquad [4.8]$$

$$CaCO_{3(s)} + SO_{2(g)} \leftrightarrow CaSO_{3(s)} + CO_2 \qquad [4.9]$$

In studies of SO_2 adsorption on porous limestones, the formation of $CaSO_4$ deposits may interfere with the flow of SO_2 into the sample, requiring diffusion through the emplaced product layer to enable further SO_2 adsorption. The formation of $CaSO_4$ on the walls of pore channels increases the thickness of the pore walls and results in the filling of pores or blocks access to the deeper pore network by filling the channel mouth at the sample surface (Simons *et al.* 1986). Restricted access of SO_2 to the sample interior would result in the a_s available for adsorption being smaller than the actual surface area of the sample. A reduction in the accessible a_s for adsorption would explain the observed temperature trend in the data. At 300°C, channel blockage may not occur to a significant extent and over the 60 minute experiment, SO_2 could diffuse throughout the pore network and adsorb on a high proportion of exposed surface sites, giving the highest S/Ca ratio. At 500°C, channel blockage by reaction products may occur to a greater extent, as evidenced by the surface area and porosity data from 0, where the greatest decrease in sample '50-7' surface area and porosity occurs at 500°C, and limits the surface area exposed to SO_2, lowering the S/Ca ratio. The observed trend in sample '50-7', which showed the highest total S content at 500°C rather than 300°C as with '50-3' and '50-5', may be a result of the decreased a_s to bulk ratio, which would increase the significance of the conversion of bulk Ca to $CaSO_4$. The consistent trend whereby S/Ca ratios are lowest at 800°C for all samples is hypothesised to result from a combination of pore blocking, sintering and the decomposition of the intermediate $CaSO_3$ phase, which occurs at 700°C (Wieczorek-Ciurowa 1996), both of which may inhibit the total amount of SO_2 retained by the sample.

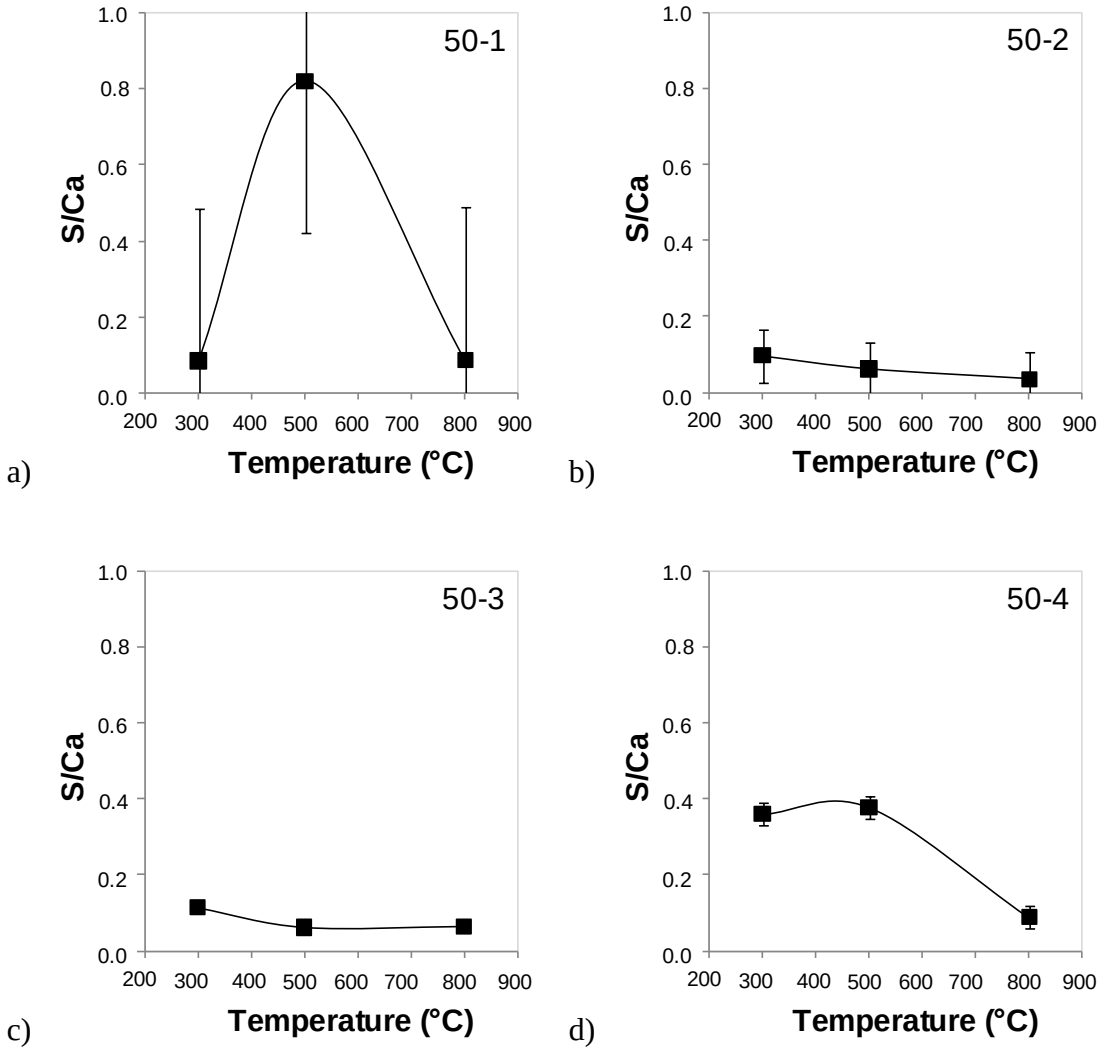

Fig. 4.31 *Variation in total S/Ca ratios with experimental temperature for the Ca-doped aluminosilicates exposed to 1% SO_2/He/Air, based on total S and Ca analysis by XRF. Error bars are calculated from the combined experimental and analytical error of ±0.1 atm. % and ±0.3 atm. % for S and Ca analysed by XRF, with the large error bars on '50-1' being a result of the magnitude of the error relative to the total S and total Ca concentrations in that sample.*

4.7. ONE-STEP SYNTHESIS CALCIUM ALUMINOSILICATES

Based on the behaviour of the '50-N' series samples, where it was hypothesised that Ca within the aluminosilicate network was unreactive to SO_2 due to its position in charge compensating roles, an additional sample series was synthesised. The new sample series was a one-step synthesis technique, which was an effort to integrate Ca more thoroughly into the aluminosilicate network. By synthesis of samples with total Ca concentrations larger than the total Al concentrations, it was intended to force Ca into network modifying roles. The identification of $CaCO_3$ as discrete crystalline phases (Fig. 4.16), however, indicated that the synthesis did not produce the sample structure desired and may have precipitated extensive crystalline phases on aluminosilicate cluster surfaces or existing as large Ca crystallites interdispersed between the macropores of the aluminosilicate cluster aggregates. Time and resource constraints prevented the detailed characterisation of samples which was possible for the other samples, and the presence of $CaCO_3$ crystalline phases was considered a serious limitation on the merits of further study of these samples. Accordingly, the data from the experiments conducted on these samples was not presented or discussed.

4.8. CONCLUSION

4.8.1. IMPLICATIONS FOR SO_2 CHEMISORPTION ON ALUMINOSILICATE SURFACES

In the experiments conducted in this chapter, it was possible to gain some insight into the chemisorption of SO_2 on aluminosilicate surfaces. It was inferred that the aluminosilicate network offers no reactive SO_2 chemisorption sites, even when containing Ca. This may be due to the latter being in charge compensating positions and offering no non-bridging terminal oxygens as Lewis base sites for SO_2 chemisorption. It would therefore be expected that where Ca is present in sufficient concentration to exceed the charge compensation requirement, Ca in network modifying roles may offer potentially reactive sites for SO_2 chemisorption. A similar behaviour may be expected in multi-component silicate glasses, as charge compensating cations will similarly be fully coordinated within the glass network. The hypothesised exclusive SO_2 chemisorption on the non-bridging oxygens of network modifying cations is further explored in Chapters 5 and 6, in studies of more complex multi-component aluminosilicate glasses.

4.8.2. THE LIMITATIONS OF POROUS XEROGELS AS MODEL SILICATE ASH SYSTEMS

When considering the presence of Ca crystalline phases on the sample surface, maximum sulphation was consistently observed at 300-500ºC, which was partially attributed to the porous nature of the aluminosilicates and the decomposition of the intermediate $CaSO_3$ phase at 800°C. The porosity of the '0-100', '50-N' and even the 'Ca-N' xerogels used in this study was found to affect the mechanisms and variables controlling the chemisorption of SO_2 and the formation of Ca-S compounds as a result of that chemisorption. The collapse of pores due to high temperature exposure, the retention of SO_2-bearing atmosphere within the xerogel pores after the experiment exposure time had elapsed and the potential for clogging of pores or pore channels by Ca-S reaction products were all hypothesised to explain the observed SO_2 chemisorption trends, and all were previously observed in existing studies on Ca-based SO_2 sorbents.

The influence of Φ on SO_2 chemisorption and reaction product formation, and the potential for pore collapse during heating, make the xerogel systems of limited merit for studies of silicate ash particles. Silicate ash particles have surfaces formed at high

temperature by fragmentation and/or rapid quenching, and crucially, do not have the extensive microporosity of the xerogel samples (Delmelle *et al.* 2005). The effect of composition or temperature of SO_2 chemisorption trends observed on the xerogel samples may therefore not be applicable to the non-porous silicate ash particle, as no pore-clogging or sintering may occur. In addition to this limitation, the surface structure and surface energies, and hence the reactivities of the chemisorption sites of the xerogels, may vary relative to the quenched high temperature fragmentation surface of the silicate ash particle. The xerogel surfaces are generated by the low temperature precipitation of colloidal particles of aluminosilicate polymers which are then calcined at temperatures of 550°C, compared to the fractured surface of ash particles which may be generated at temperatures up to 1200°C, surface energies of the former may be lowered. The observations of Chapter 5 and 6 have also highlighted the significance of ionic diffusion processes acting within the continuous volcanic glass network, which may place further limitations on the merits of deploying Ca-doped aluminosilicate xerogels as exploratory systems for considering SO_2 adsorption on volcanic glass networks at high temperatures.

4.8.4. THE USES OF SOL-GEL METHODS FOR SYNTHESIS OF MODEL ASH SYSTEMS

The various limitations of the porous xerogel systems are outlined in the previous section, and in the context of the existing experiments, are not a viable method for studying the variables under investigation. This is not to say that such techniques are devoid of merit for studying other aspects of volatile scavenging by ash. The techniques deployed in this study have been demonstrated to be easy to synthesise and replicate, and remain a cheap and reproducible way to produce high a_s aluminosilicate materials, requiring only access to wet-chemical preparation facilities.

Although such systems may be inappropriate to high temperature studies due to the filling and collapse of pores, at lower temperatures, where these phenomena are absent, they may still be of use. In Chapter 2, the possibilities of heterogeneous chemical reactions within the atmosphere were highlighted as being unexplored and potentially significant due to the large total surface area produced by eruptions. Working at low temperatures and using the high a_s aluminosilicate materials may therefore offer a simple method for studying the reactivities of specific adsorption sites on silicate ash surfaces. Such efforts would require the careful selection of model systems, and would require that the difficulties encountered in this study be resolved. In

addition to working with aluminosilicates, ferrosilicate materials could also be synthesised, and both could be doped with low concentrations of alkali and alkaline earth metals to create a range of different surface sites for study by techniques such as XPS. The issue of phase separation must be resolved, not only for the amorphous alumina and silica phases, but also for the precipitation of crystalline phases of the dopant. To achieve these objectives, future experiments should explore the effect of hydrolysis time on the alkoxide precursors to ensure their optimal dispersion into a mixed network. The concentrations of the dopant should also be lowered to create a small number of sites dispersed and integrated into the sample surface, rather than being precipitated as discrete crystal phases. By synthesising both aluminosilicate and ferrosilicate materials (by the use of Fe-alkoxide precursors) and doping them with alkali and alkaline earth cations, many of the major adsorption sites on silicate glass surfaces may be investigated. By comparing the reactivities of the sites, an estimate of the relative concentrations and phases of specific compounds which are formed during atmospheric transport could be determined. Further experiments could also study the interaction of the silicate material surfaces with atmospheric gases and pollutants, to further explore the possible effects discussed in Chapter 2.

A study as outlined above would suffer the same limitations as the work of this chapter, so if further high temperature experiments on such systems are required, a new method of synthesis must be devised. Such a mechanism would have to remove the undesirable porosity from the materials. It is possible to convert xerogel materials into non-porous materials by high temperature calcination, causing the viscous flow of the network structure into a more dense glass structure, collapsing the pores (Dunken 1982). For base-catalysed systems, however, the densification step requires high calcination temperatures which may be in excess of 1000°C (Dunken 1982), so it will be necessary to change to an acid-catalysed system in the future. Such mechanisms would also need to follow the ‘one-step’ methodology to distribute any alkali or alkaline earth cations throughout the network in order to allow bulk diffusion processes to occur. As illustrated in the ‘50-N’ series, this ‘one-step’ technique can result in heterogeneous distribution of the different amorphous phases, which is undesirable. Further development of such a method would be necessary, particularly with respect to ensuring dispersion and homogeneous distribution. With further development of the methodology, it should be possible to devise a technique for synthesis of silicate glasses for studies of volatile scavenging which does not require the complex and expensive facilities required to produce glass materials by conventional melting. However, as in

the course of this study it was possible to gain access to the latter, further development of the sol-gel method was not undertaken and the remaining chapters focus on synthetic glasses produced via the conventional methods.

CHAPTER FIVE

SO_2 CHEMISORPTION ON GLASS SURFACES.

PART I – RATIONALE, METHODOLOGY AND RESULTS.

CHAPTER 5. SO_2 CHEMISORPTION ON GLASS SURFACES. PART I – RATIONALE, METHODOLOGY AND RESULTS.

5.1. INTRODUCTION

5.1.1. CHAPTER OVERVIEW

In this chapter, the data from three separate SO_2 chemisorption experiments conducted on four glass samples with compositions equivalent to commonly erupted ash are presented. These experiments are summarised as follows;

'TEMPERATURE-VARIABLE' EXPERIMENTS (TP-V)

Exposure of volcanic glass powders to 1% SO_2/He atmospheres for 60 minutes at temperatures of 25-800°C.

'TIME-VARIABLE' EXPERIMENTS (TI-V)

Exposure of volcanic glass powders to 1% SO_2/He atmospheres at 300°C, 500°C and 800°C over time periods from 30 seconds to 4 hours.

'ATMOSPHERE-VARIABLE' EXPERIMENTS (AT-V)

Exposure of volcanic glass powders at 800°C to a range of experimental atmospheres (He-only, air-only, 1% SO_2/He/Air and a 60 minute He-only treatment preceding exposure to 1% SO_2/He/Air atmospheres.

The glass powders were fully characterised both before and after experiments by bulk analytical techniques including XRF and XRD, surface-sensitive techniques such as XPS and gas-adsorption porosimetry, and leachate analysis. The pre-experiment characterisation data are presented first, followed by the post-experiment characterisation data for each of the above experiments.

5.1.2. SPECIFIC EXPERIMENTAL RATIONALE

In the previous chapter, the use of synthetic xerogels was found not to be an appropriate methodology for the exploration of volcanic ash systems. It was instead hypothesised that under ideal conditions, experiments should use glass samples created by high temperature fusing of the oxide constituents to create chemically simple aluminosilicate and ferrosilicate glass powders containing minor element concentrations

of at most, two alkali or alkaline earth cations. To test the validity of glass powders as model systems for SO_2 chemisorption on ash surfaces, experiments were conducted on 'multi-component' aluminosilicate glasses generated by the remelting and fusing of volcanic rocks of different chemical composition and origins. Although compositionally diverse, rather than the proposed simple 'few-component' binary, ternary and perhaps quaternary glasses, the use of more complex glasses in these experiments ensures that the most common or most important SO_2 chemisorption sites likely to exist on volcanic glass particles may be represented in experiments. The experiments of this study will therefore inform any future work by guiding any study of simple 'few-component' systems.

The experiments series conducted on the glass powders, as outlined in section 5.1.1., were each designed to fulfil a specific objective. The 'TP-V' series were the preliminary experiments which were to be used to identify the reaction products of SO_2 chemisorption, and so were conducted over 60 minute exposure times in order to provide sufficient time for extensive SO_2 chemisorption to emplace quantities of salts and reaction products over the low a_s glass particles which could be identified by techniques such XRD, XRF and XPS. Such experiments are diagnostic, rather than representative, as their purpose is to provide the 'fingerprint' by which reaction products formed in shorter time duration experiments may be discerned.

The 'TI-V' experiments were intended to explore directly the influence of both temperature and exposure time after the initial 'TP-V' experiment series had been conducted. These experiments were conducted over a range of exposure times which ranged from 30 seconds to 4 hours, with the shortest exposure times intended to be representative of those within the plume. Experiments could not be conducted at the timescales for high temperature silicate ash particle exposure estimated through the model of Mastin (2007) due to the logistical difficulties in stabilising the SO_2-bearing gas stream for a 10 second exposure.

The 'AT-V' experiments were intended to explore the changes in ash particle surfaces occurring as a result of exposure to SO_2-bearing and SO_2-free atmospheres at 800°C. The samples of these experiments were analysed extensively by XPS in order to determine what impact different surface treatments had on the immediate surface configuration and on the respective reactivities of any SO_2 chemisorption sites on the glass particles surfaces.

5.2. METHODOLOGY

5.2.1. GLASS POWDER SYNTHESIS AND CHARACTERISATION

The multicomponent glasses used in the experiments of this study were synthesised by the remelting and fusing of volcanic rocks, and the resulting silicate melts are then quenched, extracted and ground to powder. The glass powders produced may have chemical compositions similar to volcanic glasses, but should not be referred to as such, as rather than the specific cooling history of their source eruption and volcano, the synthetic glasses have the thermal history and composition generated by their fusing under laboratory conditions.

The source rocks selected for remelting and fusing originated from a range of different eruptions at different volcanoes (Table 5.1) and may be described via the total-alkali silica classification system (Le Maitre *et al.* 2002) as being trachybasaltic, phonolitic, dacitic and rhyolitic (Fig. 5.1). The origins of these rocks are varied, coming from volcanoes which have a range of eruptive styles, and the rocks were also selected to cover a range of chemical compositions, varying not only in Si content, but also in Al, Na, Ca, K, Mg and Fe content (Table 5.2) in order to investigate the compositional dependence of the glass particle surface.

Table 5.1 *The origins of the volcanic rocks from which the volcanic glasses synthesised via remelting and fusing were generated.*

Volcanic glass	Source rock	Origin	Eruption
TPH	High Ca trachybasalt	Mt. Etna, Italy	2002
PHN	High K phonolite	Monté Nuovo, Italy	1538
DCT	High alkali dacite	Mt. Unzen, Japan	1991
RHY	Low Ca rhyolite	Lipari, Italy	729

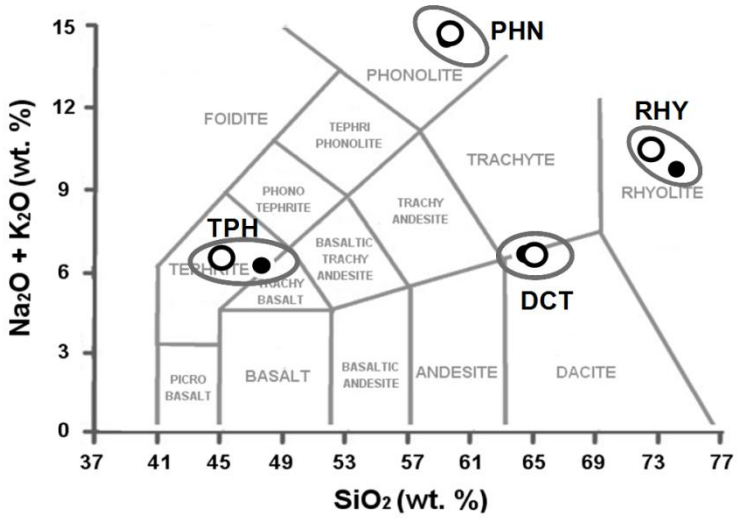

Fig. 5.1 *Total-alkali silica plot showing the composition of the glass powders used in the SO_2 chemisorption experiments, based on the chemical composition data in Table 5.2. The original source rocks (black circle) and the volcanic glasses generated from these rocks (white circle) are indicated.*

Table 5.2 *Bulk chemical composition (XRF) of the source rocks from which glasses were synthesised.*

	Chemical composition (Atm. %)			
	TPH	**PHN**	**DCT**	**RHY**
Al	6.9	8.1	6.2	5.2
Ca	4.1	0.7	1.8	0.3
Fe	3.1	0.9	1.6	0.5
K	1.0	2.8	1.0	1.9
Mg	3.5	0.0	1.7	0.0
Na	2.6	4.3	2.4	2.8
O	60.7	63.7	64.2	66.0
P	0.2	0.0	0.1	0.0
Si	17.4	19.2	20.9	23.4
Ti	0.5	0.1	0.2	0.0

The samples of volcanic rock selected for use were broken into small (< 2 cm) chips and fused in a platinum crucible at temperatures between 1350-1400°C (Table 5.3) under standard atmospheric pressure in a Nabertherm high temperature furnace (HI 04/17). During fusing, dissolved gases remaining within the rocks, particularly in the rhyolite composition, could be observed to be exsolved, 'inflating' the fragments of melt considerably. Once molten and degassed, the melt was removed from the furnace

and left to quench in open atmosphere. At the time of synthesis, it was not possible to guarantee that the melts were crystal free, but by reheating the glasses to high temperature and stirring constantly for prolonged periods (Table 5.3), any crystals were thought to be homogeneously distributed through the glass. Melt homogenisation was conducted using a Pt-Rh alloy spindle connected to a Brookfield DV-III programmeable rheometer. After homogenisation, samples were requenched under identical conditions, with the exception of the tephrite glass, which was poured whilst molten onto a steel plate to facilitate rapid quenching without crystallisation. Exact cooling times and quench rates were not determined. After quenching, the glass samples were extracted from their crucibles via drilling and were ground to powder within a rotary ball mill prior to characterisation and SO_2 chemisorption experiments.

Glass powders were dry-sieved into size fractions of particles with p_d of >250 μm, 180 μm ≤ p_d ≤ 250 μm, 125 μm ≤ p_d ≤ 180 μm, 90 μm ≤ p_d ≤ 125 μm, 63 μm ≤ p_d ≤ 90 μm and < 63 μm. As only the <63 μm fraction was used in experiments, to better represent the fine volcanic glass powders common to explosive eruptions, the large size fractions were later ground to generate more material for experiments. Samples have been stored in sealed soda-lime glass vials under standard atmospheric conditions, and at the time of writing, the materials are approximately two and a half years old.

Table 5.3 *Temperatures and times of rock fusion temperatures and times, and homogenisation temperatures and times.*

Sample	Fusion temp. (°C)	Fusion time (hrs)	Homogenisation temp. (°C)	Homogenisation time (hrs)
TPH	1400	1	1300/1400	6 / 6
RHY	1450	2	1600	20
PHN	1400	15	1500	19
DCT	1400	2	1400/1500	48 / 24

5.2.1.2. CHARACTERISATION

After synthesis and grinding, samples were characterised by bulk and surface sensitive techniques. The samples are crystal-free glasses, as demonstrated by the amorphous silica ‘halo’ identified by XRD (Warren and Biscoe 1937) and the lack of any discrete crystalline phases (Fig. 5.2), and were found to have glass transition temperatures (T_g) ranging from 591-720°C for heating at 10°C per minute, as given in

Table 5.4. The bulk chemical compositions of the glasses determined by XRF are given in Table 5.5. By reference to the total-alkali silica classification system (Fig. 5.1), the glass powders are classified as being a tephrite glass (TPH), phonolite glass (PHN), dacite glass (DCT) and a rhyolite glass (RHY).

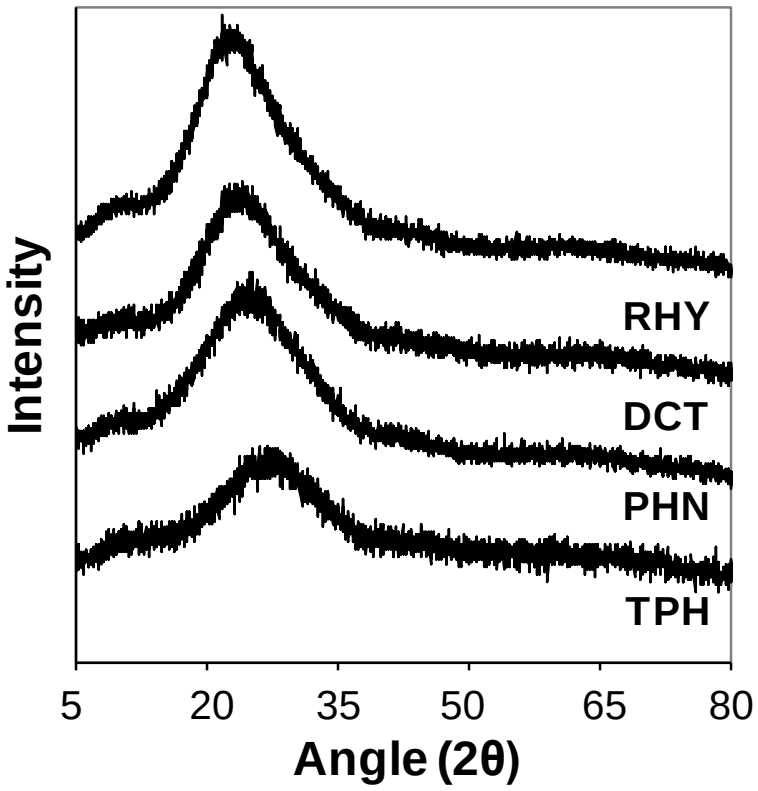

Fig. 5.2 *XRD patterns for the volcanic glass powder series.*

The a_s and the relative chemical composition of the sample surface were determined by nitrogen adsorption porosimetry and XPS. The samples have specific surface area (a_s) of between 0.6-1.5 m^2g^{-1} and were non-porous (Table 5.6), and were observed by reference to SEM optical imaging to comprise irregular glass fragments with a wide range of particle sizes and morphologies. The glass materials were also analysed by laser particle size distribution analysis and the particle size distributions of the powders was determined. The particle size distributions are illustrated in Fig. 5.3, and are approximately similar across all samples, indicating that the method of grinding used can be relied upon to produce similar particle size distributions for glass powders.

Table 5.4 *Glass transition temperatures (T_g) of the four glasses, based upon the initial deviation of the glass transition peak on the 2nd cycle of heating at 10°C per minute via differential scanning calorimetry.*

	TPH	PHN	DCT	RHY
T_g (°C)	591	637	658	720

Table 5.5 *Bulk chemical composition (XRF) of the four glass powders.*

Element	Chemical composition (Atm. %)			
	TPH	PHN	DCT	RHY
Al	7.1	8.2	6.5	5.5
Ca	4.4	0.7	1.8	0.3
Fe	3.7	0.9	1.3	0.5
K	1.1	3.4	1.1	2.6
Mg	3.6	0.0	1.3	0.0
Na	2.5	4.3	2.5	2.7
O	60.2	61.3	62.7	63.4
P	0.2	0.0	0.0	0.0
Si	16.7	21.0	22.5	25.0
Ti	0.5	0.1	0.2	0.0

The relative chemical composition, excluding adventitious carbon, of the glass surfaces was determined by XPS for each sample. Throughout the experiments of this study, the larger size fractions of the glass powders were repeatedly reground, and the surface compositions after each new grinding were recorded. Although the surface compositions presented in Table 5.7 are from the third batch of ground glass powders, when XPS analysis and interpretation is conducted, samples are always discussed in the context of the appropriate batch of ground glass powders. There are minor differences between the sample surface and bulk composition (Table 5.5, Table 5.7), although both remain multicomponent aluminosilicates. Prior to SO_2 chemisorption experiments, samples were also leached to determine whether the pre-experiment surface may contribute significantly to post-experiment leachate solutions (Table 5.8).

Table 5.6 *Sample specific surface area (a_s) and porosity (Φ) for all glass powders as determined by nitrogen adsorption porosimetry.*

	TPH	PHN	DCT	RHY
a_s ($m^2 g^{-1}$)	0.6	0.89	1.42	1.1
Φ ($cc\ g^{-1}$)	0.001	0.001	0.001	0.001

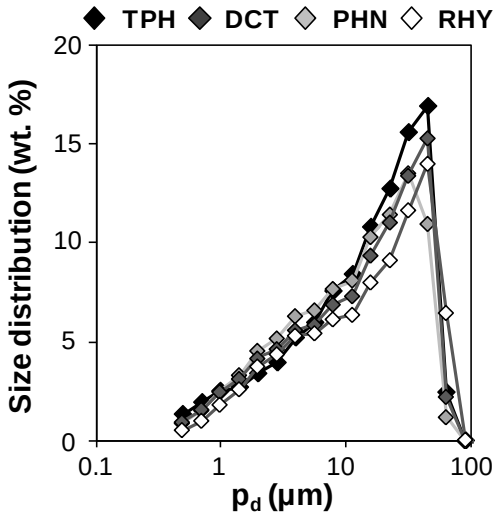

Fig. 5.3 *Particle size distribution of pre-experiment glass powders, as determined by laser particle analysis.*

Table 5.7 *Sample surface composition (atm. %) as determined by XPS.*

	XPS surface composition (atm. %)			
	TPH	PHN	DCT	RHY
Al (2p)	6.0	6.7	6.0	4.7
Ca(2p)	1.9	0.5	1.1	0.8
Fe (2p)	4.0	1.5	1.8	1.4
K (2p)	0.5	2.8	3.4	2.5
Mg (2p)	0.4	0.0	3.0	0.1
Na (1s)	2.1	8.7	3.4	7.9
O(1s)	73.9	63.6	71.5	67.1
S (2p)	0.2	0.0	0.0	0.0
Si (2p)	10.9	16.5	9.8	15.2

Table 5.8 *Composition of leachate solutions, normalised to* a_s *(Table 5.6) extracted from the initial glasses prior to use in* SO_2 *chemisorption experiments.*

Element	Leachate concentration (µmol m^{-2})			
	TPH	**PHN**	**DCT**	**RHY**
Al	1.4	1.4	0.3	0.1
Ca	11.0	0.8	2.4	2.3
Fe	0.1	0.2	0.2	0.1
K	3.6	2.1	0.8	1.7
Mg	6.2	0.1	0.8	0.1
Na	0.8	0.4	0.3	0.4
S	0	0	0	0

5.3. EXPERIMENTAL PROTOCOLS

In the 'TP-V' series, the temperatures investigated for all glass samples were 25, 100, 200, 300, 400, 500, 600, 700 and 800°C under a constant 40 sccm flow of 1% SO_2/He/Air. After the exposure to the experimental atmosphere was ended, the reactor and feedlines were purged with a 100 sccm stream of He. The duration of cooling time was that required for the sample within the furnace to cool from the experimental temperature to 200°C. At this point, it was removed from the furnace and placed within a sample vial and stored under atmospheric conditions. The post-experiment cool down and sample removal and storage conditions were maintained for all experiments of this study. The data acquired from the 'temperature-variable' experiments are provided in section 5.4.

In the 'TI-V' experiments, a range of exposure times to 1% SO_2/He/Air over three temperature periods were investigated. At 800°C, exposure times were 0.5, 1, 2, 5, 10, 20, 40, 60, 120 and 240 minutes and experiments were conducted on all glasses. At 500°C, experiments were conducted at 0.5, 1, 2, 5, 10, 20, 40 and 60 minutes for the TPH, PHN and DCT glasses, but not for the RHY, the supply of which had been exhausted at the time of the experiment. At 300°C, only a limited exploration of the exposure times was carried out due to the lack of sufficient glass materials for the same number of time points as were conducted in the 500°C and 800°C experiments. Due to the potential significance of short exposure times within the volcanic eruption plume, time series experiments at 300°C were conducted for 0.5, 1, 2, 5, 10 and 60 minutes. The data acquired from the 'time-variable' experiments are provided in section 5.5.

In the 'AT-V' experiments, which exposed the volcanic glass samples to different atmospheres at 800°C for 60 minute time periods, the effect of exposure to the following atmospheres were investigated. Glasses were exposed to He-only, air-only, and 1% SO_2/He/Air with and without a 60 minute He-only pre-treatment at the same temperature. The data of these experiments are provided in section 5.6.

5.4. RESULTS OF 'TP-V' EXPERIMENT

The glass powder samples exposed to 1% SO_2/He/Air atmospheres at 25-800°C were analysed by bulk and surface sensitive techniques, and these data are presented below.

5.4.1. TOTAL S ANALYSIS

Total S concentration in the bulk samples was determined by ICP-OES for selected samples (Table 5.9). For the four glasses, the total S concentration in the TPH varied from 16.9-196.9 µmol g^{-1}, whilst for the PHN, DCT and RHY, the range was 7.6 to 87.0 µmol g^{-1}, 8.2 to 230.7 µmol g^{-1} and 7.9 to 65.4 µmol g^{-1} respectively. This S was attributed to having an experimental origin, as prior XRF analysis had detected no S within the pre-experiment glasses.

Table 5.9 *Total S content of selected glass powders from 'TP-V' experiments, determined by ICP-OES. 'n.a.' indicates a sample not analysed, and 'n.d' indicates a sample reading below the instrument detection limit of <0.01 ppm S.*

Temp. (°C)	S_{bulk} (µmol g^{-1})			
	TPH	**PHN**	**DCT**	**RHY**
300	16.9	7.6	8.2	*n.a*
400	*n.a*	*n.a*	*n.a*	*n.a*
500	48.5	30.9	*n.a*	7.9
600	196.7	55.7	51.1	33.3
700	178.9	121.1	207.9	71.7
800	196.9	87.0	230.7	65.4

5.4.2. MINERALOGY

Selected samples of all glasses exposed to temperatures between 500-800°C were analysed by XRD and baseline subtracted for interpretation. At 700°C and 800°C, an anhydrite ($CaSO_4$) phase (Wasastjerna 1927) was identified in all samples, and at 600°C, the presence of the anhydrite primary diffraction peak at 25° 2θ was still discernible in the TPH and PHN glasses (Fig. 5.4). In the tephrite glass at 800°C, additional crystalline phases were identified, being attributed to an augite phase and an iron oxide phase (Fig. 5.5). The most prominent peaks detected were at 31° and 36°, and

combined with the surrounding secondary peaks, the crystalline phase inferred to exist was a complex Ca, Na, Al, Mg, Fe and Si bearing augite phase(Okui et al. 1998) and possibly a gamma Fe_2O_3 phase (Jorgensen et al. 2007). No other sulphate or sulphur compounds were identified in the X-ray diffraction patterns of any of the glasses. Since no crystalline peaks were identified in any glass from 500°C experiments, any crystalline phases on the sample surfaces are likely below the instrument detection limits and no further XRD analysis was conducted in glasses from lower temperature experiments.

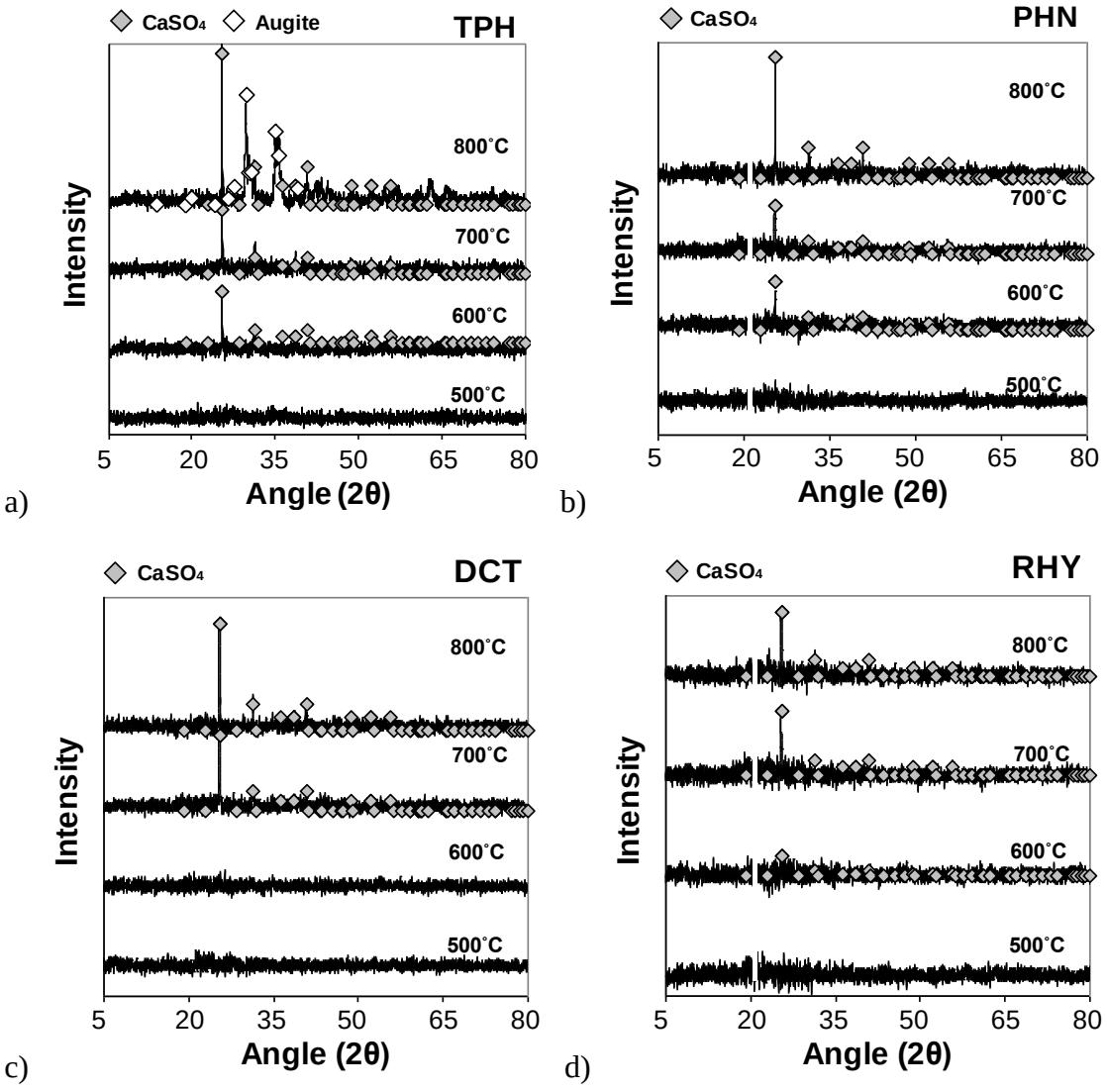

Fig. 5.4 *XRD patterns for selected 'TP-V' glass samples, background subtracted to remove the amorphous silica shoulder. The filled diamonds indicate the diffraction pattern for $CaSO_4$ (anhydrite) (Wasastjerna 1927) and a Ca, Na, Al, Mg, Fe and Si bearing augite phase (Okui et al. 1998).*

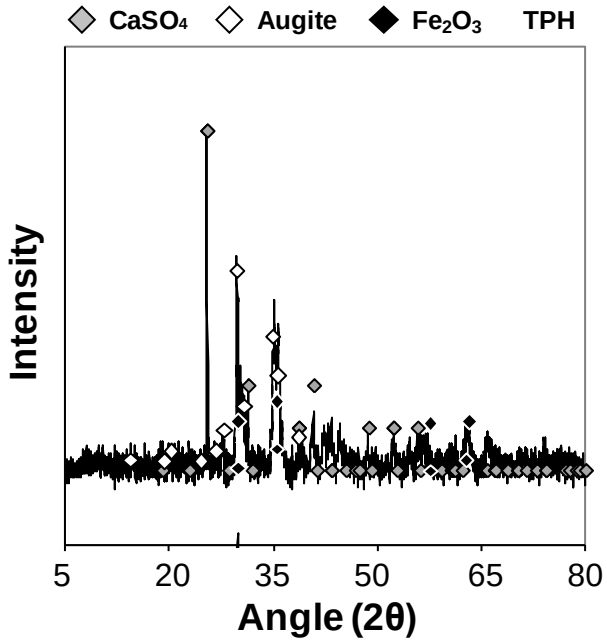

Fig. 5.5 *XRD pattern for the TPH glass exposed to 800°C temperatures in the 'TP-V' experiments, background subtracted to remove the amorphous Si shoulder. The filled diamonds indicate the diffraction pattern for $CaSO_4$ (anhydrite) (Wasastjerna 1927) and a Ca, Na, Al, Mg, Fe and Si bearing augite phase (Okui et al. 1998) and a possible gamma-Fe_2O_3.phase (Jorgensen et al. 2007).*

5.4.3. LEACHING AND LEACHATE ANALYSIS

The compositions of solutions obtained by leaching the glasses with deionised water at near-neutral pH were determined via IC and AA. These data are normalised to glass a_s (Table 5.6) summarised in Table A5 to Table A11 and illustrated in Fig. 5.6 . Soluble S increased up to 600°C in the case of the TPH glass, with a peak S concentration of 553 µmol m^{-2}, and up to 700 -800°C in the case of the other glasses, peaking at 158 µmol m^{-2}, 135 µmol m^{-2} and 61 µmol m^{-2}. Soluble S in leachate solutions is consistently highest in the tephrite glass, followed by the phonolite, dacite and rhyolite glasses in that order. In all glasses above 500°C, Ca in the leachate solutions mirrors the trend observed in soluble S, and is of similar concentration. At lower temperatures for the tephrite glass (Fig. 5.6a), Na in leachate solutions was the predominant cation and mirrored the trend in soluble S up to 400°C, where after, both Ca and Na occur in significant concentrations until the latter disappeared from solution at and above 700°C. In all samples, concentrations of Mg and K were consistently low, being in the main less than 10 µmol m^{-2}, and in the selected samples analysed for Fe and Al, concentrations were either trace or below detection limit.

Where the leachate concentrations of dissolved alkali and alkaline earth cations were low, the data must be interpreted with caution. Leaching does not only dissolve surface salts, but as discussed previously in Chapter 3, also leaches from the bulk glass material itself. Since there is no way to distinguish the two from each other, an estimate based on the pre-experiment glass leaching solutions and for experiments conducted in the absence of SO_2 was used to estimate the contribution from glass leaching and dissolution reactions. Where concentrations of the alkali and alkaline earth cations were within an estimated value of <7 µmol m^{-2}, they were considered to be the result of the leaching and dissolution of the glass surface itself, rather than the dissolution of soluble salts emplaced upon that surface. The estimate for the contribution of the glass dissolution and leaching component was derived from leaching of the pre-experiment glasses and of the glasses exposed to He-only and air-only atmospheres as part of the 'AT-V' experiments (Section 5.6.2). Based upon the respective compositions of leachate extracted from the initial glasses and during the AT-V He-only and air-only experiments (Table 5.10), an average was calculated. To err on the side of caution, one standard deviation above the mean value was used, and this value was calculated to be 7 µmol m^{-2}. This value was used for all elements, although not all elements were extracted to such extent.

The analytical error of leachate analysis is method specific, but in practice, determining or differentiating soluble S concentrations in solutions produced from leaching of the glasses below 0.1 ppm proved a practical impossibility due to minor impurities in the deionised water. The experimental variation determined from three replicate subsamples of the TPH glass was found to be ±15%, based on three replicate experiments of the tephrite glass exposed to 1% SO_2/He/Air for 60 minutes at 800°C (Table 5.11) by both IC and AA analyses. The experimental variation is likely attributed to variations in particle surface chemical compositions and the individual particle size distribution of each 0.7 g glass sample used in experiments.

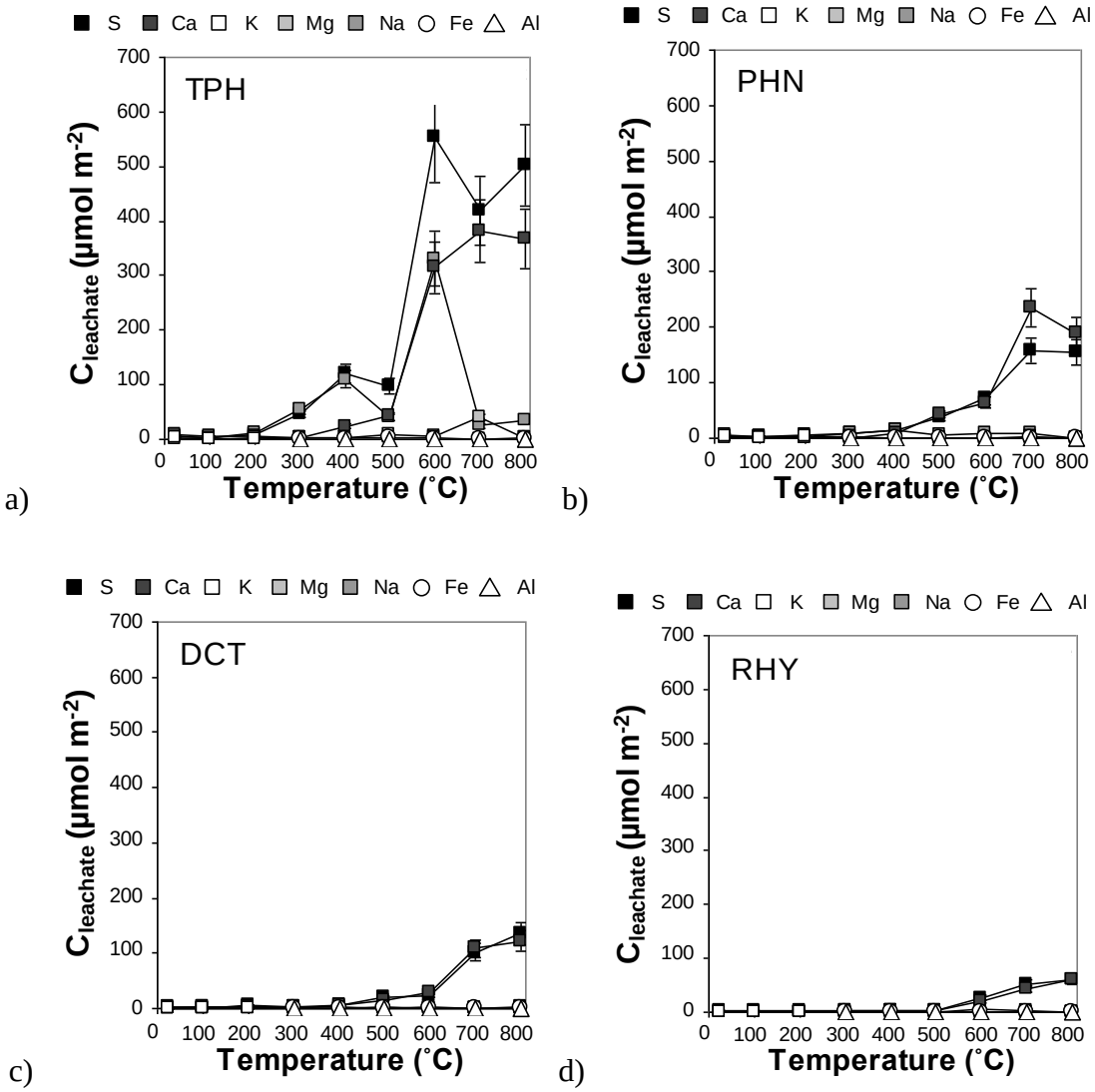

Fig. 5.6 *Concentrations of major cations (Ca, K, Mg, Na, Fe, Al) and S in leachate solutions for 'TP-V' glasses. ($C_{leachate}$) from Table A5 to Table A11, normalised to sample a_s (Table 5.6) Error bars of ±15% represent the experimental error.*

Table 5.10 *Estimated upper limit of $C_{leachate}$ calculated from the mean plus 1 standard deviation (S.D.) for the extraction of cations from the glass due to leaching and dissolution of the particle surface only, without soluble salt dissolution. Based upon the combined average of the leachate concentration values from He-only and air-only experiments at 800°C (Table 5.20,Table 5.21) and the leachate solutions extracted from the pre-experiment glasses (Table 5.8).*

Element	$C_{leachate}$ (µmol m^{-2})		
	Mean	**S.D.**	**Upper limit**
Al	0.4	1.3	1.7
Ca	3.0	3.3	6.3
Fe	0.5	1	1.5
K	1.4	2.2	3.6
Mg	0.9	2.2	3.1
Na	1.5	1.3	2.8

Table 5.11 *Experimental error calculated from $C_{leachate}$ of the alkali and alkaline earth cations and S in solutions extracted by leaching of three replicates of the TPH glass exposed to 1% SO_2/He/Air for 60 minutes at 800°C.*

Replicate	$C_{leachate}$ (µmol m^{-2})				
	S	**Na**	**Ca**	**Mg**	**K**
1	417.9	29.2	305.4	2.0	1.4
2	531.5	21.8	404.3	2.7	2.2
3	395.3	36.1	288.5	2.8	2.0
Mean	448.2	29.0	332.8	2.5	1.8
Error (%)	**12.4**	**16.7**	**14.3**	**13.8**	**17.3**
Mean Error (%)	**14.9**				

5.4.4. SCANNING ELECTRON MICROSCOPY

The TPH (and PHN glasses exposed to 800°C and 1% SO_2/He/air atmospheres were selected for analysis by SEM and spot-EDX to determine the presence of any surface deposits on the glass particles and to obtain insight into the chemical composition of these deposits.

Optical imaging of the TPH glass showed extensive surface deposits, some showing exposed faces up to 2 μm in diameter embedded in the surface (Fig. 5.7). Insight into the chemical composition of the surface deposits was obtained by spot-EDX, comparing Ca and S to Si ratios in order to determine the Ca and S content of surface deposits relative to the glass surface itself. In the TPH glass, it was not possible to differentiate between the Ca/Si and S/Si ratios of the glass surface and those of the surface deposits, whilst in the PHN glass, surface deposits were also observed and were determined by spot-EDX to have Ca/Si and S/Si ratios which were both increased by a factor 2.0-2.2 relative to the surrounding glass (Table 5.12).

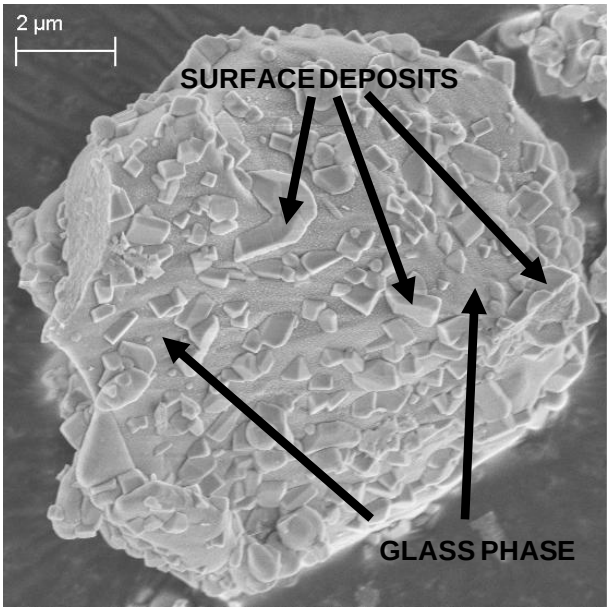

Fig. 5.7 *SEM image of 'TP-V' TPH glass exposed to 1% SO_2/He/Air for 60 minutes at 800°C, showing surface deposits embedded within the amorphous glass phase, with example features indicated by arrows.*

Table 5.12 *Spot-EDX analysis of surface deposits and glass components for the 'TP-V' TPH glass exposed to 1% SO_2/He/Air at 800°C (Fig. 5.7) from analysis of 4 randomly selected surface deposits and glass surfaces.*

Replicates	Ca/Si		S/Si	
	Glass	Deposit	Glass	Deposit
1	0.15	0.40	0.31	0.78
2	0.06	0.12	0.62	0.31
3	0.14	0.15	0.27	0.31
4	0.02	0.13	0.23	0.34
Mean	**0.09**	**0.20**	**0.36**	**0.43**
S.D.	0.07	0.14	0.18	0.23

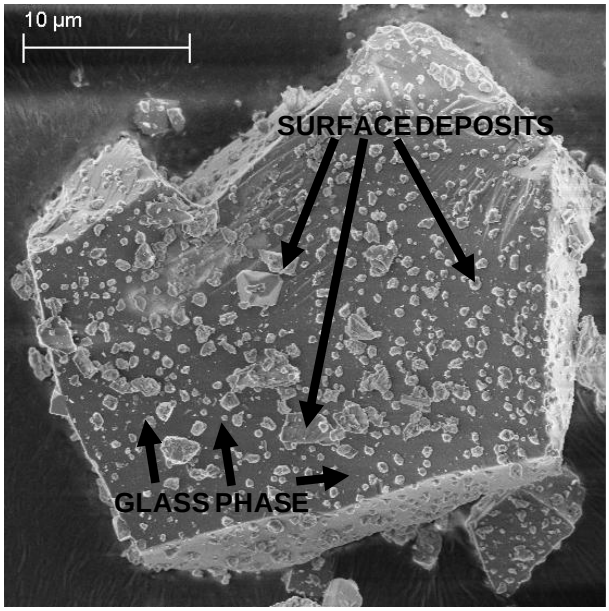

Fig. 5.8 *SEM image of 'TP-V' PHN glass exposed to 1% SO_2/He/Air for 60 minutes at 800°C, showing surface deposits embedded within the amorphous glass phase, with example features indicated by arrows.*

Table 5.13 *Spot-EDX analysis of surface deposits and glass components for the 'TP-V' PHN glass exposed to 1% SO_2/He/Air at 800°C (Fig. 5.8) from analysis of 4 randomly selected surface deposits and glass surfaces.*

Replicates	Ca/Si		S/Si	
	Glass	Deposit	Glass	Deposit
1	0.02	0.12	0.01	0.12
2	0.02	0.18	0.01	0.22
3	0.02	0.06	0.02	0.06
4	0.02	0.27	0.02	0.34
Mean	**0.02**	**0.16**	**0.01**	**0.19**
S.D.	0.00	0.09	0.01	0.13

5.4.5. X-RAY PHOTOELECTRON SPECTROSCOPY

XPS analysis was conducted on the DCT glass exposed to all temperatures between 300°C and 800°C to investigate the change in relative surface composition of the DCT with increasing temperature (Table 5.14). In addition to these data, further analysis was also conducted on all four glasses exposed to 1% SO_2/He/Air at 800° C (Table 5.15).

5.4.5.1. DATA PROCESSING AND ANALYTICAL ERROR

To analyse and interpret the XPS data, the relative surface compositional data is obtained. Interpretation of the relative surface composition data requires normalising to Si and the exclusion of adventitious carbon, and the analytical and experiment error was found to be ±9% per individual element.

When discussing changes in sample surface composition, element relative surface concentrations after the removal of the adventitious carbon contribution are normalised to Si. Si is strongly bound within the tetrahedral network and SO_2 is known from Chapter 4 to not be adsorbed on the silicate network, so normalising to Si is normalising to the most stable component of the glass network. Any increase in element/Si ratios is therefore indicative either of the enrichment of that element within the immediate glass surface, or its precipitation as a discrete deposit overlying the Si glass surface, so decreasing the contribution of Si to the relative surface composition. Similarly, a decrease in element/Si ratios is an indication of depletion from the Si glass surface layer.

The analytical and experimental errors associated with XPS are difficult to isolate from each other. The complex multi-component nature of the glass surfaces may induce some variation even from one subsample of a glass powder to the next, as was observed by analysis of solutions extracted from replicates by IC and AA. The error estimate derived is also partially a product of the subjective peak fitting and region boundary assignment involved in XPS analysis. The analytical and experimental error was estimated from three replicate subsamples of the PHN glass exposed to 1% SO_2/He for 30 minutes (Table 5.16) as part of preliminary experiments not presented in this thesis. Although the average variation in sample surface composition was ±4% for elements originating from the glass surface, the average error for S was more than twice that value. As the element of greatest interest to this study, the error in surface S concentration was used as an upper limit for experimental and analytical error. When considering element/Si ratios, the combined experimental error was therefore calculated to be ±22%.

Finally, when interpreting XPS spectra directly though the assignment of representative peaks, to show shifts in peak lineshapes which may be significant even though the concentrations of elements at the sample surface may vary, all peaks are scaled to be at the same height relative to each other. The scaling factors applied are listed where required in the figure caption.

Table 5.14 *Relative surface composition (atm. %) for the 'TP-V' DCT glass exposed to 1% SO_2/He/air atmosphere at 300°-800°C, as determined by XPS.*

Element	Temperature (°C)					
	300	**400**	**500**	**600**	**700**	**800**
Al (2p)	5.4	5.6	4.1	5.1	3.2	3.4
Ca(2p)	1.3	1.1	4.0	3.3	5.9	5.4
Fe (2p)	2.2	0.9	0.6	1.2	0.6	1.4
K (2p)	0.9	0.9	0.5	1.3	0.5	0.5
Mg (2p)	0.6	0.6	0.4	0.3	0.0	0.1
Na (1s)	3.7	3.6	3.0	2.3	2.3	2.6
O (1s)	49.9	47.1	49.7	48.0	50.1	53.0
S (2p)	0.3	0.4	3.4	3.0	6.4	6.2
Si (2p)	18.4	17.9	13.4	13.9	9.5	11.8

5.4.5.2. DCT GLASS SURFACES EXPOSED TO SO_2 AT 300-800°C

The relative surface compositions of the dacite glass exposed to 1% SO_2/He/Air at temperatures ranging from 300°C to 800°C were given in Table 5.14. Considering the alterations in the relative surface compositions as indicated by element/Si ratios, the only elements to show any variation above that attributed to experimental and analytical error were Ca, O and S (Fig. 5.9). Both Ca/Si and O/Si ratios were found to have correlations with the S/Si ratios with r^2 values in excess of 0.99 (Fig. 5.10). With particular reference to Ca/Si and S/Si, it is observed that when considering the applied ±22% error, at 500°C and above, the Ca/Si and S/Si ratios were found to be 1:1 (Fig. 5.10).

Table 5.15 *Relative surface composition (atm. %) for 'TP-V' glasses exposed to 1% SO_2/He/air atmosphere for 60 minutes at 800°C, as determined by XPS.*

Region	Relative surface composition (atm. %)			
	TPH	**PHN**	**DCT**	**RHY**
Al (2p)	5.1	4.0	3.8	3.7
Ca (2p)	5.8	1.4	4.8	1.4
Fe (2p)	1.3	1.7	2.2	1.8
K (2p)	0.2	1.0	0.3	0.9
Mg (2p)	0.1	0.2	0.3	0.1
Na (1s)	3.6	4.0	1.8	4.0
O (1s)	68.6	69	71.4	69.6
S (2p)	6.3	1.3	5.0	1.3
Si (2p)	9.0	17.4	10.4	17.2

Table 5.16 *Experimental error calculated from XPS analysis of three replicate subsamples of the PHN glass from experiments conducted for 30 minutes under 1% SO_2/He at 500°C.*

	PHN					
	Surface composition (atm. %)			Average (atm. %)	Error (%)	Av. Error (%)
Al (2p)	5.1	5.1	4.8	5.0	**1.6**	**4.0**
C (1s)	0.4	0.4	0.4	0.4	**4.1**	
Ca (2p)	59.9	59.9	59.7	59.8	**0.2**	
Fe (2p)	2.7	2.8	2.2	2.5	**5.1**	
K (2p)	7.4	8.1	7.8	7.8	**4.8**	
Na (1s)	2.3	1.9	2.4	2.2	**5.7**	
O (1s)	3.2	3.0	2.6	2.9	**9.9**	
S (2p)	13.8	13.7	14.5	14.0	**1.5**	
Si (2p)	5.2	5.2	5.6	5.3	**2.7**	

In addition to the relative surface composition data, the Ca (2p $^3/_2$) and S (2p) spectra were analysed in greater detail and interpreted via the assignment of representative components to explain any observed alterations in lineshape and peak positions (Fig. 5.11). A single doublet pair was found to describe the S (2p) spectra, and the S (2p $^3/_2$) peak binding energy was observed to increase with increasing temperature, being initially at 167.9 eV at 300°C, attributable to sulphite species (Smirnov *et al.* 2003), increasingly rapidly to 168.6 eV at 400°C and then increasing gradually to 169.1 eV at 800°C. The Ca (2p $^3/_2$) peak did not yield any information, showing only a single peak at 347.6 eV which did not alter over the temperature range (Fig. 5.11).

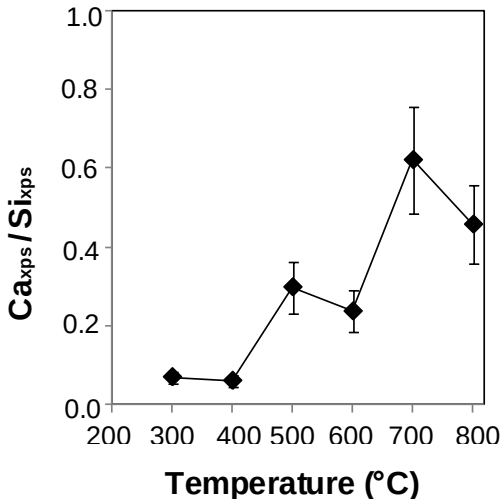

a)

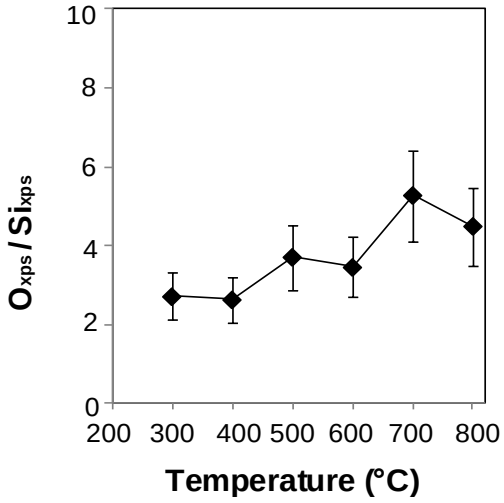

b)

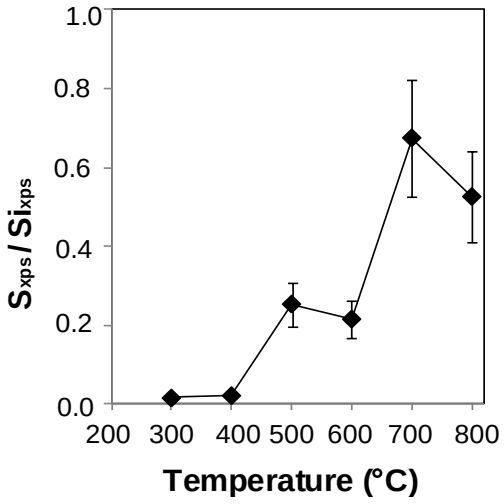

c)

Fig. 5.9 *Alterations in (a) Ca/Si, (b) O/Si and (c) S/Si ratios in the 'TP-V' experiments for the DCT glass over the temperature range 300-800°C analysed by XPS (Table 5.14). Error bars are ±22%.*

5.4.5.3. GLASSES EXPOSED TO SO_2 AT 800°C

The four 'TP-V' glasses which were exposed to 1% SO2/He/Air at 800°C were all analysed by XPS. The data presented here are the correlations between the relative surface composition and S/Si ratios at the sample surface, and the Ca (2p $^3/_2$) and S (2p) spectra. Of the constituent elements of the glass surfaces after SO_2 chemisorption (Table 5.15), only Al/Si, O/Si and Ca/Si have any relationship with S/Si. Out of the three elements identified, Ca/Si and S/Si have a direct 1:1 relationship (Fig. 5.13). Ca (2p $^3/_2$) and S (2p) peaks are fitted with the same representative components as for the DCT glass spectra. Peak positions of the S (2p $^3/_2$) peak for all glasses are observed to be between 169 eV and 168.2 eV, whilst the Ca (2p $^3/_2$) spectra may be described by a single fitted component with a peak position of between 347.8 and 348.1 eV.

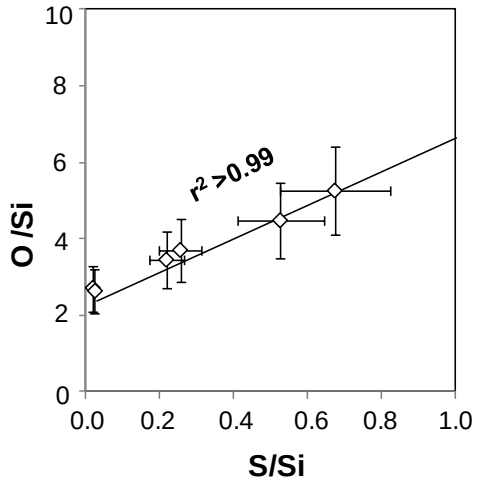

a)

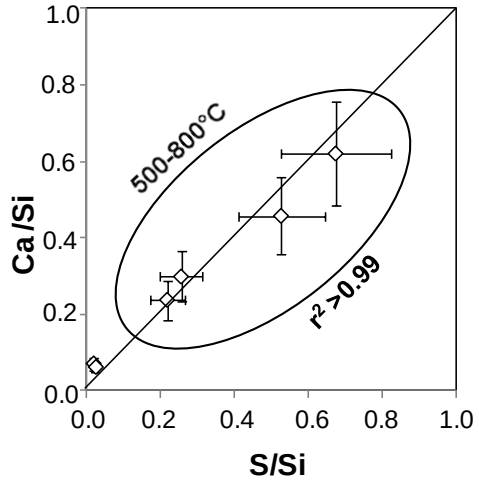

b)

Fig. 5.10 *Relationship between (a) O/Si and S/Si and (b) Ca/Si and S/Si ratios for the 'TP-V' DCT glass exposed to 1% SO_2/He/Air for 60 minutes at 300-800°C analysed by XPS (Table 5.14). Error bars ±22%.*

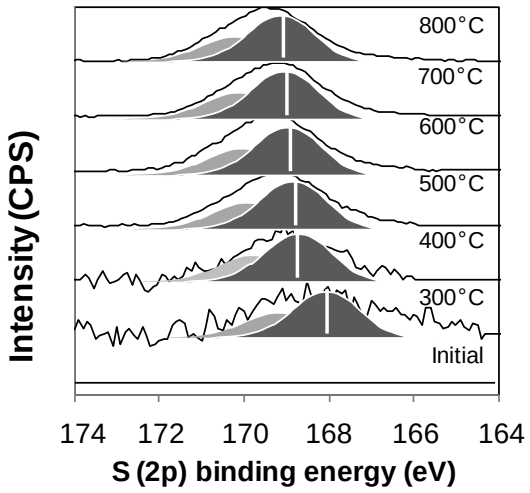

Fig. 5.11 *XPS spectra of S (2p) region and peak intensity (counts per second, CPS) for the 'TP-V' DCT glass exposed to the temperature range 300-800°C under 1% SO_2/He/air atmospheres. S (2p) spectra were fitted with a doublet pair of Gaussian-Lorentzian 30 lineshapes with FWHM of 1.8 eV. Spectra were scaled by factors of 70, 10, 10, 5, and 6% for the 400, 500, 600, 700 and 800°C spectra respectively to display them at the same scale as the spectra at 300°C.*

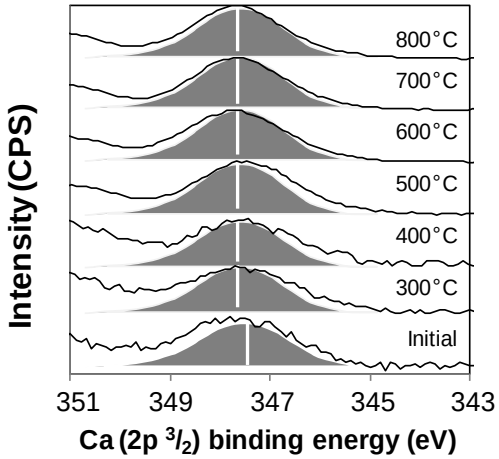

Fig. 5.12 *XPS spectra of Ca (2p $^3/_2$) region for all four 'TP-V' glasses exposed to 1% SO_2/He/Air for 60 minutes for the dacite glass exposed to the temperature range 300-800°C under 1% SO_2/He/air atmospheres. Ca (2p $^3/_2$) spectra were fitted with a Gaussian-Lorentzian 30 lineshapes with Doniach-Sunjic asymmetry parameters of 0.005,450 with FWHM of 2.4 eV. Spectra were scaled by factors of 90, 69, 56 and 68 for the 400, 500, 600, 700 and 800°C spectra respectively to display them at the same scale as the spectra at 300°C.*

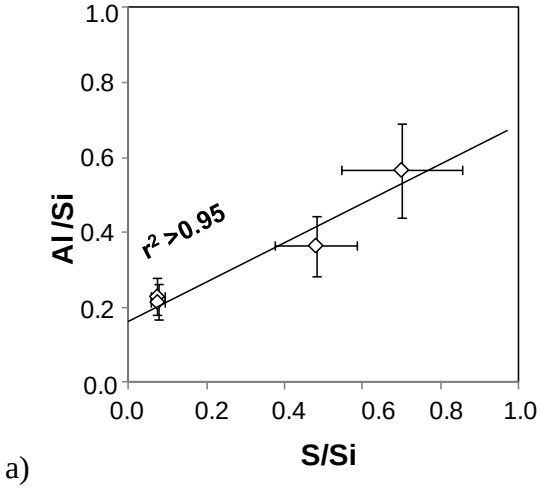

a)

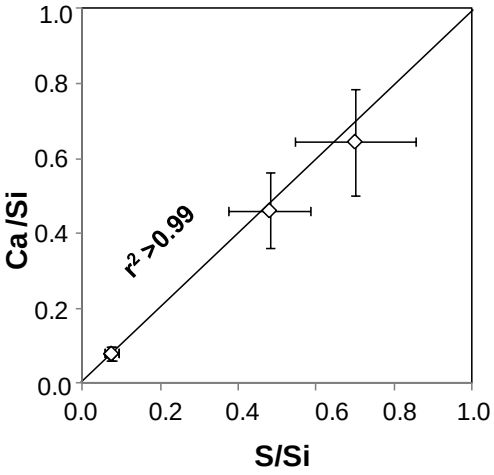

b)

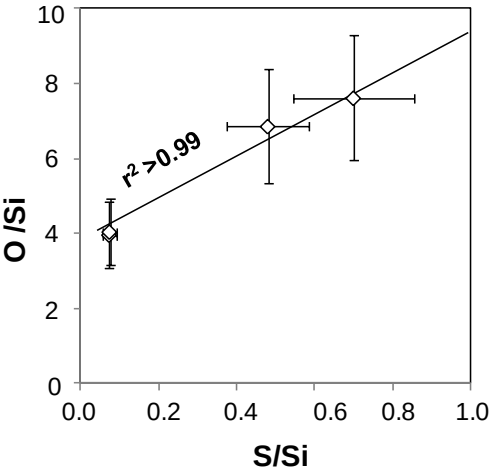

c)

Fig. 5.13 *Relationship between (a) S/Si and Al/Si, (b) S/Si and Ca/Si and (c) S/Si and O/Si and S/Si for the 'TP-V' glass series exposed to 1% SO_2/He/Air for 60 minutes at 800°C analysed by XPS (Table 5.15). Error bars of ±22% were applied and fitted trendlines were found to have r^2 values greater than 0.95.*

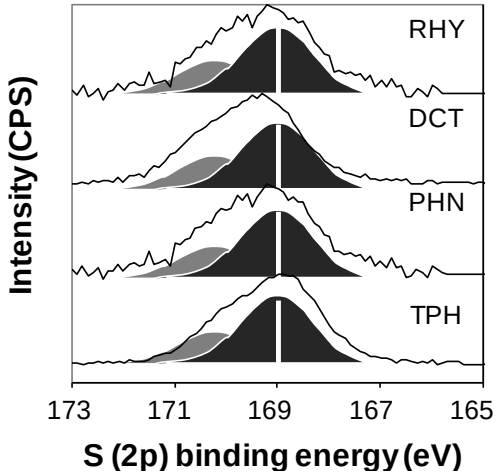

Fig. 5.14 *XPS spectra of S (2p) region for all four 'TP-V' glasses exposed to 1% SO_2/He/Air for 60 minutes at 800°C analysed by XPS (Table 5.15). S (2p) spectra were fitted with a doublet pair of Gaussian-Lorentzian 30 lineshapes with FWHM of 1.8 eV. Spectra were scaled by factors of 320, 100 and 524% for the PHN, DCT and RHY glasses to display them at the same scale as the spectra of the TPH glass.*

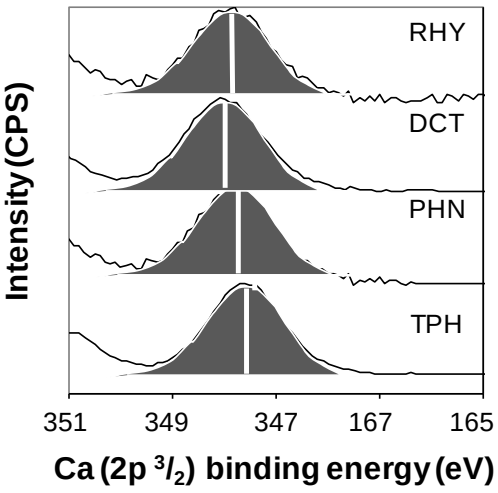

Fig. 5.15 *XPS spectra of Ca (2p $^3/_2$) region for all four 'TP-V' glasses exposed to 1% SO_2/He/Air for 60 minutes at 800°C analysed by XPS (Table 5.15). Ca (2p $^3/_2$) peaks are fitted with two components at high and low binding energies with Gaussian-Lorentzian 30 lineshapes with Doniach-Sunjic asymmetry parameters of 0.005,450 and FWHM of 2 eV. Spectra were scaled by factors of 420, 120 and 410% for the PHN, DCT and RHY glasses to display them at the same scale as the spectra of the TPH glass.*

5.4.6. TRANSMISSION ELECTRON MICROSCOPY

A sample of the 'TP-V' TPH glass exposed to 1% SO_2/He/Air for 60 mins at 800°C was taken for analysis at the TEM facilities at the Leeds Nanoscience and Nanotechnology Facility (LENNF). This technique was designed to study the near surface region of the glass particles after exposure to experimental conditions. Since the TPH glass was consistently the samples which showed greatest SO_2 chemisorption, the TPH glass after exposure to experimental atmospheres at 800°C was selected for this study.

To prepare the required thin section for TEM analysis required the use of a focused ion beam to create a lamella, or plate, with a thickness of approximately 100 nm. A region of a glass particle was sputtered with Pt, then using a Ga ion beam on a FEI Nova 200 Nanolab Field FEGSEM, the area surrounding the selected region was evaporated away. This essentially created a raised plateau less than a micron thick but several microns deep and several in length, which was then milled and polished with a lower energy beam to create the TEM thin section. After milling and polishing with the ion beam, sections with diameters of 20 µm × 5 µm × 0.1 µm were produced. These thin sections were analysed by scanning TEM on a Philips CM200 FEGTEM. Elemental maps at magnifications of 110,000× and 400,000× for all major elements and compositional analysis of selected points by EDX were obtained from these analyses. The thin section produced by this technique is displayed in Fig. 5.16.

a) 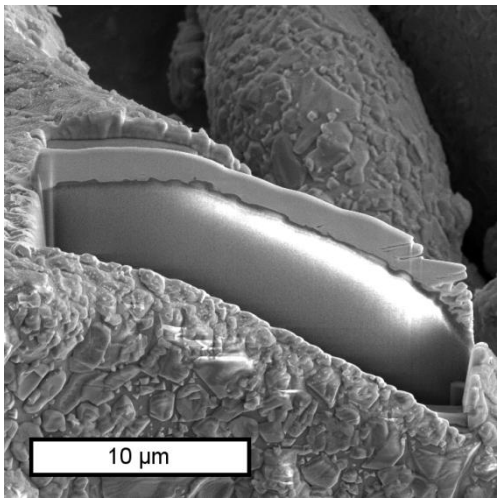

b) 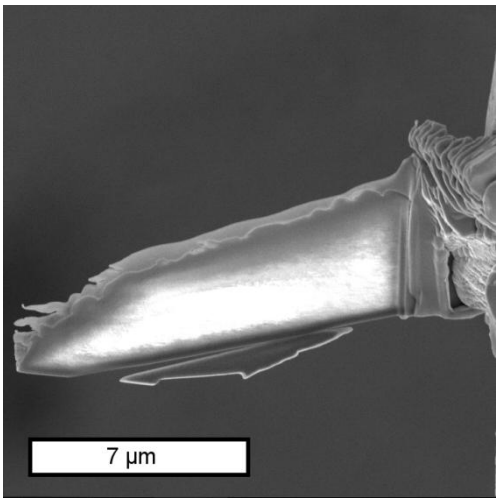

Fig. 5.16 *Thin sections produced by evaporation of material around a designated region of a particle of the TPH glass. The images are produced by FEGSEM, showing a) the lamella, the thin plate produced, still within the particle surface during FIB and b) the final thin section, after polishing and milling, embedded on the TEM sample holder.*

Analysis of the micrographs of the thin section produced by TEM indicated the presence of discrete crystalline phases at the surface and within the bulk glass itself (Fig. 5.17). Spot-EDX analysis was used to identify the compositions of selected surface and bulk crystalline phases (Fig. 5.18, Table 5.17), and STEM was used to identify the relative distributions of the elements Al, Ca, Fe, K, Mg, Na, Pt, S and Si within the glass and crystal phases in a selected region of the thin sections (Fig. 5.19).

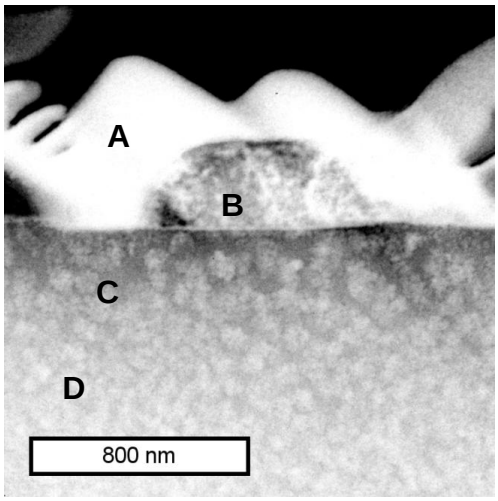

Fig. 5.17 *Contrast enhanced and colour inverted TEM micrograph of a region of the thin section shown in Fig. 5.16. The region marked A) indicates the Pt layer, and its interface with the pure black region above marks the interface between the thin section and the vacuum in the TEM. The speckled mass marked as B) is a surface crystalline deposit preserved within the Pt layer, the dull grey region beneath it (C) is the amorphous glass phase, whilst speckled regions within the glass indicate the presence of crystalline phases throughout the bulk (D).*

Spot-EDX analysis of the surface crystal phases, subsurface crystal phases and the amorphous glass component were conducted (Fig. 5.18, Table 5.17). Comparing element/Si ratios, it was possible to determine that the surface phases (1) were composed primarily of Ca and S (Table 5.17). A crystal phase immediately below the Ca-S surface deposit (3) was identified to be a Ca, Mg, Fe Al and Si bearing phase. The glass phase surrounding the crystalline phase is entirely depleted in Ca, Mg and Fe, and partially depleted in Al, which indicates that the formation of crystallites proceeded via the extraction of the relevant cations from the surrounding glass matrix.

Elemental maps of the area previously shown in Fig. 5.17 are shown in Fig. 5.19. The notable features of these data are that the surface deposit contains only Ca and S, of the major elements studied (Fig. 5.19 c, i). Beneath the Ca-S bearing crystal phase, regions depleted in Ca, Mg and Fe were identified (Fig. 5.19 c,d,f). Ca and Mg depleted

regions were semi-circular and oblate, with lateral radii of ~250 nm and vertical radii of ~150 nm, located beneath the edges of the Ca-S crystal phases. The Fe depleted region is ~100 nm deep, and extends along the interface between the glass and $CaSO_4$ crystal. Beneath these depleted regions, Fe-bearing crystal phases are identified. The Fe-crystal phases may also contain the other major elements, as they are not accompanied by concurrent areas of elemental depletions in the other elements studied. The Si region is constant in intensity, which indicates that the observed phenomena are not the result of sample thinning, and are rather a genuine feature of the region of the post-experiment glass studied.

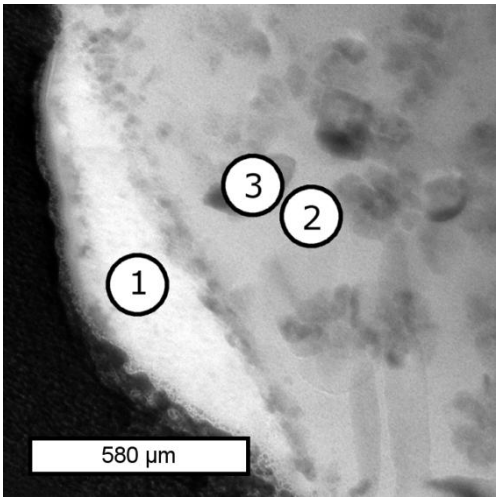

Fig. 5.18 *TEM micrograph illustrating positions of spot-EDX analysis on the TPH thin section. The black area indicates the Pt-layer deposited at the top of the thin section and corresponds to the particle surface. Points 1 and 3 are crystal phases and point 2 is an amorphous phase.*

Table 5.17 *Element/Si ratios from spot-EDX analysis of points illustrated in Fig. 5.18.*

Point	Element / Si ratios					
	Na	**Mg**	**Al**	**S**	**Ca**	**Fe**
1	0.65	n/d	0.28	6.58	8.82	0.56
2	n/d	n/d	0.19	n/d	0.03	n/d
3	n/d	0.18	0.19	n/d	0.19	0.16
Bulk	0.14	0.21	0.42	n/d	0.26	0.22

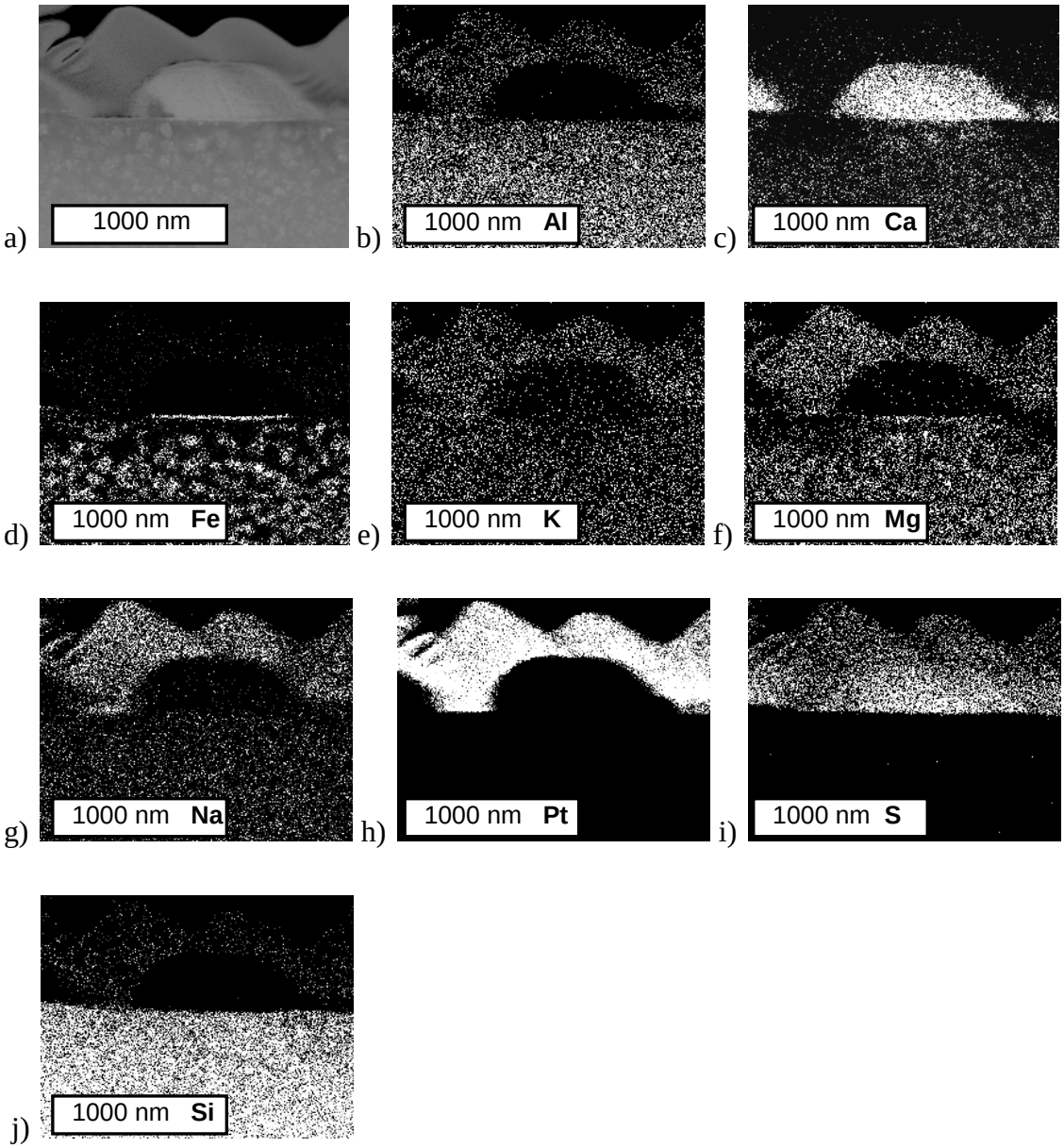

Fig. 5.19 *Darkfield micrograph (a), and elemental maps of b) Al, c) Ca, d) Fe, e) K, f) Mg, g) Na, h) Pt, i) S and j) Si for a region of the thin section of the TPH glass after exposure to 1% SO_2/He/Air at 800°C for 60 minutes, produced by STEM.*

5.5. RESULTS OF 'TI-V' EXPERIMENT

The glass powder samples exposed to 1% SO_2/He/Air atmospheres at 300°C, 500°C and 800°C over a range of exposure times ('TI-V' experiments) were analysed by bulk and surface sensitive techniques, and these data are presented below.

5.5.1. LEACHATE COMPOSITION

Analysis of solutions generated by the leaching of post-experiment glasses was conducted via the same protocols as the 'temperature-variable' experiment, but based on the trace concentrations of Fe and Al in the latter experiment, analysis of Fe and Al in these data was omitted. Leachate data for the 800°C time series are summarised in Fig. 5.20 and Table A12 to Table A16, leachate data for the 500°C experiments are summarised in Fig. 5.21 and Table A17 to Table A21, and leachate data for 300°C experiments are summarised in Fig. 5.22 and Table A22 to Table A26.

In the study of the leachate solutions from 'TI-V' 800°C experiments over the range of time exposures, it was demonstrated in Fig. 5.20 that Ca and S were the dominant ions in the leachate solution, even at exposure times of 1 minute. Concentrations of the other major alkali and alkaline earth cations remain low; with the exception of a single data point at 700°C in the TPH glass, being 40 µmol m^{-2} , concentrations of K and Mg were both consistently below the 7 µmol m^{-2} which was estimated to be attributable to the leaching and dissolution of the glass surface. Concentrations of Na were greater than the estimated contribution of glass dissolution and leaching, but were not found to be a significant contributor to the leachate solution. The trend in S concentrations in 'TI-V' leachate data at 800°C, as in the 'TP-V' experiments, has the TPH and RHY glasses as the upper and lower endmembers, and retains the PHN and DCT glasses as the intermediaries of the system which cannot be easily distinguished from each other (Fig. 5.23).

In Fig. 5.21, where 1% SO_2/He/Air experiments were conducted at 500°C for exposure times of up to 60 minutes, the trend of increased Ca with increased S observed at 800°C was not observed consistently for all glasses, as in the TPH glass, Na increased with increasing S. In the PHN and DCT glasses, Ca concentrations in the leachate solutions remained the dominant cation and increased with increasing S. In comparing the three glasses, the TPH maintains the highest concentration of S in leachate solutions

relative to the PHN and DCT, being on average increased by a factor of 2.6±1 compared to the PHN and 4.0±1.4 higher than the DCT glass (Fig. 5.24).

In experiments at 300°C (Fig. 5.22), all cation concentrations with the exception of Na in the TPH and PHN glasses were below the 7 µmol m^{-2} upper limit attributed to the contribution of glass dissolution and leaching. The S in the leachate solutions only showed a consistent trend for the tephrite glass, whilst the others remained essentially constant at concentrations less than 12 µmol m^{-2} (Fig. 5.25).

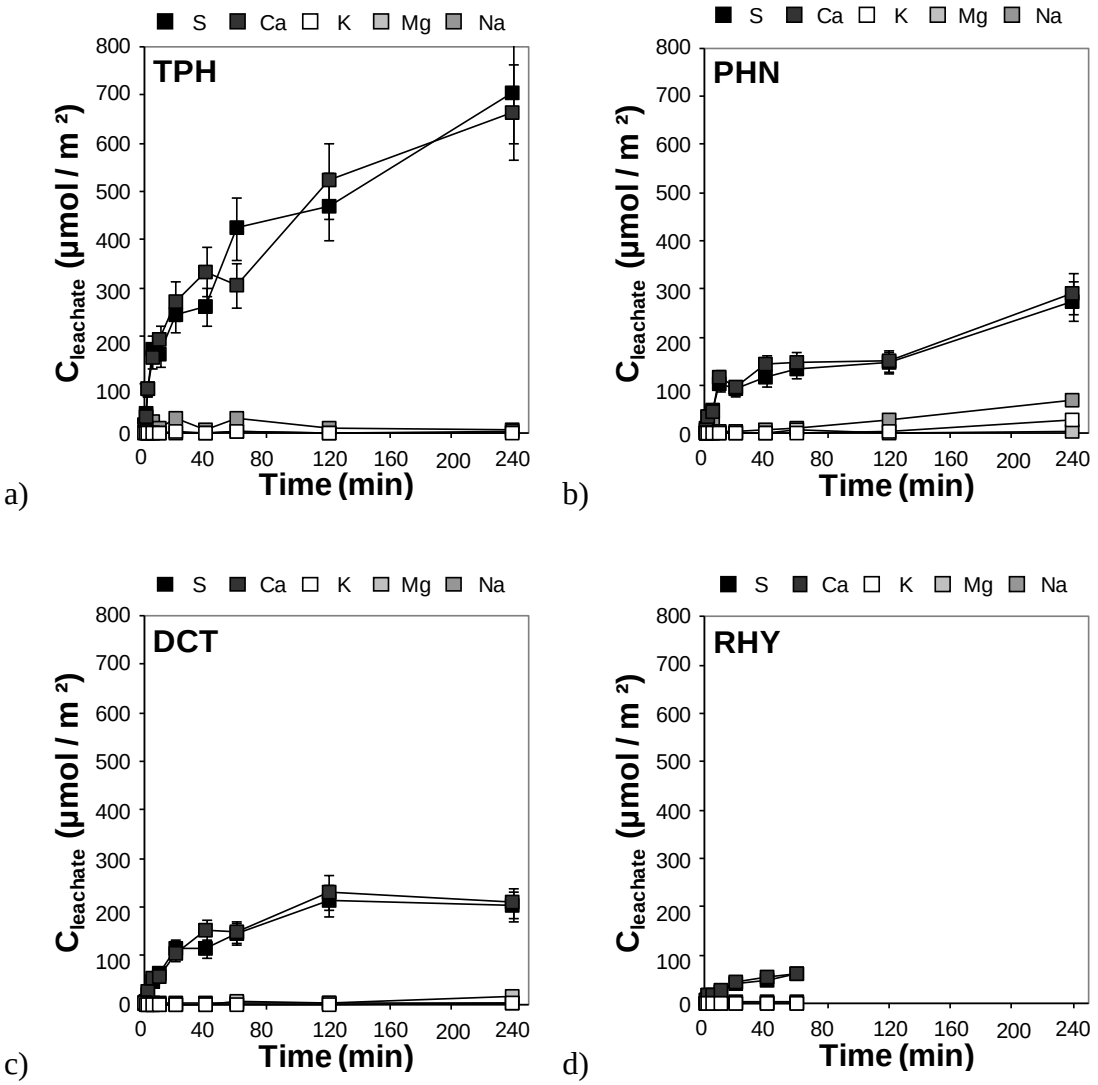

Fig. 5.20 *$C_{leachate}$ for major cations and S for 'TI-V' glasses treated at 800°C for exposure times of 0.5-240 mins under 1% SO_2/He/Air, normalised to sample a_s (Table 5.6), as per data in Table A12 to Table A16. Experimental error is ±15%.*

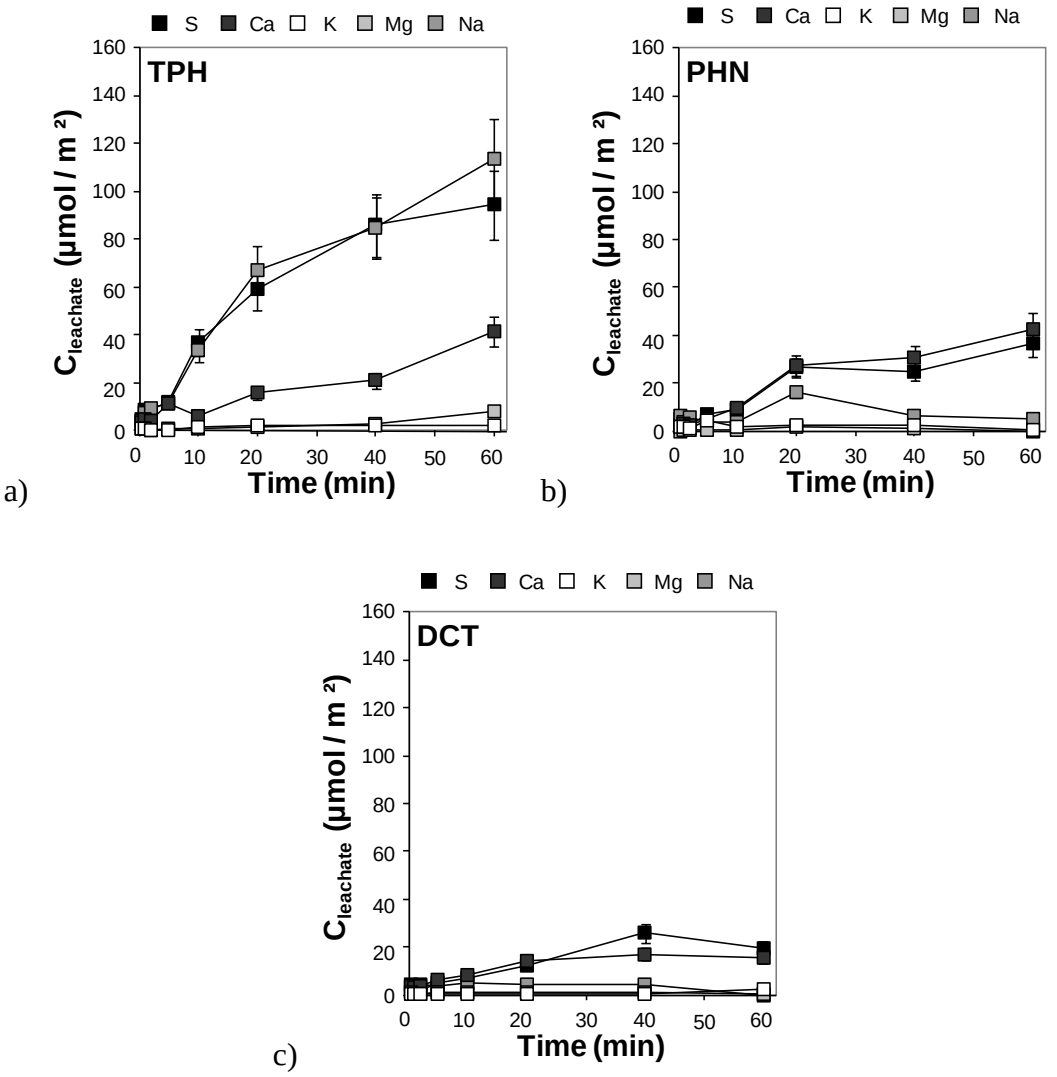

Fig. 5.21 *$C_{leachate}$ for major cations and S for 'TI-V' glasses treated at 500°C for exposure times of 0.5-60 mins under 1% SO_2/He/Air, normalised to sample a_s (Table 5.6), from data in Table A17 to Table A21. Experimental error is ±15%.*

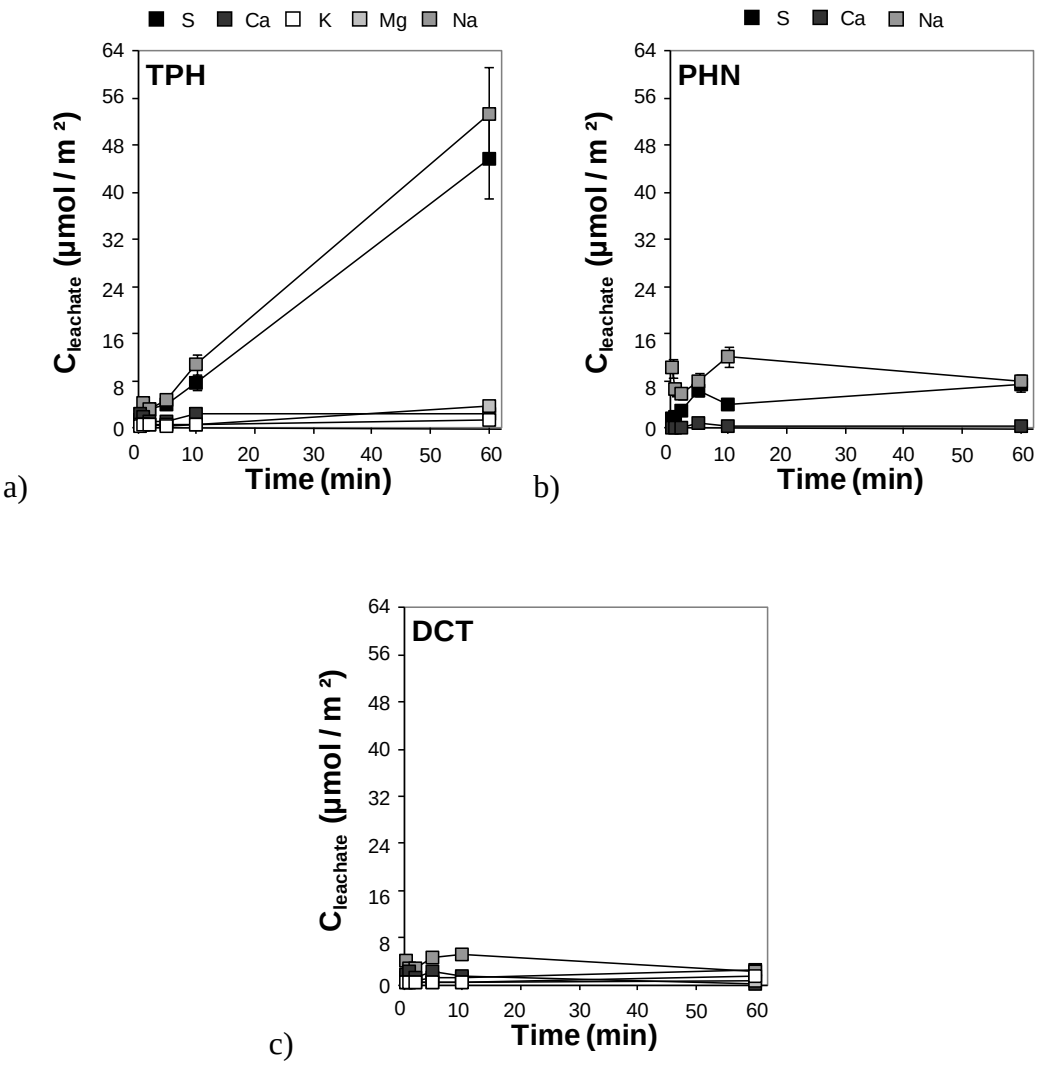

Fig. 5.22 *$C_{leachate}$ for major cations and S for 'TI-V' glasses treated at 300°C for exposure times of 0.5, 1,2 5, 10 and 60 mins under 1% SO_2/He/Air, normalised to sample a_s (Table 5.6), from data in Table A22Table A26 to Table A26. Error bars of ±15% represent the experimental error.*

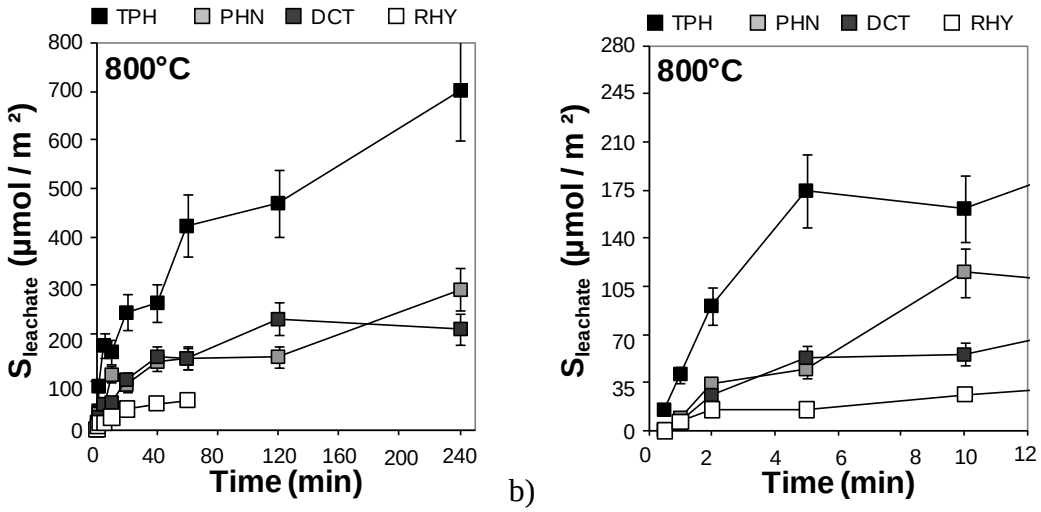

Fig. 5.23 *$S_{leachate}$ for 'TI-V' glasses treated at 800°C for exposure times of 0.5-240 minutes, normalised to sample a_s (Table 5.6), from Table A12 to Table A16. The full data are shown in a), and a higher resolution view of the short exposure time experiments are shown in b). Experimental error is ±15%.*

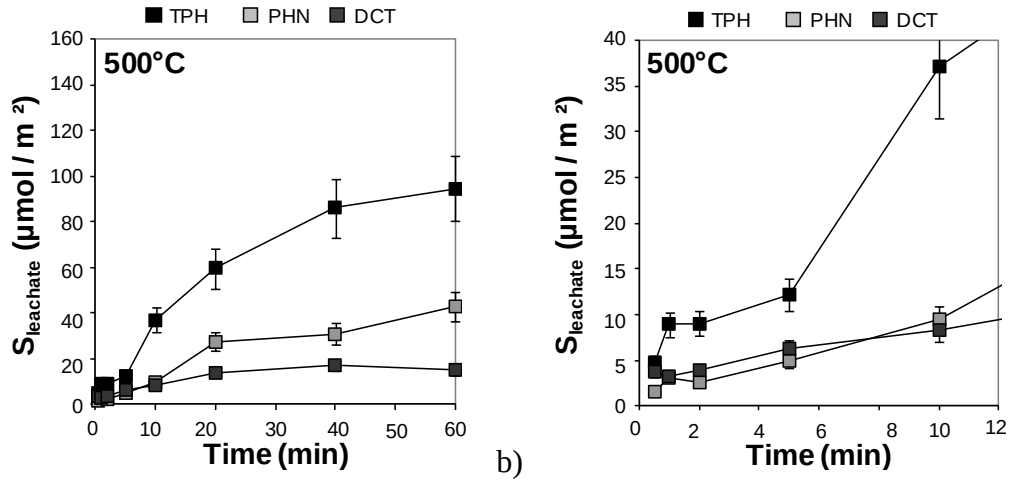

Fig. 5.24 *$S_{leachate}$ for 'TI-V' glasses treated at 500°C for exposure times of 0.5-60 minutes, normalised to sample a_s (Table 5.6), from data in Table A17 to Table A21. The full data are shown in a), and a higher resolution view of the short exposure time experiments are shown in b). Experimental error is ±15%.*

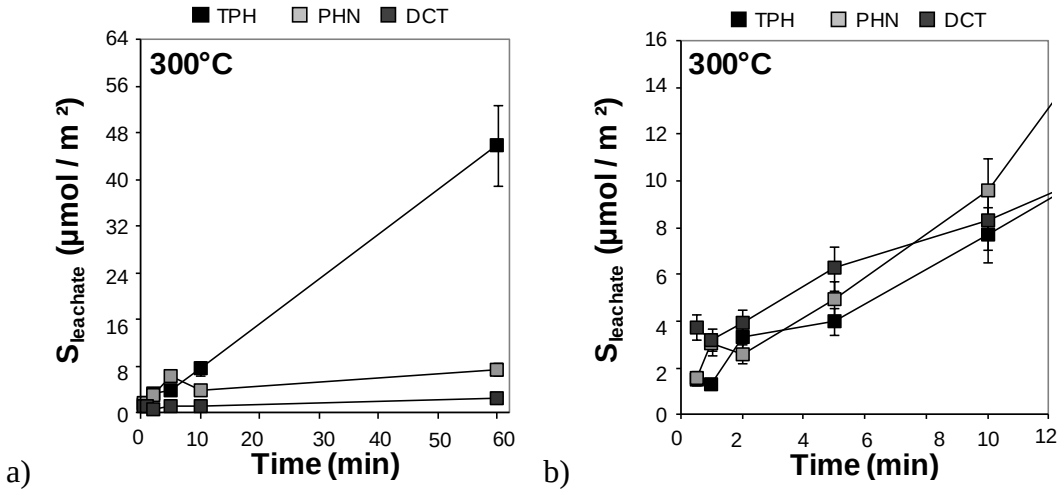

Fig. 5.25 *$S_{leachate}$ for 'TI-V' glasses treated at 300°C for exposure times of 0.5, 1,2 5, 10 and 60 mins minutes, normalised to sample a_s (Table 5.6), from data in Table A22Table A26 to Table A26. The full data are shown in a), and a higher resolution view of the short exposure time experiments are shown in b). Experimental error is ±15%.*

5.5.2. MINERALOGY

Only one sample was analysed by XRD, the 'TI-V' TPH glass exposed to 1% SO_2/He/Air for 5 minutes at 800°C (Fig. 5.26). The TPH sample was analysed in order to confirm the continued presence of anhydrite ($CaSO_4$) in the post-experiment glasses as was observed in the 'temperature-variable' experiments. No XRD analysis was performed on samples exposed to 300°C or 500°C, as there was no crystalline identified in the 'temperature-variable' experiments in the glasses exposed to 1% SO_2/He/Air for 60 minutes, so it was considered unlikely that any detectable crystalline phases would be found at lower exposure times.

The TPH glass analysed by XRD showed the main anhydrite ($CaSO_4$) diffraction peak at 25° 2θ, and so the continued presence of this crystalline phase was inferred. The presence of the crystal phases identified in 'TP-V' experiments on the TPH glass at 800°C for 60 minutes were also observed in the TPH glass exposed for 5 minutes at the same temperature.

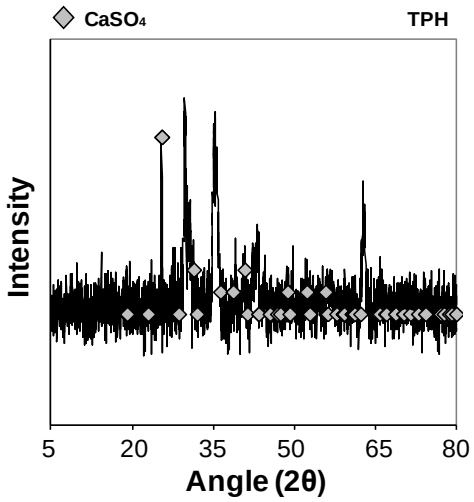

Fig. 5.26 *Baseline subtracted XRD pattern for the 'TI-V' TPH glass exposed to 1% SO_2/He/Air for 5 minutes at 800°C. The filled diamonds indicate the diffraction pattern for $CaSO_4$ (anhydrite) (Wasastjerna 1927).*

5.5.3. SCANNING ELECTRON MICROSCOPY

SEM and spot-EDX were conducted on the 'TI-V' PHN glass exposed to 1% SO_2/He/Air for 2 minutes (Fig. 5.27). The PHN glass rather than the TPH glass, was selected, as in Fig. 5.7 and Fig. 5.8, surface deposits with Ca/Si and S/Si ratios consistent with $CaSO_4$ were only discernible in the PHN glass. Although SEM did determine the presence of surface deposits on the sample surface even after only a two minute exposure, spot-EDX was not able to determine a difference between Ca/Si ratios in the glass surface and in the surface deposits.

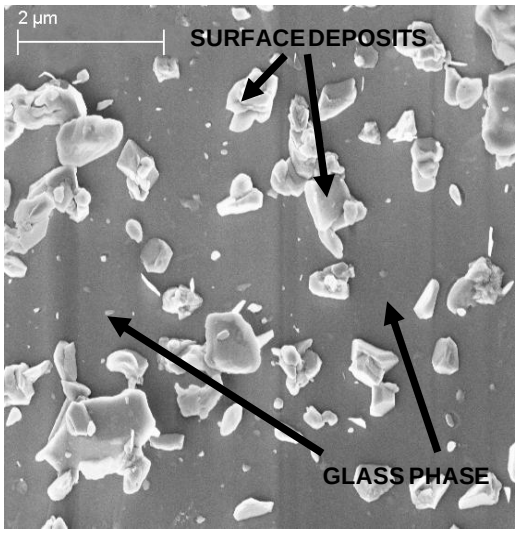

Fig. 5.27 *SEM image of 'TI-V' PHN glass exposed to 1% SO_2/He/Air at 800°C for 2 minutes, showing surface deposits on the amorphous glass phase, indicated by the arrows.*

5.5.4. X-RAY PHOTOELECTRON SPECTROSCOPY

XPS was conducted on the 'TI-V' TPH glass samples exposed to 1% SO_2/He/Air at 500°C and 800°C for time durations of 1, 10, 20 and 60 minutes. The TPH glass was analysed partially in order to determine the changes in relative surface chemical composition, but also to explore the possible role of Na in SO_2 chemisorption experiments conducted at 500°C, as leachate analysis indicated that Na and S concentrations showed a similar trend.

5.5.4.1. TPH GLASS EXPOSED TO SO_2 AT 800°C

The relative surface chemical composition of the TPH glass at 800°C are given in Table 5.18 and are displayed in Fig. 5.28. The element/Si ratios were found to show a range of behaviours, with Al/Si initially undergoing a decrease relative to the initial surface composition by a factor of three, but increasing back to that of the initial surface with increasing exposure time. Both Ca/Si and O/Si were showed a consistent increase by a factor of 1.3-4 their initial surface ratios up to the 20 minute time exposure and plateaued between 20 minutes and 60 minutes. Na/Si followed a similar trend, increasing by a factor of 4 relative to the initial surface ratios, but decreased by a factor of 2 relative to the initial Na/Si ratio in 60 minute exposure time experiments. The behaviour of K/Si was more variable, but was consistently of similar size to that of the initial surface composition. It may be possible that some of the above trends, particularly with respect to Na, may be in part due to volatilisation of metals from the glass surfaces, though this cannot be verified at this time.

Table 5.18 *Relative surface composition (atm. %) of the TPH glass exposed to 1% SO_2/He/Air atmospheres at 800°C for exposure times of the 1, 10, 20 and 60 minutes compared to those of the pre-experiment initial surface, as determined by XPS.*

Region	Surface composition (atm. %)				
	Initial	1 min	10 min	20 min	60 min
Al (2p)	7.3	2.0	2.0	1.8	5.2
Ca(2p)	1.9	4.8	5.8	6.5	5.7
Fe (2p)	1.3	3.9	2.7	2.4	0.9
K(2p)	0.4	0.2	0.3	0.2	0.3
Mg (2p)	0.6	1.8	0.9	0.7	0.0
Na (1s)	1.9	4.1	5.4	4.6	3.4
O(1s)	72.9	70.7	69.9	69.7	69.9
S (2p)	0.1	1.5	4.1	5.1	6.2
Si (2p)	11.2	11.1	8.8	9.1	8.3

5.5.4.2. TPH GLASS EXPOSED TO SO_2 AT 500°C

The relative surface composition data of the 'TI-V' TPH glass exposed to 1% SO_2/He/Air at 500°C over 1, 10, 20 and 60 minutes are presented in Table 5.19 and displayed in Fig. 5.34. The changes observed in the sample surface with increasing exposure time were found to be variable; Al/Si, Fe/Si and O/Si all showed an initial decreases by as much as half of the ratios of the pre-experiment surfaces. The behavior of Ca/Si and K/Si were highly variable as exposure time increased and showed no discernable trend. Na showed an initial increase up to the 20 minute exposure time experiment, being increased by a factor of 3 relative to the Na/Si ratio of the pre-experiment TPH surface, but decreased slightly in the 60 minute exposure time experiment. The S/Si ratios of the TPH glass followed a similar trend, increasing up to an S/Si ratio of 0.4 in the 20 minute experiments, but decreasing in the 60 minute experiment (Fig. 5.36), and Na/Si was the only element/Si ratio to show any correlation with S/Si (Fig. 5.35).

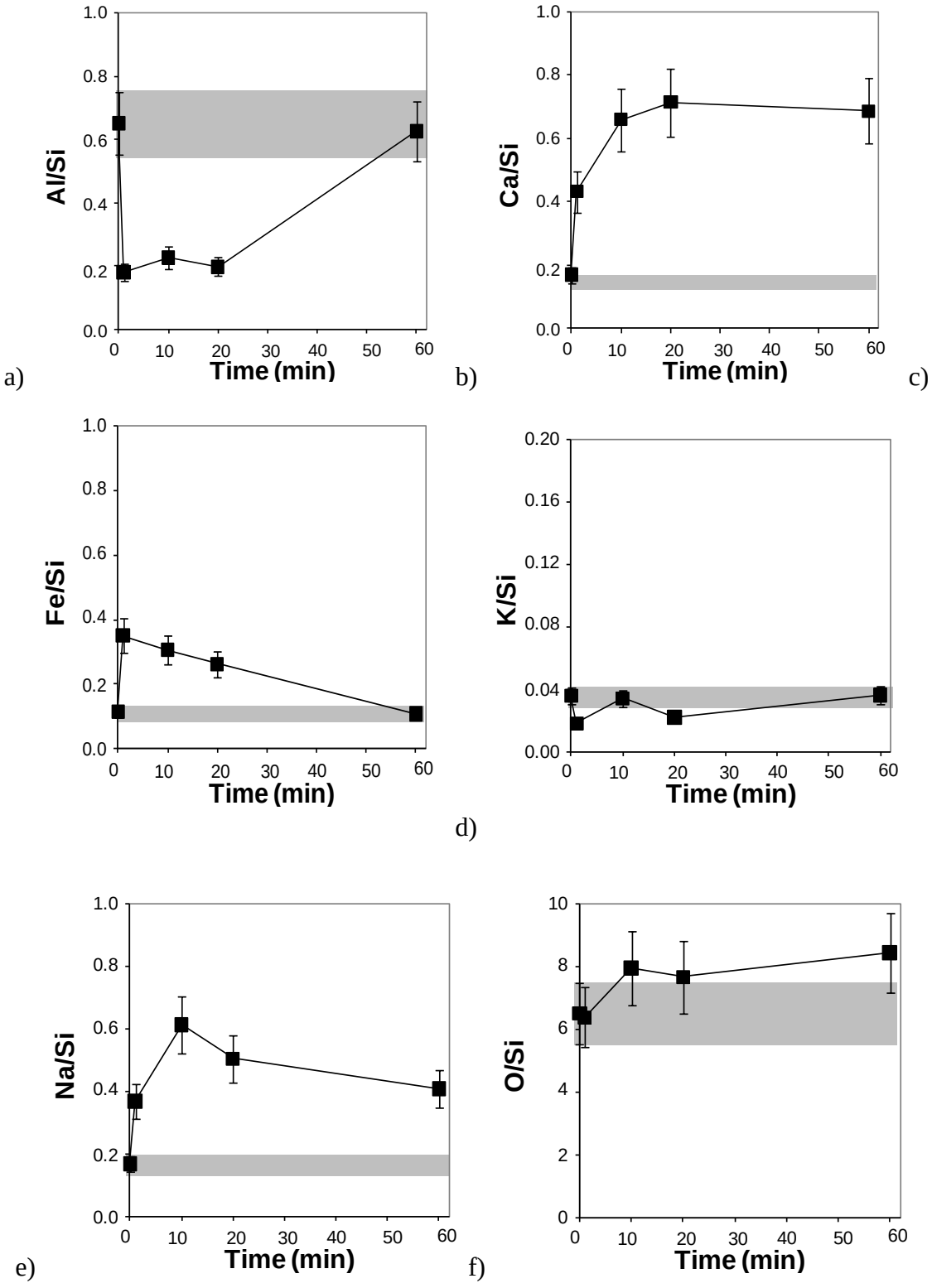

Fig. 5.28 *Element/Si ratios for 'TI-V' TPH glass surfaces after exposure to 1% SO_2/He/Air at 800°C for 1, 10, 20 and 60 minutes respectively, derived from XPS data (Table 5.18). Filled grey bands indicate the initial element/Si ratio of the sample surface (Table 5.7). Analytical and experiment error is ±22%.*

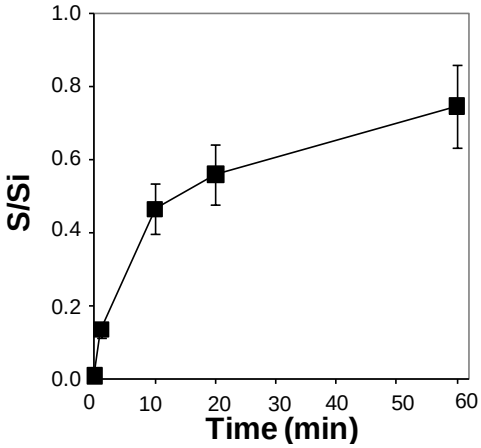

Fig. 5.29 *S/Si ratios for the surfaces of the 'TI-V' TPH glass exposed to 1% SO_2/He/Air at 800°C for 1, 10, 20 and 60 minutes, from XPS data (Table 5.18). Experimental and analytical error is ±22%.*

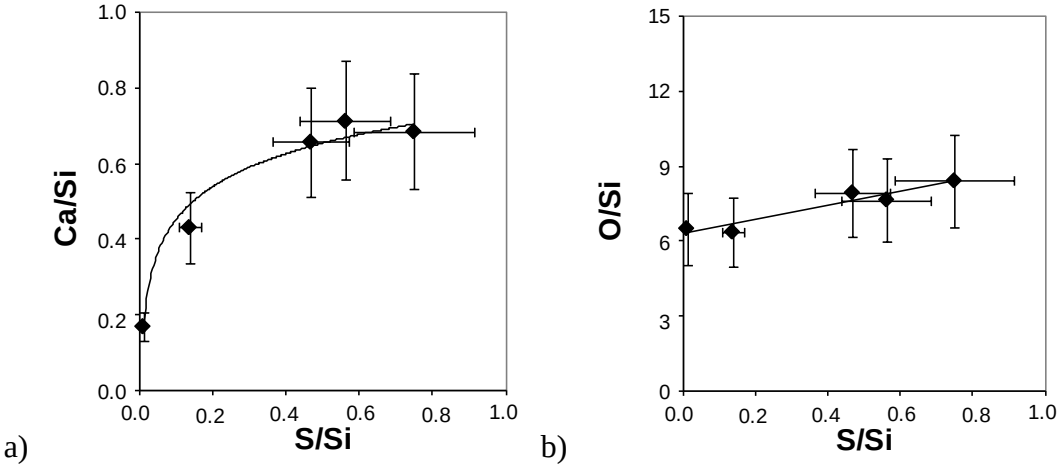

Fig. 5.30 *Relationships between (a) Ca/Si and S/Si (b) O/Si and S/Si for the surfaces of the 'TI-V' TPH glass exposed to 1% SO_2/He/Air at 800°C for 1, 10, 20 and 60 minutes, from XPS data (Table 5.18). Experimental and analytical error is ±22%.*

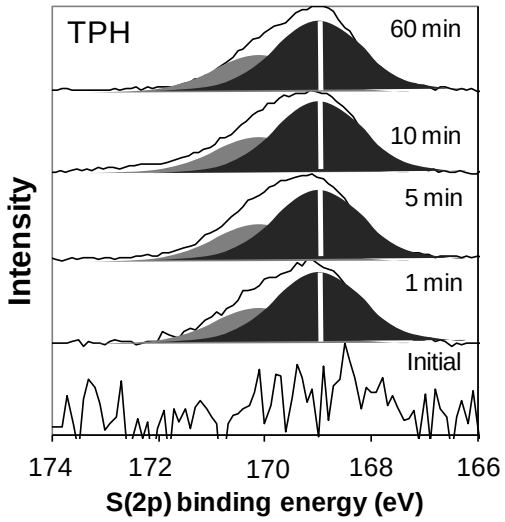

Fig. 5.31 *XPS spectra for the S (2p) spectra for the 'TI-V' TPH glass exposed to 1% SO2/He/Air for 1, 10, 20 and 60 minutes at 800°C. S (2p) spectra were fitted with a doublet pair of Gaussian-Lorentzian 30 lineshapes with FWHM of 1.7 eV. Spectra were scaled by factors of 13, 4, 3 and 5% for the 1, 10, 20 and 60 minute exposure time experiments in order to display them at the same scale as the initial surface spectra.*

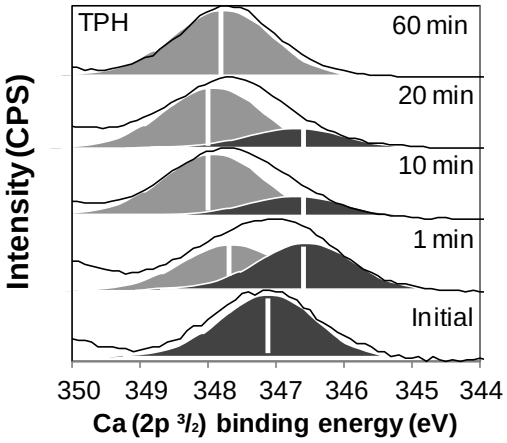

Fig. 5.32 *XPS spectra for the Ca (2p $^{3}/_{2}$) spectra for the 'TI-V' TPH glass exposed to 1% SO_2/He/Air for 1, 10, 20 and 60 minutes at 800°C. Ca (2p $^{3}/_{2}$) spectra were fitted with two Gaussian-Lorentzian 30 lineshapes with Doniach-Sunjic asymmetry parameters of 0.005,450 and FWHM of 1.6 eV. Spectra were scaled by factors of 32, 20, 19 and 35% for the 1, 10, 20 and 60 minute exposure time experiments in order to display them at the same scale as the initial surface spectra.*

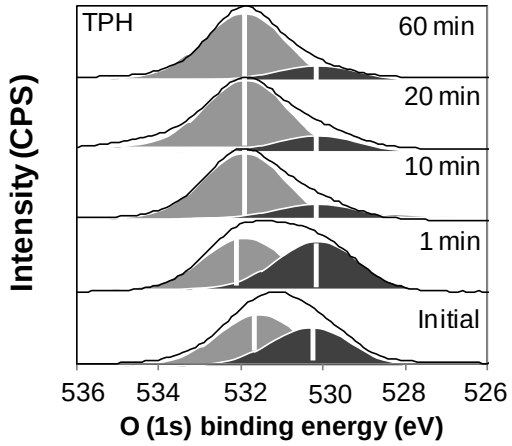

Fig. 5.33 *XPS spectra for the O (1s) spectra for the 'TI-V' TPH glass exposed to 1% SO_2/He/Air for 1, 10, 20 and 60 minutes at 800°C. O (1s) spectra are fitted with two Gaussian-Lorentzian 30 lineshapes with FWHM of 2.2 eV. Spectra were scaled by factors of 85, 55, 59 and 98% for the 1, 10, 20 and 60 minute exposure time experiments in order to display them at the same scale as the initial surface spectra.*

Table 5.19 *Relative surface composition (atm. %) of the 'TI-V' TPH glass exposed to 1% SO_2/He/Air atmospheres at 500°C for exposure times of 1, 10, 20 and 60 minutes, compared to those of the pre-experiment initial surface, as determined by XPS.*

	XPS surface composition (atm. %)				
	Initial	**1 min**	**10 min**	**20 min**	**60 min**
Al (2p)	7.2	7.7	6.9	5.6	6.3
Ca(2p)	1.9	3.6	6.6	2.5	6.3
Fe (2p)	2.8	3.3	2.7	1.9	2.5
K (2p)	0.4	0.8	0.3	1.5	0.5
Mg (2p)	0.6	1.1	1.6	0.3	2.7
Na (1s)	1.6	5.3	5.3	8.1	4.7
O (1s)	74.4	59.4	59.8	59.2	61.9
S (2p)	0.2	1.0	1.8	5.7	2.2
Si (2p)	11.0	17.7	15.1	15.1	12.9

Na/Si was the only element/Si ratio which was found to correlate with the S/Si ratios in the TPH (Fig. 5.35). Since the Na/Si ratios were the only element/Si ratios found to correlate to S/Si, the Na (1s) and S (2p) spectra were analysed and interpreted. The X-ray photoelectron spectra for the S (2p) and Na (2p) regions were therefore interpreted via peak fitting in Fig. 5.37. The S ($2p\ ^{3}/_{2}$) peak could be described by two components with binding energies of 167.8 eV and 168.9 eV, consistent with sulphite and sulphate species respectively, at all exposure times at 500°C, though the contribution of the lower binding energy component was observed to decrease with increasing exposure time. The Na (1s) peak could be described by two components with binding energies of approximately 1072 and1070 eV, although the higher binding energy component was only observed in the short time duration experiments and not in the 60 minute exposure.

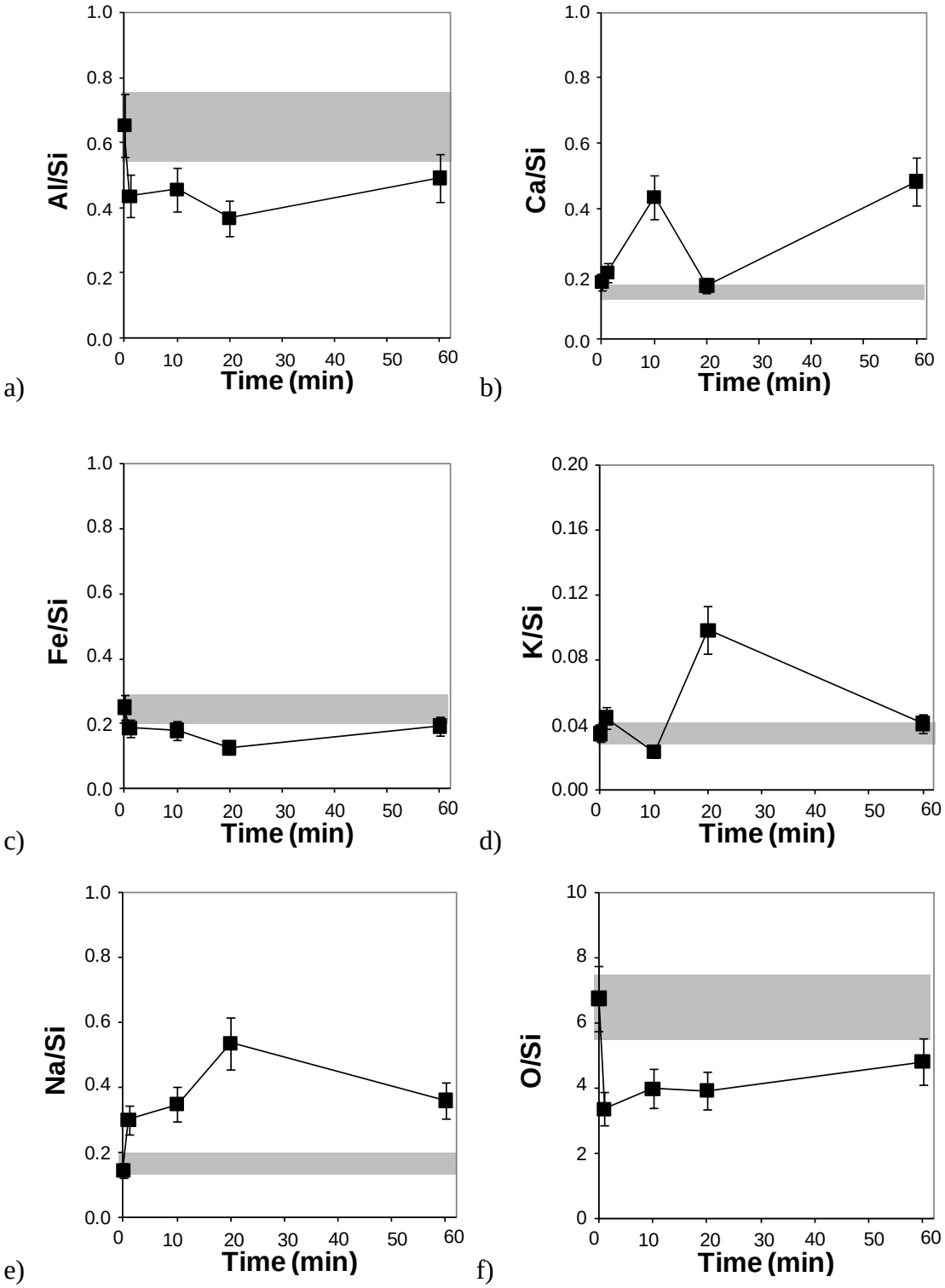

Fig. 5.34 *Element/Si ratios for 'TI-V' TPH glass surfaces after exposure to 1% SO_2/He/Air at 500°C for 1, 10, 20 and 60 minutes respectively, derived from XPS data (Table 5.19). Filled grey bands indicate the initial element/Si ratio of the sample surface (Table 5.7). Analytical and experiment error is ±22%.*

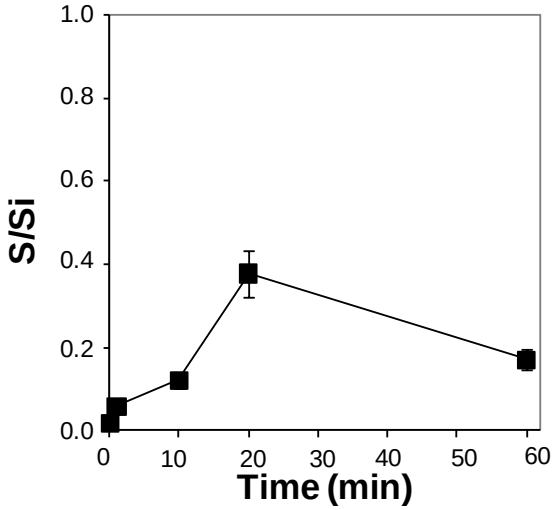

Fig. 5.35 *S/Si ratios for the surface of the 'TI-V' TPH glass exposed to 1% SO_2/He/Air at 500°C for time durations of 1, 10, 20 and 60 minutes respectively, derived from XPS data (Table 5.19). Experimental and analytical error is ±22%.*

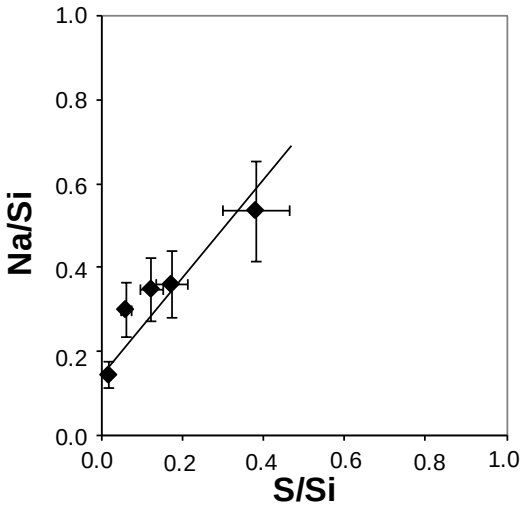

Fig. 5.36 *Comparison of Na/Si and S/Si ratios for the surface of the 'TI-V' TPH glass exposed to 500°C exposed to 1% SO_2/He/Air at 500°C for time durations of 1, 10, 20 and 60 minutes respectively, derived from XPS data (Table 5.19). Experimental and analytical error is ±22%.*

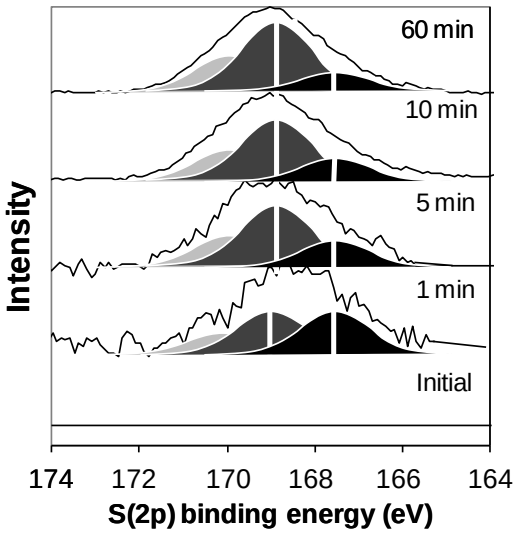

Fig. 5.37 *XPS S (2p) spectra for the 'TI-V' TPH glass exposed to 1% SO_2/He/Air for exposure times of 1, 10, 20 and 60 minutes at 500°C. S (2p) spectra were fitted with a doublet pair of Gaussian-Lorentzian 30 lineshapes with FWHM of 2 eV. The spectra were scaled by factors of 26, 27 and 70% for the 5, 10 and 60 minute exposure time experiments to display them on the same scale as the spectra of the 1 minute exposure time experiment.*

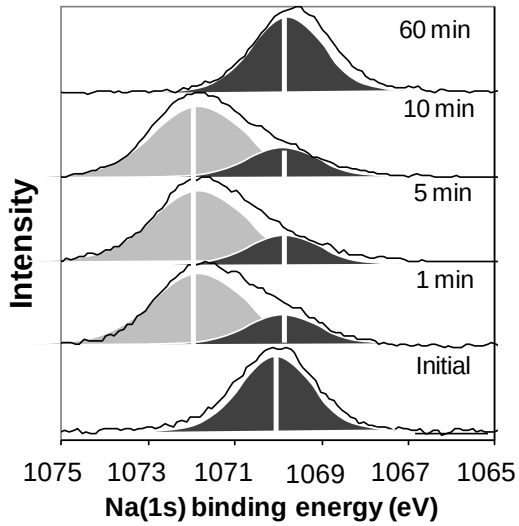

Fig. 5.38 *XPS Na (1s) spectra for the 'TI-V' TPH glass exposed to 1% SO_2/He/Air for exposure times of 1, 10, 20 and 60 minutes at 500°C. S (2p) spectra were fitted with a doublet pair of Gaussian-Lorentzian 30 lineshapes with FWHM of 2 eV. The spectra were scaled by factors of 102, 90, 60 and 62% for the 1, 5, 10 and 60 minute exposure time experiments to display them on the same scale as the spectra of the initial pre-experiment surface.*

5.6. RESULTS OF 'ATMOSPHERE-VARIABLE' EXPERIMENTS

The 'AT-V' data from the four glasses exposed to 800°C temperatures for 60 minutes in the presence of He, air, SO_2/He/Air and SO_2/He/Air with a 60 minute He-only pre-treatment are presented below.

5.6.1. LEACHATE ANALYSIS

The leachate solutions from the 'AT-V' experiments were analysed for all elements other than Fe and Al. Under He-only and air-only atmospheres (Table 5.20, 0), concentrations of all elements were less than 10 µmol m^{-2}, therefore being primarily attributable to the leaching and dissolution of the glass surface itself rather than any surface deposits formed. In leachate solutions from the He-only and air-only atmospheres, it was observed that a small amount of S was extracted from the glasses, but this was consistently in concentrations lower than 10 µmol m^{-2}.

Table 5.20 *$C_{leachate}$ of 'AT-V' glasses treated under He-only atmospheres for 60 minutes at 800°C and normalised to sample* a_s *(Table 5.6).*

Element	$C_{leachate}$. (µmol m^{-2})			
	TPH	**PHN**	**DCT**	**RHY**
S	0.8	0.0	0.2	3.9
Al	*n.a*	*n.a*	*n.a*	*n.a*
Ca	0.0	0.7	0.1	0.1
Fe	*n.a*	*n.a*	*n.a*	*n.a*
K	1.7	1.8	0.2	0.4
Mg	0.0	0.5	0.0	1.9
Na	3.5	0.9	0.2	0.4

Table 5.21 *$C_{leachate}$ of 'AT-V' glasses treated under air-only atmospheres for 60 minutes at 800°C and normalised to sample* a_s *(Table 5.6).*

Element	$C_{leachate}$ (µmol m^{-2})			
	TPH	**PHN**	**DCT**	**RHY**
S	1.8	0.0	7.9	4.3
Al	*n.a*	*n.a*	*n.a*	*n.a*
Ca	1.4	3.4	1.2	1.9
Fe	*n.a*	*n.a*	*n.a*	*n.a*
K	1.4	0.4	0.8	0.3
Mg	0	0.1	0.1	0
Na	1.9	1.8	2.8	4.0

The leachate compositions from glass samples exposed to 1% SO_2/He/Air atmospheres (Table 5.22) were discussed in section 5.4. In the untreated and pre-treated 1% SO_2/He/Air experiments, the TPH and RHY had consistently the highest and lowest soluble S concentrations in leachate solutions, but whilst in the 1% SO_2/He/Air experiments, the phonolite glass released greater concentrations of soluble S than the dacite glass, in the pre-treated experiments, this trend was reversed. In both data sets, Ca was observed to be the dominant cation in the leachate solutions, and in both systems, Ca and S were observed to show a linear relationship with each other (Fig. 5.39). Comparison of the two data sets, however, illustrated that the S content of the leachate solutions relative to the Ca concentration in solution was markedly reduced in the pre-treatment experiment compared to the 1% SO_2/He/Air experiments.

Table 5.22 *$C_{leachate}$ of 'AT-V' glasses treated under 1% SO_2/He/Air atmosphere for 60 minutes at 800°C and normalised to sample* a_s *(Table 5.6).*

Element	$C_{leachate}$ (µmol m^{-2})			
	TPH	**PHN**	**DCT**	**RHY**
S	**501.5**	**153.6**	**135.4**	**60.9**
Al	*n.a*	*n.a*	*n.a*	*n.a*
Ca	**366.2**	**188.8**	**122.0**	**61.0**
Fe	*n.a*	*n.a*	*n.a*	*n.a*
K	**1.6**	**0.0**	**0.3**	**0.4**
Mg	**2.4**	**0.0**	**0.3**	**0.0**
Na	**35.0**	**1.1**	**2.1**	**2.1**

Table 5.23 *$C_{leachate}$ of 'AT-V' glasses treated under 1% SO_2/He/Air for 60 minutes at 800°C with a 60 minute He-only pre-treatment at 800°C normalised to sample* a_s *(Table 5.6).*

Element	$C_{leachate}$ (µmol m^{-2})			
	TPH	**PHN**	**DCT**	**RHY**
S	305.2	113.3	89.1	51
Al	*n.a*	*n.a*	*n.a*	*n.a*
Ca	375.2	94.2	141.6	52
Fe	*n.a*	*n.a*	*n.a*	*n.a*
K	5.9	3.2	2.6	0.2
Mg	0.3	0	0.3	0.5
Na	0.5	1.2	0	3.5

5.6.3. MINERALOGY

The samples selected for XRD analysis were the TPH glass exposed to 1% SO_2/He/Air, 1% SO_2/He/Air with a 60 minute He-only pre-treatment, and air-only atmospheres (Fig. 5.40). The analysis confirmed the continued existence of the crystalline anhydrite ($CaSO_4$) phase identified in the 'temperature-variable' and 'time-variable' experiments, and its absence under air-only atmospheres. The relative height of the $CaSO_4$ peak in comparison to that of the other crystalline phases detected was observed to be lower in the sample exposed to the 1% SO_2/He/Air atmosphere after the He-only pre-treatment than in the sample without pre-treatment. In the 800°C sample exposed to SO_2 bearing atmospheres, the peaks previously identified as augite and a possible iron oxide phase were still identifiable, but under the air-only atmosphere, the augite phase disappeared and only the iron oxide phase could be identified.

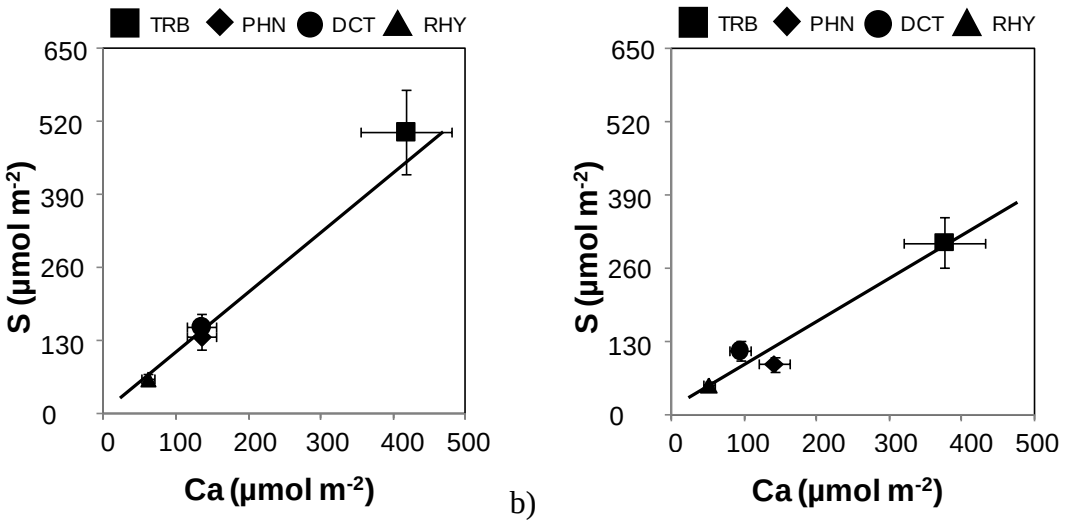

Fig. 5.39 *Comparison of S and Ca concentrations in leachate solutions from the 'AT-V' glass samples exposed to 1% SO_2/He/Air at 800°C a) without He-only pre-treatment (Table 5.22) and b) with He-only pre-treatment (Table 5.23).*

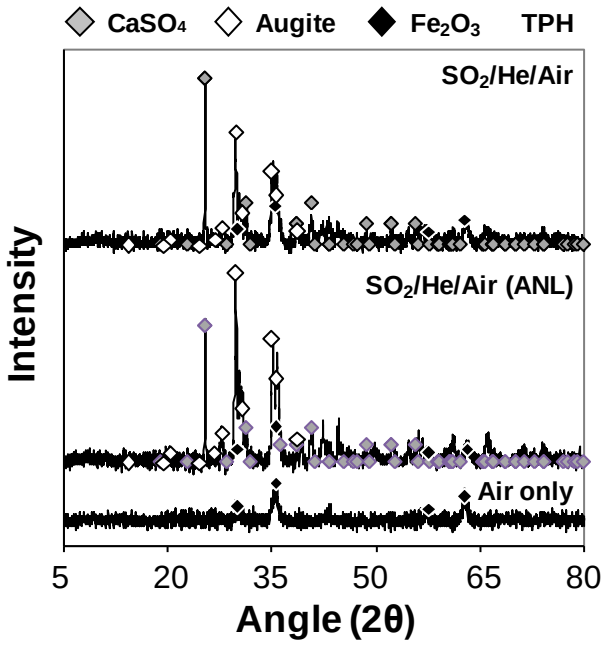

Fig. 5.40 *XRD patterns for the 'AT-V' TPH glass exposed at 800°C to air only and 1% SO_2/He/Air without and with pre-treatment under He-only atmosphere. Filled diamonds indicate the positions of the anhydrite ($CaSO_4$) (Wasastjerna 1927), a Ca, Na, Al, Mg, Fe and Si bearing augite phase (Okui et al. 1998) and gamma-Fe_2O_3(Jorgensen et al. 2007) diffraction peaks.*

5.6.4. SCANNING ELECTRON MICROSCOPY

The PHN glass pre-treated under He-only and exposed to 1% SO_2/He/Air at 800°C was analysed by SEM (Fig. 5.41) and spot-EDX (Table 5.24). As the TPH glass analysed without pre-treatment previously had surface deposits emplaced which could not be determined as containing more Ca and S than the surrounding glass surface, it was necessary to analyse the PHN glass in order for meaningful comparison of the surface deposit compositions. Optical imaging by SEM conducted on the PHN glass showed the continued presence of surface deposits with particle sizes of less than 2-3 µm existing on the silicate glass surfaces. The surface deposit compositions were investigated by spot-EDX and were found to be enriched in S/Si and Ca/Si relative to the surrounding glass. From analysis of four separate surface deposits, the average ratio of S/Si and Ca/Si had parity and therefore supported the continued presence of Ca-S compounds as surface deposits (Table 5.24).

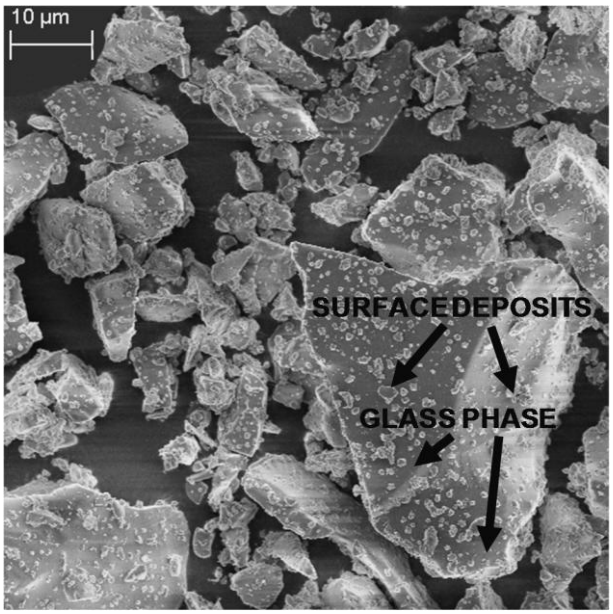

Fig. 5.41 *SEM image of 'AT-V' PHN glass exposed to 1% SO_2/He/Air at 800°C with a 60 minute high temperature He-only pre-treatment, showing surface deposits on the amorphous glass particle surface, indicated by the arrows.*

Table 5.24 *Ca/Si and S/Si ratios of glass and surface deposits on the 'AT-V' PHN glass after exposure to 1% SO_2/He/Air at 800°C with a 60 minute high temperature pre-treatment under He-only atmosphere, determined by spot-EDX.*

Replicates	Ca/Si		S/Si	
	Glass	Deposit	Glass	Deposit
1	0.00	0.06	0.02	0.09
2	0.01	0.05	0.02	0.08
3	0.01	0.15	0.02	0.20
4	0.02	0.06	0.03	0.08
Mean	**0.01**	**0.08**	**0.02**	**0.11**
S.D.	**0.01**	**0.05**	**0.00**	**0.06**

5.6.5. THERMOGRAVIMETRIC ANALYSIS

In the initial stages of this study, a brief usage of thermogravimetric analysis (TGA) as a characterisation technique was undertaken. It was initially intended that the different chemical phases formed during SO_2 adsorption studies could be discerned by the mass loss rates and thermal anomalies as the sample was heated under an inert atmosphere. This technique could not be used as intended, as in the first experiments, the samples permanently fused into the alumina crucibles, destroying them. As such, only two samples of glass were ever analysed, the TPH and the RHY. These data are included here as they are relevant to the discussion of the AT-V experiment series.

The samples were heated up to 1000°C at a ramp rate of 1°C per minute under an N_2 atmosphere resulted in the TPH glass being permanently fused into the alumina crucibles used in TGA. Without access to HF for crucible cleaning via silicate dissolution, TGA could not be used further. Of the two samples analysed (Fig. 5.42), the TPH glass showed ain increase in sample mass above 600°C, whilst the mass of the RHY glass decreased. The temperature of the individual glasses relative to a known standard was also observed to vary; differential thermal analysis showed that the RHY glass exhibited a negative thermal anomaly relative to the reference standard, indicating endothermic behaviour throughout heating. In the TPH glass underwent a similar decrease, but was punctuated by a further negative thermal anomaly trough at 700°C, and a sharp positive excursion indicating an exothermic reaction at 870°C.

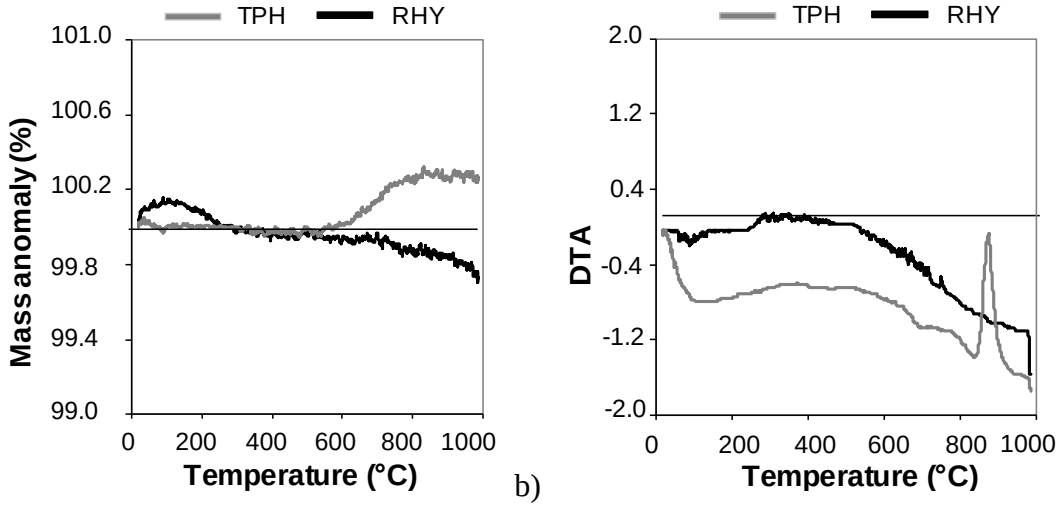

Fig. 5.42 *TGA data for the TPH and RHY glasses showing (a) the changes in sample mass relative to that of the initial sample and (b) the deviation in the temperature of the sample relative to an alumina crucible standard.*

5.6.7. X-RAY PHOTOELECTRON SPECTROSCOPY

XPS was conducted on all samples which were part of the 'AT-V' experiment series. The relative surface compositions of each glass under each experimental atmosphere are given in Table 5.25 and Table 5.26 for the He-only and air-only atmospheres, in Table 5.15 for the 1% SO_2/He/Air atmospheres and in Table 5.27 for the 1% SO_2/He/Air experiments with the 60 minute He-only pre-treatment at 800°C. The relative surface compositions of the 'atmosphere-variable' experiment series were analysed and interpreted in relation to each other and to the relative surface composition of the initial pre-experiment glasses.

Based upon the observed trends in relative surface compositions, the XPS spectra of the S (2p), Ca (2p) and Fe (2p) regions were subjected to more detailed analysis by the fitting of representative peaks to the spectra. The O (1s) spectra was also analysed, as of all the regions analysed by XPS, the O (1s) region showed drastic alterations in the peak lineshape which could be identified qualitatively even without more detailed analysis. These data are presented and interpreted (Fig. 5.45 to Fig. 5.57).

5.6.7.1. SURFACE COMPOSITIONAL VARIATIONS

Comparison of the relative surface compositions of all 'AT-V' samples relative to those of the pre-experiment initial sample surface (Fig. 5.43,Table 5.7) were found to show a number of changes in the relative abundance of different elements at the surfaces, as inferred from fluctuations in the element/Si ratios. Of the element/Si ratios of the glasses exposed to all experiment atmospheres, the only samples where clear trends in behaviour were observed were for S/Si, Ca/Si and Fe/Si.

Table 5.25 *Relative surface composition for 'AT-V' glasses exposed to He only atmospheres for 60 minutes at 800°C, determined by XPS.*

Region	Surface composition (atm. %)			
	TPH	**PHN**	**DCT**	**RHY**
Al (2p)	6.6	4.2	5.3	4.8
Ca (2p)	1.8	1.2	1.6	0.5
Fe (2p)	5.4	2.9	2.6	1.6
K (2p)	0.5	3.3	2.7	1.0
Mg (2p)	2.5	0.8	1.7	0.2
Na (1s)	3.2	6.5	2.9	4.1
O (1s)	70.5	69.4	74.7	69.4
S (2p)	0.5	0.2	0.25	0.4
Si (2p)	9.2	11.5	8.4	18.0

Table 5.26 *Relative surface composition for 'AT-V' glasses exposed to air only atmospheres for 60 minutes at 800°C, determined by XPS.*

Region	Surface composition (atm. %)			
	TPH	**PHN**	**DCT**	**RHY**
Al (2p)	4.9	4.6	4.6	4.8
Ca (2p)	1.3	1.2	1.1	0.5
Fe (2p)	6.4	4.3	4.4	1.6
K(2p)	0.4	0.4	0.4	1
Mg (2p)	3.2	1.6	1.6	0.2
Na (1s)	3.5	2.4	2.4	4.1
O(1s)	69.7	71.7	71.3	69.4
S (2p)	0.7	0.3	0.5	0.4
Si (2p)	9.8	13.5	13.6	18.0

Table 5.27 *Relative surface compositions for 'AT-V' glasses exposed to 1% SO_2/He/Air for 60 minutes at 800°C with a 60 minute He-only pre-treatment at 800°C, determined by XPS.*

Region	Surface composition (atm. %)			
	TPH	PHN	DCT	RHY
Al (2p)	3.6	3.7	3.4	5.5
Ca (2p)	4.9	1.5	4.3	1.6
Fe (2p)	2.1	3.2	4.1	0.9
K (2p)	1.3	2.2	1.2	2.0
Mg (2p)	0.3	0.0	0.0	0.0
Na (1s)	3.4	4.5	3.2	7.5
O (1s)	74.1	71.5	72.4	64.5
S (2p)	3.4	0.6	2.8	1.1
Si (2p)	7.0	12.6	8.6	16.8

S/Si ratios (Fig. 5.43a) at the sample surface were consistently enriched across all samples relative to those of the initial surface, with ratios of 0.05-0.7 for SO_2 exposed glasses, and even in SO_2-free atmospheres, up to 0.05 S/Si ratios indicated the presence of some surface S. The highest S/Si ratios were consistently observed for all samples under 1% SO_2/He/Air without pre-treatment, and the pre-treated glasses had S/Si between 30-40% lower than those of the untreated glasses, with the exception of the rhyolite glass, which was 15% lower. Slight increases in surface S /Si ratios for the He-only and air-only experiments were observed to greatest extent in the tephrite glass, but their values relative to those of the glasses exposed to SO_2-bearing atmospheres were very low.

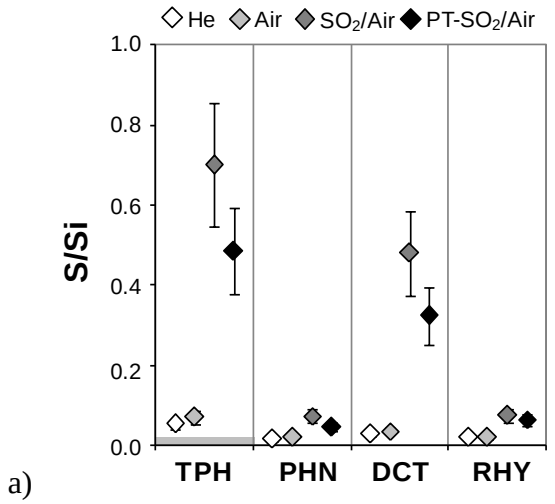

a)

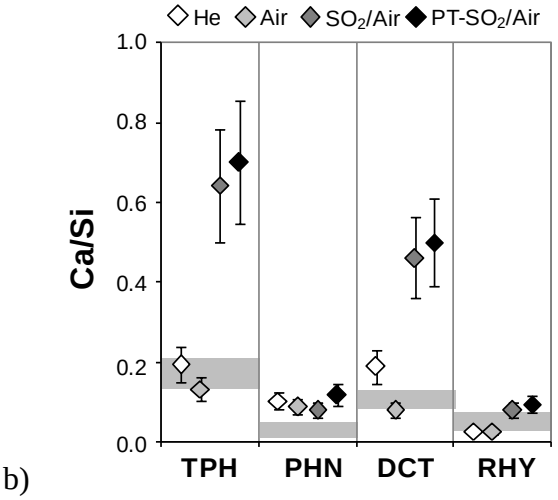

b)

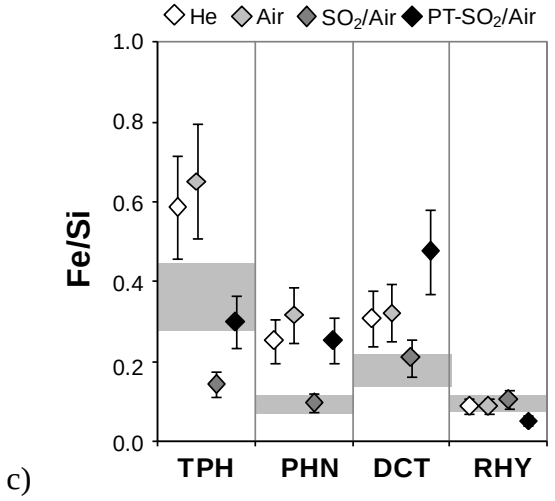

c)

Fig. 5.43 *Variation in element/Si ratios for S, Ca and Fe for the four 'AT-V' glass samples treated at 800°C for 60 minutes under He only (Table 5.25), air only (Table 5.26), 1% SO_2/He/Air (Table 5.15) and 1% SO_2/He/Air with He-only pre-treatment (Table 5.27). The grey shaded region indicates the element / Si ratios of the pre-experiment initial relative surface composition (Table 5.7), including the applied experimental and analytical error of 22%.error.*

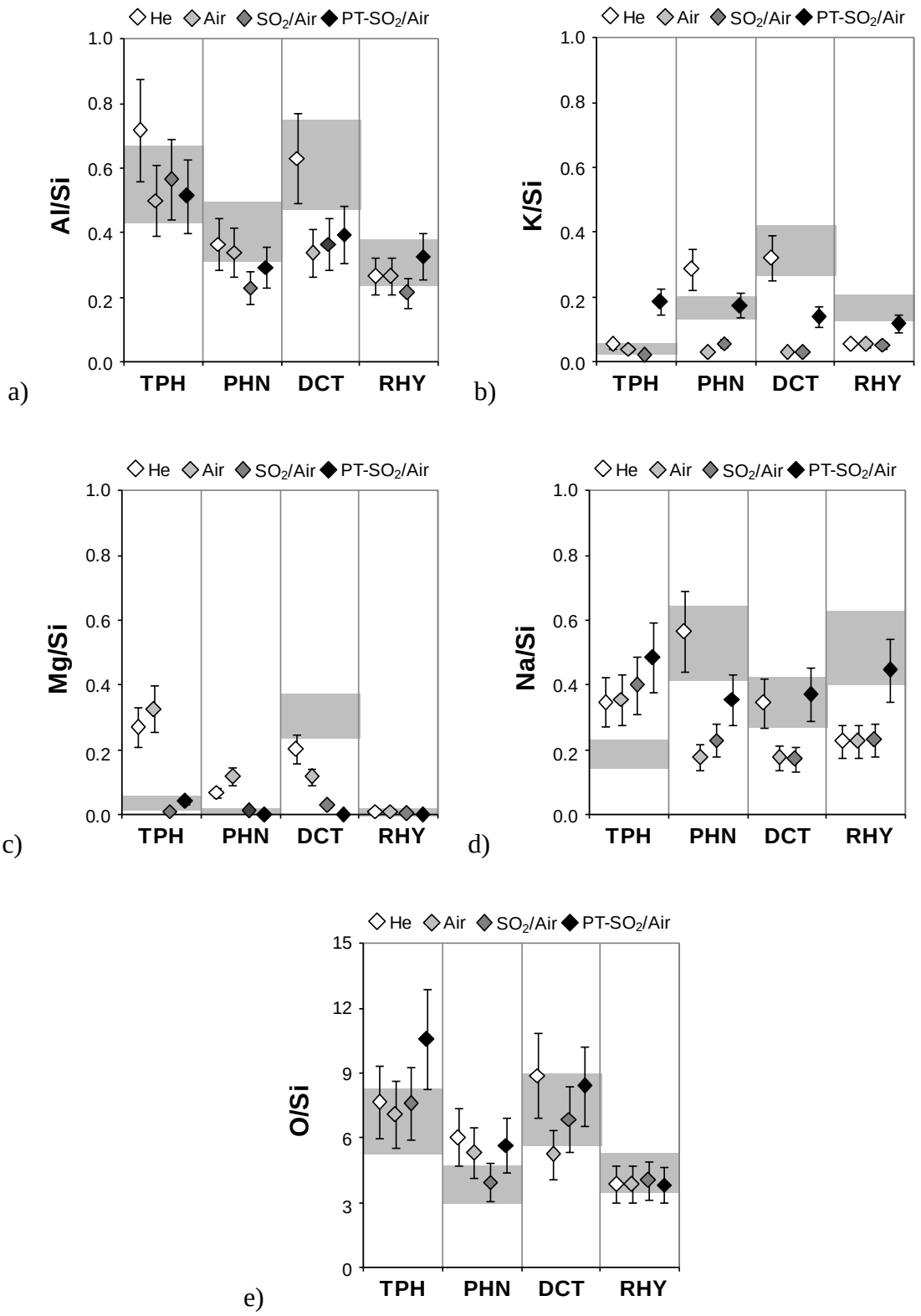

Fig. 5.44 *Variation in element/Si ratios for Al, K, Mg, Na and O for the four 'AT-V' glass samples treated at 800°C for 60 minutes under He only (Table 5.25), air only (Table 5.26), 1% SO_2/He/Air (Table 5.15) and 1% SO_2/He/Air with He-only pre-treatment (Table 5.27). The grey shaded region indicates the element / Si ratios of the pre-experiment initial relative surface composition (Table 5.7), including the applied experimental and analytical error of 22% error.*

Ca/Si ratios were observed to be enriched under all experimental atmospheres in the PHN glass (Fig. 5.43b), but not to the same extent as the TPH and DCT glasses under SO_2-bearing atmospheres. In all other glasses under air-only and He-only atmospheres, apart from the dacite glass exposed to He-only, which was increased by a factor of 2, all Ca/Si ratios were within the range of the pre-experiment surface composition ratios. In the presence of SO_2, Ca/Si ratios were increased by a factor of 4-6 in the TPH and DCT glasses, and by a factor of 2 in the PHN and RHY glasses.

Fe/Si ratios (Fig. 5.43c) varied from sample to sample and under the different experimental atmospheres, but the TPH, PHN and DCT glasses showed consistent enrichment by factors of between 2 and 3 relative to their initial surface compositions under He-only and air-only atmospheres. In SO_2 bearing atmospheres, Fe/Si ratios were doubled in the pre-treated glasses in comparison to those without the He-only pre-treatment for the TPH, PHN and DCT glasses, but not for the RHY glasses.

Whilst S/Si, Ca/Si and Fe/Si showed distinct trends which were easily discernible, the behaviour of the other major element/Si ratios was inconsistent and showed no clear trends in behaviour. Of the remaining element/Si ratios, some showed no variation in behaviour relative to the initial surface of the glass, such as Al/Si (Fig. 5.44). The element/Si ratios for K, Mg and Na (Fig. 5.44) all showed variable behaviour from which it was difficult to discern any major trends. In the SO_2-bearing atmospheres, Na/Si ratios were always higher by a factor of 1.25-2 in the untreated glasses compared to the pre-treated glasses, whilst K/Si ratios were consistently higher by factors of 2-10. In the TPH glass, it was also notable that Na/Si ratios were all consistently higher than the initial surface. Mg/Si ratios were similarly inconsistent, but did show enrichments by factors of 5-6 in the TPH and PHN glasses under He-only and air-only relative to the pre-experiment initial surface ratios, but were consistently depleted in the DCT and unchanged in the RHY. The O/Si ratios (e) did not show any consistent trend across all experimental atmospheres, but in SO_2-bearing atmospheres, the untreated glass O/Si ratios were higher in the TPH, PHN and DCT glasses by factors of 1.1-1.5.

5.6.7.2. S (2P) SPECTRA INTERPRETATION AND PEAK FITTING

In the S (2p) XPS spectra for the 'AT-V' glasses treated under SO_2 bearing atmospheres, the S ($2p\ ^3/_2$) peak can be described by a single component with a binding energy of approximately 168.9 eV (Fig. 5.45), indicative of sulphate species.

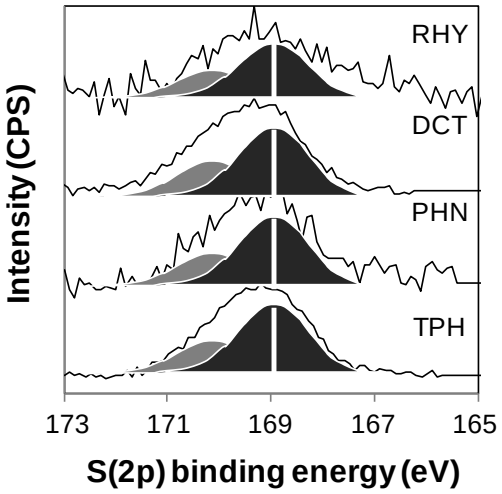

Fig. 5.45 *S (2p) region of the XPS spectra for 'AT-V' glasses exposed to 1% SO_2/He/Air at 800°C for 60 minutes with the He-only pretreatment. S (2p) spectra have been fitted with a doublet pair of Gaussian-Lorentzian 30 lineshapes with Doniach-Sunjic asymmetry parameters of 0.005,450 and FWHM of 1.8 eV. The spectra were scaled by factors of 520, 98 and 362% for the PHN, DCT and RHY glasses to plot them on the same scale as the spectra of the TPH glass.*

5.6.7.3. CA (2P $^3/_2$) SPECTRA INTERPRETATION AND PEAK FITTING

The Ca (2p $^3/_2$) spectra for all 'AT-V' glasses at all experimental conditions for the 'atmosphere-variable' experiment are displayed in Fig. 5.46a to Fig. 5.49a. Based upon the variations observed in the lineshape and its peak position, the Ca (2p $^3/_2$) spectra was fitted with a single component in the initial spectra with a binding energy which varied between 347.0 and 347.5 eV. Under experimental atmospheres and high temperature exposure, additional peaks could be fitted around that core peak, under He-only and air-only atmospheres, a lower binding energy peak at 346.2-346.7 eV was observed, whilst under SO_2 bearing atmospheres, a higher binding energy peak at 348 eV was identified, in addition to the previously identified lower binding energy peak in the pre-treated SO_2 chemisorption experiments. The variations in the relative contributions of the two binding components are given in Table A27 to Table A30 and are displayed Fig. 5.46b to Fig. 5.49b. Of the four glasses, only the RHY glass shows no apparent change under He-only and air-only samples, and there is no noticeable difference between the peaks exposed to 1% SO_2/He/Air with and without the He-only pre-treatment.

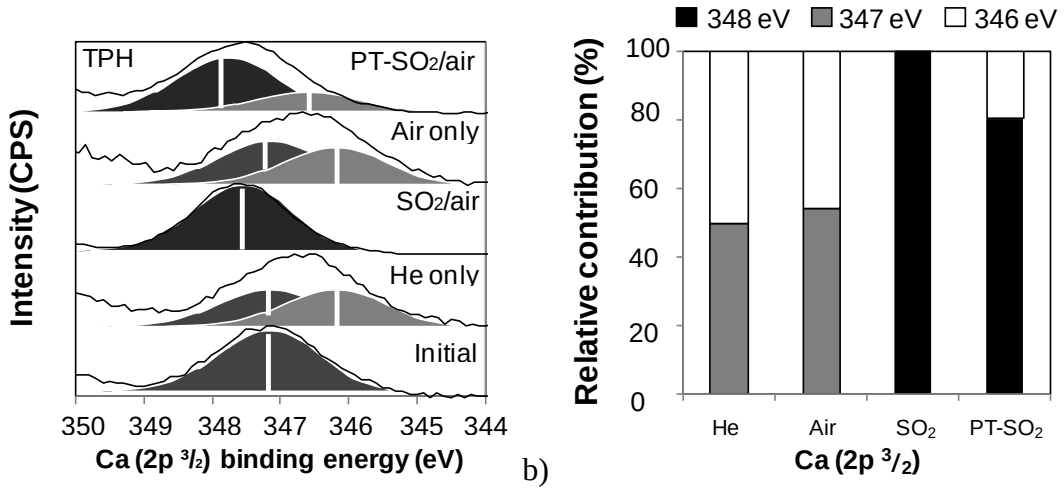

Fig. 5.46 *Ca (2p $^3/_2$) region of the XPS spectra for the 'AT-V' TPH glass exposed to 1% SO_2/He/Air at 800°C for 60 minutes with the He-only pretreatment. The spectra are described by three Gaussian-Lorentzian 30 lineshapes with Doniach-Sunjic asymmetry parameters of 0.005,450 and FWHM of 1.9 eV. The relative contributions of the fitted components are illustrated in (b). Spectra have been scaled by factors of 127, 198, 74 and 75% for the He-only, 1% SO_2/He/Air, air-only and glasses exposed to 1% SO_2/He/Air with an He-only pre-treatment to plot them on the same scale as the spectra of the initial surface.*

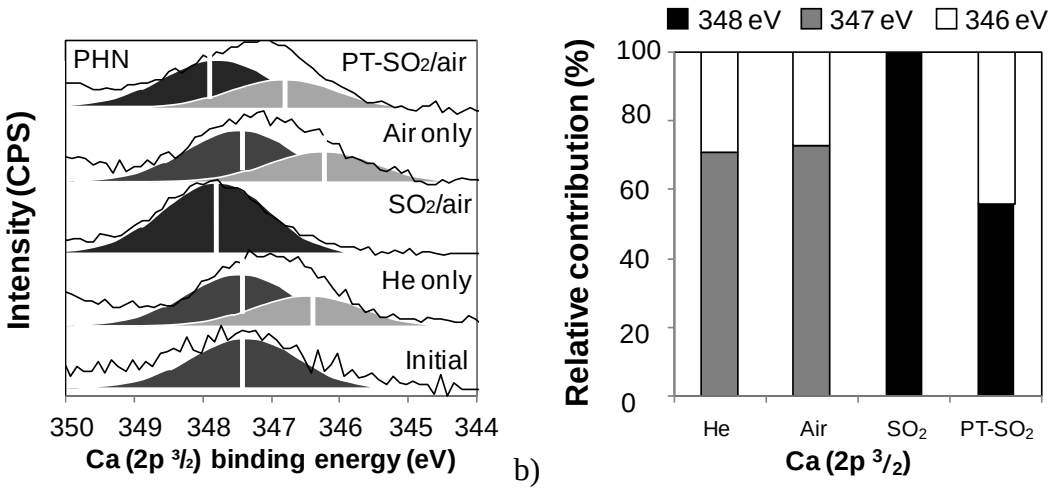

Fig. 5.47 *Ca (2p $^{3}/_{2}$) region of the XPS spectra for the 'AT-V' PHN glass exposed to 1% SO_2/He/Air at 800°C for 60 minutes with the He-only pretreatment. The spectra are described by three Gaussian-Lorentzian 30 lineshapes with Doniach-Sunjic asymmetry parameters of 0.005,450 and FWHM of 2 eV. The relative contributions of the fitted components are illustrated in (b). Spectra have been scaled by factors of 40, 36, 24 and 30% for the He-only, 1% SO_2/He/Air, air-only and glasses exposed to 1% SO_2/He/Air with an He-only pre-treatment to plot them on the same scale as the spectra of the initial surface.*

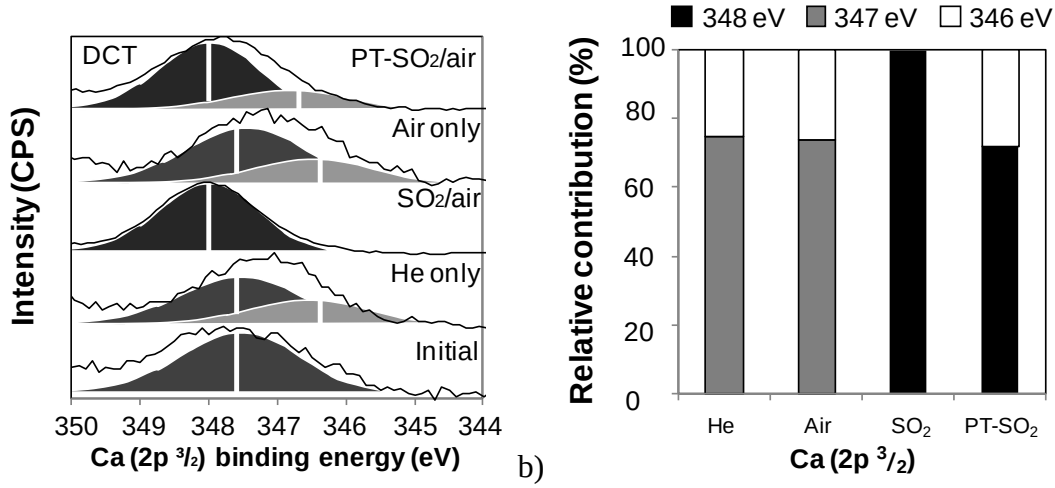

Fig. 5.48 *Ca (2p $^{3}/_{2}$) region of the XPS spectra for the 'AT-V' DCT glass exposed to 1% SO_2/He/Air at 800°C for 60 minutes with the He-only pretreatment. The spectra are described by three Gaussian-Lorentzian 30 lineshapes with Doniach-Sunjic asymmetry parameters of 0.005,450 and FWHM of 2 eV. The relative contributions of the fitted components are illustrated in (b). Spectra have been scaled by factors of 67, 79, 15 and 26% for the He-only, 1% SO_2/He/Air, air-only and glasses exposed to 1% SO_2/He/Air with an He-only pre-treatment to plot them on the same scale as the spectra of the initial surface.*

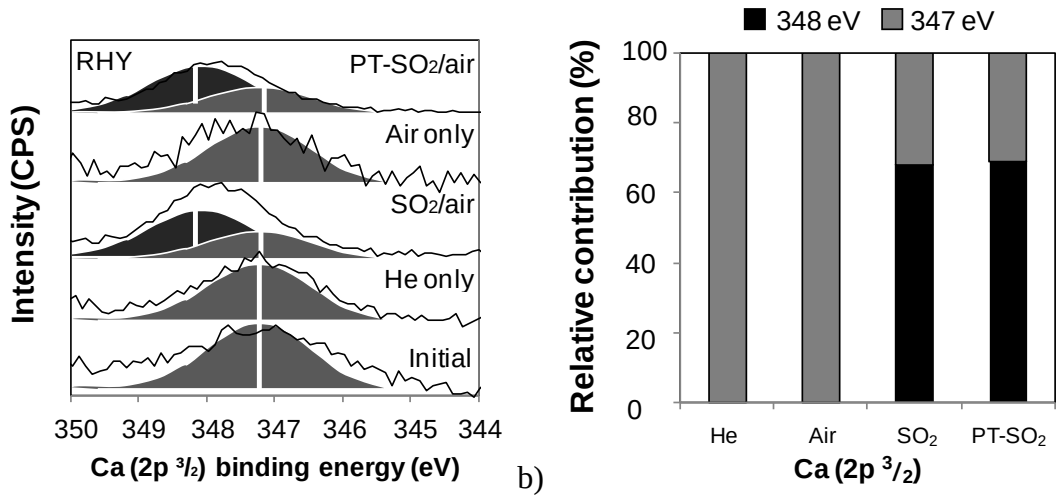

Fig. 5.49 *Ca (2p $^{3}/_{2}$) region of the XPS spectra for the 'AT-V' RHY glass exposed to 1% SO_2/He/Air at 800°C for 60 minutes with the He-only pretreatment. The spectra are described by three Gaussian-Lorentzian 30 lineshapes with Doniach-Sunjic asymmetry parameters of 0.005,450 and FWHM of 2 eV. The relative contributions of the fitted components are illustrated in (b). Spectra have been scaled by factors of 81, 137, 20 and 18% for the He-only, 1% SO_2/He/Air, air-only and glasses exposed to 1% SO_2/He/Air with an He-only pre-treatment to plot them on the same scale as the spectra of the initial surface.*

5.6.7.4. FE (2P $^{3}/_{2}$) SPECTRA INTERPRETATION AND PEAK FITTING

The Fe (2p $^{3}/_{2}$) spectra for all glasses at all experimental conditions for the 'atmosphere-variable' experiment are displayed in Fig. 5.50a to Fig. 5.53a. Based upon the variations observed in the lineshape and its peak position, the Fe (2p $^{3}/_{2}$) spectra was fitted with two distinct components for all samples, with binding energies of approximately 707-708 eV and 710-711 eV. The relative contribution of the two fitted peak components was observed to vary under different experimental atmospheres relative to the initial surface; the variations in the relative contributions of the two binding components are given in Table A31 to Table A34 and are illustrated in Fig. 5.50b to Fig. 5.53b. In all glasses apart from the rhyolite, the Fe (2p $^{3}/_{2}$) fitted peaks are observed to vary most significantly under air-only atmospheres, where the contribution of the high binding energy component was observed to increase by up to 22% for the TPH, PHN and DCT glasses, but was not altered in the RHY glass., whilst in the rhyolite sample, there was little difference between the initial and post-experiment surfaces under any atmosphere. In the presence of He-only atmospheres, increases in the contribution of the high binding energy component were also observed in the TPH and DCT glasses, but not in the PHN and RHY glasses.

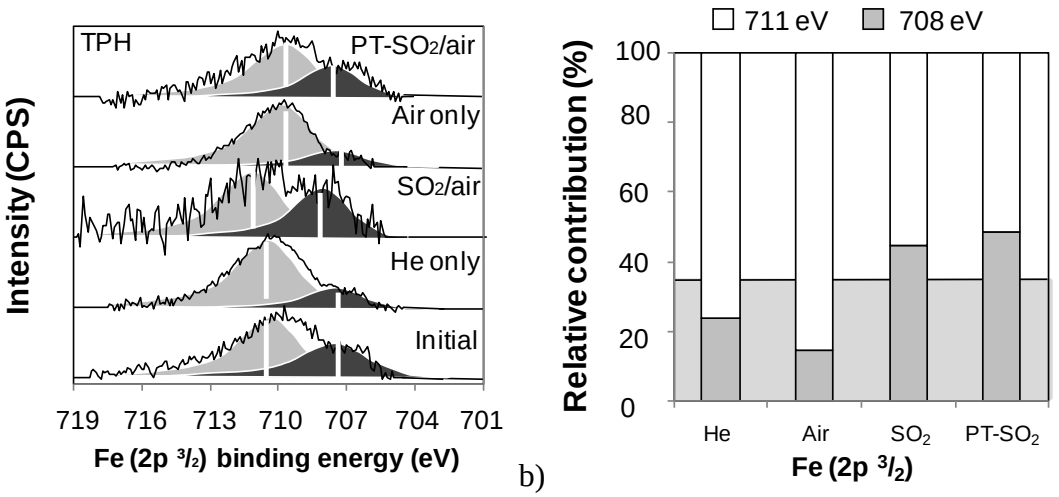

Fig. 5.50 *Fe (2p $^{3}/_{2}$) region of the XPS spectra for the 'AT-V' TPH glass exposed to 1% SO_2/He/Air at 800°C for 60 minutes with the He-only pretreatment. The spectra are fitted with two Gaussian-Lorentzian 30 lineshapes with Doniach-Sunjic asymmetry parameters of 0.005,450 and FWHM of 3 eV. The relative contributions of the fitted components are illustrated in (b). Spectra have been scaled by factors of 66, 62, 374 and 171% for the He-only, 1% SO_2/He/Air, air-only and glasses exposed to 1% SO_2/He/Air with an He-only pre-treatment to plot them on the same scale as the spectra of the initial surface.*

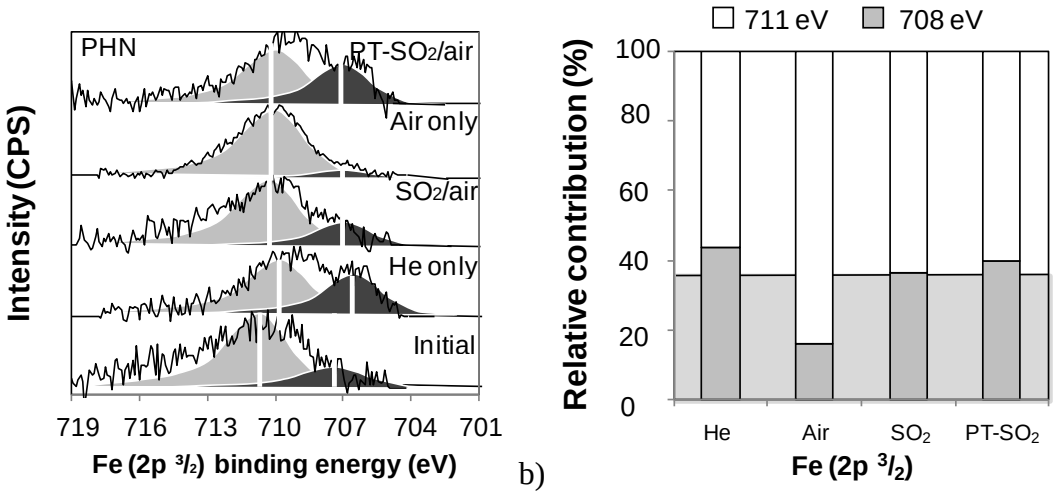

Fig. 5.51 *Fe (2p $^{3}/_{2}$) region of the XPS spectra for the 'AT-V' PHN glass exposed to 1% SO_2/He/Air at 800°C for 60 minutes with the He-only pretreatment. The spectra are fitted with two Gaussian-Lorentzian 30 lineshapes with Doniach-Sunjic asymmetry parameters of 0.005,450 and FWHM of 3 eV. The relative contributions of the fitted components are illustrated in (b). Spectra have been scaled by factors of 50, 21, 59 and 42% for the He-only, 1% SO_2/He/Air, air-only and glasses exposed to 1% SO_2/He/Air with an He-only pre-treatment to plot them on the same scale as the spectra of the initial surface.*

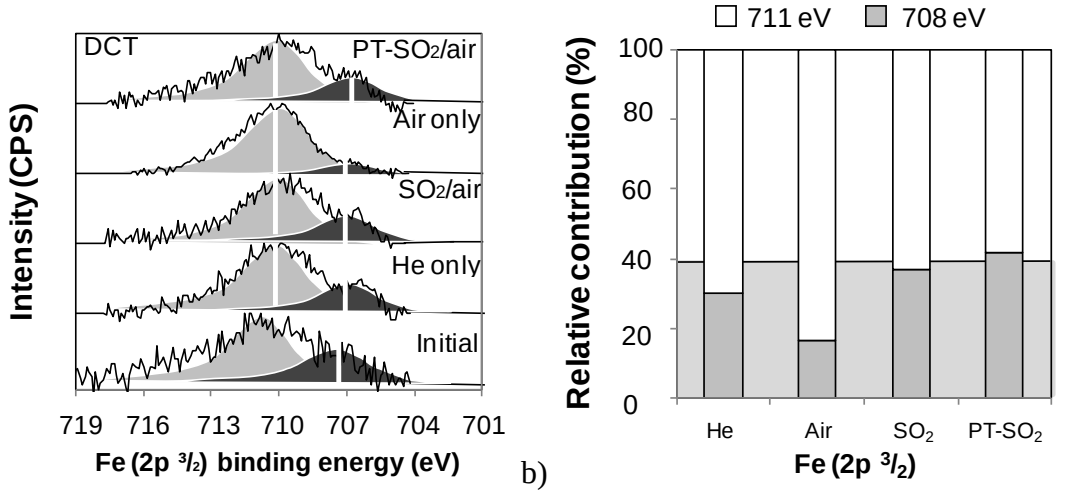

Fig. 5.52 *Fe (2p $^{3}/_{2}$) region of the XPS spectra for the 'AT-V' DCT glass exposed to 1% SO_2/He/Air at 800°C for 60 minutes with the He-only pretreatment. The spectra are fitted with two Gaussian-Lorentzian 30 lineshapes with Doniach-Sunjic asymmetry parameters of 0.005,450 and FWHM of 3 eV. The relative contributions of the fitted components are illustrated in (b). Spectra have been scaled by factors of 47, 28, 50 and 60% for the He-only, 1% SO_2/He/Air, air-only and glasses exposed to 1% SO_2/He/Air with an He-only pre-treatment to plot them on the same scale as the spectra of the initial surface.*

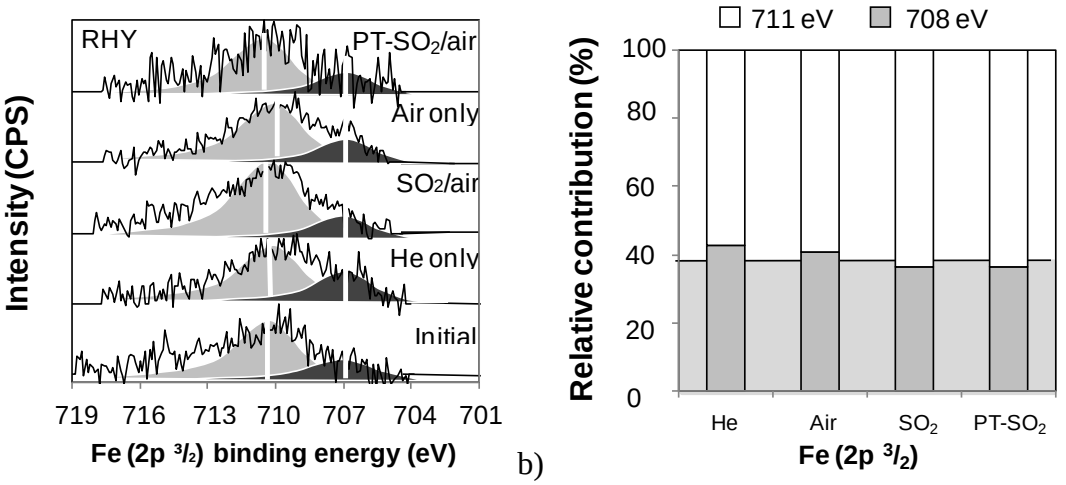

Fig. 5.53 *Fe (2p $^{3}/_{2}$) region of the XPS spectra for the'AT-V' RHY glass exposed to 1% SO_2/He/Air at 800°C for 60 minutes with the He-only pretreatment. The spectra are fitted with two Gaussian-Lorentzian 30 lineshapes with Doniach-Sunjic asymmetry parameters of 0.005,450 and FWHM of 3 eV. The relative contributions of the fitted components are illustrated in (b). Spectra have been scaled by factors of 70, 65, 53 and 250% for the He-only, 1% SO_2/He/Air, air-only and glasses exposed to 1% SO_2/He/Air with an He-only pre-treatment to plot them on the same scale as the spectra of the initial surface.*

5.6.7.5. O (1S) SPECTRA INTERPRETATION AND PEAK FITTING

The O (1s) spectra for all 'AT-V' glasses at all experimental conditions for the 'atmosphere-variable' experiment are displayed in Fig. 5.54a to Fig. 5.57a. Based upon the variations observed in the lineshape and its peak position, the O (1s) spectra was fitted with two distinct components for all samples, with binding energies of approximately 531.5 to 532.0 eV and 529.5 eV to 530.5 eV. The relative contributions of the two fitted peak components were observed to vary under different experimental atmospheres relative to the initial surface. The variations in the relative contributions of the two binding components are given in Table A35 to Table A38 and illustrated in Fig. 5.54b to Fig. 5.57b. In all glasses apart from the RHY glass, the relative contribution of the lower binding energy component increased by up to 22% under He-only and air-only atmospheres, but decreased in all glasses, including the RHY glass, after exposure to 1% SO_2/He/Air atmospheres. In samples which were exposed to 1% SO_2/He/Air after the 60 minute He-only pre-treatment, the changes on the relative contribution of the low binding energy component of the O (1s) spectra were higher in the TPH, PHN and DCT glasses relative to the experiments without pre-treatment by as much as 25%.

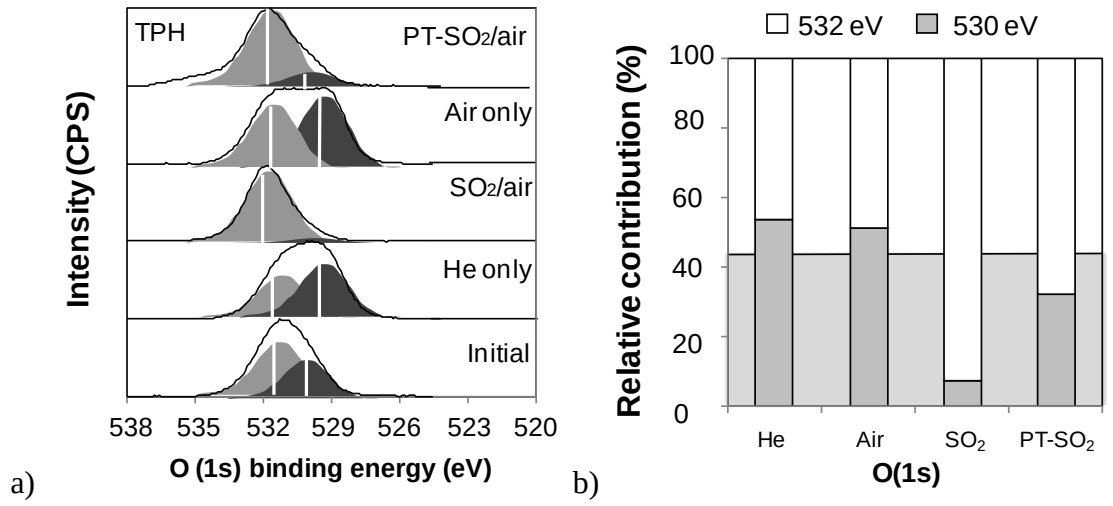

Fig. 5.54 *O (1s) region of the XPS spectra for the 'AT-V' TPH glass exposed to 1% SO_2/He/Air at 800°C for 60 minutes with the He-only pretreatment. The spectra are fitted with two Gaussian-Lorentzian 30 lineshapes and FWHM of 2.2 eV. The relative contributions of the fitted components are illustrated in (b). Spectra have been scaled by factors of 75, 57, 104 and 57% for the He-only, 1% SO_2/He/Air, air-only and glasses exposed to 1% SO_2/He/Air with an He-only pre-treatment to plot them on the same scale as the spectra of the initial surface.*

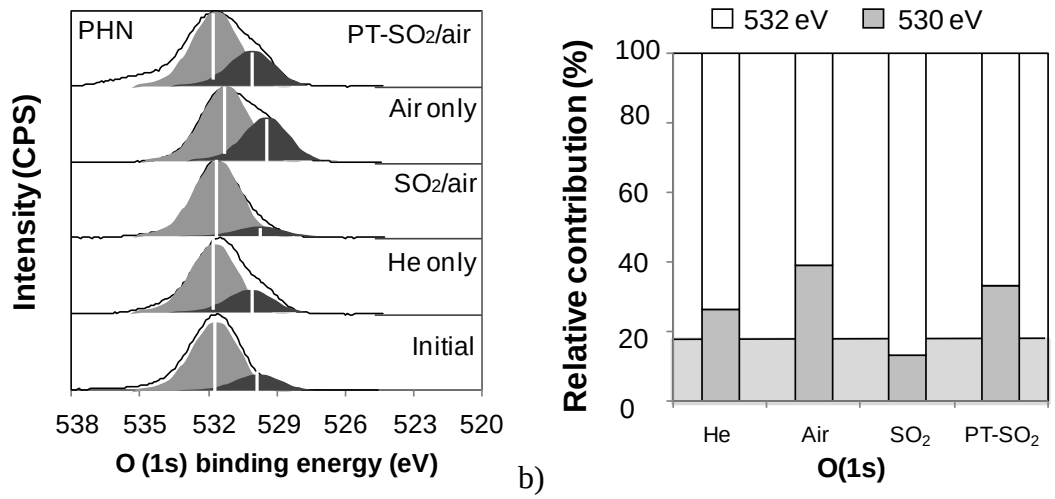

Fig. 5.55 *O (1s) region of the XPS spectra for the 'AT-V' PHN glass exposed to 1% SO_2/He/Air at 800°C for 60 minutes with the He-only pretreatment. The spectra are fitted with two Gaussian-Lorentzian 30 lineshapes and FWHM of 2.2 eV. The relative contributions of the fitted components are illustrated in (b). Spectra have been scaled by factors of 84, 100, 133 and 86% for the He-only, 1% SO_2/He/Air, air-only and glasses exposed to 1% SO_2/He/Air with an He-only pre-treatment to plot them on the same scale as the spectra of the initial surface.*

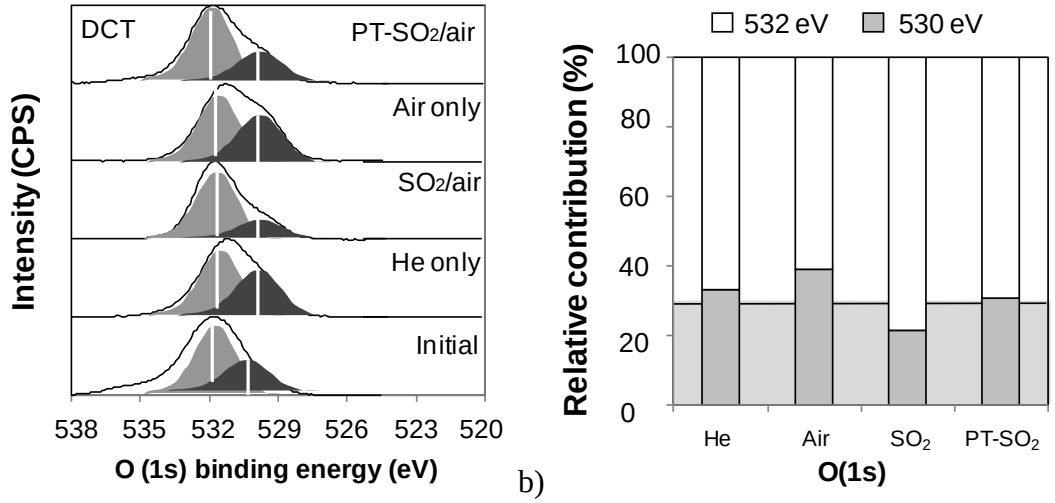

Fig. 5.56 *O (1s) region of the XPS spectra for the 'AT-V' DCT glass exposed to 1% SO_2/He/Air at 800°C for 60 minutes with the He-only pretreatment. The spectra are fitted with two Gaussian-Lorentzian 30 lineshapes and FWHM of 2.2 eV. The relative contributions of the fitted components are illustrated in (b). Spectra have been scaled by factors of 96, 100, 133 and 84% for the He-only, 1% SO_2/He/Air, air-only and glasses exposed to 1% SO_2/He/Air with an He-only pre-treatment to plot them on the same scale as the spectra of the initial surface.*

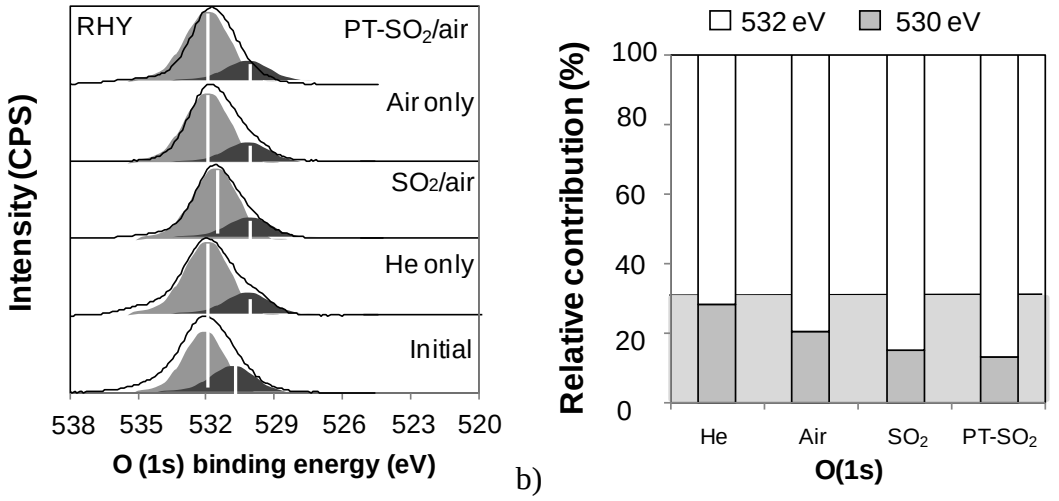

Fig. 5.57 *O (1s) region of the XPS spectra for the 'AT-V' RHY glass exposed to 1% SO_2/He/Air at 800°C for 60 minutes with the He-only pretreatment. The spectra are fitted with two Gaussian-Lorentzian 30 lineshapes and FWHM of 2.2 eV. The relative contributions of the fitted components are illustrated in (b). Spectra have been scaled by factors of 87, 151, 157 and 46% for the He-only, 1% SO_2/He/Air, air-only and glasses exposed to 1% SO_2/He/Air with an He-only pre-treatment to plot them on the same scale as the spectra of the initial surface.*

CHAPTER SIX

SO_2 CHEMISORPTION ON GLASS SURFACES.

PART II – MECHANISMS OF SO_2 CHEMISORPTION

CHAPTER 6. SO_2 CHEMISORPTION ON GLASS SURFACES. PART II – MECHANISMS OF SO_2 CHEMISORPTION

6.1. CHAPTER OVERVIEW

The data presented in Chapter 5 are interpreted in this chapter in two separate sections. In section 6.2, the reaction products formed by the reaction of SO_2 are identified and characterised. In section 6.3, the mechanisms driving SO_2 chemisorption and reaction product formation in the samples are investigated. The implications and context of these sections are then considered in Chapter 7.

6.2. REACTION PRODUCTS OF SO_2 CHEMISORPTION ON VOLCANIC GLASS

In this section, the reaction products formed during SO_2 chemisorption on the glass surfaces in the course of the 'TP-V', 'TI-V' and 'AT-V' experiments are identified through interpretation of leachate data, XPS, XRD and SEM.

6.2.1. LEACHATE DATA AS A MEASURE OF TOTAL SO_2 UPTAKE AND REACTION PRODUCTS

Leachate analysis is a useful tool for the identification of the reaction products formed by the SO_2 chemisorption reaction. S_{total}, assuming that all S is derived from the chemisorption of SO_2, is considered to be deposited at or near to the sample surface, and therefore may be normalised to a_s in the same manner as $S_{leachate}$ for comparison between the two. The normalised data are displayed in Table 6.1, and are compared to the $S_{leachate}$ data in Fig. 6.1.

Table 6.1. *Total S content of volcanic glasses exposed to 1% SO_2/He/Air at 25-800°C for 60 minutes, normalised to sample a_s (Table 5.6), determined by ICP-OES. Analytical error values for this analysis were not available.*

Temp. (°C)	S_{bulk}(µmol m^{-2})			
	TPH	**PHN**	**DCT**	**RHY**
300	28.2	8.5	5.7	
400				
500	80.9	34.7		7.2
600	327.8	62.5	36.0	30.3
700	298.2	136.1	146.4	65.2
800	328.2	97.8	162.5	59.5

In comparing $S_{leachate}$ to S_{total}, it is observed that with the exception of TPH, comparison between the two data series show that the other glasses have approximately equal $S_{leachate}$ to S_{total} after normalisation to a_s. The TPH glass shows a consistent enrichment in $S_{leachate}$ with S_{total}, which would seem to be contradictory, but this is attributed to differences between the subsamples used in the leachate analysis of the TPH glass and the subsamples used in total S analysis. The TPH glass, of all the glasses,

experienced the greatest degree of fusing after experiments in temperatures above 600°C, which is represented by the three highest data points on Fig 6.2, and the disparity between $S_{leachate}$ and S_{total} is attributed to this. The subsamples which were used for leachate analysis were taken from the fused particle surface, whilst the subsamples used for total S analysis were taken from the inner core of the particle at a much later date, and the inner core of the fused particle may therefore have been less accessible to SO_2, hence giving a lower S_{total} than $S_{leachate}$. Since $S_{leachate}$ represents all or a significant fraction of the S_{total} in all the glass samples, it is assumed that all adsorbed SO_2 forms soluble surface salts, and hence that leachate data can be used as a measure of total SO_2 uptake and reaction product formation.

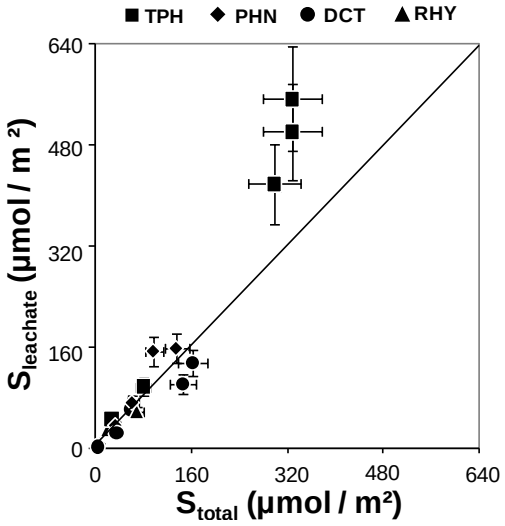

Fig. 6.1 *Comparison between $S_{leachate}$ (Table A5) and S_{total} (Table 5.9), normalised to a_s (Table 5.6), with ±15% experimental error.*

6.2.2. IDENTIFYING REACTION PRODUCTS FROM LEACHATE ANALYSIS

The primary cations in leachate solutions in the glasses have been recognised to be Ca and Na, and this would indicate that the most likely salts to exist are those of $CaSO_4$ and Na_2SO_4. Using the existing leachate methodology described in Chapter 3, the solubilities of $CaSO_4$ and Na_2SO_4 at 25°C are calculated to be approximately 600 µmol g^{-1} and 79000 µmol g^{-1} of glass leached (Lide 2005), which even in the undiluted initial leachates were values which were never exceeded. It is therefore reasonable to discuss the leachate compositions of Na, Ca and S as being a result of the dissolution of these soluble salts.

At temperatures below 400°C, it is not possible to identify any reaction products in leachate solutions. Leachate concentrations in samples from low temperature

experiments are, apart from the TPH glass at 300-400°C for S, Na and Ca, below or approximately equal to the 7 μmol m^{-2} limit which was estimated to represent the contribution to leachate solutions from glass dissolution and leaching. The few values which exceed the imposed limit are the Na concentrations in the TPH glass (Fig. 6.2), which in 60 minute experiments at 300°C were seven times larger than the imposed 7 μmol m^{-2} limit (Table A7) and had a Na/S molar ratio of 1:1 (Fig. 6.2). If the reaction products formed at low temperature is Na-S compounds such as Na_2SO_4 or Na_2SO_3, the Na/S molar ratio should be approximately 2:1, but the observed Na/S ratios may still indicate that in the TPH glass, a significant majority of the adsorbed SO_2 at both 200°C and 300°C could exist as Na-S compounds. Based upon the observed Na/S ratios in both 'TP-V' (Fig. 6.2) and 'TI-V' experiments (Fig. 6.3), below 400°C, it is hypothesised that for the TPH glass, Na-S compounds are a major, but not the sole, reaction product at low temperatures after both brief and prolonged exposure to SO_2.

At moderate temperatures, between 400-600°C, the concentrations of the major cations of Na and Ca in 60 minute exposure time experiments are consistently higher than the glass dissolution and leaching contribution, whilst those of the other cations remain below the imposed 7 μmol m^{-2} limit (0 - Table A11). In the TPH glass exposed to SO_2 at temperatures of 400-600°C, leachate Na/S ratios continue to indicate that between 50-25% of all soluble S compounds may exist as Na-S compounds (Fig. 6.2), provided that Ca-S compounds make up the remaining mass of S in solution. Short time duration experiments on the TPH glass at 500°C may also indicate the presence of a 50% contribution to the leachate solutions from Na-S compounds, as Na/S ratios of 1:1 are consistently observed in SO_2 exposure times of 60 minutes down to less than 5 minutes at temperatures of 500°C (Fig. 6.4).

In the other glasses, the presence of Na-S compounds is not supported by leachate compositions. In all other samples and temperatures, Ca-S compounds are inferred to exist based upon the approximate 1:1 Ca:S molar ratios in the leachate solution (Fig. 6.4), consistent with dissolution of simple Ca-S compounds including $CaSO_4$, and $CaSO_3$. Ca-S compounds are inferred to exist even in short time duration experiments down to SO_2 exposure times of approximately 10 minutes, before Ca concentrations are lower than the glass dissolution and leaching contribution (Fig. 6.4).

At high temperatures greater than 600°C, all samples show identical trends in leachate composition, containing only Ca and S as major constituents and with Ca/S

molar ratios of approximately 1:1 (Fig. 6.2). These data indicate that Ca-S compounds are likely to be the sole or predominant reaction product, as although in the TPH glass, Na remains detectable, Na/S ratios indicate that Na-S compounds could only account for less than 10% of the reaction products formed, with Ca-S compounds being able to account for the remainder. At 800°C, even in at exposure times down to 2 minutes, all glasses retain the 1:1 Ca:S molar ratios above the 7 μmol m^{-2} limit (Fig. 6.5).

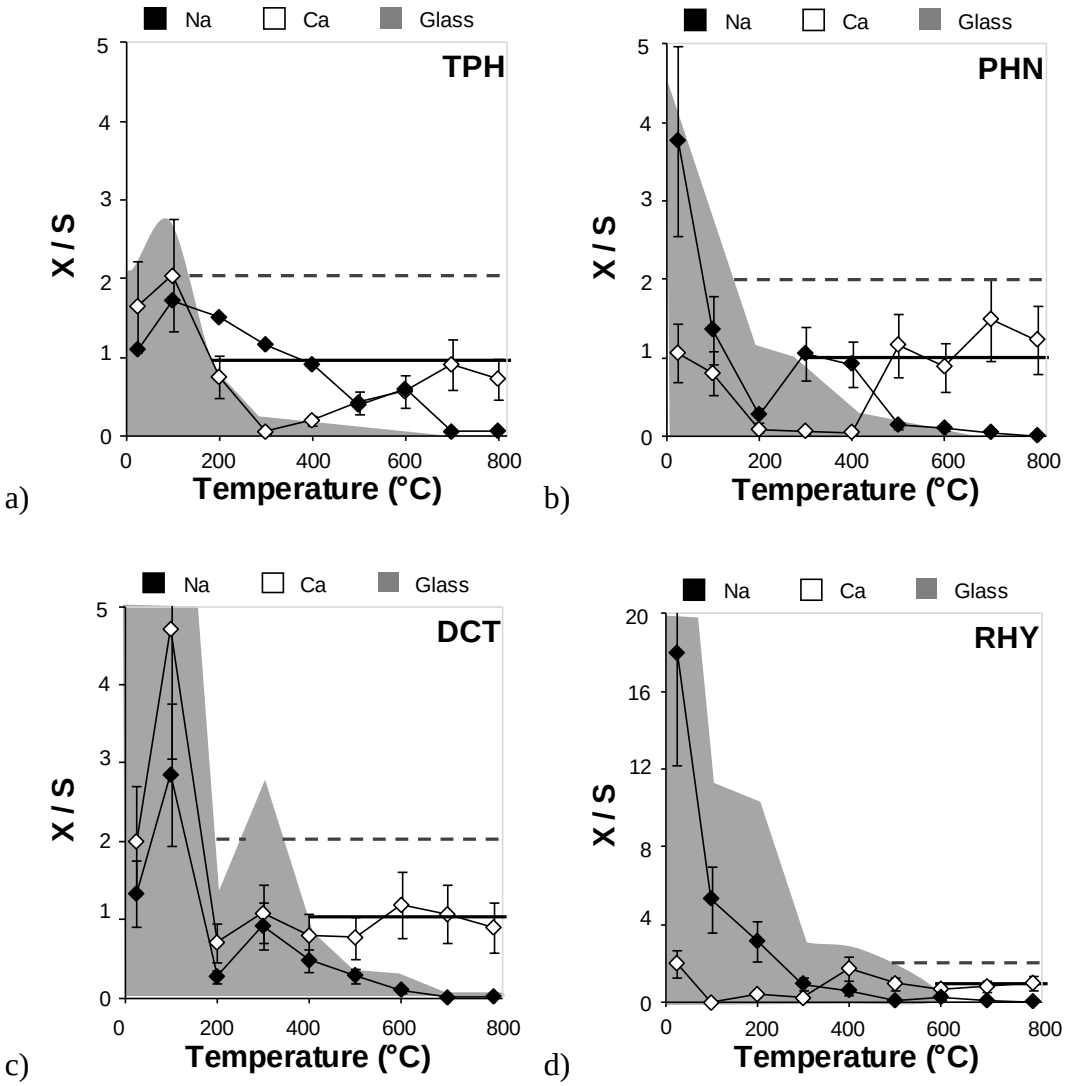

Fig. 6.2 *Plots of X/S ratios, where X is the concentration of Na or Ca in leachate solutions and S is the concentration of S in leachate solutions against temperature for the 'TP-V' experiment series. To illustrate the contribution of the glass dissolution and leaching component previously discussed in Chapter 5. The X/S ratio is therefore set with a cation value of 7 μmol m^{-2}, the previously assigned contribution of glass dissolution and leaching, and any X/S ratio which falls below the X/S ratio associated with glass dissolution and leaching must be attributed to that source. The dashed line indicates the leachate Na:S molar ratio which would be consistent with a solution originating from dissolution of Na_2SO_4, whilst the black line indicates the Ca:S molar ratio consistent with a solution derived from dissolution of $CaSO_4$.*

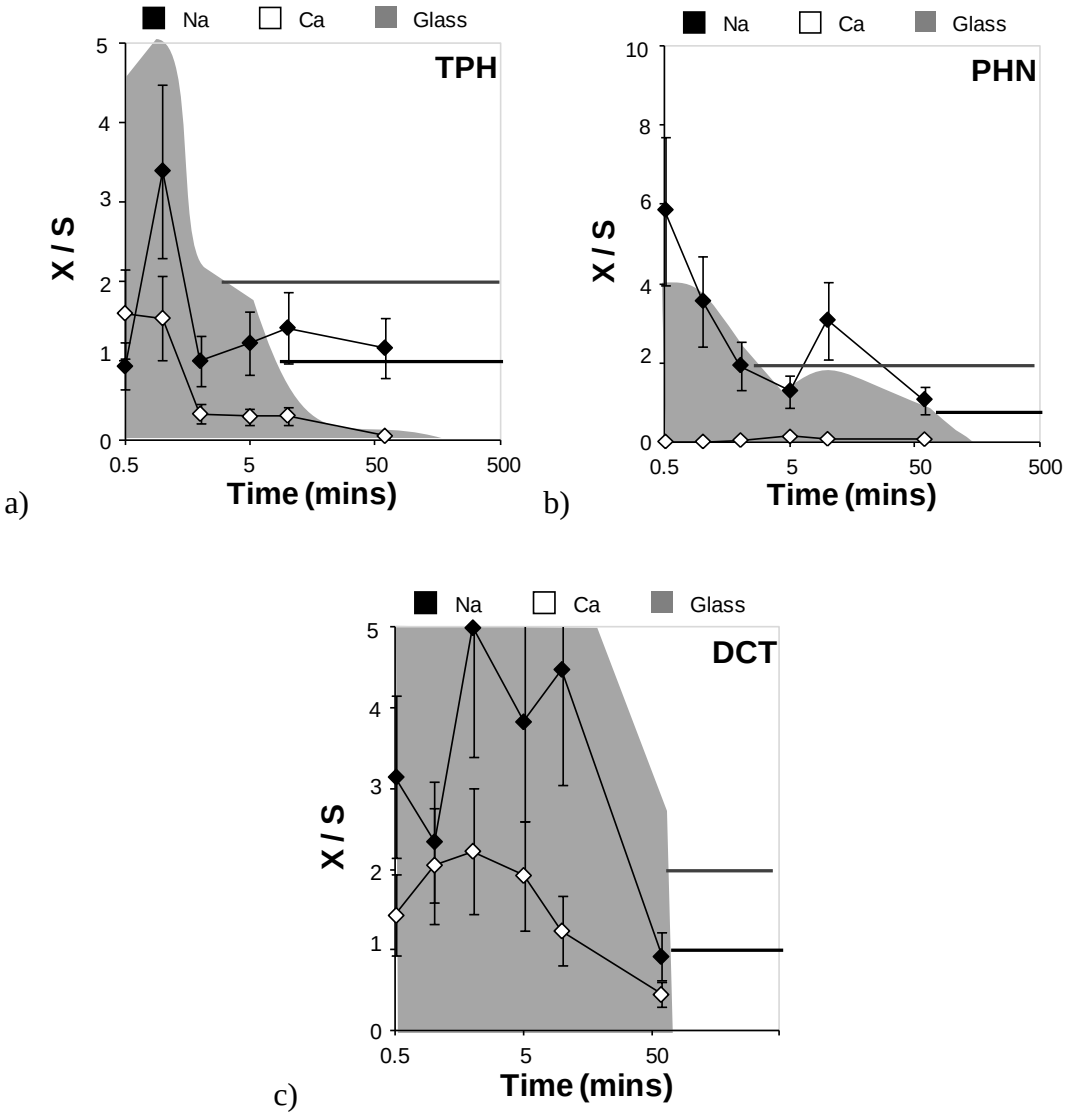

Fig. 6.3 *Plots of X/S ratios, where X is Na or Ca in leachate solutions and S is S in leachate solutions against exposure time for all glasses exposed to 1% SO_2/He/Air at 300°C as part of the 'TI-V' experiment series. To illustrate the contribution of the glass dissolution and leaching component previously discussed in Chapter 5. The X/S ratio is therefore set with a cation value of 7 µmol m^{-2}, the previously assigned contribution of glass dissolution and leaching, and any X/S ratio which falls below the X/S ratio associated with glass dissolution and leaching must be attributed to that source. The dashed line indicates the leachate Na:S molar ratio which would be consistent with a solution originating from dissolution of Na_2SO_4, whilst the black line indicates the Ca:S molar ratio consistent with a solution derived from dissolution of $CaSO_4$.*

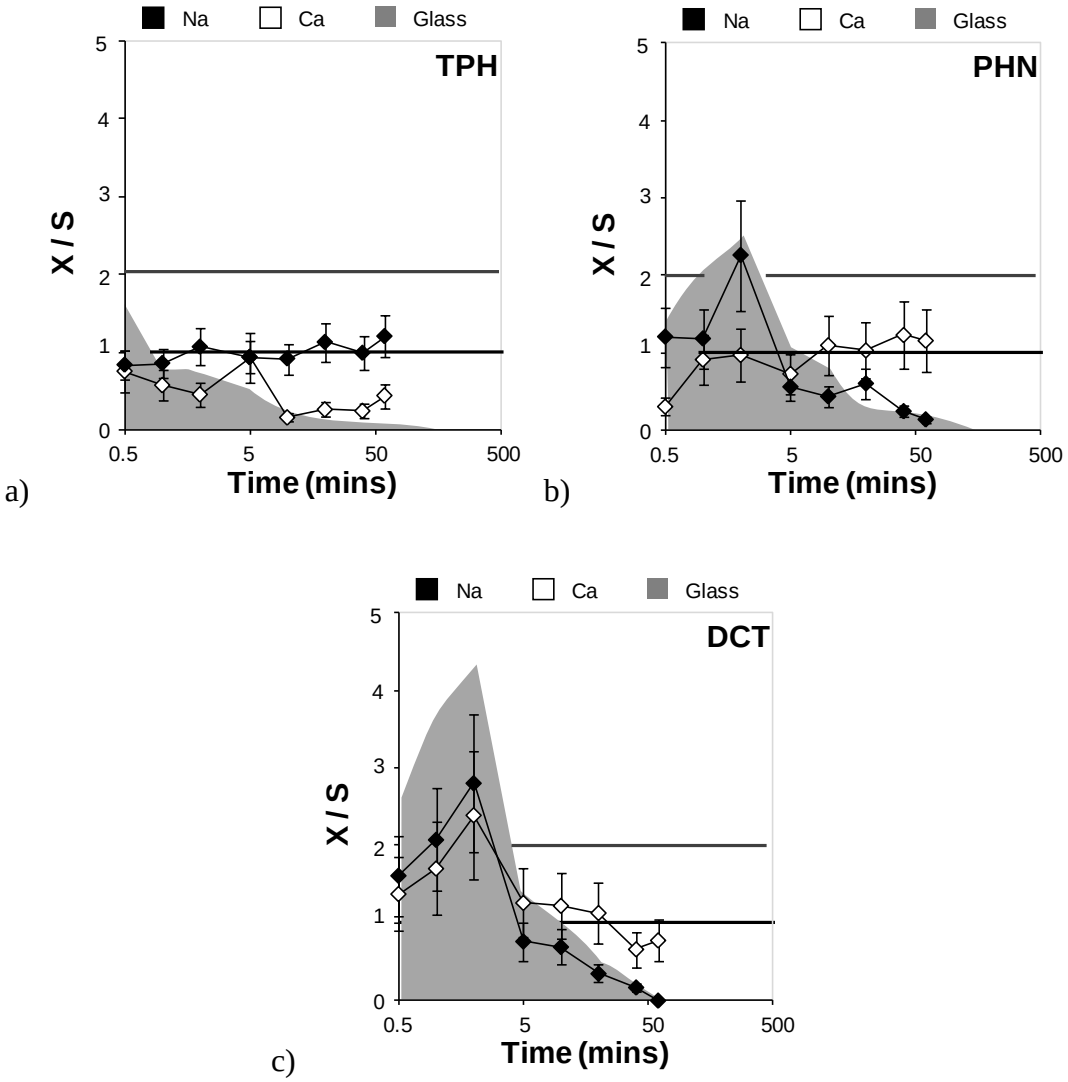

Fig. 6.4 *Plots of X/S ratios, where X is Na or Ca in leachate solutions and S is S in leachate solutions against exposure time for all glasses exposed to 1% SO_2/He/Air at 500°C as part of the 'TI-V' experiment series. To illustrate the contribution of the glass dissolution and leaching component previously discussed in Chapter 5. The X/S ratio is therefore set with a cation value of 7 µmol m^{-2}, the previously assigned contribution of glass dissolution and leaching, and any X/S ratio which falls below the X/S ratio associated with glass dissolution and leaching must be attributed to that source. The dashed line indicates the leachate Na:S molar ratio which would be consistent with a solution originating from dissolution of Na_2SO_4, whilst the black line indicates the Ca:S molar ratio consistent with a solution derived from dissolution of $CaSO_4$.*

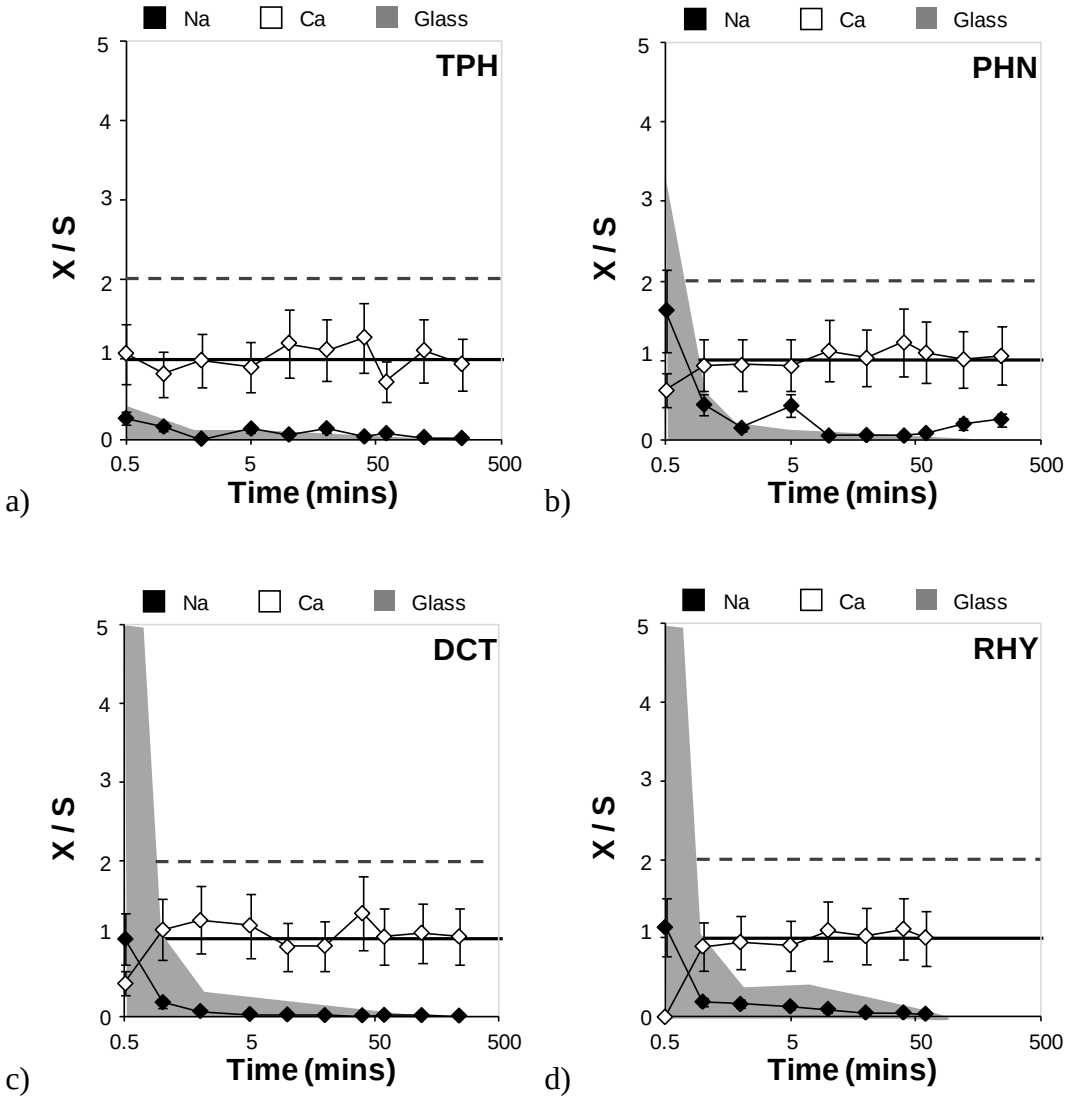

Fig. 6.5 *Plots of X/S ratios, where X is Na or Ca in leachate solutions and S is S in leachate solutions against exposure time for all glasses exposed to 1% SO_2/He/Air at 800°C as part of the 'TI-V' experiment series. To illustrate the contribution of the glass dissolution and leaching component previously discussed in Chapter 5. The X/S ratio is therefore set with a cation value of 7 µmol m^{-2}, the previously assigned contribution of glass dissolution and leaching, and any X/S ratio which falls below the X/S ratio associated with glass dissolution and leaching must be attributed to that source. The dashed line indicates the leachate Na:S molar ratio which would be consistent with a solution originating from dissolution of Na_2SO_4, whilst the black line indicates the Ca:S molar ratio consistent with a solution derived from dissolution of $CaSO_4$.*

It has not been possible to verify the exact nature of the reaction products formed under every experimental atmosphere and on every glass sample, but using XRD, XPS, SEM and spot-EDX via both SEM and TEM, it is possible to provide some insight into the Na-S and Ca-S compounds which have been formed.

Reference to previous leachate studies on glasses of similar compositions provides the first indications that the Na-S and Ca-S compounds formed are confined to a near-surface or even surface region. It was inferred from the approximate parity between $S_{leachate}$ and S_{total} that all the SO_2 adsorbed formed soluble salts, and hence that all soluble salts were removed in leaching. The maximum depth to which the reaction products may be found is therefore dictated by the maximum depth to which cations and anions are leached from the glass. The depth of leaching may be inferred from existing studies on alkaline-earth alkali silicate glasses using an identical leaching methodology to that of this study, as in the studies of Koenderink *et al.* (2000). Using Rutherford backscattering spectrometry to determine the depth of Ca and Na extraction and elastic recoil detection to determine the depth of H^+ penetration, Koenderink *et al.* (2000) observed that the depth probed by leaching was 47 nm in a four hour period, but that the depth from which Ca was extracted was significantly smaller, less than 20 nm. Since the glasses were not compositionally identical, it is cautiously estimated that any Ca-S and Na-S compounds formed must originate from a layer less than 50 nm in depth.

6.2.3. FORMATION OF Na_2SO_4 IN LOW SI GLASSES

Although only inferred to exist in the TPH glass at all temperatures below 600°C and over both short and long SO_2 exposure times, and possibly in the PHN glass at temperatures less than 500°C in 60 minute SO_2 chemisorption experiments (Fig. 6.2), the possibility of Na-S compounds on the glass surfaces was explored through XPS analysis.

The S ($2p\ ^3/_2$) peak of the 'TI-V' TPH glass at 500°C has been interpreted with two fitted components with peak midpoints at 169 eV and 167.7 eV (Fig. 5.37), attributed to sulphate and sulphite species respectively and consistent with those observed for both Ca and Na sulphates and sulphites (Baltrusaitis *et al.* 2007; Wagner 1975). By XPS analysis, Na/Si and S/Si ratios from the samples were found to correlate with each other under all exposure times, with an approximate 1:1 relationship (Fig. 5.36), and the ratio of Na/Si was observed to increase relative to its initial pre-exposure

value, which would be consistent with the emplacement of a Na-bearing deposit over the underlying silicate glass surface.

In addition to these data, the interpretation of the Na (1s) spectra (Fig. 5.38) also provides evidence for the formation of Na_2SO_4. In the initial TPH surface, the Na (1s) spectra was fitted with a single component attributed to Na in the glass network at 1069 eV, but under the effects of SO_2 at 500°C up to exposure times of 20 minutes, the Na (1s) spectra was observed to develop a higher binding energy component at 1071.8 eV, consistent with the formation of an ionic salt rather than a glass network bond with more covalent character, consistent with previously observed binding energies of Na_2SO_4 (Turner *et al.* 1980; Wagner 1975). There was no evidence for the presence of the Na_2SO_4 component in the samples exposed to SO_2 chemisorption for 60 minutes at 500°C, even though leachate compositions still indicate that Na-S compounds are likely to exist. There is no explanation for the apparent absence of the Na_2SO_4 peak in the latter sample. To further explore the formation of Na-S compounds in the TPH sample at 500°C would require further studies conducted under SO_2-free atmospheres at the same temperature, combined with spot-EDX analysis via SEM or TEM to further verify the existence of Na_2SO_4 on the sample surface.

6.2.4. FORMATION OF $CaSO_4$ IN ALL GLASSES AT HIGH TEMPERATURE

Study of samples exposed to SO_2 at 800°C for 60 minutes by XPS determined that the Ca-S ratios and peak binding energies identified previously were indicative of surface $CaSO_4$. The identification of $CaSO_4$ was based on the 1:1 ratio between Ca/Si and S/Si observed in the surface probed by XPS (Fig. 5.13) and on the shifts observed in the binding energies of the S (2p) and Ca ($2p\ ^3/_2$) spectra relative to those of the initial untreated glass (Fig. 5.46 to Fig. 5.49). The initial Ca ($2p\ ^3/_2$) spectra for all glasses was fitted with a single component at approximately 347.0 - 347.3 eV. In Chapter 4, it was noted that a Ca peak at 347 eV could be attributed to Ca in the glass network in a range of possible configurations, but most likely either as Ca in network modifying roles (i.e. Ca-silicate) or Ca as a terminal cation exposed by glass fracture with adsorbed CO_2 or H_2O (i.e. $CaCO_3$, $Ca(OH)_2$). Under the effects of SO_2 for 60 minute exposure times, the peak at 347 eV was entirely replaced by a 347.6-348.0 eV peak, with the exception of the RHY, which still showed a 20% contribution from the 347.3 eV fitted peak. The peak at 347.6 - 348.0 eV was previously attributed to the presence of $CaSO_4$ (Baltrusaitis *et al.* 2007). The increase in binding energy from 347 eV to 348 eV is interpreted to be a result of the ionic nature of the salt which removes

valence electrons from coordination with a neighbouring cation and hence, results in a shielding effect on the core electrons from the nucleus. In addition to the observed alteration in the Ca ($2p\ ^{3}/_{2}$) spectra, S ($2p\ ^{3}/_{2}$) binding energies (Fig. 5.14) are also consistent with the presence of both Na_2SO_4 (Turner and Schreifels 1996; Wagner 1975) and $CaSO_4$ (Baltrusaitis *et al.* 2007), but is assumed to be the latter due to the absence of any shift in the Na (1s) spectra as in the 'TI-V' TPH at 500°C.

At least some of the Ca-S compounds formed in the 'TP-V' chemisorption experiments at 800°C are therefore discrete $CaSO_4$ deposits on the sample surfaces. The observed increase of surface Ca/Si ratios in the glasses exposed to SO_2 relative to those surfaces without SO_2 exposure (Fig. 5.43) is indicative the deposition of Ca bearing phases over the underlying silicate surface, obscuring it. Since the components of the aluminosilicate network remain identifiable, it is likely that the deposit is patchily distributed rather than entirely covering the glass surface. This is consistent with the observations derived from SEM analysis. Both the TPH and PHN glasses exposed to 1% SO_2/He/Air for 60 minutes at 800°C showed extensive formation of surface deposits (Fig. 5.7, Fig. 5.8). In the PHN glass, spot-EDX analysis was able to determine that the deposits analysed had Ca/Si and S/Si ratios consistent with the presence of surface $CaSO_4$ (Fig. 5.8). Although the same identification could not be made via SEM analysis of the TPH glass, spot-EDX and elemental mapping was able to identify the Ca-S compounds on the TPH glass (Fig. 5.18, Table 5.17, Fig. 5.19). The difficulties in identifying the crystal phases formed in the TPH glass by SEM (Table 5.12) is attributed to the presence of additional crystallites which form extensively in the underlying glass. Spot-EDX analysis of the crystals within the glass via the TEM identified a Ca, Mg, Fe and Al bearing phase, consistent with the identification of augite by XRD (Fig. 5.40). In SEM analysis, the presence of such crystallites would interfere with the weaker signal of smaller surface crystallites and deposits. From data from both XRD (Fig. 5.4) and XPS (Fig. 5.14), the Ca-S bearing phases formed on the TPH surface are concluded to be $CaSO_4$ alone. Since only $CaSO_4$ was identified in the other glasses, it is therefore concluded that all surface deposits in all glasses are $CaSO_4$ at 800°C.

It was previously hypothesised that the maximum depth of $CaSO_4$ formation was limited to the maximum depth of leaching, a near surface region less than 50 nm deep. TEM analysis of the TPH glass has demonstrated that no S has infiltrated into the bulk glass and that $CaSO_4$ compounds are solely confined to the surface. Since the solubility

of S is higher in low Si glasses than in high Si glasses, it is reasonable to assume that no S has infiltrated the other glasses either, and therefore that in all glasses, -S compounds are purely surficial. This hypothesis is supported by analysis of the optical SEM images of the PHN glass (Fig. 6.6). A flat or near-flat plane of an exposed particle was selected for analysis, and five random regions were selected. By contrast enhancement, it was possible to separate the glass and deposit phases through use of open-source image analysis tools (GIMP 2.6), and so to determine the coverage of the surface in the five regions by the surface deposits to be 35±9% (Fig. 6.6). The approximate size of each particle along its longest axis was estimated to be between 100 nm and 3500 nm in diameter through scaling (Fig. 6.6). The range of depths of the deposits was estimated to be between 50 nm and 1000 nm by the analysis of a plane oriented parallel with the viewing angle, placing the deposits in profile (Fig. 6.6). Using the estimated deposit dimensions and coverage from image analysis, it is therefore possible to estimate the mass of $CaSO_4$ on the surface for comparison with the observed leachate data. If the density of $CaSO_4$ is 2960 kg m^{-3}(Lide 2005), the calculated molar mass of $CaSO_4$ on the glass surface is between 378 µmol m^{-2} and 7560 µmol m^{-2}. The actual mass of $CaSO_4$ formed, assuming that all Ca and S in leachate solutions was in that phase, was 153 µmol m^{-2}, and even assuming that only the largest deposits (p_d ~ 1000 nm) were $CaSO_4$, only a surface coverage of <1% would be required to generate the observed mass of $CaSO_4$. Based on these estimates, it is considered to be feasible for the chemisorption of SO_2 on the glasses at 800°C under the 'TP-V' experimental conditions to result in the formation of $CaSO_4$ compounds solely at the surface.

Although there is strong evidence to indicate the presence of $CaSO_4$ crystallites at 800°C in 60 minute SO_2 chemisorption experiments, it has not been possible to gather a similar degree of evidence for all other experiments. It is possible, however, to infer the presence of such deposits using the limited data available. XRD has identified discrete $CaSO_4$ deposits at temperatures down to 600°C after exposure to SO_2 for 60 minutes in the TPH and PHN glasses, and to 700°C in the other glasses (Fig. 5.4). No other S bearing phases were identified. Molar ratios of leachate Ca and S were consistent with the presence of $CaSO_4$. The XPS data from the DCT glass analysed across all temperatures between 300°C and 800°C is indicative of the presence of $CaSO_4$ down to temperatures of 400°C, as S (2p) peaks remain unchanged at 169 eV at temperatures of 400°C and above (Fig. 5.11), the correlation between Ca/Si and S/Si ratios is consistent down to 500°C (Fig. 5.13) and the enrichment in the Ca/Si ratios relative to the pre-experiment surface of the DCT glass indicate that $CaSO_4$ may be

being deposited on the sample surface down to temperatures of 500°C (Fig. 6.7). The Ca ($2p\ ^3/_2$) peak does not provide any evidence to support the hypothesis further, as only a single broad peak could be fitted to the spectra from that analysis (Fig. 5.12). Overall, these results suggest that $CaSO_4$ is deposited as crystalline surface deposits at temperatures at least as low as 500°C, but the concentrations of adsorbed S at these temperatures may limit the extent to which such phenomena can be observed. At the present time, it can only be confidently stated that $CaSO_4$ crystallites are formed on the surface at 600°C and above. Further microscope analysis is required to identify the presence of crystallites at temperatures below 600°C.

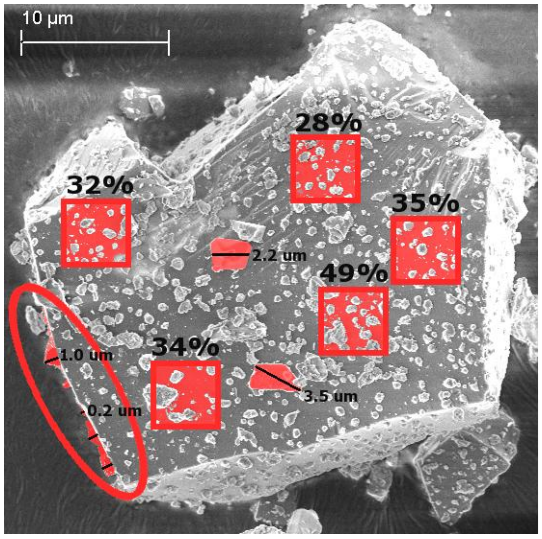

Fig. 6.6 *Digital image analysis of Fig. 5.8, illustrating the regions and deposits analysed to derive the estimated surface coverage (red squares) and deposit dimensions (red shaded deposits) of the PHN glass exposed to 1% SO_2/He/Air.*

The time-series experiments indicated that the formation of $CaSO_4$ deposits on the sample surface may occur at the highest temperatures even at brief timescales on the order of minutes. It is known from leachate analysis that the primary reaction product at 800°C time series experiments is a Ca-S compound (Fig. 5.22); XRD analysis confirmed the presence of the primary $CaSO_4$ diffraction peak in the TPH glass after only a 5 minute exposure to SO_2 at 800°C (Fig. 5.26); and SEM analysis of the PHN glass exposed to SO_2 for 2 minutes at 800°C showed the presence of surface deposits of unknown composition (Fig. 5.27). These observations are consistent with the formation of $CaSO_4$ deposits on the sample surface, and may indicate that only a brief exposure time is required to initiate their formation.

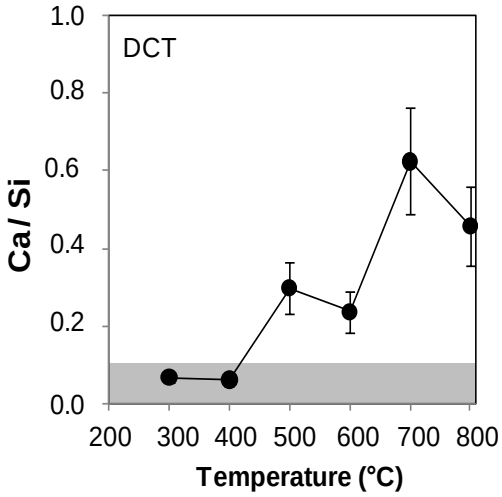

a)

Fig. 6.7 *Ca/Si ratios of the 'TP-V' DCT glass exposed to 1% SO_2/He/Air for 60 minutes at 300°C to 800°C relative to the ratio of Ca/Si in the initial DCT surface, indicated by the grey filled region.*

6.3. MECHANISM OF SO_2 CHEMISORPTION AND REACTION PRODUCT FORMATION

In the following section, the mechanisms and controlling variables driving the SO_2 chemisorption and reaction product formation on the glass surfaces in this study are detailed.

6.3.1. BASIC MECHANISM OF REACTION PRODUCT FORMATION

In studying the reaction products formed during SO_2 chemisorption on glass surfaces, it has been inferred that all of the reaction products are deposited on the glass surface as discrete crystalline phases. Considering $CaSO_4$ only, the mass of reaction products formed on the sample surface was considerable. It was previously demonstrated in Fig. 6.1 that $S_{leachate}$ is approximately equal to S_{total}, and therefore, $Ca_{leachate}$ must be indicative of all $CaSO_4$ formed during SO_2 chemisorption experiments. By comparing $Ca_{leachate}$ to the total Ca in the glasses, Fig. 6.8 shows that the amount of Ca which is converted to $CaSO_4$ is as much as 50-60% of the total Ca in those glasses. It has already been demonstrated that $CaSO_4$ is deposited on the sample surface, and it is also known that no previous enrichment in the initial surface Ca/Si ratios relative to those of the bulk glass existed which could explain the high Ca extraction. It is therefore hypothesised that in order to emplace such quantities of $CaSO_4$ on the sample surface, a mechanism must exist to resupply the surface of the glass with Ca by diffusion from the bulk particle. The proposed mechanism for SO_2 chemisorption would therefore actually consist of a three component model, including SO_2 chemisorption onto surface sites, the formation of the crystalline $CaSO_4$ reaction product, and a diffusion mechanism which sustains that reaction to emplace the quantities of $CaSO_4$ observed.

6.3.2. SO_2 CHEMISORPTION SITES ON THE GLASS SURFACE

The identification of specific chemisorption sites was achieved through interpretation of XPS analysis on the surfaces of the glasses exposed to SO_2 under the conditions of the ‘atmosphere variable’ experiments.

XPS observations in section 6.2.4. found that the initial Ca (2p 3/2) peaks at 347.0-347.3 eV were converted to a peak at 347.6 – 348.0 eV consistent with the formation of $CaSO_4$. The contribution of the peak at 348 eV was found to be 100% in the TPH, PHN and DCT glasses, but approximately 20% in the RHY (Fig. 5.46, Fig.

5.49). The near total conversion of the peak attributed to the initial glass surface to $CaSO_4$ is representative of the conversion of Ca-based chemisorption sites on the glass surface to $CaSO_4$, as the lack of any remnant peak at 347 eV indicates that $CaSO_4$ deposits have formed over all Ca sites, apart from in the case of the RHY glass. The RHY glass behaved differently, and the remnant peak at 347 eV may represent Ca-based chemisorption sites which have low reactivity to SO_2 or which SO_2 is otherwise unable to access. From these data it is concluded that all or the majority of Ca in the glass surface is reactive to SO_2 during the temperature variable experiments.

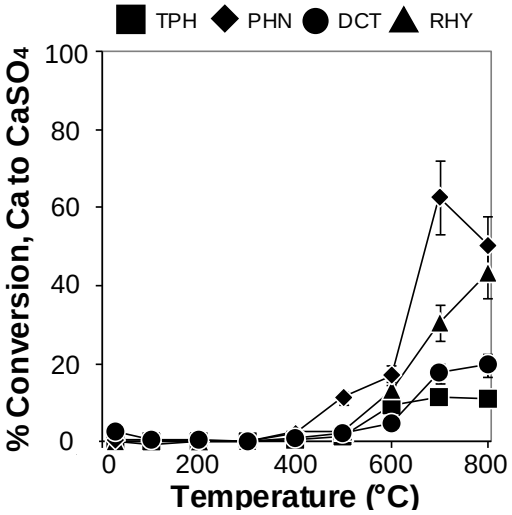

Fig. 6.8 *Conversion of Ca to $CaSO_4$ from the leachate compositions of the 'TP-V' experiment series (Table A5 to Table A11) and the bulk Ca content of the glasses (Table 5.5), displayed as % of the total mass of Ca in each glass.*

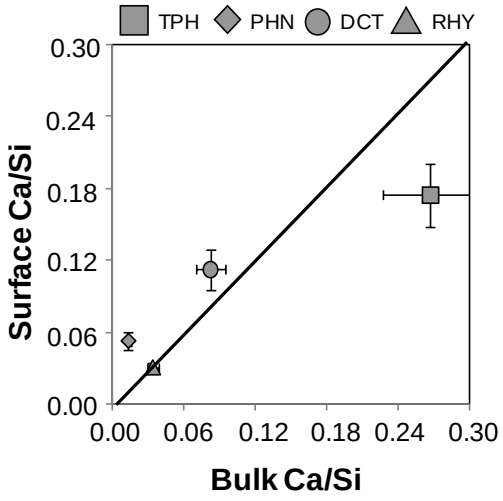

Fig. 6.9 *Ca/Si ratios of the initial pre-experiment glass surface, derived from XPS analysis (Table 5.7) compared to Ca/Si ratios of the pre-experiment bulk glass from data in Table 5.5.*

During the 'AT-V' experiments, it was concluded that the reactivity of the Ca sites on the sample surface was altered by high temperature exposure to different experiment atmospheres. The effect of the He-only pre-treatment was observed to result in a decrease in the relative contribution of S to the glass surface, as determined by XPS, and to the total mass of $CaSO_4$ formed during the SO_2 chemisorption experiments, as inferred from leachate analysis (Fig. 6.10). The decreased relative contribution of S to the glass surface composition is interpreted as a decrease in the number of surface sites which are adsorbing SO_2 and forming crystalline $CaSO_4$ deposits. The hypothesised decrease in chemisorption on Ca surface sites is most pronounced in the TPH, PHN and DCT glasses, which show S/Si ratios which are 27-35% lower than their untreated counterparts, whilst the RHY glass shows no deviation. In the case of the SO_2 chemisorption inferred from leachate analysis, the trend is different, in that total S is decreased to greatest extent in the DCT and TPH samples by 35% and 27%, and by 15% for the RHY and PHN glasses.

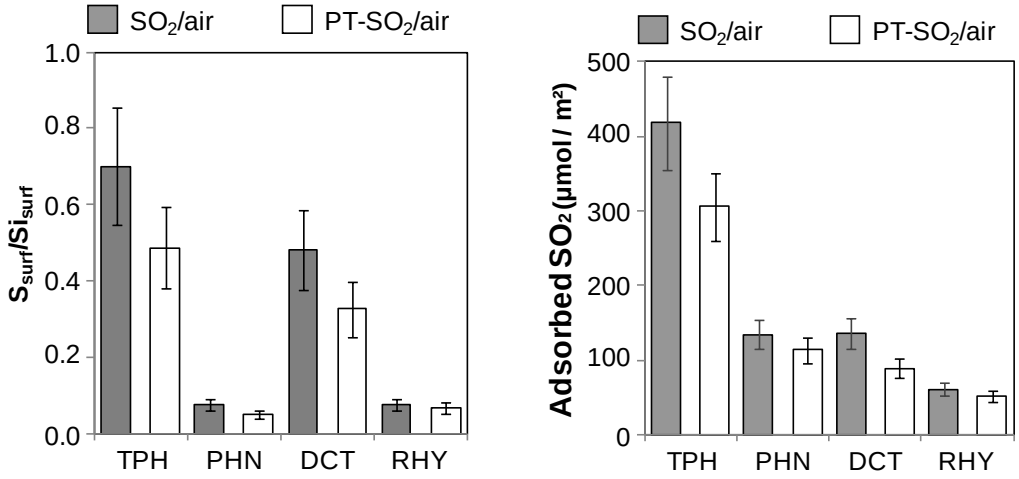

Fig. 6.10 *Comparison of (a) the surface S/Si ratios and (b) the total SO_2 estimated by leachate S concentrations for the volcanic glass samples exposed to 1% SO_2/He/Air at 800°C for 60 minutes with and without the 60 minute pre-treatment.*

The He-only pre-treatment prior to the introduction of SO_2 is hypothesised to reduce the reactivity of some Ca-based chemisorption sites to SO_2 by altering the glass structure surrounding them. Comparison of the ratios of Ca/Si and S/Si, which without pre-treatment demonstrated a 1:1 ratio for the TPH, PHN and DCT glasses, showed that with pre-treatment, the ratios of the pre-treated sample surface are depleted in S by 30% relative to Ca (Fig. 6.11). If the Ca ($2p\ ^3/_2$) peak at 348 eV is assumed to represent $CaSO_4$ entirely, the total mass of Ca which has reacted with $CaSO_4$ on the sample

surface can be estimated, and Fig. 6.12, shows that plotting the total contribution to the surface of the 348 eV fitted peak gives the same approximate parity between S/Si and Ca/Si ratios observed in untreated glasses. The contribution of the lower binding energy component increased by 36 ± 12% on average for the PHN, TPH and DCT glasses, but was unchanged in the RHY. This may be interpreted as an alteration to the surface structure and bonding environment of the lower Si content glasses, converting accessible Ca-based chemisorption sites into unreactive sites on the glass surface.

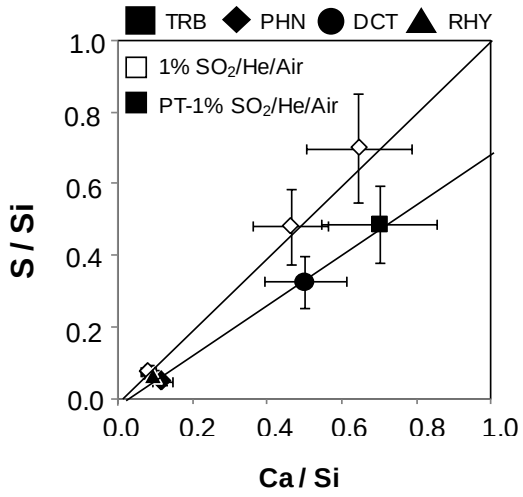

Fig. 6.11 *Comparison of Ca/Si and S/Si ratios from XPS analysis of the pre-treated (Table 5.27) glasses (black) and untreated (Table 5.15) glasses (white) exposed to 1% SO_2/He/Air at 800°C for 60 minutes. XPS experimental and analytical error of ±22 % is applied.*

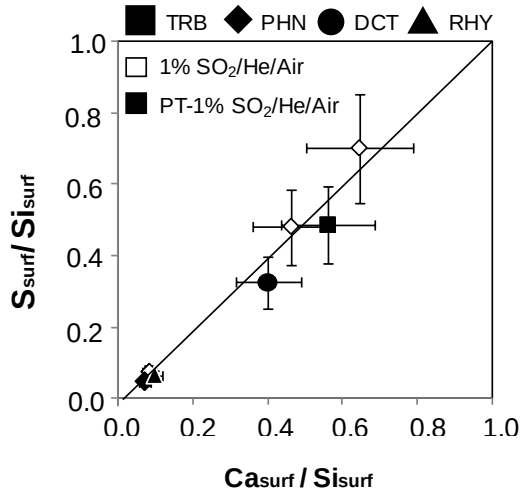

Fig. 6.12 *Comparison of the ratio of the relative surface composition attributed to the 348 eV component and S/Si ratios from XPS analysis of the pre-treated glasses (black) and untreated glasses (white) exposed to 1% SO_2/He/Air at 800°C for 60 minutes (Table A27 to 0, Table 5.15,Table 5.27). XPS experimental and analytical error of ±22 % is applied.*

The presence of surface sites which are poorly reactive to SO_2 is also evidenced in the time-series analysis of the TPH glass exposed to 1% SO_2/He/Air at 800°C (Fig. 5.32). The spectra show that over exposure times of up to 20 minutes, there remains a small peak at a low binding energy relative to $CaSO_4$. In the initial glass surface, the Ca peak was found at 347.3-347.0 eV, but from 1 minute to 20 minute exposure times at 800°C, the binding energy peak was fitted at 346.5 eV. The disappearance of the low binding energy peak with increasing exposure time supports the hypothesis that some surface sites are only poorly reactive to SO_2 chemisorption. Identifying these sites in more detail is not possible at this time.

The data presented above indicates that not only are there some Ca sites on the sample surface which are unreactive to SO_2, but that the number and reactivity of these sites on the sample surface may be altered by high temperature exposure and interaction with different experimental atmospheres. The changes to the sample surface may then in turn alter the degree of SO_2 chemisorption and hence impact on the total mass of reaction products formed. These phenomena can be explained as a combination of surface and bulk interactions, but this first requires a further discussion of the underlying mechanism of SO_2 adsorption, reaction product formation and Ca resupply.

6.3.3. SURFACE SEGREGATION OF $CaSO_4$

Irrespective of the adsorption sites upon which SO_2 adsorption occurs, the formation of crystal deposits at the glass surfaces is known to occur as a response to the disequilibrium and stresses imparted to the glass fracture surface. The removal of certain compounds from the surface to form discrete crystalline phases independent of that surface is one possible way to reduce the high surface energy and tension generated by the fracture (Dunken 1982). The glass surfaces used in the chemisorption experiments are generated from the fracture of the bulk glass network, which as previously discussed in Chapter 4, creates a surface of broken bonds which have a high surface tension and energy due to the absent third dimension of coordination. The fracture free surface energies of soda-lime glasses were found to range between 1.7 - 11 J m^{-2} (Bikerman 1978), whilst as in liquids, surface tension and free surface energy are equivalent, the free surface energy of a fully relaxed melt surface can be calculated for temperatures of 900°C. The melt surface energy may be calculated by reference to the initial glass surface composition (Table 5.7), equation [6.1] and the surface tensions (σ_i) of the individual components (Dietzel 1942) of the glass to be 0.5 – 0.6 J m^{-2} (Table

6.2). The free surface energy of the glasses used in this experimental study could therefore range from 0.5 J m^{-2} to up to 2 orders of magnitude greater energy.

$$\sigma = \sum \sigma_i C_i \qquad [6.1]$$

Table 6.2. *Calculated surface energies assuming a relaxed melt surface at 900°C based on equation [6.1] (Dietzel 1942; Scholze 1990) and XPS surface compositions of the initial glass surfaces (Table 5.7) and those with compositions as observed in surfaces exposed to 1% SO_2/He/Air at 800°C for 60 minutes (Table 5.15) without pre-treatment assuming (1) that all compounds apart from S made up the melt surface and (2) that all compounds apart from Ca and S made up the melt surface.*

	Calculated surface energy (J m^{-2})			
	TPH	**PHN**	**DCT**	**RHY**
Initial	0.67	0.53	0.67	0.51
Exposed surface 1	0.69	0.51	0.65	0.51
Exposed surface 2	0.58	0.49	0.56	0.48

If the formation and segregation of crystal deposits from the glass surface occurs to lower the energy of that surface, then the same would be expected of $CaSO_4$ crystals. The chemisorption and oxidation of SO_2 onto a Ca-based surface site may draw sufficient electron density from the bond with the underlying surface to weaken that bond and permit the removal of Ca from the glass network. Removing Ca from the glass surface decreases the overall surface energy of the melt (Scholze 1990), and the surface energy at the interface between the particle and the atmosphere. The free surface energy of the $CaSO_4$ (100) crystal plane, for example, is approximately 0.540 J m^{-2} (Walton and Whitman 1964), whilst the glass surface is unlikely to be fully relaxed and may not achieve the calculated 0.5-0.6 J m^{-2} surface energies, as these were calculated for 900°C temperatures after full equilibration of the surface. Glass surface energies are therefore likely to exceed those of the $CaSO_4$ crystals, even with the effect of SO_2 chemisorption reducing the overall surface energy by perhaps up to 0.08 J m^{-2} (Parikh 2006). $CaSO_4$ crystallisation and segregation from the glass surface might create a lower energy surface-atmosphere interface than previously existed.

The formation of surface crystallites, whether sulphur bearing or otherwise, is inferred to occur as a component of surface reequilibration, but is likely to be dependent

on the activation energy required to initiate surface segregation. Since the energy available increases with increasing temperature, the surface segregation mechanism may be temperature dependent. In studies of Na_2SO_4 on glass surfaces in response to an SO_3 bearing atmosphere, a 'bloom' of Na_2SO_4 was observed on the sample surface even at temperatures of 250-300°C, and therefore, surface segregation may act at all temperatures investigated (Volf 1984). As the bond between Ca in network modifying roles in the glass network is stronger than those of Na (Scholze 1990), it may be that the energy required for surface segregation of $CaSO_4$ crystals is higher than that for Na_2SO_4 and so may not occur until a higher temperature. As an illustration of this, in studies of CaF_2 and $CaSiF_6$ on glass surfaces, Óskarsson (1980) observed the transition from the latter to the former at approximately 600ºC, possibly indicating the removal of Ca from the glass network. However, in the case of $CaSO_4$, XPS analysis in the previous section did indicate that in the DCT glass, formation of discrete $CaSO_4$ deposits may occur even at temperatures of 500°C, and perhaps even 400°C.

6.3.4. CA MIGRATION THROUGH THE BULK VIA DIFFUSION

The segregation of $CaSO_4$ and perhaps Na_2SO_4 is considered to remove a Ca, or Na, cation from the glass network, which leaves a divalent or monovalent cation vacancy in the glass network which is then filled by diffusion from the underlying glass. This hypothesis is based upon the observed regions of Ca depletion which were observed by TEM element mapping (Fig. 5.19), as one interpretation of the TEM Ca map is that Ca is being extracted from that region and drawn to the area beneath the $CaSO_4$ deposit, which is in essence a diffusion reaction. Since Ca is the dominant cation which reacts with SO_2 in experiments, this is the cation which is the focus of discussion.

Removing Ca from the network may reduce the specific free surface energy, the free energy increase per unit surface area, of the melt if the network structure reequilibrates to the new composition. Such a reduction is illustrated by calculations of specific free surface energy using equation [6.1] (Scholze, 1990), comparing the surface energies for the glass surface after exposure to 1% SO_2/He/Air at 800°C assuming that Ca is either a part of the glass network or removed from that network by surface segregation to form $CaSO_4$ (Table 6.2). If Ca diffuses to the surface, however, the surface energy may not be reduced and so the continued segregation of Ca via SO_2 chemisorption, leaving a vacancy which is then filled and then segregates may be the basic mechanism for the resupply of Ca to the surface.

6.3.4.1. CHARGE COMPENSATION REQUIREMENT

Extracting Ca from the bulk glass particle to the surface is a mechanism by which charge is transferred out of the bulk particle and to the surface. If the extraction of Ca is sustained, the removal of ($^{2+}$) charge from the glass would eventually make further extraction of Ca impossible due to the strong negative charge within the bulk glass. To preserve the electrical neutrality of the glass, and to maintain the bulk to surface flow of divalent Ca cations may require a charge compensation mechanism (Douglas and Isard 1949). It is hypothesised that in order to maintain electrical neutrality, the outward flux of divalent cations from the glass is compensated by an inward flux of electron holes (h^+). Such a mechanism is well known in studies of high temperature oxidation of basaltic glass (Cook and Cooper 2000; Cooper et al. 1996). In those previous studies, the inward flux of electron holes is derived from the oxidation of Fe(II) to Fe(III), and created a structural alteration which behaves as a divalent cation vacancy. The Fe oxidation reaction propagates into the glass, and is charge compensated by the counterflux of divalent cations to maintain electrical neutrality forms MgO and CaO microcrystallites at the glass surface.

Such a mechanism is consistent with some of the observations of this study. The depleted Ca and Mg regions identified by TEM (Fig. 5.19) indicate that these cations are mobile, which is consistent with the proposed divalent cation diffusion mechanism above. The formation of the augite and Fe-bearing phases (Fig. 5.19) are also consistent with this hypothesis. The oxidation reaction would drive the formation of sulphates by providing the supply of Mg and Ca to the surface via the vacancies produced by Fe oxidation. When the chemical potential gradient imparted by the SO_2/air atmosphere is removed, any Fe, Ca and Mg remaining in close association may then precipitate with neighbouring Al and Si to form the augite phase. The formation of Fe-bearing phases, including augite, underlying the $CaSO_4$ deposits is also consistent with the oxidation of Fe(II) to Fe(III). In the oxidation studies, precipitation of ferrites occurred when there were insufficient alkali metals available to stabilise Fe(III) in tetrahedral coordination (Smith and Cooper 2000). In the tephrite glass in this study, with its high Ca content, high Fe, Ca and Mg content would likely leave insufficient Na to meet the charge compensation requirements, and the formation of the Fe-bearing crystals would therefore be expected.

6.3.4.2. ACTIVATION ENERGY REQUIREMENT

In order for a diffusion mechanism as described above to occur requires activation energy to initiate the jump from a filled to vacant site. Provided that the formation of reaction products increases exponentially with increasing temperature, and so follows an Arrhenian first order reaction, activation energy can be calculated from equation [6.2].

$$A = A_0 \exp\left(\frac{Q}{RT}\right) \qquad [6.2]$$

In equation [6.2], A and A_0 are the final and initial values of the variable under investigation, Q is the activation energy, and R and T are the ideal gas constant and the experimental temperature in Kelvin respectively (Doremus 1973). Since Ca, S and Na, the latter up to 500ºC, all show a first order relationship (Fig. 6.13), activation energy can therefore be calculated between 300ºC and 800 ºC for Ca and S, and between 200-500 ºC for Na in the TPH glass.

The rate of Ca extraction from the glass, as measured by leachate compositional data, is used as an estimate for the rate of increase of $CaSO_4$ formation on the sample surface. It has already been established that leaching extracts all soluble salts emplaced on the glass surface, but S cannot be relied upon to measure $CaSO_4$ formation due to the concurrent presence of Na_2SO_4 in the TPH glass. The rate of increase in Ca extraction is calculated from Table A13, Table A18 and Table A23 for the TPH and PHN glass at 10-60 minute exposure times, where the rate of Ca increase in the leachate is constant, indicating steady-state reactions. The activation energy of the mechanism driving Ca formation can be estimated (Fig. 6.14, Fig. 6.15), as the natural logarithm of the rate is related to the activation energy by the gradient of the relationship to inverse temperature (Housecroft and Constable 1997).

Both the PHN and TPH glasses indicate an approximate activation energy between 60-75 kJ mol^{-1} (Fig. 6.14, Fig. 6.15), though the quality of the data at 300°C is a limiting factor on this calculation, and between 500 and 800°C, the activation energy may be lower than the estimated value. Calculations between 500°C and 800°C indicate that the activation energies may be between 20-35 kJ mol^{-1}. The activation energy for diffusion of divalent cations in response to Fe surface oxidation through a basaltic glass heated between 400-1400°C in argon and air atmospheres was found to be of the order of 100 kJ mol^{-1} for glass chunks. However, for glass powders with p_d greater than 300

μm, the activation energy was found to be on the order of 20-32 kJ mol^{-1} (Burkhard 2001).

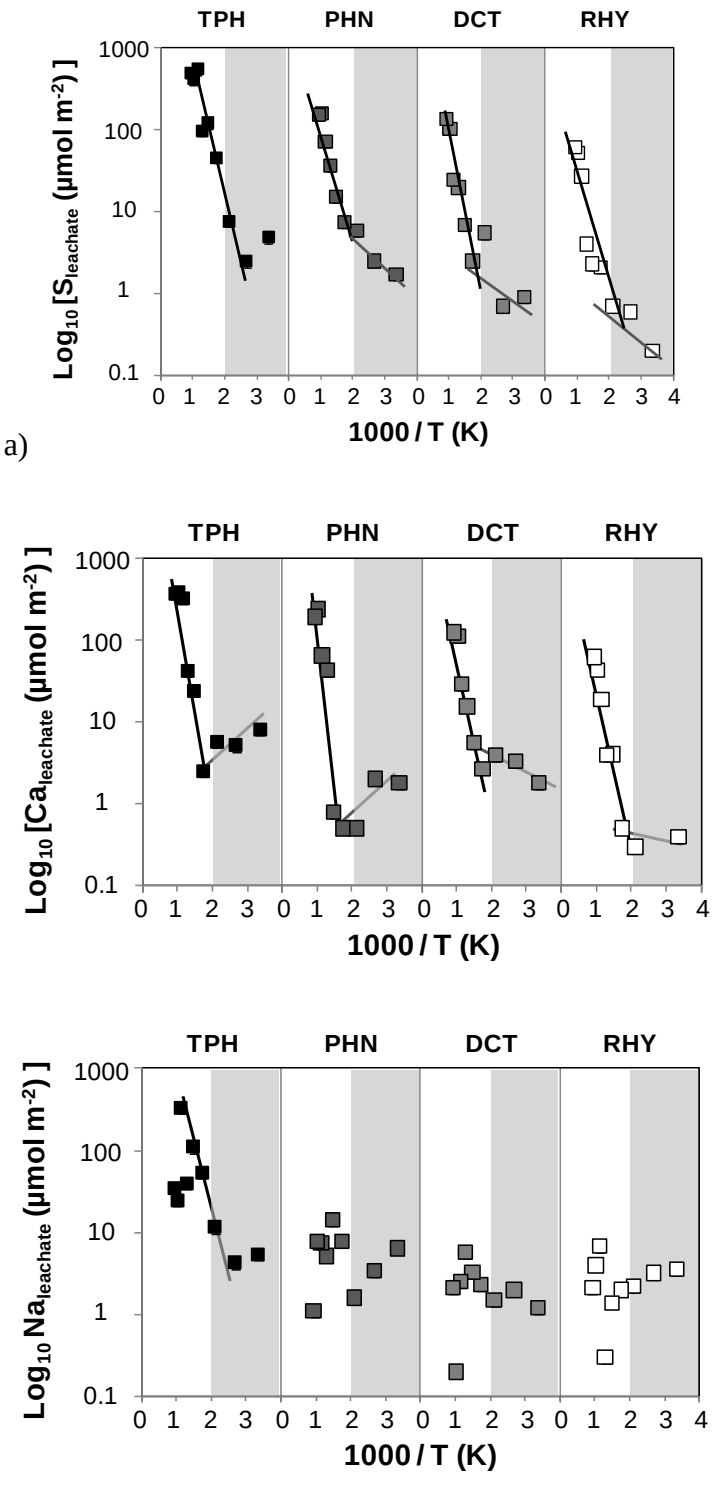

Fig. 6.13 *$S_{leachate}$ (a), $Ca_{leachate}$ (b) and $Na_{leachate}$ (c) compositions plotted on a log_{10} scale against the inverse of experimental temperature for the 'TP-V' experiment series (Table A5 to Table A7).*

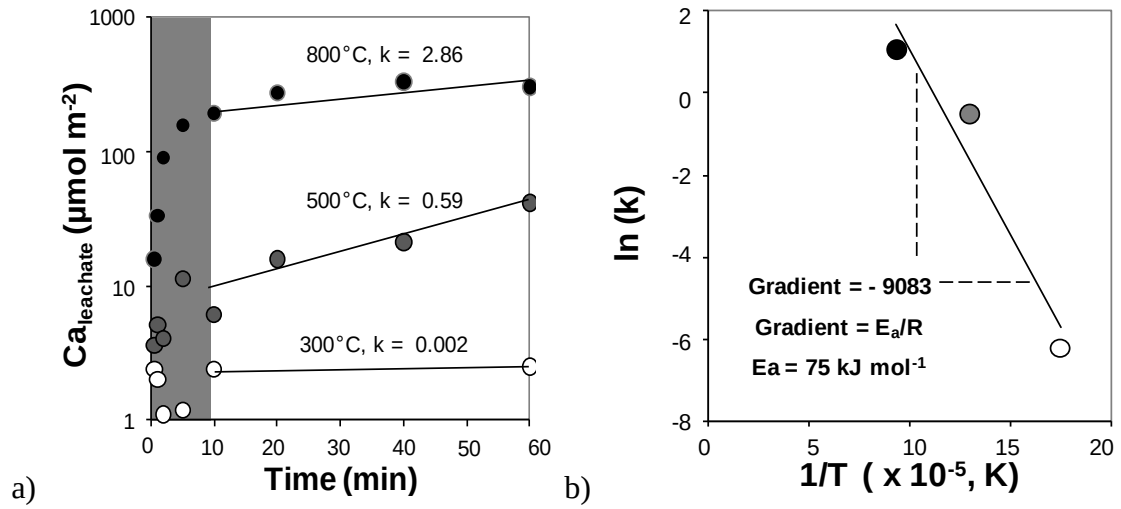

Fig. 6.14 *Rate of $CaSO_4$ formation (a) as interpreted from the increase in Ca in leachate solutions for the TPH glass exposed to 300°C, 500°C and 800°C for exposure times from 10-60 minutes (Table A13, 0, Table A23), as per the 'TI-V' experiments, and the activation energy (b) for the rate-limiting step as calculated from the relationship between [ln (k)] and the inverse of temperature, with an r^2 value of 0.93. Note that the small number of data points for 300°C experiments is a limiting factor in these calculations.*

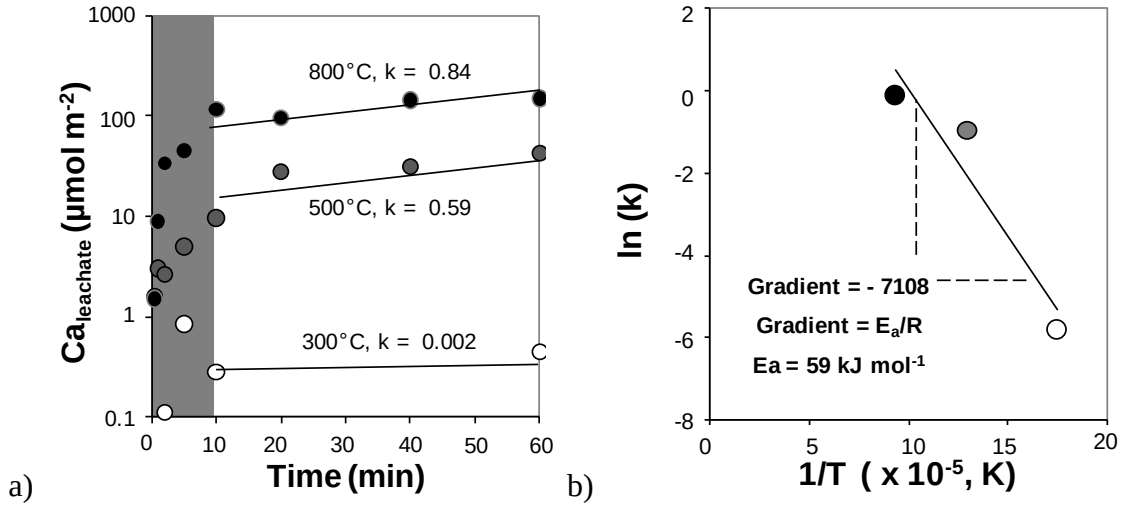

Fig. 6.15 *Rate of $CaSO_4$ formation (a) as interpreted from the increase in Ca in leachate solutions for the PHN glass exposed to 300°C, 500°C and 800°C for exposure times from 10-60 minutes (Table A13, 0, Table A23), as per the 'TI-V' experiments, and the activation energy (b)for the rate-limiting step as calculated from the relationship between [ln (k)] and the inverse of temperature, with an r^2 of 0.90. Note that the small number of data points for 300°C experiments is a limiting factor in these calculations.*

The close match between these values, irrespective of the smaller particle sizes in the current study, cannot be disregarded. It should be noted, however, that these activation energies also fall within the range of reported values for both chemisorption of SO_2 onto Ca chemisorption sites in fly ash and CaO and $Ca(OH)_2$ (22, 41, 134 kJ mol^{-1}) exposed to a 4000 ppm SO_2 stream in an N_2 atmosphere between 60-140°C (Lee *et al.* 2005), four times higher than that used by this study. It is not currently possible to determine the rate-limiting reaction, whether it is the adsorption of SO_2 onto the surface sites or the diffusion of Ca through the bulk. Given the prior industrial studies, it is likely that ionic diffusion through the glass is the rate-limiting reaction (Douglas and Isard, 1949), but further experiments will be required to determine this.

The activation energies calculated across the whole temperature range and between 500-800ºC are markedly different. This may be in part a result of the apparent plateauing effect which can be observed in the raw data (Fig. 6.16), but not discernible in the exponential plots of Fig. 6.13. This effect is apparent in Ca and S concentrations in leachate solutions between 600-800°C for the TPH and 700-800°C for the other three glasses (Fig. 6.16).

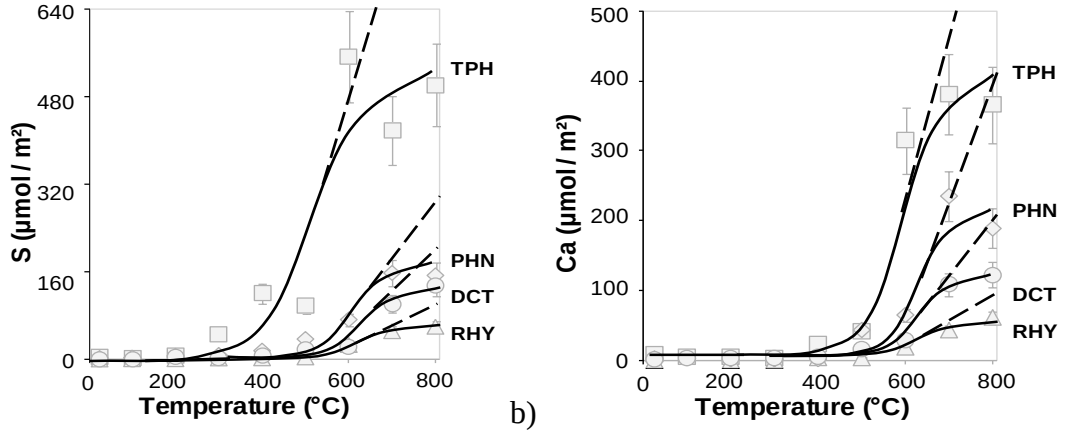

Fig. 6.16 *Total a) S and b) Ca from leachate solutions against experimental temperature for the 'TP-V' experiments, fitted with S-type trend lines showing the approximate trends in their respective rate of increase. The dashed line indicates the projected increase in S and Ca if the plateauing effect observed at high temperature did not occur.*

The plateauing effect may be a result of the diffusion mechanism, as the effect begins for all glasses at or near the glass transition temperatures, where it has been hypothesised that surface structural rearrangements may occur, which may alter the diffusion rate of mobile cations through the glass. A diffusion related hypothesis may also be plausible due to the disappearance of Na from leachate solutions of the TPH

glass above 600°C. Na_2SO_4 is known to be stable above this temperature (Lide 2005), and has been observed to be form up to temperatures of 1000°C in silicate glasses previously (Douglas and Isard 1949). The absence of Na_2SO_4 at high temperature in this study may therefore be related to a structural phenomena within the network. The plateauing effect may also be at least partially attributable to the decomposition of $CaSO_3$, as the intermediate step in the formation of $CaSO_4$, previously discussed in Chapter 4.

6.3.4.3. DIFFUSION LENGTHS AND COEFFICIENTS

The length over which diffusion acts is given by equation [6.3] ((Mehler 2007), and by rearranging that equation, the diffusion coefficient (*D*) can be determined if the time and distance of diffusion is known. It is therefore possible to estimate the diffusion lengths and coefficients through simple geometric calculations, using the spherical approximation, the particle size distribution and the total mass of Ca extracted over the 60 minute, 800°C experiments.

$$l = 2\sqrt{Dt} \qquad [6.3]$$

The observed total Ca extractions of 60, 40, 20 and 10% as observed in 60 minute experiments for the PHN, RHY, DCT and TPH glasses respectively can be calculated to require the total removal of Ca from a layer of glass which propagates 700 nm, 700 nm, 250 nm and 110 nm into each spherical particle. It should be noted that these estimated depths will be constant across each particle, and so in the smaller particles, total Ca extraction will be much higher than the estimates above, and with larger particles, much lower. Diffusion does not extract all Ca from the estimated depths given above, rather extracting more in proximity to the origin and less at distance. This relationship is described by a specific function, *erfc*, the complementary error function, and so the actual distance from which Ca is extracted and by which diffusion coefficients may be estimated is given by equation [6.4] (Frischat 1975).

$$c(x,t) = c_0 erfc\left(\frac{x}{2\sqrt{Dt}}\right) \qquad [6.4]$$

In equation [6.4], *c(x,t)* is the concentration of Ca at a distance (*x*) and time (*t*), depending on the initial concentration of Ca at the point of extraction (c_0), where *D* is the diffusion coefficient (Frischat 1975). By integrating using a trapezoidal approximation under the curves shown in Fig. 6.17, the total mass of Ca extracted to the

surface in these calculations can be estimated. By comparison to the experimental data can be used to iteratively estimate the diffusion coefficients for each of the glasses. These diffusion coefficients for the TPH, PHN, DCT and RHY glasses are 2.4×10^{-14}, 1.1×10^{-12}, 1.4×10^{-13} and 1×10^{-12} cm^2 s^{-1} respectively.

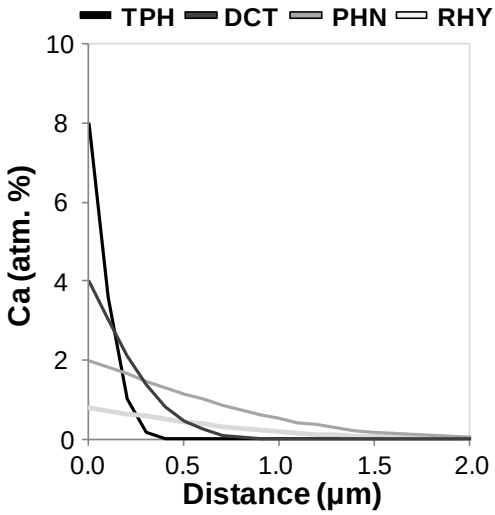

Fig. 6.17 *Change in concentration of Ca in glass with distance according to equation 6.2 and previously stated assumptions.*

It should be noted, however, that the spherical approximation has already been recognised to underestimate particle a_s. Using equation [1.1], the particle size distribution and the spherical approximation can be used to calculate a geometric a_s, which for all glasses is between 0.35 and 0.40 m^2g^{-1}. Reference to Table 5.6 shows that for all glasses, these are underestimates and the effect of this on the diffusion coefficient estimates is not known. It is likely that with a higher surface area available for extraction, that the same amount of Ca could be extracted from a shorter depth, which would in turn lower the diffusion coefficients observed. This phenomenon would be most strongly observed for the non-TPH glasses, as these have the higher measured a_s values.

It is possible to verify the estimated diffusion coefficients, at least for the TPH glass, using the experimental data derived from TEM analysis in Fig. 5.19 . If it is assumed that the Mg and Ca depleted regions indicate the furthest extent of divalent cation diffusion, then diffusion lengths may be of the order of 500 nm horizontally, but only 200 nm vertically. Using equation [6.1] gives a diffusion coefficient for the TPH glass which is between 2.7×10^{-14} and 1.7×10^{-13} cm^2 s^{-1}, between 1 and 2 orders of magnitude higher than the estimated diffusion coefficients via the geometric method. It

should also be noted that the diffusion coefficients calculated for the oxidation of basaltic glass powders via the divalent cation / iron oxidation mechanisms at 800°C by Cook *et al.* (1996) were 5.9×10^{-12} cm^2 s^{-1}. Although higher than the geometric method, the estimates derived from TEM analysis are therefore not inconsistent with the hypothesis previously outlined.

6.3.4.4. EXTENT OR SIGNIFICANCE OF DIFFUSION AT SHORTER TIMESCALES

In the previous discussion, the 60 minute experiments have been consistently used to explore the diffusion hypothesis, but this timescale is far beyond the likely exposure time to high temperature conditions within the volcanic eruption plume. It may therefore be questioned whether such diffusion mechanisms have any relevance in brief high temperature exposure times. It is inferred from limited analysis of sample exposed to SO_2 for brief time periods that $CaSO_4$ formation and segregation may still occur, as discrete surface deposits are still identified in the PHN sample exposed to SO_2 for 2 minutes, accompanied by a 1:1 relationship between leachate S and Ca. It may be questioned whether at such brief timescales whether the mass of reaction products which could be formed would require any significant diffusion of Ca in order to occur, and hence could be simply approximated by the surface reactivity.

Based on the 'TI-V' experiment data, if diffusion is the rate-limiting reaction, Fig. 6.14 and Fig. 6.15 indicate that the diffusion mechanism is the dominant mechanism at timescales of 10 minutes and above at 500°C and 800°C. It is possible to explore a possible diffusion hypothesis at the shorter timescales at 800°C by the proportionality between the mass of reaction products formed on the sample surface and the square root of the exposure time (Douglas and Isard 1949; Frischat 1975). Based upon Fig. 6.18 to Fig. 6.21, it is found that in 800°C experiments, the proportionality with the square root of time for all samples on long exposure times extends down to exposure times of between 2 and 5 minutes, with r^2 values ranging from 0.99 to 0.81, below which may be fitted an additional trendline with r^2 values consistently greater than 0.99. From these data, it can be hypothesised that if diffusion were the rate limiting hypothesis, then it is feasible for it to be relevant on exposure times of at least 2 minutes, and furthermore, that the secondary relationship observed at exposure times less than 2 minutes may be more likely to be the result of the chemisorption of SO_2 onto the initial exposed Ca-based surface sites at a faster rate than the rate of diffusion before all surface sites are filled, and the fore-mentioned diffusion mechanism becomes rate limiting.

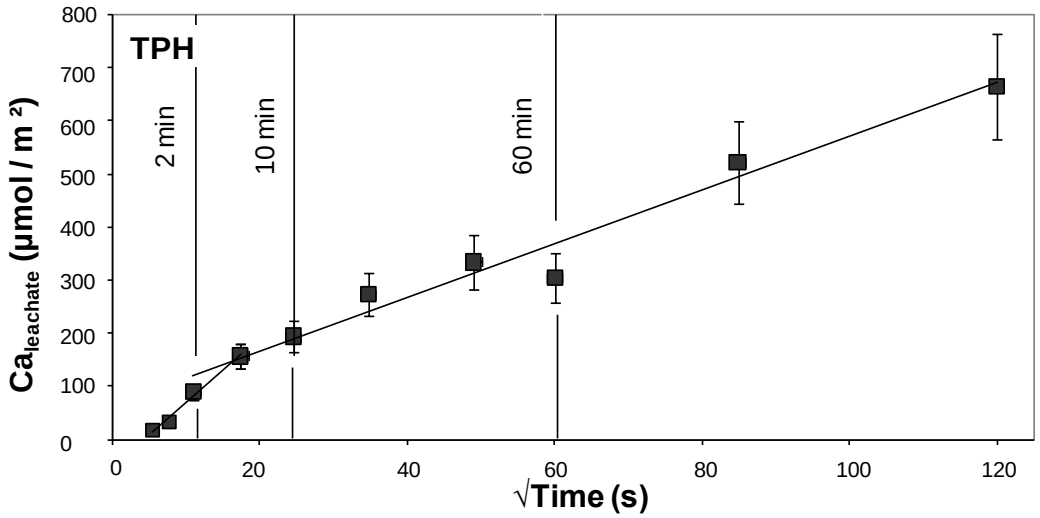

Fig. 6.18 *Leachate Ca concentrations, normalised to sample a_s, for the TPH glass exposed to 1% SO_2/He/Air at 800°C over exposure times of 30 seconds to 230 minutes, as per the 'TI-V' experiments. Fitted trend lines have r^2 of 0.99 (left) and 0.97 (right).*

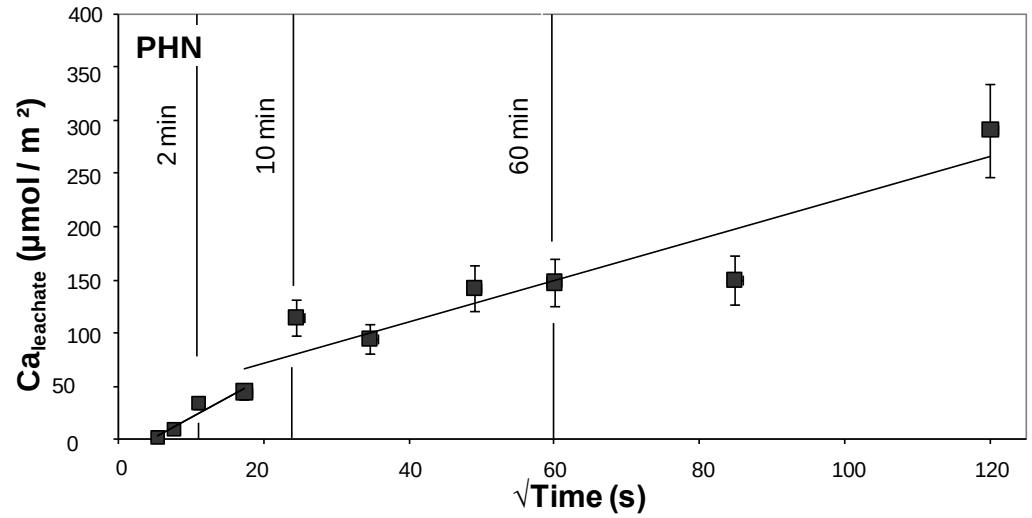

Fig. 6.19 *Leachate Ca concentrations, normalised to sample a_s, for the PHN glass exposed to 1% SO_2/He/Air at 800°C over exposure times of 30 seconds to 230 minutes, as per the 'TI-V' experiments. Fitted trend lines have r^2 of 0.99 (left) and 0.88 (right).*

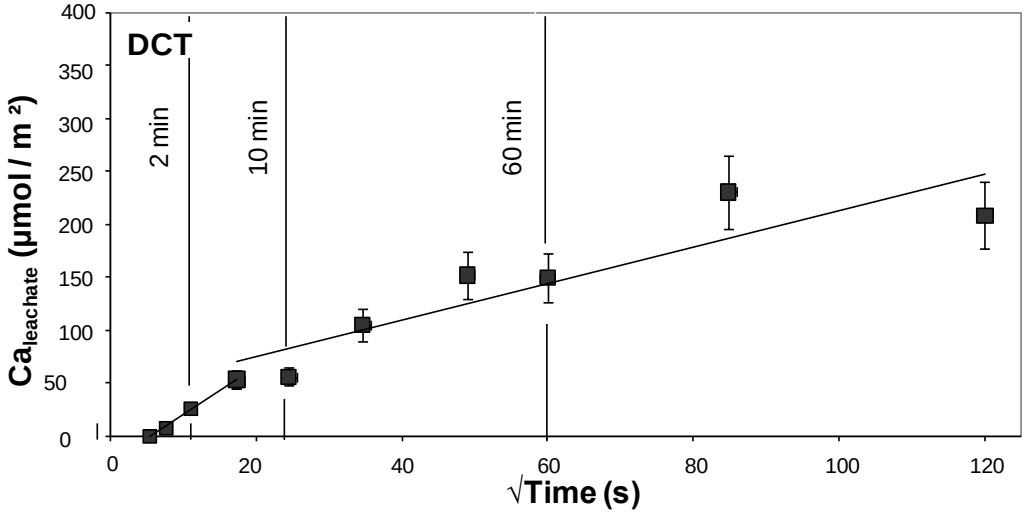

Fig. 6.20 *Leachate Ca concentrations, normalised to sample a_s, for the DCT glass exposed to 1% SO_2/He/Air at 800°C over exposure times of 30 seconds to 230 minutes, as per the 'TI-V' experiments. Fitted trend lines have r^2 of 0.99 (left) and 0.81 (right).*

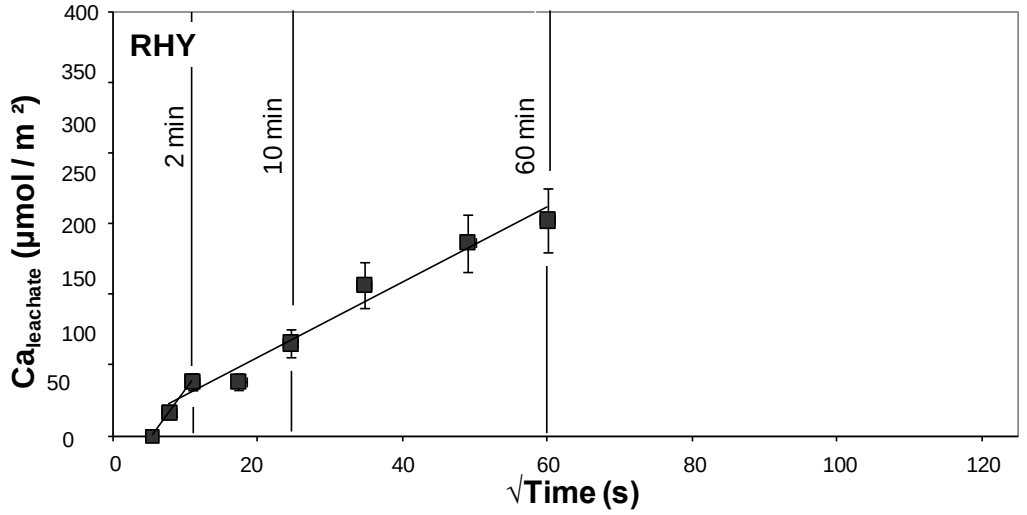

Fig. 6.21 *Leachate Ca concentrations, normalised to sample a_s, for the RHY glass exposed to 1% SO_2/He/Air at 800°C over exposure times of 30 seconds to 230 minutes, as per the 'TI-V' experiments. Fitted trend lines have r^2 of 0.99 (left) and 0.97 (right).*

6.3.4.5. A COMPOSITIONAL DEPENDENCE ON DIFFUSION?

Previous sections have illustrated that a diffusion mechanism, most likely a divalent cation / iron oxidation mechanism as outlined by Cooper *et al.* (1996) can explain the observed phenomenon. This phenomenon has been observed to act over extensive distances, relative to the immediate sample surface, into the bulk glass, and it would therefore be expected that there would be a compositional effect on cation migration imparted by the bulk network structure.

It is known that the interdiffusion of two charge carrying units in opposite directions, as in the case of divalent cation migration and the oxidation of Fe in the glass, is a complex subject but is determined by a complicated relationship between the individual self diffusion coefficients of the involved species (Schaeffer 1984). If the charge compensating mechanism of Ca diffusion is the inward propagation of a restructuring of the glass network, namely of iron oxidation, then the diffusion rate of the chemical diffusion reaction may be proportional to the network forming species (Schaeffer 1984), and so may also be proportional to the viscosity of the glass. It is possible to compare the estimated diffusion rates from the section above to the glass viscosity to test the validity of this compositional relationship. The glass viscosities may be calculated by the model of Giordano *et al.* (2008) and are illustrated over the temperature range 600-1100°C in Fig. 6.22.

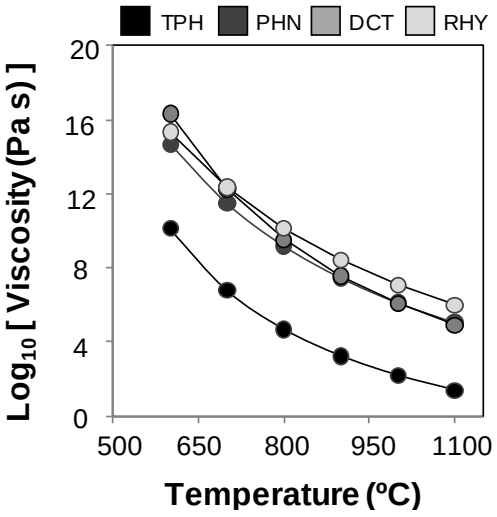

Fig. 6.22 *Calculated viscosities of the TPH, PHN, DCT and RHY glasses based on their bulk chemical composition (Table 5.5) at temperatures above 600°C, being the lower limit of the diffusion model of Giordano et al. (2008).*

If diffusion was solely dependent on the viscosity of the glass network and its impedance of the interdiffusion, the two should be proportional. It is clear from Fig. 6.23 that this is not the case. Rather than the TPH glass having the fastest diffusion coefficient, it apparently has the lowest, and it is the PHN and RHY glasses which have the apparently faster diffusion rates. There may be a number of explanations for these phenomena and it is illustrated that any compositional dependence on the migration of divalent cations across the range of glasses is not a simple one.

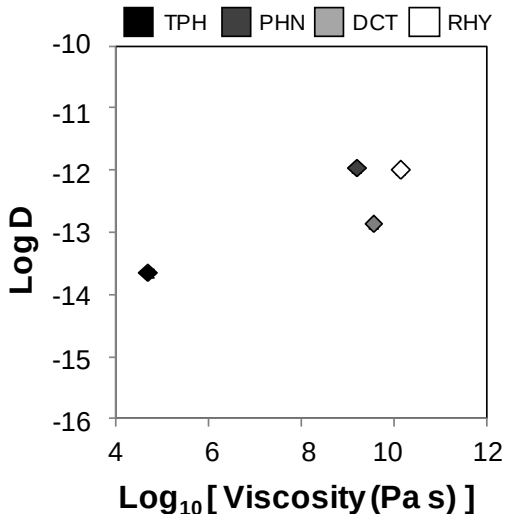

Fig. 6.23 *Relationship between the estimated diffusion coefficients (D) and the viscosity of the glasses calculated in Fig. 6.22*

A possible explanation for the greater decrease in the TPH and DCT glass may be due to what is referred to as a 'mixed-alkaline-earth' effect (Kirchheim 2003). In such a phenomenon, the presence of both Mg and Ca in the glass network impedes the flow of the other through the network and can slow diffusion rates of both. This is a well recognised phenomenon for combinations of alkali metals (Scholze 1990), but has only been identified for alkaline earth metals by Kirchheim (2003). Since both the RHY and PHN glasses contain no Mg, this would offer a simple explanation for their much more extensive Ca extraction relative to the total mass of Ca in the glass, and their apparently faster diffusion coefficients. It should also be noted, however, that additional phenomena may explain the disparity which cannot be investigated in the course of this study. The four glasses do all have different cooling histories, which may exert some influence on the structure of the network and hence the mobilities of the ions. Furthermore, it was previously recognised that the difference between geometric surface area and actual surface area may result in lower diffusion coefficients than those estimated.

There may be an additional influence on diffusion through the glass which would explain the significantly lower diffusion coefficient in the TPH glass than the others. This may be in part due to the behaviour of the glasses during heating, which can be partially explored via the He-pre-treatment experiments in the AT-V series.

6.3.4.6. EFFECT OF HIGH-TEMPERATURE PRE-TREATMENT ON CA DIFFUSION

Based on the XPS study, the most significance alteration to the sample surfaces after exposure to He-only and air-only atmospheres was that the O (1s) spectra is broadened and the contribution of the lower binding energy component of two fitted components at 532 eV and 530 eV is increased by up to 21% (Fig. 5.54 to Fig. 5.57). The alterations observed in the oxygen spectra for these samples, which are not observed in the 1% SO_2/He/Air spectra, occur under both He-only and air-only atmospheres. They therefore cannot be solely attributed to the addition of oxygen from the atmosphere to the sample surface. The changes in the O (1s) spectra must therefore be attributed to the alteration of the bonding environment of the surface in response to high temperature exposure rather than the experimental atmosphere.

The changes in the O (1s) spectra at high temperature may be the result of Fe diffusion to the glass surface, its coordination as a network former and crystallisation of Fe-bearing phases within the glass. In aluminosilicate glasses, the O (1s) spectra may be interpreted as containing a high energy peak (532 eV), attributed to bridging oxygen (Mekki *et al.* 1996). In the case of bridging oxygens, the valence electrons are shared between the O (1s) electron and the network forming cations, and so the shielding effect of those electrons is reduced and the energy required to remove the core electrons is higher. In contrast, the lower binding energy peak (530 eV) is attributed to the non-bridging oxygens (Mekki *et al.* 1996), as these have lower coordinations and hence greater shielding of the core electrons from the nucleus. In studies of ferrosilicate glasses by Holland *et al.* (1999), Mekki *et al.* (1996) and others, it was hypothesised that the introduction of Fe into a silicate network resulted in a binding energy component attributable to Si-O-Fe which could be fitted at approximately 530.5 eV. It can be seen from Fig. 6.24 that the fitting of a third peak would account for the distortion of the O (1s) spectra observed in this study via broadening the peak. However, since multi-component glasses are complex and multiple peaks could feasibly be fitted with a strong rationale for doing so, these additional peaks are not fitted in Fig. 5.54 to Fig. 5.57.

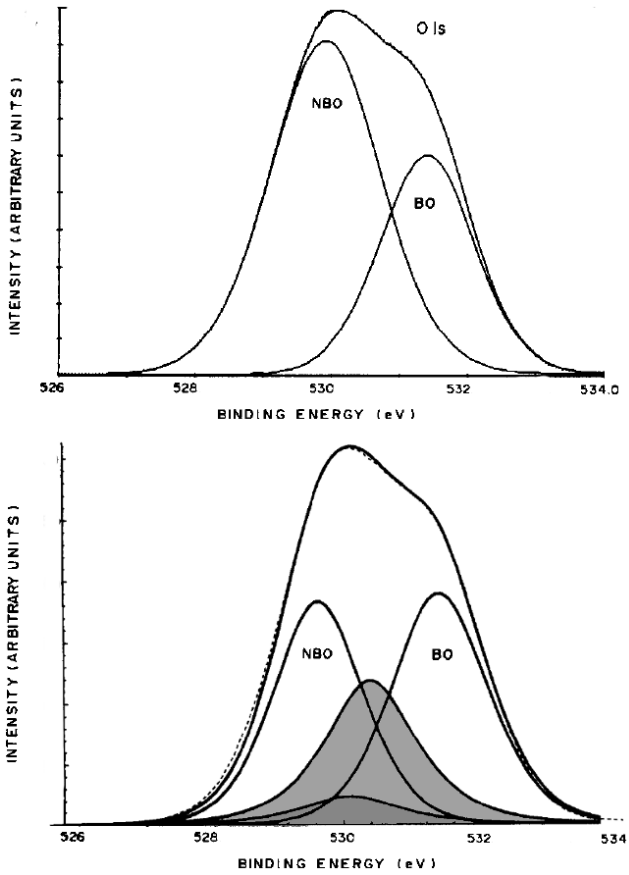

Fig. 6.24 *Illustrative comparison of the non-bridging oxygen (NBO) and bridging oxygen (BO) interpretation of the O (1s) spectra of iron sodium silicate glasses and the interpretation of Mekki et al.(1996) with the additional peaks attributed to* Fe^{2+} *(dark grey) and* Fe^{3+} *(light grey) coordinated with Si. Modified after Mekki et al. (1996).*

Further examination of the Fe ($2p\ ^3/_2$) spectra further indicate that the shifts in the O (1s) spectra can be attributed to anomalous behaviour of Fe. The ratios of Fe/Si in the glass surface after exposure to He-only and air-only atmospheres at 800ºC are increased relative to the pre-experiment surface by a factor of 2-8 in all samples. Although consistently higher under air-only atmospheres, the difference is within experimental and analytical error (Fig. 5.43c). The changes in Fe/Si ratios may be explained by the diffusion of Fe from the bulk glass into the surface, which is consistent with the observed decrease in Fe/Si ratios in the 'TI-V' experiments (Fig. 5.28c). If Fe remained unchanged within the bulk glass during the latter experiments, the Fe/Si ratios would remain constant, as both would decrease as $CaSO_4$ crystals overlaid the silicate glass. The mechanism of Fe diffusion to the surface remains uncertain at this time, but due to its greater prevalence at short time durations, it may be a product of heating under the He-atmosphere prior to the experiments.

In the presence of air, the diffusion of Fe to the glass surface is hypothesised to result in the formation of Fe as discrete Fe-bearing crystal phases within the glass. This effect was hypothesised to occur from the deviation in the Fe ($2p^{3}/_{2}$) spectra of the 800ºC air-only atmosphere experiment from that of the initial pre-experiment surface. Relative to the initial Fe ($2p^{3}/_{2}$) spectra, fitted with two broad peaks at 711 eV and 709 eV, the contribution of the high binding energy component under air-only atmospheres is increased by 20 ±2% in the TPH, PHN and DCT glasses, whilst the average increase in He-only atmospheres is 3±9% spectra (Fig. 5.50 to Fig. 5.53). The deviation of the Fe (2p) spectra is attributed to an increase in the coordination of highly coordinated (>2) Fe, which would be consistent with the binding energies of Fe_2O_3 (711 eV, Wagner 1975). Fe_2O_3 crystallites were inferred to exist in the TPH glass exposed to air-only atmospheres at 800ºC by interpretation of XRD (Fig. 5.40). Since the deviation is most strongly observed in the presence of O_2, the oxidation reaction may be enhanced by the presence of environmental oxygen, but not necessarily solely dependent on it. Further analysis is needed to explore the hypothesised structural rearrangement of Fe, particularly as interpretation of Fe ($2p^{3}/_{2}$) spectra is tentative, but the enrichment of Fe at the surface may offer an explanation for the observed decrease in chemisorption on Ca sites and the alterations to the O (1s) spectra (Fig. 5.54 to Fig. 5.57).

If, as hypothesised, the divalent cation / iron oxidation mechanism is the driving force for the formation of $CaSO_4$, then the enrichment at the surface and oxidation of Fe to form discrete Fe-bearing crystal phases within the glass will directly act against that mechanism. If there is an increase in Fe in the glass network surface as a network forming unit, it is necessary for charge compensation to occur to provide the absent ($^{1+}$) charge from the substitution of the trivalent cation into the network forming unit. Charge compensation may be fulfilled by Ca, Na, K and Mg. Alkali cations may stabilise Fe within the glass network, but alkaline-earth cation stabilising Fe are known to be unstable and previous workers observed that crystallisation of Fe-bearing phases occurred instead (Cooper and Cook, 2000). This could offer an explanation for the presence of iron oxide or multi-component Fe bearing phases in the TPH glass. Crystallisation of multi-component Fe-bearing crystal phases would generate a component of the Ca peak which would be unreactive with SO_2, which would explain the observed trends in the XPS data (Fig. 5.46 to Fig. 5.49). The formation of such phases may be supported by XPS spectra, as the binding energy of Ca as a Ca-ferrosilicate is lower than that for a Ca-aluminosilicate (Ball et al. 1987), and so an augite or other Ca-bearing ferro-aluminosilicate would have a lower binding energy as a

result. The appearance of a lower binding energy component at 346.0-346.5 eV in the He-only and air-only atmospheres and the retention of this peak under SO_2 after pre-treatment (Fig. 5.46 to Fig. 5.49) is therefore explained as the structural rearrangement of the glasses and their crystallisation, albeit not on the same scale as the TPH and not in high enough concentrations to be detected by XRD. If the hypothesised crystallisation occurred during the annealing period or during the early minutes of the experiment, Fe would be removed from the glass network and diffusion would be impeded.

This hypothesis would suggest that the diffusion of Ca through the glass network and its reaction at the glass surface is sensitive not only to the specific composition of the glass network, but also to more dynamic processes which may change that network over time, either before or during exposure to SO_2. The behaviour of the TPH glass, producing the lowest estimated diffusion coefficient, as identified in the previous section may therefore be a result of its lower viscosity at 800°C and hence its greater likelihood of crystallisation. This, combined with its high Fe content may have disrupted and impeded diffusion, whilst in the other glasses, with much lower Fe contents and higher viscosities, this effect would be less apparent. This hypothesis is consistent with the observed XPS data. In the AT-V experiments, the decrease in surface S was equally large in the TPH, PHN and DCT glasses (20-40%) but the decrease in total $CaSO_4$ formation inferred from leachate solutions was twice as large in the TPH and DCT (30%) than the PHN (15%). Both the TPH and DCT glasses are the most Fe-rich, and crystallisation at the immediate 10 nm deep surface layer probed by XPS is likely to have continued to different depths in each sample, further impeding diffusion through the network.

.

6.5. CONCLUSION

The chemisorption of SO_2 onto the glass surfaces is hypothesised to occur on the oxide sites associated with alkali and alkaline earth cations, most notably Na and Ca, depending on the respective distributions of these cations in charge compensating positions. In charge compensating positions, alkali and alkaline earth cations may be unreactive or of limited reactivity to SO_2, whilst in network modifying roles, association with basic non-bridging oxygen sites may permit chemisorption to occur. Chemisorption of SO_2 is hypothesised to result in the formation of soluble sulphate compounds as discrete crystalline phases on to the sample surface, which in the concentrations observed and using the leachate method described, are entirely soluble. The sulphate deposits on the surface are formed in order to lower the surface energy of the glass surface, and this may occur at temperatures of 500°C and above, and possibly at lower temperatures, but without further analysis, this cannot be verified. At 500°C and above, the chemisorption of SO_2 may proceed according to a complex interaction between the surface and the bulk properties of the glass particle.

At high temperatures in experiments conducted at timescales of 60 minutes, a significant fraction of the mass of Ca and Na, depending on the temperature and composition of the glass, was required to migrate to the surface in order to produce the observed quantities of $CaSO_4$ and Na_2SO_4. For $CaSO_4$, a diffusion mechanism was suspected to occur, where the segregation of the crystalline phases from the surface was hypothesised to create an alkaline earth vacancy to initiate a diffusion pathway and Ca migration to the surface. The diffusion mechanism was considered to be rate-limiting at temperatures in excess of 500°C, and possibly at lower temperatures, and a diffusion hypothesis would explain the observed exponential increase in reaction product formation up to 700°C. The diffusion mechanism may be the rate limiting reaction at timescales of 10 minutes or more at 500°C, and at timescales as brief as 2 minutes at 800°C.

In the course of this discussion, it was suggested that the mechanism of diffusion may be via a chemical diffusion reaction. In such a reaction, Ca migration to the surface was charge compensated by the inward propagation of a glass restructuring which behaves as an Fe oxidation reaction. The proposed mechanism of diffusion remains speculative, but it is founded on a number of existing studies of divalent cation diffusion in response to glass oxidation reactions under high temperature exposure. If Ca

migration were charge compensated by an inward propagating glass restructure would require the diffusion rates to be proportional to the viscosity of the glass, but there are many additional factors which may influence the diffusion rates and further study is necessary to cast further light on this.

The mechanisms proposed are speculative, but it seems likely that the reaction which emplaces sulphur salts on glass surfaces is driven by the reactivity and number of surface sites, the mechanisms which may alter one or both of these, and the diffusion of Ca cations from the bulk to those sites. The diffusion mechanism itself may be in turn limited by a number of complex factors, including the composition and structure of the bulk glass itself. The significance of the high temperature coupled interaction between surface and bulk glass properties in application to SO_2 chemisorption and reaction product formation on volcanic ash systems is considered in Chapter 7.

CHAPTER SEVEN

SO_2 CHEMISORPTION ON GLASS SURFACES.

PART III – IMPLICATIONS FOR IN-PLUME PROCESSES

CHAPTER 7. SO_2 ADSORPTION EXPERIMENTS ON VOLCANIC GLASS. PART III – IMPLICATIONS FOR IN-PLUME PROCESSES

7.1. SUMMARY OF KEY FINDINGS

This study has shown that chemisorption of SO_2 onto the surface of silicate glass of various compositions proceeds on basic oxide sites associated with network modifying cations, namely Ca above 500°C in the DCT, PHN and RHY, and above 600°C in the TPH. At lower temperatures, SO_2 chemisorption may occur on basic oxide sites associated with Na in low Si glasses, but this remains speculative. The chemisorption of SO_2 forms above 500°C forms a sulphate salt, $CaSO_4$ and possibly Na_2SO_4, which segregates from the glass surface to lower the overall surface energy, and in doing so, initiates a cation diffusion pathway from the bulk glass to that surface. The outward diffusion of divalent cations may be charge-compensated by an inward propagation of a structural rearrangement of the glass network which oxidises divalent Fe to trivalent Fe. The compositional dependence of the chemisorption and diffusion model is suggested to be a combination of the number and reactivity of the chemisorption sites on the surface, and the bulk chemical properties which dictate the rate of divalent cation / iron oxidation interdiffusion. The compositional dependence remains uncertain, estimates of the diffusion coefficients suggest that a number of complex compositional factors may influence the mass of $CaSO_4$ which forms, but the total mass of $CaSO_4$ formed in the glasses consistently increases with decreasing Si content. As a diffusion or chemisorption controlled reaction, the formation of $CaSO_4$ on the sample surface was found to be temperature dependent, increasing exponentially up to 700°C, and plateauing above that temperature. Whether the observed plateau was a response to thermal decomposition or to alterations in diffusion rates due to the restructuring of the glass surface is not known. The specific rate-limiting mechanism and the controlling factors remain unknown. It is likely that a complex coupled surface-bulk interaction is associated with the high temperature chemisorption of SO_2 onto silicate glass surfaces.

7.2. IMPROVING THE EXISTING METHODOLOGY

This study has identified a significant role for high temperature SO_2 scavenging via diffusion processes in experiment studies. To explore this mechanism of scavenging in more detail requires that the additional variables which remain unconstrained be investigated. The most important of these variables include the effects of an in-plume atmosphere, the effects of in-plume exposure times and the complexities of volcanic ash surfaces. The experimental methodologies used in this study have been demonstrated to be successful, but it will be necessary for any future study to make modifications and improvements to the existing reactor design, protocols and analytical techniques. Some of the proposed improvements to the existing method and the additional modifications which could be made are outlined below.

7.2.1. MODIFICATIONS TO EXPERIMENTAL DESIGN AND PROTOCOLS

The primary modification to the reactor design in any future work would be to include additional gases, namely H_2O, CO_2, HCl and if possible, HF to better represent the in-plume atmosphere. Further experiments would need to explore the adsorption of these gases in isolation, as well as in combination. The alterations to the reactor to incorporate these gases is primarily via the acquisition of new cylinders and feedlines, but also with the addition of new mass flow controllers automatically controlled from a central computer unit. In addition to the gas cylinders and related equipment, a Fourier Transform Infrared Spectrometer (FTIR) or other instrument which can measure gas chemical composition would be necessary to monitor the gas stream before entering the reactor and after, and could measure the in-situ, real time chemisorption of the gases during experiments. By providing measurements of SO_2 uptake, gas measurements would reduce the need for destructive analytical techniques on the glass materials.

It may also be necessary to modify the experimental protocol, specifically to alter the cooling regime used after the experiment. It was observed in Chapters 5 and 6 that the surface deposits on some of the glasses observed by SEM could not be identified by EDX as being surface S compounds, and were explained by the presence of crystal phases formed during quenching. Eliminating any post experiment crystallisation or other alterations is desirable, as such effects may limit interpretation and may alter the experimental surface. Rapid quenching of the glass surface may be one way to remove post-experiment alterations, as this would preserve the surface of the glass as it was at the end of the SO_2 experiment, rather than after 1 hour and 15 minutes

under He from 800°C to 200°C. At the end of the experiments, the reactor tubes should therefore be instantly removed from the furnace and exposed to atmospheric temperatures. Such a method was tested at the completion of this study, and the reactor tube was determined to be at a safe temperature for unprotected handling within approximately 5 minutes of removal. Although the possibility of some crystallisation during cooling may still occur, the contribution of surface crystallisation occurring after SO_2 chemisorption experiments would be reduced by this method. Preliminary experiments indicate that rapid removal may better preserve the post experiment surface, as leachate analysis found that the soluble S extracted from that sample was 23% higher than that of the sample which was left to cool for the longer time period.

7.2.2. MODIFICATIONS TO ANALYTICAL TECHNIQUES

There are two limitations to the analytical techniques used in this study; the first is that many of the techniques used have difficulty in identifying soluble salts on glass surfaces where concentrations become low; and the second is that it was not possible with the available time and resources to conduct depth sensitive analytical techniques which could have verified the diffusion hypothesis.

It has been repeatedly observed throughout this study that identifying low temperature surface compounds by XPS, XRD, leachate analysis and SEM-EDX is difficult. In the case of XPS, XRD and SEM-EDX, the overwhelming background signal of the underlying glass surface compared to the low surface concentrations of salts prevents identification of surface deposits. Leachate analysis is limited by the difficulties in separating low concentrations of soluble salts from the contribution of glass dissolution and leaching to the solution. Leachate analysis may be the easiest way to identify possible surface deposits, but this would require an extensive suite of 'blank' experiments conducted over a range of temperatures and exposure times in order to characterise the leaching of the glass after experiments in the absence of SO_2. A more constrained estimate for the contribution of glass dissolution and leaching would enable any trends in chemisorption occurring below 500°C to be explored; reference to Fig. 6.2 to Fig. 6.5 shows that the 7 μmol m^{-2} contribution of glass dissolution and leaching has been a limiting factor in interpreting leachate data from lower temperature experiments.

Future studies should also expand the suite of surface sensitive techniques which were used, and indeed, should perhaps rely on such techniques more heavily rather than relying on techniques such as leachate analysis and XRD. The use of TEM has already

been demonstrated to be an invaluable tool for constraining diffusion coefficients, but also offers the potential to specifically identify the phase of surface and near-surface crystal deposits by electron diffraction. In experiments where concentrations of surface salts may be too low to be detected by bulk techniques such as XRD, the merits of TEM coupled with electron diffraction are clear. A further technique which may have significant application is the use of elastic recoil detection (ERD) for identifying the ingress of H^+ into the ash particle surface. Using this technique, it should therefore be possible to determine the diffusion rates of any leaching and chemisorption-diffusion mechanisms which are driven by H^+ exchange (R.L. Thompson, pers. comm. 2010).

In addition to the expansion of the suite of analytical techniques used to study volatile scavenging via the experimental methods described above, future research would be complemented by the study of natural ash materials using the same analytical techniques. The new insights gained from the experimental work could therefore be applied directly to the ash particles, providing far more insight into in-plume processes than any previous technique has provided. In previous studies, leachate analysis (Witham et al. 2005), SEM-EDX (Cannata et al. 2010; Lautze et al. 2010) and XPS analysis (Delmelle et al. 2007) have been the only techniques by which the ash surface had been investigated. As has been previously discussed in the course of this study, XPS analysis is a technique which must be used with caution, as without a pre-eruption surface to study, identifying features attributable to in-plume transition is virtually impossible. Leachate analysis too has been acknowledged to be limited in separating surface salts and the underlying material, and offers no way to identify which salts are formed and under what conditions they were precipitated. SEM, as also indicated by this study, may be of limited use when considering small surface deposits due to the much thicker underlying glass or ash layer.

Studies of ash surfaces and underlying near-surface regions by high resolution techniques such as TEM offer a way to differentiate between the different volatile scavenging techniques which could occur. If salts were emplaced by aqueous acid alteration and leaching of the glasses, for example, then the exchange between leachable cations and H^+ may create a hydrated surface layer enriched in H^+ and depleted in cations such as Na, Ca etc. (Koenderink *et al.* 2000; Spadaro *et al.* 2002). This layer could be identified using ERD and comparing the layer of H^+ ingress with cation extraction observed via TEM. If, on the other hand, the surface salts were precipitated by a high temperature mechanism such as the divalent cation Fe oxidation reaction,

divalent cation depletions would be observed, but would not be accompanied by an H^+ gradient, but rather by an inward propagating Fe oxidation front. Finally, if salt condensation mechanisms emplaced the observed soluble salts, then as a condensation process, this would have no effect on the underlying material and no remarkable features should be distinguished by TEM or other surface / near-surface sensitive techniques. Studies of natural ash samples using such techniques would therefore offer a way to validate the findings of the experimental work.

7.3. CONSTRAINING HIGH TEMPERATURE SCAVENGING

The key variables for future study, briefly outlined in the opening paragraph of the previous section, are beyond the scope of this investigation due to time and resource constraints. It is however possible to consider these variables in a speculative manner and to offer some limited predictions of what future researchers may need to consider or investigate when studying said variables.

7.3.1. THE EFFECT OF THE IN-PLUME ATMOSPHERE

The experiments of this study were conducted under 1% SO_2/He/Air, rather than under representative in-plume gas atmospheres. Using the findings of this study, it is possible to offer some predictions as to the likely influence of the different gases within the eruption plume atmosphere, so offering a starting point for future investigation of the effect of the in-plume atmosphere. These predictions are drawn from existing studies of industrial glasses and high temperature desulphurisation sorbents.

H_2O, as the most abundant volatile species within the eruption plume, may be the most likely gas to influence the observed SO_2 chemisorption-diffusion mechanism. Based on existing studies of SO_2 chemisorption on industrial soda-lime silicate glasses (Douglas and Isard 1949), it was inferred, as in this study, that diffusion of a network modifying cation (Na) drove SO_2 chemisorption. The formation of Na_2SO_4 on the glass surfaces increased exponentially with increasing temperature and a chemisorption-diffusion mechanism was hypothesised to occur. Experiments conducted in 0, 2 and 70% H_2O with 1% SO_2 in an N_2 carrier gas below temperatures of 700°C lead Douglas and Isard (1949) to propose that diffusion of Na to the surface was charge compensated by the diffusion of H^+, and so increased with increasing H_2O content in the atmosphere. In the glasses of this study, it may be possible that similar mechanisms will be observed under in-plume atmospheres. If Ca^{2+} remains the diffusing cation in all glasses apart from the TPH, this would require $2H^+$ to charge compensate the outward $^{2+}$ diffusion, so the effect of H_2O at low temperatures may be less than in the case of alkali exchange. From the previous discussion on determining the mechanisms of volatile scavenging, diffusion of H^+ into the sample during SO_2 chemisorption may limit the ability to differentiate low temperature adsorption and acid-alteration mechanisms. It would still, however, be possible to distinguish between high temperature or low temperature scavenging mechanisms by the extent of diffusion. Above 700°C, the formation of Na_2SO_4 in the industrial glass study (Douglas and Isaard, 1949) was hypothesised to be

driven by the interdiffusion between the outward migration of $2Na^+$ and a concurrent flux of O^{2-} out of the glass to maintain electrical neutrality. It may be the case that at higher temperatures and in the Fe-bearing aluminosilicate glasses of this study, rather than the Na-Ca silicate glasses of the 1949 study, that the divalent cation / Fe oxidation interdiffusion may occur instead. Alternatively, it may be possible that the latter mechanism gives way to the former mechanism as temperatures increase (Burkhard 2001), but this is still speculative.

The chemisorption-diffusion mechanism occurring at high temperatures is also dependent on the number of surface sites capable of chemisorbing the volatile species from the atmosphere and their respective reactivities. In the presence of more than one scavengeable volatile in the gas phase, there may be competing reactions occurring between the volatiles which may dictate which is most extensively scavenged, but these remain unknown but for some inferences drawn from industrial research.

Chemisorption on Ca-based sorbent surfaces in HCl and SO_2 bearing flue gas atmospheres is well studied in industrial literature, and concludes that HCl retention by Ca in the presence of SO_2 does not occur. Simultaneous adsorption experiments under flue-gas conditions (2000 ppm HCl, 1000 ppm SO_2, 5% O_2, 10% CO_2) hypothesised that $CaCl_2$ was consumed by reaction [7.7] or [7.8], and lead to $CaSO_4$ formation (Partanen *et al.* 2005). After ten minutes at 850°C under the flue gas atmosphere, CaO conversion to $CaCl_2$, which was 30% in the absence of SO_2, was reduced to 8% conversion, and decreased with increasing exposure time, whilst under the same conditions, CaO conversion to $CaSO_4$ was tripled from ~10% under HCl free atmosphere to ~30% in the flue gas atmosphere. The effect of eruption plume water vapour contents on this reaction is not known, but may enhance reaction [7.8] in the continued conversion of $CaCl_2$ to $CaSO_4$ [7.8].

$$CaCl_2(s,l) + SO_2(g) + O_2(g) \leftrightarrow CaSO_4(s) + Cl_2(g) \qquad [7.7]$$

$$2CaCl_2(s,l) + SO_2(g) + O_2(g) + H_2O(g) \leftrightarrow 2CaSO_4(s) + 4HCl(g) \qquad [7.8]$$

The possible competing reactions between SO_2 and HF are unknown, but in high temperature (627-927°C) reactions between SO_2 and CaF_2 in atmospheres with more than 90% H_2O content, it was found that the oxidation of SO_2 to SO_3 during the experiments enabled reaction [7.9] to occur (Jacob *et al.* 1987). The phase diagrams of the reaction between CaF_2, SO_3 and H_2O are shown in Fig. 7.1, and if it is assumed that

concentrations of SO_3 within the volcanic eruption plume at 627-927°C are equivalent to the SO_3 concentrations thermodynamically calculated to exist in fumarole discharges (10-100 ppt, Heald *et al.* 1963), then any in-plume HF concentration lower than 1000 ppm may be partitioned into the vapour phase, permitting SO_2 adsorption on CaO sites to occur.

$$CaF_2(s) + SO_3(g) + H_2O(g) \leftrightarrow CaSO_4(s) + 2HF(g) \qquad [7.9]$$

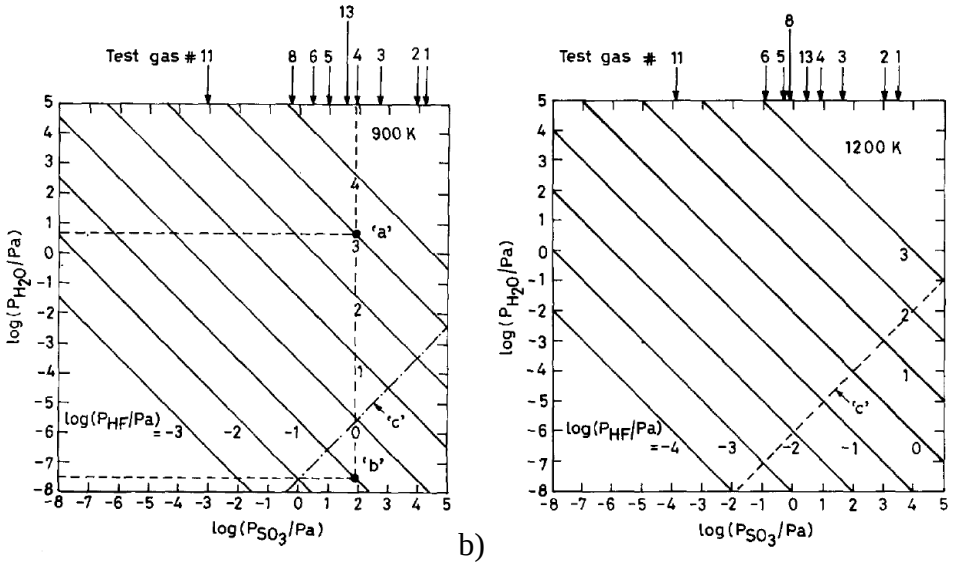

Fig. 7.1 *Equilibrium relationship between log PSO_3 and log PH_2O at different partial pressures of HF at a) 900K (627°C) and b) 1200K (927°C), from Jacob et al. (1987)*

7.3.2. REPRESENTING ASH SYSTEMS IN HIGH TEMPERATURE SCAVENGING STUDIES

This experiment studied glass surfaces derived from low temperature grinding, but in future efforts to quantify the mechanism of chemisorption-diffusion, it may be necessary to work on closer analogues to volcanic ash surfaces. These analogues should not simply be confined to exploring the additional effect on chemisorption of any exposed crystal surfaces on the particle surface, or the effect of crystals distributed throughout a glassy particle on diffusion rates, but should also consider the mechanisms which may shape the particle surface during fragmentation, abrasion or in-plume transition. It was demonstrated by the 'AT-V' experiments that a high temperature exposure to different experimental atmospheres altered the number and reactivity of surface sites on glass particles, and so altered the concentrations of salts emplaced. It might therefore be questioned whether any high temperature processes and mechanisms acting on ash surfaces within the eruption plume or perhaps even during the initial

fragmentation event, may alter the number and reactivity of surface sites on ash surfaces within the eruption plume and so alter concentrations of soluble salts emplaced. There is currently no knowledge of the significance of high temperature surface alteration occurring within the eruption plume or at the fragmentation level, and this may therefore be an important area for future study.

7.3.3. AVAILABLE TIMESCALES FOR DIFFUSION MECHANISMS

To determine the timescale over which diffusion mechanisms and volatile scavenging processes may act requires a more detailed consideration of the possible environments in which high temperature gas and ash may be combined. It is important to note that this is not just confined to the volcanic eruption plume, which has been the focus of this study, but also to other volcanic settings, in both the subterranean and subaerial environments.

7.3.3.1. THE VOLCANIC ERUPTION PLUME

In volcanic eruption plumes, existing estimates for cooling have indicated that it may only take 1-10 seconds for an 800°C plume to cool to 500°C (Mastin, 2007). This clearly presents a very limited time frame for high temperature scavenging interactions, but the existing 1D models of plume thermal evolution may not be sufficient to explore cooling rates from magmatic to atmospheric temperatures throughout a turbulent, convecting eruption plume.

A possible analogue may be gained from 2D modelling studies of mushroom clouds generated by nuclear initiations, which may have some comparability with volcanic eruption plumes. Both are turbulent, convecting clouds fed by an initial heat input. In an unpublished study by Sandman (2005), a turbulent, convecting cloud generated by a point source injection of a fireball with an atmospheric potential temperature of 1000°C was modelled using a 2D variant of the US Department of Defence 1D-DELFIC model. The results of the modelling study showed that the plume equilibrated rapidly to atmospheric temperature, but isolated regions within the plume head maintained atmospheric potential temperatures in excess of 500°C for up to 3 minutes after initiation. If such regions of sustained high temperature existed within a volcanic eruption plume, the high temperature exposure time may still be on the order of seconds-minutes, but would present a much longer time than is currently predicted. If moderate temperatures are maintained within the core of the plume head during the eruption, any ash particles large and dense enough to sink through the eruption column,

but light enough to be re-entrained by convection before sedimentation into the regions of elevated temperature and re-exposed to higher temperature scavenging mechanisms.

Future studies should therefore aim to develop more complex models of in-plume physical processes, particularly those in high temperature environments, as there are currently insufficient data to draw any further speculation on likely high temperature gas-ash interaction times within the volcanic eruption plume.

7.3.3.2. PYROCLASTIC FLOWS

In addition to the eruption plume itself, there are other subaerial volcanic settings where ash and other ejecta could remain in contact with high temperature gases for sufficient duration for significant volatile scavenging to occur. The most important of these may be within pyroclastic flows and surges, as these flows of ash and gas can have temperatures up to 1100°C and are comparatively insulated relative to the plume (Nakada 2000). Since the gas and ash mixture within the pyroclastic flow has already passed through the high temperature eruption plume environment, it is apparent that extending the high temperature contact time will therefore increase the amount of volatiles which are scavenged. Volatile scavenging within a pyroclastic flow is not just confined to its passage down the flanks of the volcano, but could also occur after it has been deposited or emplaced. Pyroclastic deposits can be emplaced at moderate and high temperatures, occasionally being hot enough to soften and melt ash particles sufficiently to weld them together (Houghton and Wilson 2000). A similar phenomenon was observed in this study, albeit not on such a scale. The cooling rates within emplaced pyroclastic deposits vary widely, but can be very slow; Bishop Tuff pyroclastic flows were estimated to have cooling rates between 1-10 °C s^{-1} up to 2.5 m from the cold ground, but in deeper deposits, cooling rates were estimated to be of the order of 10^{-8} °C s^{-1}(Wallace et al. 2002). It could take years, decades or even centuries at the stated rates for the deposits to reach the same temperature as their surroundings, but it is likely that any scavenging of trapped gases by the deposit may be limited by the escape of gases or their dissolution by rain or groundwater. It is therefore likely that any volatile scavenging occurring within the deposit will occur on a brief timescale, perhaps only for a period of hours after the eruption. Irrespective of the duration, it is likely that it would be significantly longer than that within the eruption plume.

7.3.3.3. THE VOLCANIC CONDUIT

The findings of this study have also raised the possibility that volatile scavenging may occur prior to subaerial transition, within the volcanic conduit itself. It has already been acknowledged that diffusion rates increase with increasing temperature, so the volcanic conduit and subsurface environment could be favourable environments for diffusion mechanisms.

During an explosive eruption, within the volcanic conduit, rapid cooling of the gas phase via air entrainment does not occur. Near-magmatic temperatures may therefore be maintained during the ascent of the gas and particle mixture to the volcanic vent. The depth at which fragmentation occurs within the volcanic conduit may be as much as several km below the vent (Sparks, 1997), and the rate of ascent can be rapid. Sparks *et al.* (1997) estimated that it would take approximately 30-60 seconds for a fragmenting magma body to ascend a 3000 m conduit. Based on indirect observations of the colour changes occurring in 3-5 cm pumice fragments in response to high temperature exposure, Moriizumi *et al.* (2009) estimated that such large particles may be slowed by their size and interaction with conduit walls, and their ascent times could be orders of magnitude longer (12-207 minutes). For smaller ash particles, which may remain within the core of the gas mixture rather than at the conduit walls, the estimates of Sparks *et al.* (1997) may be more appropriate. The potential for high temperatures to be maintained without rapid cooling presents an opportunity for chemisorption-diffusion mechanism to be maintained, albeit for only a minute or less, but could be a key contributor to the high temperature volatile scavenging mechanism.

Although not strictly a gas-ash interaction process, the possibility for diffusion processes occurring within the conduit raises a further question of whether volatiles could be scavenged by conduit walls. This would have particular relevance during persistent passive degassing without any form of ash emission. Magmatic gases percolating up the volcanic conduit to the surface could be scavenged by high temperature surrounding walls, forming surface salts. Such interactions could involve a diffusion component, as cations could be extracted from the conduit wall to form the fore-mentioned salts. Scavenging within the conduit could therefore sequester volatiles from passive degassing emissions. Salts on the conduit walls could then be eroded and suspended during later eruptions, and could comprise a component of the salt condensation model as solid aerosols which adhere to ash particle surfaces.

7.3.3.4. BELOW THE FRAGMENTATION LEVEL?

Considering where high temperature conditions and prolonged interaction between volcanic gases and molten rock surfaces occur, the possibility that volatile scavenging could occur prior to fragmentation has been raised by recent authors. Tuffen (unpublished data, 2010) observed a Ca depletion gradient in an Icelandic rhyolite glass (B, Fig. 7.2) initially at T_g which had been intruded by a rhyolitic melt (A, Fig. 7.2) with vesicles containing an S fluid or vapour phase (Fig. 7.2). One possible explanation for such a depletion is considered to be the extraction of Ca by reaction with the S bearing fluid via a similar diffusion mechanism to that outlined in this study. Fig. 7.2 shows that the phenomenon observed in the obsidian glasses acted over an extensive distance relative to that observed in this study, and using the estimated diffusion coefficient of the rhyolite glass in this work, it can be estimated that the observed Ca depletion gradient could have formed over 9 months in the magma chamber.

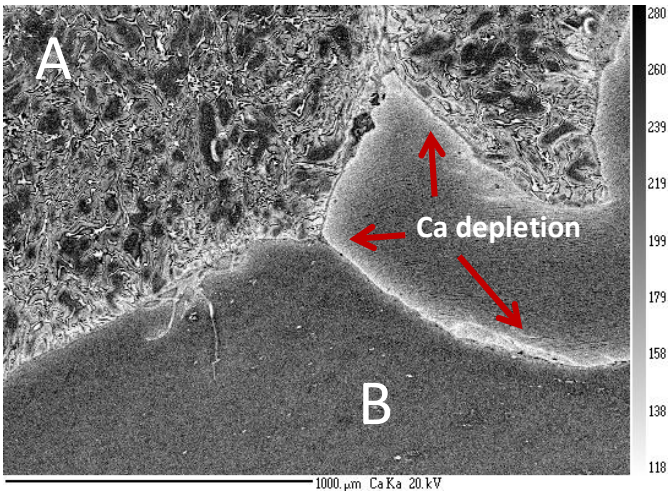

Fig. 7.2 *Colour inverted electron microprobe elemental Ca map of two rhyolite glass samples, one (A) being a degassed obsidian which may have originally contained S bearing vapour or fluid phases, and the other (B) being the rhyolite glass into which (A) was intruded and shows a Ca depletion at the interface between the two glasses. Image and interpretation provided courtesy of H. Tuffen (Environment Department, University of Lancaster, UK).*

The black regions within obsidian A in Fig. 7.2 are indicative of Ca rich regions or pockets, which may suggest that Ca did accumulate at the interface of S-bearing vesicles (Tuffen, pers. comm. 2009). If the magma melt was then fragmented, any Ca-S bearing deposits formed at the vesicle walls could remain emplaced as soluble surface salts to be leached within the environment, or could be volatilised into the vapour phase and could be deposited via salt condensation onto ash surfaces later during the eruption.

7.4. CONCEPTUAL MODEL OF VOLATILE SCAVENGING

Based on the conclusions of this study and on the new awareness of bulk processes in volatile scavenging mechanisms, it is possible to draw some tentative and speculative theories which may update and replace the existing three stage conceptual model of Óskarsson (1980).

It was hypothesised earlier that the subsurface environment may be a key area for scavenging of volatiles. This may be particularly the case in more viscous, silicic magmas as viscous bodies of magma may be restrained by surrounding magma and remain emplaced for prolonged periods. More fluid lavas might simply flow through or around any obstacles and any diffusion processes acting over a prolonged period in the pre-eruptive environment may therefore not occur. Although this study has suggested that under identical experimental conditions, a low Si glass or melt will scavenge more S than a high Si glass or melt, pre-eruptive processes acting over months or years could increase scavenging by more viscous magmas.

After fragmentation, volatile scavenging may occur within the insulated volcanic conduit prior to subaerial emission. The duration of such a scavenging mechanism is likely to depend on the ascent rate and the distance to the surface. It may be the case that for large explosive eruptions, this subterranean scavenging is only a small contribution to the scavenging processes which may occur within the later developing plume and other subaerial settings. Volatile scavenging within the conduit may have however be the sole or primary mechanism of scavenging in effusive eruptions or the small ash explosions occurring during passive degassing at volcanoes such as Stromboli (i.e. Burton *et al.* 2007). These eruptions may be driven by the ascent of gas bubbles as a coalesced mass, or slug, from depths of up to 3 km from the surface. The gas slugs burst at the surface, disrupting the film of melt surrounding them and producing a shower of molten fragments which may be thrown for several hundred metres into the air (Burton *et al.* 2007). The released gases will rapidly ascend, and the melt particles are likely to be ejected along ballistic trajectories, so there may be only limited contact between the gas and ash phase in the subaerial environment, placing the focus of volatile scavenging within the conduit itself.

The actual mechanism of volatile scavenging within the conduit is likely to be a mixture of salt condensation and a chemisorption-diffusion method similar to that outlined in this study. This may however be highly dependent on the redox state of the

source magma. Under oxidising conditions, the mechanism of volatile scavenging via the chemisorption-diffusion mechanism could include the divalent cation/iron oxidation mechanism outlined in this study, or possibly a co-diffusion between cations and O^{2-} anions out of the glass (Douglas and Isard 1949). In a reducing atmosphere, an alternative mechanism may operate, though this is highly speculative and merits further study. Reducing atmospheres are known to reverse the Fe oxidation mechanism invoked in this study, which would drive divalent cations deeper into the bulk glass and away from the surface and would also reduce Fe^{3+} to a divalent form which would also diffuse into the bulk (Smedskjaer and Yue 2009). It may be possible that as Fe^{3+} at the surface is reduced to Fe^{2+}, but before it diffuses into the glass, it could react with the volatiles within the atmosphere and undergo surface segregation to form discrete Fe-bearing volatile salt compounds. This could be a mechanism for the formation of ocean fertilising salts postulated to exist by Frogner *et al.* (2001), and would be an entirely novel finding which could significantly enhance existing research into that field.

After transition from the conduit into the subaerial setting, volatile scavenging mechanisms may continue to be driven by salt condensation and chemisorption-diffusion mechanisms. It is likely that within the turbulent, cooling eruption plume that this will occur under oxidising conditions as air is rapidly entrained into the plume. Diffusion mechanisms are therefore hypothesised to proceed via the divalent cation / Fe-oxidation interdiffusion or cation / O^{2-} codiffusion mechanisms. As the plume cools, however, these mechanisms may give way to the H^{+} exchange mechanism hypothesised to occur by Douglas and Isard (1949). This mechanism is likely to proceed more slowly than those at higher temperatures, but the longer duration of exposure to moderate temperatures and the abundance of water vapour within turbulent convecting plumes and pyroclastic flows may increase the significance of such a mechanism.

As the plume cools and aqueous acids begin to condense, the chemisorption-diffusion mechanism may be replaced by an aqueous leaching and glass dissolution mechanism. Depending on the pH of the aqueous acid layer, leaching of cations from the glass via exchange with H^{+} could result in the formation of significant soluble surface salts as the aqueous layer evaporates. Exposure to ‘strongly acidic’ gases from the Bocca Nuovo crater at Mt. Etna were reported to leach large concentrations of alkali, alkaline earth and transition metals from basalt glass blocks (2 × 6 × 0.5 cm) suspended 10 m above the vent (Spadaro *et al.* 2002). In 4 hours of exposure, the CaO content of the blocks was decreased from ~10 wt. % to ~8 wt. % (Spadaro *et al.* 2002),

corresponding to an extraction depth of 300 nm over the four hour period across the block surface. Though clearly a slower process than high temperature volatile scavenging mechanisms, it should be noted that longer exposure times to low temperature conditions is likely to increase the significance of such mechanisms.

The aqueous acid condensation mechanism has a further crucial implication, as it may also dissolve surface salts emplaced by the higher temperature mechanism, essentially 'resetting' the surface. The cations and anions dissolved into the aqueous acid solution may precipitate as an alternative deposit when the solution evaporates compared to that which was originally formed. For example, although this study has consistently observed the formation of anhydrite, after dissolution and reprecipitation, Ca-S compounds would take the form of hydrated phases such as gypsum or bassanite. Such a precipitation-dissolution-reprecipitation mechanisms would offer an explanation for the observations of Gilbert and Lane (1994) within the context of a high temperature volatile scavenging model. These authors observed calcium sulphate, although not specifying the specific phase, growing between ash aggregates as the aqueous layer evaporated in the atmosphere and on deposition. Such a hypothesis is also consistent with the observations of gypsum deposits on the surfaces of ash via SEM / EDX mapping from a paroxysmal explosion at Stromboli during 2007 (Cannata *et al.* 2010; Lautze *et al.* 2010), which were concluded to originate from an in-plume source (J. Taddeucci, pers. comm. 2010).

7.5. THE FUTURE – A COMPREHENSIVE VOLATILE SCAVENGING MODEL?

The ultimate objective of all research in this area is a comprehensive model of volatile scavenging from the magma chamber and the fragmentation level, through the conduit and plume and atmosphere until the moment at which gas and ash are no longer in contact. Such a comprehensive model remains a distant prospect at the current time, requiring extensive further study in a range of fields before it can be realised. The identification of diffusion coefficients in this study has, however, demonstrated that it is possible to obtain quantitative estimates for the rates at which scavenging processes may occur via experimental techniques. If similar detailed investigations of the other scavenging mechanisms were to be conducted and the variables constrained across all the likely volcanic settings, a comprehensive model of volatile scavenging within the volcanic system does not seem like an unrealistic objective.

As a proof of concept of the potential for such a model, a simple numerical model of the diffusion mechanism in the TPH glass at 800°C was constructed. The model attempted to predict, without reference to leachate data, the scavenging of SO_2 at 800°C over time points equal to those explored in 'TP-V' experiments. The divalent cation diffusion coefficient was derived from direct observations from the TEM micrographs, and was calculated to be 2.7×10^{-14} cm^2 s^{-1}, corresponding to a vertical diffusion length of approximately 200 nm. The model was derived from equations [6.3] and [6.4], and used the spherical approximation and particle size distribution of the TPH glass. It was further assumed that all Ca sites on the sample surfaces are homogeneously distributed and that all Ca is accessible to diffusion. By integration of the *erfc* function, a mathematical function which describes an S-shaped distribution, and using the trapezoidal approximation, the mass of Ca extracted over the diffusion length could be calculated. Assuming that that mass of Ca over the specified length was removed from all particles, the mass of Ca which should therefore be extracted by diffusion to form $CaSO_4$ at the sample surface was calculated for the experimental exposure times investigated in the TI-V experiment series. The model was validated by comparison to the scavenging of SO_2 over the same exposure times, as determined from leachate analysis. The measured and modelled data are shown in Fig. 7.3. The model shows a good fit to the experimental data, although consistently under predicting at longer durations and over predicting at the shortest durations, which may be attributable to

changes in diffusion rates as the glass structure undergoes heating, relaxation and crystallisation. Similar calculations could be derived for the other glasses and at further temperatures to derive diffusion coefficients for all the compositions investigated. This would require further study by TEM for each of the glasses which time constraints have not permitted in this study.

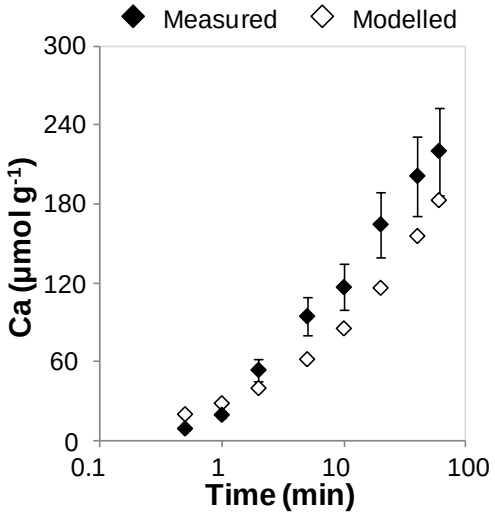

Fig. 7.3 *Comparison of modelled $Ca_{leachate}$ concentrations compared to the observed $Ca_{leachate}$ concentrations for the TPH glass exposed to 800°C TI-V experimental conditions.*

Using the above model, it is not unreasonable to suggest that all or a significant majority of Ca in leachate solutions could be derived from a high temperature diffusion mechanism which in turn reacts with the volatiles within the eruption plume to form a range of surface salts. Reference back to Table 2.1 indicates that the maximum mass of Ca found in a sampling of 28 ash leachate data sets was 554 µmol g^{-1}, whilst the lowest was 0.6 µmol g^{-1} and the median value was 13.25 µmol g^{-1}. Assuming that diffusion rates and chemical compositions are equivalent to the TPH glass, it can be calculated that it would take less than 4 seconds to emplace 13.25 µmol g^{-1} at high temperature. Ca in the majority of the ash leachate solutions studied could easily be accounted for by a high temperature in-plume volatile scavenging mechanism. The highest Ca measurement from the 28 leachate data sets which cannot be attributed to hydrothermal alteration is 60 µmol g^{-1}, which would require only 5 minutes of exposure to 800°C to be generated. In light of the previous discussions of the possibility of sustained chemisorption-diffusion mechanisms acting at high and moderate temperatures within the volcanic conduit, eruption plume and pyroclastic deposits, such an exposure time is not unrealistic.

The above proof-of-concept model has demonstrated the validity of modelling from knowledge of bulk chemical properties (i.e. the diffusion coefficient), and so has demonstrated the viability of a comprehensive volatile scavenging model in the future. The benefits of such a model are clear, offering the potential for definitively constraining volatile scavenging, and perhaps more importantly, being a key tool for hazard response during and after an eruption. In Chapter 2, it was noted that many of the hazards posed by leaching of soluble salts and acids from ash surfaces are poorly constrained due to the difficulties in predicting leachate compositions and pH without extensive sampling across the ashfall zone. By the time ash samples have been recovered, leached and analysed, acute chemical effects on vulnerable ecosystems could already have occurred and it may be too late to prevent environmental or financial damage to the afflicted community. This limitation could be bypassed with a comprehensive model of volatile scavenging, as such a model could use existing knowledge of likely ash and lava compositions erupted by the specific volcano to determine which diffusion coefficients should be used. Fumarole measurements or data from previous or similar eruptions could be used for a rough estimate of gas compositions which could then be used within the model to estimate the possible compounds formed and their relative concentrations on ash surfaces. With these data, it might therefore be possible to provide ‘worst-case scenario’ estimates for vulnerable communities and ecosystems, perhaps even before the eruption has actually begun. Such a model could therefore enable preparatory or pre-emptive rather than reactive disaster response to take place, and could potentially saves lives and livelihoods for those living in the shadow of the volcano.

APPENDIX ONE

TABLES AND ANCILLARY DATA

APPENDIX ONE. TABLES AND ANCILLARY DATA

Table A1 *XPS spectra peak binding energies (eV) and relative contributions of the fitted components of the Ca (2p 3/2) spectra for the initial surface of the '50-1' Ca-doped aluminosilicate and the surfaces of the samples after exposure to 1% SO2/He/Air at 300°C, 500°C and 800°C.*

	Component 1		Component 2	
Treatment	**B.E. (eV)**	**R.C. (%)**	**B.E. (eV)**	**R.C. (%)**
Initial	**348.3**	**55.2**	**347.4**	**44.8**
300°C	**348.5**	**55.2**	**347.4**	**45.0**
500°C	**348.5**	**58.3**	**347.4**	**42.0**
800°C	**348.5**	**85.7**	**347.4**	**15.0**

Table A2 *XPS spectra peak binding energies (eV) and relative contributions of the fitted components of the Ca (2p 3/2) spectra for the initial surface of the '50-1' Ca-doped aluminosilicate and the surfaces of the samples after exposure to 1% SO2/He/Air at 300°C, 500°C and 800°C.*

	Component 1		Component 2	
Treatment	**B.E. (eV)**	**R.C. (%)**	**B.E. (eV)**	**R.C. (%)**
Initial	348.4	52.1	347.4	47.9
300°C	348.4	67.3	347.4	32.7
500°C	348.4	63.2	347.4	36.8
800°C	348.4	57.2	347.4	42.8

Table A3 *XPS spectra peak binding energies (eV) and relative contributions of the fitted components of the Ca (2p 3/2) spectra for the initial surface of the '50-1' Ca-doped aluminosilicate and the surfaces of the samples after exposure to 1% SO2/He/Air at 300°C, 500°C and 800°C.*

	Component 1		Component 2	
Treatment	**B.E. (eV)**	**R.C. (%)**	**B.E. (eV)**	**R.C. (%)**
Initial	348.5	38.5	347.4	61.5
300°C	348.5	50.2	347.4	49.8
500°C	348.5	53.2	347.4	46.8
800°C	348.5	52.4	347.4	47.6

Table A4 *XPS spectra peak binding energies (eV) and relative contributions of the fitted components of the Ca (2p 3/2) spectra for the initial surface of the '50-1' Ca-doped aluminosilicate and the surfaces of the samples after exposure to 1% SO2/He/Air at 300°C, 500°C and 800°C.*

	Component 1		Component 2	
Treatment	**B.E. (eV)**	**R.C. (%)**	**B.E. (eV)**	**R.C. (%)**
Initial	348.4	32.2	347.4	67.8
300°C	348.4	67.1	347.4	32.9
500°C	348.4	62.3	347.4	37.7
800°C	348.4	63.2	347.4	36.8

Table A5 *Soluble S extracted from aqueous leaching of the volcanic glasses exposed to 1% SO_2/He/Air for 60 minutes, as determined by ion chromatography. Experiments are considered to be subject to ±15% error.*

Temp. (°C)	$S_{leachate}$ (µmol m^{-2})			
	Tephrite	**Phonolite**	**Dacite**	**Rhyolite**
25	4.9	1.7	0.9	0.2
100	2.5	2.5	0.7	0.6
200	7.7	5.8	5.5	0.7
300	45.9	7.5	2.5	2.1
400	120.9	15.3	6.9	2.3
500	97.7	36.7	19.8	4.0
600	553.4	72.5	24.4	27.0
700	418.7	158.1	101.8	52.6
800	501.5	153.6	135.4	60.9

Table A6 *Soluble Ca extracted from aqueous leaching of the volcanic glasses exposed to 1% SO_2/He/Air for 60 minutes, as determined by atomic absorption. Experiments are considered to be subject to ±15% error.*

Temp. (°C)	$Ca_{leachate}$ (µmol m^{-2})			
	Tephrite	**Phonolite**	**Dacite**	**Rhyolite**
25	8.1	1.8	1.8	0.4
100	5.1	2.0	3.3	b/d
200	5.8	0.5	3.9	0.3
300	2.5	0.5	2.7	0.5
400	24.0	0.8	5.5	4.0
500	41.6	42.7	15.3	3.9
600	314.8	64.3	29.0	18.9
700	381.7	235.4	108.8	43.1
800	366.2	188.8	122.0	61.0

Table A7 *Soluble Na extracted from aqueous leaching of the volcanic glasses exposed to 1% SO_2/He/Air for 60 minutes, as determined by atomic absorption. Experiments are considered to be subject to ±15% error.*

Temp. (°C)	$Na_{leachate}$ (µmol m^{-2})			
	Tephrite	**Phonolite**	**Dacite**	**Rhyolite**
25	5.4	6.4	1.2	3.6
100	4.3	3.4	2.0	3.2
200	11.6	1.6	1.5	2.2
300	53.4	7.9	2.3	2.0
400	110.1	14.1	3.3	1.4
500	39.2	5.2	5.7	0.3
600	330.8	7.5	2.5	6.9
700	24.6	7.8	0.2	4.0
800	35.0	1.1	2.1	2.1

Table A8 *Soluble Mg extracted from aqueous leaching of the volcanic glasses exposed to 1% SO_2/He/Air for 60 minutes, as determined by atomic absorption. Experiments are considered to be subject to ±15% error.*

Temp. (°C)	$Mg_{leachate}$ (µmol m^{-2})			
	Tephrite	**Phonolite**	**Dacite**	**Rhyolite**
25	0.8	0.0	0.0	0.1
100	b/d	b/d	0.2	b/d
200	2.0	1.1	0.4	0.1
300	3.8	0.4	0.8	0.2
400	3.1	0.1	0.4	0.3
500	8.4	b/d	0.6	b/d
600	5.2	b/d	1.3	0.1
700	40.3	2.0	0.0	0.3
800	2.4	b/d	0.3	b/d

Table A9 *Soluble K extracted from aqueous leaching of the volcanic glasses exposed to 1% SO_2/He/Air for 60 minutes, as determined by atomic absorption. Experiments are considered to be subject to ±15% error.*

Temp. (°C)	$K_{leachate}$ (µmol m^{-2})			
	Tephrite	**Phonolite**	**Dacite**	**Rhyolite**
25	1.9	2.5	0.1	0.3
100	0.4	0.6	b/d	0.3
200	0.5	1.8	b/d	0.3
300	2.3	2.6	1.3	0.5
400	2.7	0.2	0.1	1.2
500	3.6	0.2	2.1	0.0
600	3.7	0.2	0.1	0.2
700	1.4	0.1	0.3	b/d
800	1.6	0.0	0.3	0.4

Table A10 *Soluble Fe extracted from aqueous leaching of the volcanic glasses exposed to 1% SO_2/He/Air for 60 minutes, as determined by intercoupled plasma optical emission spectroscopy. Experiments are considered to be subject to ±15% error.*

Temp. (°C)	$Fe_{leachate}$ (µmol m^{-2})			
	Tephrite	**Phonolite**	**Dacite**	**Rhyolite**
25				
100				
200				
300	0.0	0.0	0.0	0.0
400	0.0	0.0	0.0	0.0
500	0.0	0.0	0.0	0.0
600	0.6	0.0	0.0	0.0
700	0.0	0.0	0.0	0.0
800	0.0	0.0	0.0	0.0

Table A11 *Soluble Al extracted from aqueous leaching of the volcanic glasses exposed to 1% SO_2/He/Air for 60 minutes, as determined by intercoupled plasma optical emission spectroscopy. Experiments are considered to be subject to ±15% error.*

Temp. (°C)	$Al_{leachate}$ (µmol m^{-2})			
	Tephrite	Phonolite	Dacite	Rhyolite
25				
100				
200				
300	0.0	0.1	0.4	0.3
400	0.0	0.1	0.2	0.1
500	3.6	0.1	0.0	0.0
600	0.0	0.3	0.0	0.0
700	0.0	b/d	0.0	0.0
800	0.0	b/d	0.0	0.0

Table A12 *Soluble S extracted from aqueous leaching of the volcanic glasses exposed to 1% SO_2/He/Air at 800°C for times of 0.5-240 mins, as determined by ion chromatography. Experiments are considered to be subject to ±15% error.*

Time (min)	$S_{leachate}$ (µmol m^{-2})			
	Tephrite	Phonolite	Dacite	Rhyolite
0.5	14.8	2.4	0.7	0.7
1	40.7	9.5	6.0	7.4
2	90.9	35.6	20.6	16.3
5	174.7	48.1	45.6	17.0
10	161.6	102.6	62.2	24.0
20	243.9	91.5	115.1	41.9
40	263.0	115.9	114.6	49.2
60	423.9	134.5	145.7	60.9
120	470.2	148.0	213.8	
240	704.9	274.7	202.4	

Table A13 *Soluble Ca extracted from aqueous leaching of the volcanic glasses exposed to 1% SO_2/He/Air at 800°C for times of 0.5-240 mins, as determined by atomic absorption. Experiments are considered to be subject to ±15% error.*

Time (min)	$Ca_{leachate}$ (µmol m^{-2})			
	Tephrite	Phonolite	Dacite	Rhyolite
0.5	15.9	1.5	0.3	0.0
1	33.4	8.9	6.7	6.6
2	89.9	33.6	25.5	15.4
5	157.6	44.8	53.4	15.4
10	194.1	115.2	55.9	26.3
20	273.4	94.6	104.9	42.8
40	334.4	142.5	152.1	54.7
60	305.4	147.9	149.6	61.1
120	522.5	150.4	230.3	
240	664.7	291.0	208.4	

Table A14 *Soluble Na extracted from aqueous leaching of the volcanic glasses exposed to 1% SO_2/He/Air at 800°C for times of 0.5-240 mins, as determined by atomic absorption. Experiments are considered to be subject to ±15% error.*

Time (min)	$Na_{leachate}$ (µmol m^{-2})			
	Tephrite	Phonolite	Dacite	Rhyolite
0.5	3.8	3.9	0.7	0.8
1	6.2	4.2	1.1	1.4
2	0.0	5.3	1.4	2.6
5	22.1	20.6	1.4	2.2
10	8.4	5.4	1.5	2.3
20	31.5	5.4	1.8	2.1
40	7.3	6.1	1.5	2.5
60	29.2	11.4	2.7	2.1
120	9.3	29.6	3.3	
240	5.5	70.5	1.8	

Table A15 *Soluble Mg extracted from aqueous leaching of the volcanic glasses exposed to 1% SO_2/He/Air at 800°C for times of 0.5-240 mins, as determined by atomic absorption. Experiments are considered to be subject to ±15% error.*

Time (min)	$Mg_{leachate}$ (µmol m^{-2})			
	Tephrite	**Phonolite**	**Dacite**	**Rhyolite**
0.5	1.2	0.4	0.5	0.3
1	1.2	0.5	0.6	0.5
2	0.0	0.0	0.2	0.0
5	0.8	0.2	0.2	0.0
10	0.2	0.2	0.1	0.0
20	0.0	0.2	0.2	0.0
40	0.0	0.4	0.2	0.0
60	2.0	7.4	4.3	0.0
120	0.2	2.4	1.4	
240	1.5	3.1	15.0	

Table A16 *Soluble K extracted from aqueous leaching of the volcanic glasses exposed to 1% SO_2/He/Air at 800°C for times of 0.5-240 mins, as determined by atomic absorption. Experiments are considered to be subject to ±15% error.*

Time (min)	$K_{leachate}$ (µmol m^{-2})			
	Tephrite	**Phonolite**	**Dacite**	**Rhyolite**
0.5	0.5	0.6	0.3	0.2
1	0.4	0.5	0.2	0.2
2	0.0	0.7	0.0	0.0
5	0.3	1.3	0.0	0.0
10	0.0	0.5	0.0	0.0
20	3.6	0.4	0.0	0.0
40	0.0	0.5	0.0	0.0
60	1.4	0.8	0.0	0.4
120	0.2	4.0	0.1	
240	0.2	27.9	0.3	

Table A17 *Soluble S extracted from aqueous leaching of the volcanic glasses exposed to 1% SO_2/He/Air at 500°C for times of 0.5-240 minutes, as determined by ion chromatography. Experiments are considered to be subject to ±15% error.*

Time (min)	$S_{leachate}$ (µmol m^{-2})			
	Tephrite	**Phonolite**	**Dacite**	**Rhyolite**
0.5	4.8	5.14	2.73	
1	8.9	3.30	1.88	
2	9.0	2.66	1.64	
5	12.2	6.77	4.98	
10	37.1	8.67	6.79	
20	59.6	26.47	12.37	
40	86.0	25.08	25.96	
60	94.45	36.73	19.78	

Table A18 *Soluble Ca extracted from aqueous leaching of the volcanic glasses exposed to 1% SO_2/He/Air at 500°C for times of 0.5-240 minutes, as determined by atomic absorption. Experiments are considered to be subject to ±15% error.*

Time (min)	$Ca_{leachate}$ (µmol m^{-2})			
	Tephrite	**Phonolite**	**Dacite**	**Rhyolite**
0.5	3.6	1.60	3.75	
1	5.1	3.03	3.20	
2	4.1	2.60	3.92	
5	11.3	4.97	6.27	
10	6.1	9.56	8.29	
20	15.8	27.44	13.96	
40	21.2	30.97	17.12	
60	41.7	42.70	15.32	

Table A19 *Soluble Na extracted from aqueous leaching of the volcanic glasses exposed to 1% SO_2/He/Air at 500°C for times of 0.5-240 minutes, as determined by atomic absorption. Experiments are considered to be subject to ±15% error.*

Time (min)	$Na_{leachate}$ (µmol m^{-2})			
	Tephrite	**Phonolite**	**Dacite**	**Rhyolite**
0.5	4.0	6.2	4.4	
1	7.6	3.9	3.9	
2	9.6	6.0	4.6	
5	11.4	3.8	3.8	
10	33.9	3.8	4.7	
20	67.2	16.0	4.3	
40	84.9	6.2	4.4	
60	113.7	5.2	0.0	

Table A20 *Soluble Mg extracted from aqueous leaching of the volcanic glasses exposed to 1% SO_2/He/Air at 500°C for times of 0.5-240 minutes, as determined by atomic absorption. Experiments are considered to be subject to ±15% error.*

Time (min)	$Mg_{leachate}$ (µmol m^{-2})			
	Tephrite	**Phonolite**	**Dacite**	**Rhyolite**
0.5	0.7	0.0	0.9	
1	0.8	0.3	0.5	
2	0.6	0.3	0.7	
5	0.9	0.1	0.8	
10	0.9	0.2	0.9	
20	1.4	1.6	1.1	
40	2.7	1.3	1.3	
60	8.4	0.0	0.6	

Table A21 *Soluble K extracted from aqueous leaching of the volcanic glasses exposed to 1% SO_2/He/Air at 500°C for times of 0.5-240 minutes, as determined by atomic absorption. Experiments are considered to be subject to ±15% error.*

Time (min)	$K_{leachate}$ (µmol m^{-2})			
	Tephrite	**Phonolite**	**Dacite**	**Rhyolite**
0.5	0.9	1.5	0.2	
1	0.7	1.7	0.2	
2	0.6	1.3	0.2	
5	0.6	4.5	0.7	
10	1.8	1.7	0.3	
20	2.4	2.7	0.2	
40	2.0	2.7	0.2	
60	2.2	0.2	2.2	

Table A22 *Soluble S extracted from aqueous leaching of the volcanic glasses exposed to 1% SO_2/He/Air at 300°C for times of 0.5-60 minutes, as determined by ion chromatography. Experiments are considered to be subject to ±15% error.*

Time (min)	$S_{leachate}$ (µmol m^{-2})			
	Tephrite	**Phonolite**	**Dacite**	**Rhyolite**
0.5	1.5	1.76	1.27	
1	1.3	1.86	1.15	
2	3.3	3.02	0.58	
5	4.0	6.34	1.20	
10	7.7	3.98	1.16	
20				
40				
60	45.9	7.48	2.49	

Table A23 *Soluble Ca extracted from aqueous leaching of the volcanic glasses exposed to 1% SO_2/He/Air at 300°C for times of 0.5-60 minutes, as determined by atomic absorption. Experiments are considered to be subject to ±15% error.*

Time (min)	$Ca_{leachate}$ (µmol m^{-2})			
	Tephrite	**Phonolite**	**Dacite**	**Rhyolite**
0.5	2.4	0.0	1.82	
1	2.0	0.0	2.36	
2	1.1	0.11	1.29	
5	1.2	0.84	2.31	
10	2.4	0.28	1.44	
20				
40				
60	2.5	0.45	1.14	

Table A24 *Soluble Na extracted from aqueous leaching of the volcanic glasses exposed to 1% SO_2/He/Air at 300°C for times of 0.5-60 minutes, as determined by atomic absorption. Experiments are considered to be subject to ±15% error.*

Time (min)	$Na_{leachate}$ (µmol m^{-2})			
	Tephrite	**Phonolite**	**Dacite**	**Rhyolite**
0.5	1.4	10.3	4.0	
1	4.4	6.6	2.7	
2	3.3	5.8	2.9	
5	4.9	8.1	4.6	
10	10.9	12.2	5.2	
20				
40				
60	53.4	7.9	2.3	

Table A25 *Soluble Mg extracted from aqueous leaching of the volcanic glasses exposed to 1% SO_2/He/Air at 300°C for times of 0.5-60 minutes, as determined by atomic absorption. Experiments are considered to be subject to ±15% error.*

Time (min)	$Mg_{leachate}$ (µmol m^{-2})			
	Tephrite	Phonolite	Dacite	Rhyolite
0.5	0.7		0.5	
1	0.6		0.5	
2	0.6		0.5	
5	0.6		0.5	
10	0.7		0.5	
20				
40				
60	3.8		0.8	

Table A26 *Soluble K extracted from aqueous leaching of the volcanic glasses exposed to 1% SO_2/He/Air at 300°C for times of 0.5-60 minutes, as determined by atomic absorption. Experiments are considered to be subject to ±15% error.*

Time (min)	$K_{leachate}$ (µmol m^{-2})			
	Tephrite	Phonolite	Dacite	Rhyolite
0.5	0.5		0.3	
1	0.7		0.3	
2	0.6		0.3	
5	0.4		0.3	
10	0.7		0.3	
20				
40				
60	1.39		1.4	

Table A27 *Peak binding energies (eV) and relative contributions of the fitted components of the Ca (2p $^{3}/_{2}$) spectra for the initial surface of the tephrite glass and the tephrite glass after exposure to the following conditions at 800°C, He-only, air-only, 1% SO_2/He/Air and 1% SO_2/He/Air after a 60 minute He-only pre-treatment at 800°C.*

	Component 1		Component 2		Component 3	
Atm.	B.E. (eV)	R.C. (%)	B.E. (eV)	R.C. (%)	B.E. (eV)	R.C. (%)
Initial	347.6	0	347.1	100.0	346.7	0.0
He-only	347.6	0	347.1	49.8	346.4	50.2
Air-only	347.6	0	347.1	54.1	346.4	45.9
SO_2	347.6	100	347.1	0.0	346.4	0.0
PT-SO_2	347.6	80.32	347.1	0.0	346.8	19.7

Table A28 *Peak binding energies (eV) and relative contributions of the fitted components of the Ca (2p $^{3}/_{2}$) spectra for the initial surface of the phonolite glass and the phonolite glass after exposure to the following conditions at 800°C, He-only, air-only, 1% SO_2/He/Air and 1% SO_2/He/Air after a 60 minute He-only pre-treatment at 800°C.*

	Component 1		Component 2		Component 3	
Atm.	B.E. (eV)	R.C. (%)	B.E. (eV)	R.C. (%)	B.E. (eV)	R.C. (%)
Initial	347.6	0	347.1	100.0	346.7	0.0
He-only	347.6	0	347.1	71.0	346.4	29.0
Air-only	347.6	0	347.1	73.0	346.4	27.0
SO_2	347.6	100	347.1	0.0	346.4	0.0
PT-SO_2	347.6	56	347.1	0.0	346.8	44.0

Table A29 *Peak binding energies (eV) and relative contributions of the fitted components of the Ca (2p $^{3}/_{2}$) spectra for the initial surface of the dacite glass and the dacite glass after exposure to the following conditions at 800°C, He-only, air-only, 1% SO_2/He/Air and 1% SO_2/He/Air after a 60 minute He-only pre-treatment at 800°C.*

	Component 1		Component 2		Component 3	
Atm.	B.E. (eV)	R.C. (%)	B.E. (eV)	R.C. (%)	B.E. (eV)	R.C. (%)
Initial	347.9	0	347.5	100.0	346.6	0.0
He-only	347.9	0	347.5	75.0	346.6	25.0
Air-only	347.9	0	347.5	74.0	346.6	26.0
SO_2	347.9	100	347.5	0.0	346.6	0.0
PT-SO_2	347.9	72	347.5	0.0	346.6	28.0

Table A30 *Peak binding energies (eV) and relative contributions of the fitted components of the Ca (2p $^{3}/_{2}$) spectra for the initial surface of the rhyolite glass and the rhyolite glass after exposure to the following conditions at 800°C, He-only, air-only, 1% SO_2/He/Air and 1% SO_2/He/Air after a 60 minute He-only pre-treatment at 800°C.*

	Component 1		Component 2		Component 3	
Atm.	B.E. (eV)	R.C. (%)	B.E. (eV)	R.C. (%)	B.E. (eV)	R.C. (%)
Initial	347.9	0	347.3	100.0	346.6	0
He-only	347.9	0	347.3	100.0	346.6	0
Air-only	347.9	0	347.3	100.0	346.6	0
SO_2	347.9	68	347.3	32.0	346.6	0
PT-SO_2	347.9	69	347.3	31.0	346.6	0

Table A31 *Peak binding energies (eV) and relative contributions of the fitted components of the Fe ($2p^{3}/_{2}$) spectra for the initial surface of the tephrite glass and the tephrite glass after exposure to the following conditions at 800°C, He-only, air-only, 1% SO_2/He/Air and 1% SO_2/He/Air after a 60 minute He-only pre-treatment at 800°C.*

	Component 1		Component 2	
Treatment	**B.E. (eV)**	**R.C. (%)**	**B.E. (eV)**	**R.C. (%)**
Initial	710.6	67.8	708.0	32.2
He-only	710.5	76.4	707.2	23.6
Air-only	710.0	85.7	708.0	14.4
SO_2	711.2	55.5	707.5	44.5
PT-SO_2	711.2	51.5	707.8	48.5

Table A32 *Peak binding energies (eV) and relative contributions of the fitted components of the Fe ($2p^{3}/_{2}$) spectra for the initial surface of the phonolite glass and the phonolite glass after exposure to the following conditions at 800°C, He-only, air-only, 1% SO_2/He/Air and 1% SO_2/He/Air after a 60 minute He-only pre-treatment at 800°C.*

	Component 1		Component 2	
Treatment	**B.E. (eV)**	**R.C. (%)**	**B.E. (eV)**	**R.C. (%)**
Initial	711.0	63.9	708.0	36.1
He-only	709.8	56.3	706.7	43.7
Air-only	710.2	84.0	708.0	16.0
SO_2	710.7	63.6	708.0	36.4
PT-SO_2	709.8	60.4	707.1	39.6

Table A33 *Peak binding energies (eV) and relative contributions of the fitted components of the Fe ($2p^{3}/_{2}$) spectra for the initial surface of the dacite glass and the dacite glass after exposure to the following conditions at 800°C, He-only, air-only, 1% SO_2/He/Air and 1% SO_2/He/Air after a 60 minute He-only pre-treatment at 800°C.*

	Component 1		Component 2	
Treatment	**B.E. (eV)**	**R.C. (%)**	**B.E. (eV)**	**R.C. (%)**
Initial	711.2	61.4	708.0	38.6
He-only	710.2	70.1	708.2	30.0
Air-only	711.2	83.5	708.0	16.5
SO_2	710.2	63.0	707.5	37.1
PT-SO_2	710.4	58.2	707.8	41.8

Table A34 *Peak binding energies (eV) and relative contributions of the fitted components of the Fe ($2p^{3}/_{2}$) spectra for the initial surface of the rhyolite glass and the rhyolite glass after exposure to the following conditions at 800°C, He-only, air-only, 1% SO_2/He/Air and 1% SO_2/He/Air after a 60 minute He-only pre-treatment at 800°C.*

	Component 1		Component 2	
Treatment	**B.E. (eV)**	**R.C. (%)**	**B.E. (eV)**	**R.C. (%)**
Initial	710.9	61.0	708.0	39.1
He-only	710.4	57.4	707.4	42.6
Air-only	710.4	59.1	707.5	40.9
SO_2	710.8	63.5	708.0	36.5
PT-SO_2	710.7	63.4	708.0	36.6

Table A35 *Peak binding energies (eV) and relative contributions of the fitted components of the O(1s) spectra for the initial surface of the tephrite glass and the tephrite glass after exposure to the following conditions at 800°C, He-only, air-only, 1% SO_2/He/Air and 1% SO_2/He/Air after a 60 minute He-only pre-treatment at 800°C.*

	Component 1		Component 2	
Treatment	**B.E. (eV)**	**R.C. (%)**	**B.E. (eV)**	**R.C. (%)**
Initial	531.6	57.7	530.3	42.3
He-only	531.6	46.3	529.5	53.7
Air-only	531.5	48.7	529.8	51.3
SO_2	531.7	92.7	529.7	7.3
PT-SO_2	531.9	67.6	530.4	32.4

Table A36 *Peak binding energies (eV) and relative contributions of the fitted components of the O(1s) spectra for the initial surface of the phonolite glass and the phonolite glass after exposure to the following conditions at 800°C, He-only, air-only, 1% SO_2/He/Air and 1% SO_2/He/Air after a 60 minute He-only pre-treatment at 800°C.*

	Component 1		Component 2	
Treatment	**B.E. (eV)**	**R.C. (%)**	**B.E. (eV)**	**R.C. (%)**
Initial	531.7	80.2	530.3	19.8
He-only	531.6	73.5	529.5	26.5
Air-only	531.6	61.1	529.8	38.9
SO_2	531.9	86.8	529.7	13.2
PT-SO_2	531.8	66.8	530.4	33.2

Table A37 *Peak binding energies (eV) and relative contributions of the fitted components of the O(1s) spectra for the initial surface of the dacite glass and the dacite glass after exposure to the following conditions at 800°C, He-only, air-only, 1% SO_2/He/Air and 1% SO_2/He/Air after a 60 minute He-only pre-treatment at 800°C.*

	Component 1		Component 2	
Treatment	**B.E. (eV)**	**R.C. (%)**	**B.E. (eV)**	**R.C. (%)**
Initial	532.0	69.9	530.5	30.1
He-only	531.6	67.0	530.0	33.1
Air-only	531.5	61.0	529.7	39.0
SO_2	532.0	78.7	530.0	21.4
PT-SO_2	532.0	69.4	530.0	30.6

Table A38 *Peak binding energies (eV) and relative contributions of the fitted components of the O(1s) spectra for the initial surface of the rhyolite glass and the rhyolite glass after exposure to the following conditions at 800°C, He-only, air-only, 1% SO_2/He/Air and 1% SO_2/He/Air after a 60 minute He-only pre-treatment at 800°C.*

	Component 1		Component 2	
Treatment	**B.E. (eV)**	**R.C. (%)**	**B.E. (eV)**	**R.C. (%)**
Initial	531.7	69.6	530.3	30.4
He-only	531.9	71.8	529.5	28.2
Air-only	531.9	79.5	529.8	20.5
SO_2	531.9	84.7	529.7	15.3
PT-SO_2	531.9	86.8	530.4	13.2

Appendix Two

Abstracts And Posters

APPENDIX TWO. ABSTRACTS AND POSTERS

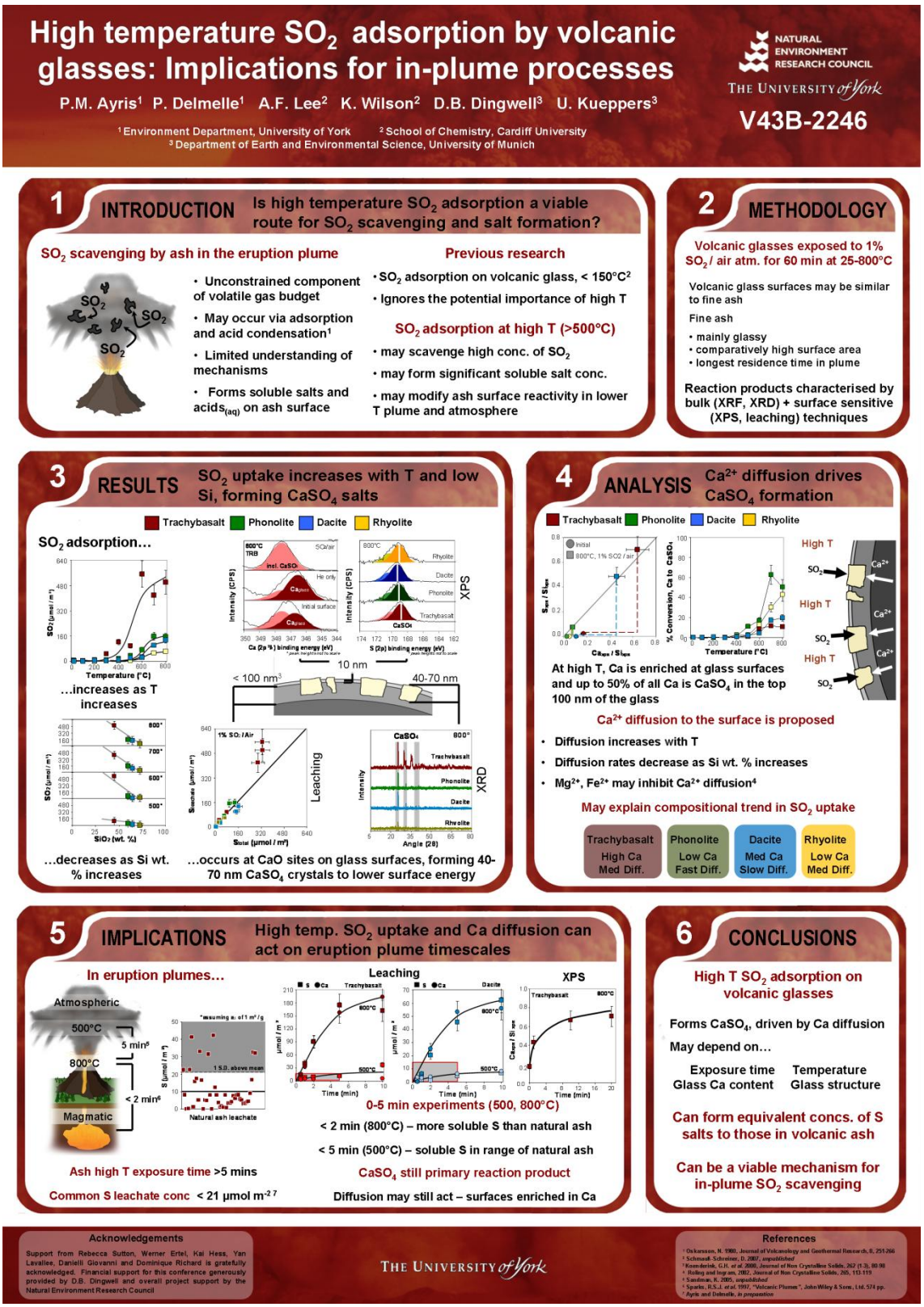

Fig. B.1 *Poster presented at the American Geophysical Union Fall Meeting, 2009.*

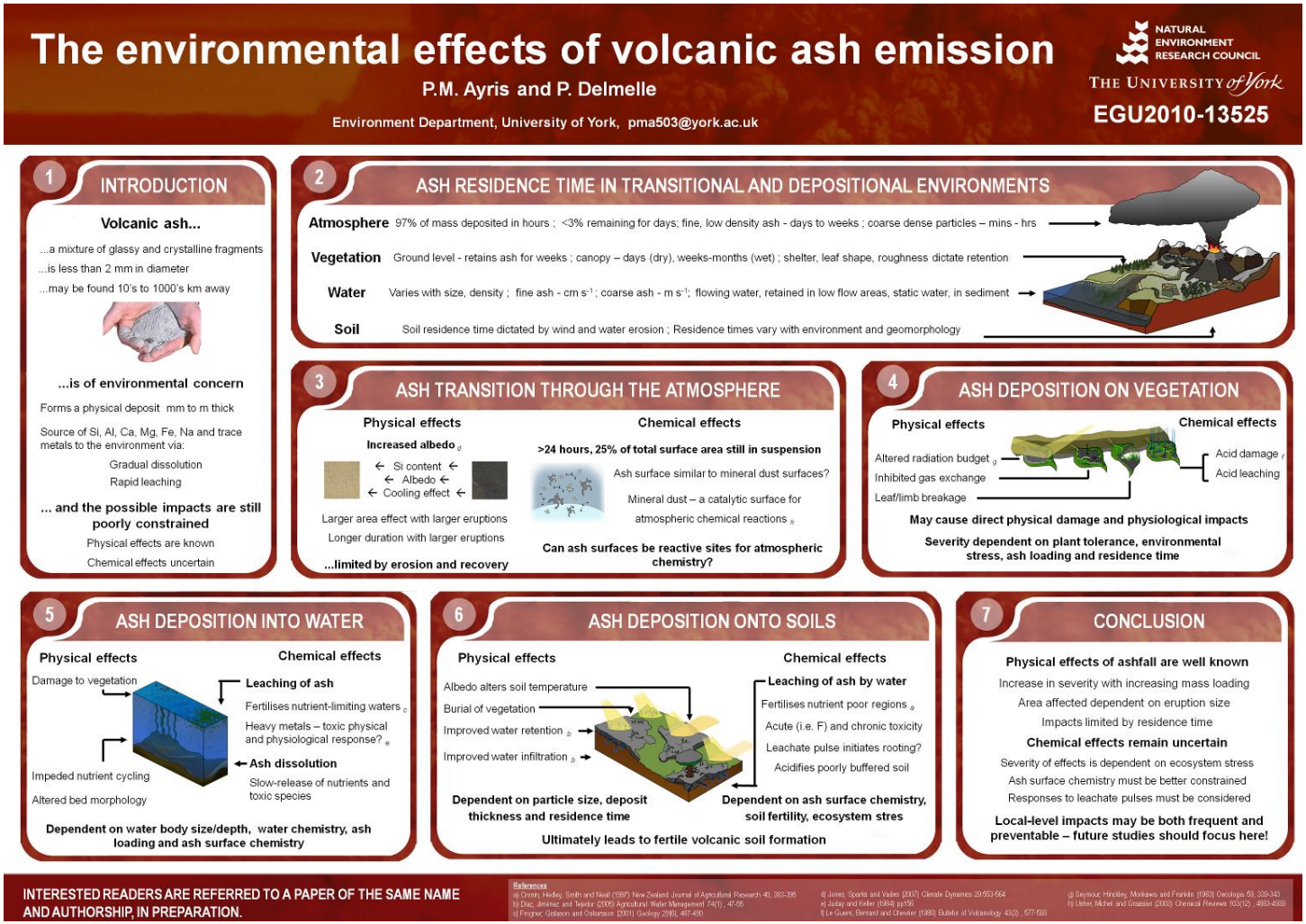

Fig. B.2 *Poster presented at the European Geosciences Union General Assembly, 2010*

Geophysical Research Abstracts
Vol. 12, EGU2010-939-1, 2010
EGU General Assembly 2010

High temperature SO_2 adsorption by volcanic glasses: New implications for gas scavenging processes in the eruption plume

Paul M. Ayris (1), Pierre Delmelle (1), Adam F. Lee (2), Karen Wilson (2), Donald B. Dingwell (3), and Ulrich Kueppers (3)

(1) Environment Department, University of York, Heslington, York, United Kingdom, (2) School of Chemistry, Cardiff University, Cardiff, United Kingdom, (3) Department of Earth and Environmental Sciences, University of Munich, Munich, Germany

The impacts of volcanic ash in the environment may be modified by gas scavenging processes by ash surfaces within the volcanic eruption plume. Current understanding of the potential environmental impacts associated with in-plume modifications to ash surface chemical properties, i.e. through the emplacement of soluble surface salts, is impeded by a limited understanding of the mechanisms controlling gas scavenging within the plume. During SO_2 adsorption experiments on volcanic glasses at 25-800°C, crystalline $CaSO_4$ was found to be the sole reaction product at >500°C. $CaSO_4$ was hypothesised to be formed by segregation from the glass surface driven by Ca diffusion from the glass interior. This study has illustrated that gas scavenging reactions are not simply a product of gas adsorption and acid condensation on solid ash particle surfaces, but may be controlled by more complex processes acting on molten ash surfaces in the high temperature eruption plume. It may be possible that these high temperature processes may extend into the subsurface volcanic or magmatic environments. Surface modification at high temperature may dictate the extent of gas scavenging and the formation of any associated reaction products upon ash surfaces, and so may influence the extent of any potential environmental impacts occurring after ash emission.

Fig. B.3 *Abstract of oral presentation given at the European Geosciences Union General Assembly, 2010.*

Reference List

REFERENCE LIST

Adams CM, Hutchinson TC (1987) Comparative abilities of leaf surfaces to neutralise acidic raindrops. II. The influence of leaf wettability, leaf age and rain duration on changes in droplet pH and chemistry on leaf surface. New Phytologist 106(3):437-456

Adams JW, Rodriguez D, Cox RA (2005) The uptake of SO_2 on Saharan dust: a flow tube study. Atmospheric Chemistry and Physics Discussions 5:2643-2676

Allard P, Burton M, Muré F (2005) Spectroscopic evidence for a lava fountain driven by previously accumulated magmatic gas. Nature 433:407-410

Anderson T (1908) Report on the eruptions of the Soufriere in St. Vincent in 1902, and on a visit to Montagne Pelee in Martinique. Part II. The changes in the districts and the subsequent history of the volcanoes. Proceedings of the Royal Society of London. Series A 208(278-303)

Antos JA, Zobel DB (1982) Snowpack modification of volcanic tephra effects on forest understory plants near Mount St. Helens. Ecology 63(6):1969-1972

Antos JA, Zobel DB (1985) Plant form, developmental plasticity, and survival following burial by volcanic tephra. Canadian Journal of Botany 63:2083-2090.

Antos JA, Zobel DB (1985) Recovery of forest under- stories buried by tephra from Mount St. Helens. Vegetatio 64:103-111.

Antos JA, Zobel DB (1985) Upward movement of underground plant parts into deposits of tephra from Mount St. Helens. Canadian Journal of Botany 63:2091-2096.

Antos JA, Zobel DB (1987) How plants survive burial: a review and initial responses to tephra from Mount St. Helens. In: Bilderback DE (ed) Mount St. Helens 1980: Botanical consequences of the explosive eruptions. University of California Press, Berkeley, CA, pp 246-261

Antos JA, Zobel DB (2005) Plant responses in forests of the tephra-fall zone. In: Dale VH, Swanson FJ, Crisafulli CM (eds) Ecological responses to the 1980 eruption of Mount St. Helens. Springer, New York, pp 47-58

Armienta MA, Cruz-Renya SDI, Morton O, Cruz O, Ceniceros N (2002) Chemical variations of tephra-fall deposit leachates for three eruptions from Popocatepetl volcano. Journal of Volcanology and Geothermal Research 113:61-80

Armienta MA, Martin-Del-Pozzo AL, Espinasa R, Cruz O, Ceniceros N, Aguayo A, Butron MA (1998) Geochemistry of ash leachates during the 1994-1996 activity of Popocatépetl volcano. Applied Geochemistry 13(7):841-850

Atkins P (2001) The Elements of Physical Chemistry. Oxford University Press, Oxford, p 548

Bailey GW (2002) Metal and major-ion redox chemistry of the hypoxic and anoxic zones: An overview. In: Thurston RV (ed) Fish Physiology, Toxicology, and Water Quality. Proceedings of the Sixth International Symposium, La Paz B.C.S. Mexico January 22-26, 2001. United States Environmental Protection Agency, La Paz, Mexico., pp 219-272

Bains S, Norris RD, Corfield RM, Faul KL (2000) Termination of global warmth at the Palaeocene/Eocene boundary through productivity feedback. Nature 407:171-174

Bair HE (1994) Glass transition measurements by DSC. In: Seyler RJ (ed) Assignment of the Glass Transition. American Society for Testing and Materials, Philadelphia, pp 50-74

Baird C (2000) Environmental Chemistry. W.H. Freeman and Company, New York, p 528

Ball MC, Simmons RE, Sutherland I (1987) Surface composition of anhydrous tricalcium aluminate and calcium aluminoferrite. Journal of Materials Science 22:1975-1979

Baltrusaitis J, Usher CR, Grassian VH (2007) Reactions of sulfur dioxide on calcium carbonate single crystal and particle surfaces at the adsorbed water carbonate interface. Physical Chemistry Chemical Physics 6:3011-3024

Barker P, Telford R, Merdaci O, Williamson D, Taieb M, Vincens A, Gibert E (2000) The sensitivity of a Tanzanian crater lake to catastrophic tephra input and four millenia of climate change. The Holocene 10(3):301-310

Barker S (2007) Origin of cementing calcite in "carbonatite" tuffs. Geology 35(4):371-374

Barr TL (1983) An XPS study of Si as it occurs in adsorbents, catalysts, and thin films. Applications of Surface Science 15(1-4):1-35

Bay RC, Bramall N, Price PB (2004) Bipolar correlation of volcanism with millennial climate change. Proceedings of the National Academy of Sciences of the United States of America 101(17):6341-6345

Bekki S (1994) Oxidation of volcanic SO_2: A sink for stratospheric OH and H_2O. Geophysical Research Letters 22(8):913-916

Bernard A, Le Guern F (1986) Condensation of volatile elements in high-temperature gases of Mount St. Helens. Journal of Volcanology and Geothermal Research 28(1-2):91-105

Bertin EP (1970) Principles and Practice of X-ray Spectrometric Analysis. Plenum press, London, p 679

Bhat KN, Ranatunga TD, Taylor RW, Senwo ZN, April RH, Jackson B (2005) Nutrient and metal contents of volcanic ash and soils from Montserrat Island, West Indies. In: The ASA-CSSA-SSSA International Annual Meeting.

Bikerman JJ (1978) Surface energy of solids. Topics in Current Chemistry 77:1-66

Biondi F, Estrada IG, Gavilanes Ruiz JC, Torres AE (2003) Tree growth response to the 1913 eruption of Volcan de Fuego de Colima, Mexico. Quaternary Research 59(3):293

Black RA, Mack RN (1984) Aseasonal leaf abcscission in *Populus* induced by volcanic ash. Oecologia 64(3):295-299

Black RA, Mack RN (1986) Mount St. Helens ash: Recreating its effects on the steppe environment and ecophysiology. Ecology 67(5):1289-1302

Bluth GJS, Rose WI, Sprod IE, Krueger AJ (1997) Stratospheric loading of sulfur from explosive volcanic eruptions. The Journal of Geology 105:671-683

Bonadonna C, Ernst GGJ, Sparks RSJ (1998) Thickness variations and volume estimates of tephra fall deposits: the importance of particle Reynolds number. Journal of Volcanology and Geothermal Research 81(3-4):173-187

Brinker CJ, Scherer GW (1985) Sol --Gel --Glass: I. Gelation and gel structure. Journal of Non-Crystalline Solids 70:301-322

Bryan SE, Cook A, Evans JP, Colls PW, Wells MG, Lawrence MG, Jell JS, Greig A, Leslie R (2004) Pumice rafting and faunal dispersion during 2001–2002 in the Southwest Pacific: record of a dacitic submarine explosive eruption from Tonga. Earth and Planetary Science Letters 227(1-2):135-154

Buerger MJ (1942) X-ray Crystallography. John Wiley & Sons, Inc., London, p 531

Burkhard DJM (2001) Crystallization and oxidation of Kileaua basalt glass: processes during reheating experiments. Journal of Petrology 42(3):507-527

Burnham RJ (1993) Plant deposition in modern volcanic environments. Transactions of the Royal Society of Edinburgh. Earth sciences 84(3-4):275-281

Burton M, Allard P, Muré F, La Spina A (2007) Magmatic gas composition reveals the source depth of slug-driven Strombolian explosive activity. Science 317:227-230

Cannata C, Taddeucci J, Lautze N, De Rosa R, Donato P, Scarlato P (2010) Ash Features from Present-day Activity at Stromboli. Geophysical Research Abstracts 12:EGU2010-15294

Carey SN, Bursik MI (2000) Volcanic plumes. In: Sigurdsson H, Houghton B, McNutt S, Rymer H, Stix J (eds) Encyclopedia of Volcanoes. Academic Press, London, pp 527-545

Cashman KV, Sturtevant B, Papale P, Navon O (2000) Magmatic fragmentation. In: Sigurdsson H, Houghton B, McNutt S, Rymer H, Stix J (eds) Encyclopedia of Volcanoes. Academic Press, London, pp 421-430

Cather SM, Dunbar NW, McDowell FW, McIntosh WC, Scholle PA (2009) Climate forcing by iron fertilization from repeated ignimbrite eruptions: The icehouse–silicic large igneous province (SLIP) hypothesis. Geosphere 5(3):315-324

Chang R (1994) Chemistry. McGraw-Hill, Inc., London, p 1042

Christenson B (2000) Geochemistry of fluids associated with the 1995–1996 eruption of Mt. Ruapehu, New Zealand: signatures and processes in the magmatic-hydrothermal system. Journal of Volcanology and Geothermal Research 97(1-4):1-30

Christie AB, Lee J, Sutherland I, Walls JM (1983) An XPS study of ion-induced compositional changes with group II and group IV compounds. Applications of Surface Science 15(1-4):224-237

Churakov SV, Tkachenko SI, Korzhinskii MA, Bocharnikov RE, Shmulovich KI (2000) Evolution of composition of high-temperature fumarolic gases from Kudryavy volcano, Iturup, Kuril Islands: the thermodynamic modeling. Geochemistry International 38(5):436-451

Cochran VL, Bezdicek DF, Elliott LF, Papendick RI (1983) The effect of Mount St. Helens' volcanic ash on plant growth and mineral uptake. Journal of Environmental Quality 12:415-418

Collins BD, Dunne T (1986) Erosion of tephra from the 1980 eruption of Mount St. Helens. Geological Society of America Bulletin 97(7):896-905

Collins BD, Dunne T (1988) Effects of forest land management on erosion and revegetation after the eruption of Mount St. Helens. Earth Surface Processes and Landforms 13:193-205

Collins BD, Dunne T, Lehre AK (1983) Erosion of hillslopes north of Mount St. Helens, Washington, May 1980-May 1981. Zeitschrqt fur Geomorphologie Suppl. Bd. 46:103-121

Cook GB, Cooper RF (2000) Iron concentration and the physical processes of dynamic oxidation in an alkaline earth aluminosilicate glass. American Mineralogist 85:397-406

Cook RJ, Barron JC, Papendick RI, Williams I, G.J. (1981) Impact on agriculture of the Mt. St. Helens eruptions. Science 211(4477):16-22

Cooper RF, Fanselow JB, Poker DB (1996) The mechanism of oxidation of a basaltic glass: chemical diffusion of network modifying cations. Geochimica et Cosmochimica Acta 60:3253-3265

Cresser MS, Killham K, Edwards T (1993) Soil chemistry and its applications. Cambridge University Press, Cambridge, p 192

Cronin SJ, Hedley MJ, Neall VE, Smith RG (1998) Agronomic impact of tephra fallout from the 1995 and 1996 Ruapehu volcano eruptions, New Zealand. Environmental Geology 34(1):21-30

Cronin SJ, Hedley MJ, Smith RG, Neall VE (1997) Impact of Ruapehu ash fall on soil and pasture nutrient status 1. October 1995 eruptions. New Zealand Journal of Agricultural Research 40:383-395

Crowley SS, Dufek DA, Stanton RW, Ryer TA (1994) The effects of volcanic ash disturbances on a peat forming environment: Environmental disruption and taphonomic consequences. Palaios 9(2):158-174

Dahlgren RA (2008) Acid deposition effects on soils. In: Chesworth W (ed) Encyclopedia of Soil Science. Springer, Dordrecht, pp 2-7

Dahlgren RA, Ugolini FC, Casey WH (1999) Field weathering rates of Mt. St. Helens tephra. Geochimica et Cosmochimica Acta 63(5):587-598

Dale VH, Swanson FJ, Crisafulli CM (2005) Ecological responses to the 1980 eruption of Mount St. Helens. Springer, New York, p 342

Davis BL, Johnson LR, Griffen DT, Phillips WR, Stevens RK, Maughan D (1981) Quantitative analysis of Mt. St. Helens ash by X-ray diffraction and X-ray fluorescence spectrometry. Journal of Applied Meteorology 20:922-933

de Moor JM, Fischer TP, Hilton DR, Hauri E, Jaffe LA (2005) Degassing at Anatahan volcano during the May 2003 eruption: Implications from petrology, ash leachates, and SO_2 emissions. Journal of Volcanology and Geothermal Research 146:117-138

Delmelle P, Delfosse T, Delvaux B (2003) Sulfate, chloride and fluoride retention in Andosols exposed to volcanic acid emissions. Environmental Pollution 126:445-457

Delmelle P, Lambert M, Dufrêne Y, Gerin P, Óskarsson N (2007) Gas/aerosol-ash interaction in volcanic plumes: new insights from surface analysis of fine volcanic ash. Earth and Planetary Science Letters 259(1-2):159-170.

Delmelle P, Stix J (2000) Volcanic gases. In: Sigurdsson H, Houghton B, McNutt S, Rymer H, Stix J (eds) Encyclopedia of Volcanoes. Academic Press, London, pp 803-815

Delmelle P, Villiéras F, Pelletier M (2005) Surface area, porosity and water adsorption properties of fine volcanic ash particles. Bulletin of Volcanology 67:160-169

Dentener FJ, Carmichael GR, Zhang Y, Lelieveld J, Crutzen PJ (1996) Role of mineral aerosol as a reactive surface in the global troposphere. Journal of Geophysical Research 101(D17):22689-22889

Diaz F, Jiménez C, Tejedor M (2005) Influence of the thickness and grain size of tephra mulch on soil water evaporation. Agricultural Water Management 74(1):47-55

Dietzel A (1942) Praktische bedeutung von berechnung der oberflächenspannung von gläsern, glasuren und emails. Sprechsaal 75:82-85

Dise NB, Verry ES (2001) Suppression of peatland methane emission by cumulative sulfate deposition in simulated acid rain. Biogeochemistry 53(2):143-160

Doremus RH (1973) Glass Science. Wiley-Interscience, Chichester, p 349

Douglas RW, Isard JO (1949) The action of water and of sulphur dioxide on glass surfaces. Journal of the Society of Glass Technology 33:289-335

Dubos E (2006) Albedo. In: Lal R (ed) Encyclopedia of Soil Science. CRC Press, New York, pp 64-66

Duggen S, Croot P, Schacht U, Hoffman L (2007) Subduction zone volcanic ash can fertilize the surface ocean and stimulate phytoplankton growth: evidence from biogeochemical experiments and satellite data. Geophysical Research Letters 34(L01612):doi:10.1029/2006GL027522

Duggen S, Olgun N, Croot P, Hoffman L, Dietze H, Teschner C (2010) The role of airborne volcanic ash for the surface ocean biogeochemical iron-cycle: a review. Biogeosciences Discussions 6:6441–6489

Dunken HH (1982) Glass surfaces. In: Tomozawa M, Doremus RH (eds) Treatise on Materials Science and Technology. Academic Press, New York, New York, pp 1-74

Dwivedi RK, Gowda G (1985) Thermal stability of aluminium oxides prepared from gel. Journal of Materials Science Letters 4:331-334

Edmonds M, Gerlach TM, Herd RA, Sutton AJ, Elias T (2005) The composition of volcanic gas issuing from Pu`u `O`o, Kilauea Volcano, Hawaii, 2004-5. AGU Fall Meeting Abstracts 8:V13G-08

Edmonds M, Oppenheimer C, Pyle DM, Herd RA (2003) Rainwater and ash leachate analysis as proxies for plume chemistry at Soufriere Hills Volcano, Montserrat. Geological Society Special Publications 213:203-218

Edwards KJ, Dugmore AJ, Blackford JJ (2004) Vegetational response to tephra deposition and land-use change in Iceland: a modern analogue and multiple working hypothesis approach to tephropalynology. Polar Record 40(213):113-120

Eggler WA (1948) Plant communities in the vicinity of the volcano El Paricutin, Mexico, after two and a half years of eruption. Ecology 29(4):415-436

Eggler WA (1967) Influence of volcanic eruptions on xylem growth pattern. Ecology 48(4):644-647

Eicher GJ, Rounsefell GA (1957) Effects of lake fertilization by volcanic activity on abundance of salmon. Limnology and Oceanography 2(2):70-76

El-Swaify SA, Dangler EW, Armstrong CL (1982) Soil erosion by water in the tropics. In: College of Tropical Agriculture and Human Resources, Univ. of Hawaii Research Extension Series 024. Honolulu, p 172

Elliot LF, Tittemore D, Papendick RI, Cochran VI, Bezdicek DF (1982) The effect of Mount Saint Helens' ash on soil microbial respiration and numbers. Journal of Environmental Quality 11:164-166

Erbil HY (2006) Surface Chemistry of Solid and Liquid Interfaces. Blackwell, Oxford, p 352

Fadley CS, Shirley DA (1970) Multiplet splitting of metal-atom electron binding energies. Physical Review A. General Physics. 2(4):1109-1120

Farges F, Keppler H, Flank A-M, Lagarde P (2009) Sulfur K-edge XANES study of S sorbed onto volcanic ashes. Journal of Physics: Conference Series 190:doi:10.1088/1742-6596/1190/1081/012177

Ferguson RI, Church M (2004) A simple universal equation for grain settling velocity. Journal of Sedimentary Research 74(6):933-937

Flaathen TK, Gislason SR (2007) The effect of volcanic eruptions on the chemistry of surface waters: The 1991 and 2000 eruptions of Mt. Hekla, Iceland. Journal of Volcanology and Geothermal Research 164:293-316

Forde B, Lorenzo H (2001) The nutritional control of root development. Plant and Soil 232:51-68

Francis P, Horrocks L, Oppenheimer C (2000) Monitoring gases from andesite volcanoes. Philosophical Transactions: Mathematical, Physical and Engineering Sciences 358:1567-1584

Frenzel SA (1983) Effects of volcanic ash on the benthic environment of a mountain stream, Northern Idaho. In: USGS Water-Resources Investigation Reports 82-4106. p 32

Frischat GH (1975) Ionic Diffusion in Oxide Glasses. Transtech Publications, Bay Village, Ohio, p 181

Frogner Kockum PC, Herbert RB, Gislason SR (2006) A diverse ecosystem response to volcanic aerosols. Chemical Geology 231:57-66

Frogner P, Gislason SR, Óskarsson N (2001) Fertilizing potential of volcanic ash in ocean surface waters. Geology 29(6):487-490

Frogner PC, Herbert RB, Gislason SR (2006) A diverse ecosystem response to volcanic aerosols. Chemical Geology 231:57-66

Fuchs M, Stanhill G, Moreshet S (1976) Effect of increasing foliage and soil reflectivity on the solar radiation balance of wide-row grain sorghum. Agronomy Journal 68:865-871

Funk WH (1980) Effects of ash fallout on eastern Washington lakes and the upper Spokane river. In: Cassidy JJ (ed) Conference on the aftermath of Mount St. Helens. Pullman, Washington, 1980. Proceedings. Washington State University, Pullman, Washington, pp 18-19

Gauci V, Blake S, Stevenson D, Highwood EJ (2008) Halving of the Northern wetland CH4 source by a large Icelandic volcanic eruption. Journal of Geophysical Research:In press

Gauci V, Dise NB, Fowler R (2002) Controls on suppression of methane flux from a peat bog subjected to simulated acid rain sulfate deposition. Global Biogeochemical Cycles 16(1):10.1029/2000GB001370

Gilbert JS, Lane SJ (1994) The origin of accretionary lapilli. Bulletin of Volcanology 56:398-411

Giles TM, Newnham RM, Lowe DJ, Munro AJ (1999) Impact of tephra fall and environmental change: a 1000 year record from Matakana Island, Bay of Plenty, North Island, New Zealand. Geological Society, London, Special Publications 161:11-26

Giordano D, Russell JK, Dingwell DB (2008) Viscosity of magmatic liquids: a model. Earth and Planetary Science Letters 271:123-134

Goldin A (1982) Influence of volcanic ash from the May 18, 1980, eruption of Mount St. Helens on the properties of soils. Journal of Soil and Water Conservation 37(3):185-189

Goldman CR (1960) Primary productivity and limiting factors in three lakes of the Alaska peninsula. Ecological Monographs 30(2):207-230

Golterman HL, Clymo KE, Clymo RS (1975) Physiological limnology: an approach to the physiology of lake ecosystems. Elsevier, Amsterdam, p 489

Goodman AL, Bernard ET, Grassian VH (2001) Spectroscopic study of Nitric acid and water adsorption on oxide particles: enhanced nitric acid uptake kinetics in the presence of adsorped water. Journal of Physical Chemistry A 105:6443-6457

Goodman AL, Underwood GM, Grassian VH (1999) Heterogeneous reaction of NO_2: Characterization of gas-phase and adsorbed products from the reaction, $2NO_2(g) + H_2O_{(a)} \rightarrow HONO_{(g)} + HNO_{3(a)}$ on hydrated silica particles. Journal of Physical Chemistry A 106(36):7217-7223

Gordon N, McMahon TA, Finlayson BL, Gippel CJ, Nathan RJ (2004) Stream Hydrology. An Introduction for Ecologists. Second edition. John Wiley & Sons., Chichester, p 429

Goudie AS, Middleton NJ (2001) Saharan dust storms: nature and consequences. Earth-Science Reviews 56(1):179-204

Goworek J (2000) Thermogravimetric approach for determining porosity of silica gels. In: Papirer E (ed) Adsorption on silica surfaces. Marcel Dekker, Inc., New York, pp 167-204

Granberg G, Sundh I, Svensson BH, Nilsson M (2001) Effects of temperature, and nitrogen and sulfur deposition, on methane emission from a boreal mire. Ecology 82(7):1982-1998.

Grattan JP, Gilbertson DD (1994) Acid-loading from Icelandic Tephra falling on acidified ecosystems as a key to understanding archaeological and environmental stress in Northern and Western Britain. Journal of Archaeological Science 21:851-859

Griggs RF (1915) The effect of the eruption of Katmai on land vegetation. Bulletin of the American Geographical Society 47(3):193-203

Griggs RF (1919) The beginnings of revegetation in Katmai Valley. The Ohio Journal of Science 19:318

Grishin SY, del Moral R, Krestov PV, Verkholat VP (1996) Succession following the catastrophic eruption of Ksudach volcano (Kamchatka, 1907). Plant Ecology 127(2):129-153

Grobbelaar JU (1985) Phytoplankton productivity in turbid waters. Journal of Plankton Research 7(5):653-663

Gu Y, Gierke JS, Bluth GJS, Rose WI (1999) A Laboratory Study of Sulfur Dioxide Adsorption onto Fine Dacitic Volcanic Ash. In: Fall Meeting, American Geophysical Union. San Francisco

Guiner A, Dexter DL (1963) X-ray Studies of Materials. Interscience Publishers, London, p 156

Haeckel M, van Beusekom J, Wiesner MG, König I (2001) The impact of the 1991 Mount Pinatubo tephra fallout on the geochemical environment of the deep-sea sediments in the South China Sea. Earth and Planetary Science Letters 193:151-166

Haines BL, Jernstedt JA, Neufeld HS (1985) Direct Foliar Effects of Simulated Acid Rain. II. Leaf Surface Characteristics. New Phytologist 99(3):407-416

Harris E, Mack RN, Ku MSB (1987) Death of steppe cryptograms under the ash from Mount. St. Helens. American Journal of Botany 74(8):1249-1253

Hayes SK, Montomery DR, Newhall CG (2002) Fluvial sediment transport and deposition following the 1991 eruption of Mount Pinatubo. Geomorphology 45:211-224

Heald EF, Naughton JJ, Lynus Barnes Jr I (1963) The chemistry of volcanic gases. 2. Use of equilibrium calculations in the interpretation of volcanic gas samples. Journal of Geophysical Research 68(2):545-557

Hegedues AJ, Fukker K (1956) Contribution to thermoanalytical study of the decomposition and reduction of sulfates. Zeitschrift Fuer Anorganische Und Allgem Eine Chemie

284:20-30

Heiken G, Wohletz K (1992) Volcanic Ash. University of California Press, London, p 246

Hiemenz PC, Rajagopalan R (1997) Principles of Colloid and Surface Chemistry. Marcel Dekker, Inc., New York, p 650

Highwood EJ, Stevenson DS (2003) Atmospheric impact of the 1983-1984 Laki Eruption: Part II. Climatic effect of sulphate aerosol. Atmospheric Chemistry and Physics Discussions 3:1599-1629

Hinckley TK, Imoto H, Lee KT, Lacker S, Morikawa Y, Vogt KA, Grier CG, Keyes MR, Teskey RO, Seymour VA (1984) Impact of tephra deposition on growth in confiers: the year of the eruption. Canadian Journal of Forest Research 14(5):731-739

Hinkley TK, Smith KS (1982) Leachate chemistry of ash from the May 18, 1980 eruption of Mount St. Helens. U.S. Geological Survey Professional Paper 1397-B:27-64

Hinkley TK, Smith KS, Taggart JE, Brown JT (1982) Chemical and mineralogic aspects of observed fractionation of ash from May 18, 1980 eruption of Mount St. Helens. U.S. Geological Survey Professional Paper 1397-A:10-22

Hobbs PV, Hegg DA, Radke LF (1983) Resuspension of volcanic ash from Mount St. Helens. Journal of Geophysical Research 88(C6):3919-3921

Hogg P, Squires P, Fitter AH (1995) Acidification, nitrogen deposition and rapid vegetational change in a small valley mire in Yorkshire. Biological Conservation 71(2):143-153

Holland D, Mekki A, Gee A, McConville CF, Johnson JA, Appleyard P, Thomas M (1999) The structure of sodium iron silicate glass – a multi-technique approach. Journal of Non-Crystalline Solids 253(1-3):192-202

Horwell CJ, Fenoglio I, Vala Ragnarsdottir K, Sparks RSJ, Fubini B (2003) Surface reactivity of volcanic ash from the eruption of Soufrière Hills volcano, Montserrat, West Indies with implications for health hazards. Environmental Research 93:202-215

Hossain A (2004) Properties of volcanic pumice based cement and lightweight concrete. Cement and concrete research 34(2):283-291

Hotes S, Poschlod P, Sakai H, Inoue T (2001) Vegetation, hydrology and development of a coastal mire in Hokkaido, Japan, affected by flooding and tephra deposition. Canadian Journal of Botany 79:341-361

Hotes S, Poschlod P, Takahashi H, Grootjans AP, Adema E (2004) Effects of tephra deposition on mire vegetation: a field experiment in Hokkaido, Japan. Journal of Ecology 92:624-634

Houghton BF, Wilson CJN (2000) Pyroclastic transport and deposition. In: Sigurdsson H, Houghton B, McNutt S, Rymer H, Stix J (eds) Encyclopedia of Volcanoes. Academic Press, San Diego, pp 545-554

Housecroft CE, Constable EC (1997) Chemistry. Pearson Education Limited, Harlow, p 1158

Inbar M, Ostera HA, Parica CA, Remesal MB, Salani FM (1995) Environmental assessment of 1991 Hudson volcano eruption ashfall effects on southern Patagonia region, Argentina. Environmental Geology 25:119-125

Jackson RB, Caldwell MM (1989) The timing and degree of root proliferation in fertile-soil microsites for three cold-desert perennials. Oecologia 81:149-153

Jacob KT, Iwase M, Waseda Y (1987) A galvanic sensor for SO_3/SO_2 based on the $CaF_2/CaSO_4$ couple. Solid State Ionics 23:245-252

Jones GS, Gregory JM, Stott PA, Tett SFB, Thorpe RB (2005) An AOGCM simulation of the climatic response to a volcanic supereruption. Climate Dynamics 25(7-8):725–738

Jones MP (1987) Applied Mineralogy. A Quantitative Approach. Graham & Trotman, London, p 259

Jones MT, Gislason SR (2008) Rapid releases of metal salts and nutrients following the deposition of volcanic ash into aqueous environments. Geochimica et Cosmochimica Acta 72(15)

Jones MT, Sparks RSJ, Vades PJ (2007) The climatic impact of supervolcanic ash blankets. Climate Dynamics 29:553-564

Jorgensen JE, Mosegaard L, Thomsen LE, Jensen TR, Hanson JC (2007) Formation of gamma-Fe_2O_3 nanoparticles and vacancy ordering: an in situ x-ray powder diffraction study. Journal of Solid State Chemistry 180:180-185

Juday RE, Keller EJ (1984) The effect of ash fallout on water quality in Western Montana. In: Department of Chemistry, University of Montana, pp 1-147

Juday RE, Keller EJ (1984) Effect of ash fallout on water quality in western Montana. Final report. Department of Chemistry, University of Montana, p 156

Kaiser MJ, Attrill MJ, Jennings S, Thomas DN, Barnes DKA, Brierley AS, Polunin NVC, Raffaelli DG, Williams PJlB (2005) Marine Ecology. Processes, Systems and Impacts. Oxford University Press, Oxford, p 557

Kellman M, Hudson J, Sanmugadas K (1982) Temporal variability in atmospheric nutrient influx to a tropical ecosystem. Biotropica 14(1):1-9

Kennedy RA (1980) Ash from Mt. St. Helens. Nature 287(5783):581

Kent M, Owen NW, Dale P, Newnham RM, Giles TM (2001) Studies of vegetation burial: a focus for biogeography and biogeomorphology? Processes in Physical Geography 25(4):455-482

Kilian R, Biester H, Behrmann J, Baeza O, Fesq-Martin M, Hohner M, Schimpf D, Friedmann A, Mangini A (2006) Millennium-scale volcanic impact on a superhumid and pristine ecosystem. Geology 34(8):609-612

Kirchheim R (2003) On the mobility of alkaline earth ions in mixed alkali alkaline earth silicate glasses. Journal of non-crystalline solids 328:157-163

Koenderink GH, Brzesowsky RH, Balkenende AR (2000) Effect of the initial stages of leaching on the surface of alkaline earth sodium silicate glasses. Journal Of Non-Crystalline Solids 262(1-3):80-98

Krammer G, Brunner C, Khinast J, Staudinger G (1997) Reaction of $Ca(OH)_2$ with SO_2 at low temperature. Industrial Engineering and Chemical Research 36(5):1410–1418

Kratos (2006) AXIS Ultra HSA. In: Kratos Analytical,

Kurenkov II (1966) The influence of volcanic ashfall on biological processes in a lake. Limnology and Oceanography 11(3):426-429

Lagalante AF (1999) Atomic absorption spectroscopy: a tutorial review. Applied Spectroscopy Reviews 34(3):173-189

Lamparski LL, Nestrick TJ, Cutie SS (1990) The impact on the environment of airborne particulate matter from the eruption of Mount Saint Helens in May 1980. In: Clement R, Kogel R (eds) Emissions from combustion processes: origin, measurement, control. Lewis Publishers., Chelsea, MI, p 491

Lautze N, Taddeucci J, Andronico D, Tornetta L, Cannata C, Cristaldi A (2010) Developments in analysis of basaltic ash applied to recent activity at Stromboli and Etna volcanoes. Geophysical Research Abstracts 12:EGU2010-15296

Le Guern F, Bernard A, Chevrier RM (1980) Soufriere of Guadeloupe 1976-1977 eruption - mass and energy transfer and volcanic health hazards. Bulletin of Volcanology 43(3):577-593

Le Maitre RW, Streckeisen A, Zanettin B, Le Bas MJ, Bonin B, Bateman P, Bellieni G, Dudek A, Efremova S, Keller J, Lamere J, Sabine PA, Schmid R, Sorensen H, Woolley AR (2002) Igneous Rocks: A Classification and Glossary of Terms, Recommendations of the International Union of Geological Sciences, Subcommission of the Systematics of Igneous Rocks. Cambridge University Press, Cambridge, p 256

Lee DB (1996) Effects of the Eruptions of Mount St. Helens on Physical, Chemical and Biological Characteristics of Surface Water, Ground Water, and Precipitation in the Western United States. In: U.S. Geological Survey Water-Supply Paper 2438.

Lee KT, Bhatia S, Mohamed AR (2005) Kinetic model for the reaction between SO_2 and coal fly ash/CaO/$CaSO_4$ sorbent. Journal of Thermal Analysis and Calorimetry 79:691-695

Legod MA, de Waal D, Potgieter JH, Potgieter SS (2001) Technical note. Rapid determination of $CaCO_3$ in mixtures utilising FT-IR spectroscopy. Minerals Engineering 14(9):1107-1111

Lide D (2005) CRC Handbook Chemistry and Physics, 85th Edition. CRC Press LLC, Boca Ranton, p 2656

Lowell S, Shields JE (1984) Powder Surface Area and Porosity. John Wiley & Son, Inc., New York, p 234

Luhr JF (1990) Experimental Phase Relations of Water- and Sulfur-Saturated Arc Magmas and the 1982 Eruptions of El Chichón Volcano. Journal of Petrology 31(5):1071-1114

Luhr JF, Carmichael ISE, Varekamp JC (1984) The 1982 eruptions of El Chichón volcano, Chiapas, Mexico: Mineralogy and petrology of the anhydrite-bearing pumices. Journal of Volcanology and Geothermal Research 23:69-108

Lyles L (1988) 4. Basic wind processes. Agriculture, Ecosystems and Environment 22-23:91-101

Lynch JM, Elliot LF (1983) Aggregate stabilization of volcanic ash and soil during microbial degradation of straw. Applied and Environmental Microbiology 45(4):1398-1401

Mack RN (1981) Initial effects of ashfall from Mount St. Helens on vegetation in Eastern Washington and adjacent Idaho. Science 213(4507):537-539

Mahler RL (1984) Influence of Mount St. Helens volcanic ash on alfalfa growth and nutrient uptake. Commun. Soil Sci. Plant Anal. 15(4):449-460

Major JJ, Yamakoshi T (2004) Decadal-scale change of infiltration characteristics of a tephra-mantled hillslope at Mt. St. Helens, Washington. Hydrological Processes 19:3621-3630

Malmer N (1993) Mineral nutrients in vegetation and surface layers of Sphagnum-dominated peat-forming systems. Advances in Bryology 5:223–248

Manville V, Hodgson KA, Houghton BF, Keys JRH, White JDL (2000) Tephra, snow and water: complex sedimentary responses at an active snow-capped stratovolcano, Ruapehu, New Zealand. Bulletin of Volcanology 62:278-293

Martin GA, Watt SFL, Pyle D, Mather TA, Matthews NE, Georg RB, Day JA, Fairhead T, Witt MLI, Quayle BM (2009) Environmental effects of ashfall in Argentina from the 2008 Chaitén volcanic eruption. Journal of Volcanology and Geothermal Research 184(3-4):462-472

Martin RS, Mather TA, Pyle DM, Watt SFL, Daya JA, Collins SJ, Wright TE, Aiuppac A, Calabresec S (2009) Sweet chestnut (Castanea sativa) leaves as a bio-indicator of volcanic gas, aerosol and ash deposition onto the flanks of Mt Etna in 2005–2007. Journal of Volcanology and Geothermal Research 179(1-2):107-119

Mass C, Robock A (1982) The short-term influence of the Mount St. Helens volcanic eruption on surface temperature in the Northwest United States. Monthly Weather Review 110:614-619

Mastin LG (2007) A user-friendly one-dimensional model for wet volcanic plumes. Geochemistry Geophysics Geosystems 8(3):doi:10.1029/2006GC001455

Materials OoWaH (1976) Quality criteria for water. In: U.S. Environmental Protection Agency, Washington D.C., p 543

Mather TA, Pyle DM, Oppenheimer C (2003) Tropospheric volcanic aerosol. Geophysical Monograph 139:189-212

Matsumoto A, Chen H, Tsutsumi K, Grün M, Unger K (1999) Novel route in the synthesis of MCM-41 containing framework aluminum and its characterization. Microporous and Mesoporous Materials 32(1-2):55-62

McCash EM (2001) Surface Chemistry. Oxford University Press, Oxford, p 178

McCormick MP, Thomason LW, Trepete CR (1995) Atmospheric effects of the Mt. Pinatubo eruption. Nature 373:399-404

Mcknight DM, Feder GL, Stiles EA (1981) Toxicity of volcanic-ash leachate to a blue-green alga. Results of a preliminary bioassay experiment. Environmental Science and Technology 15(3):362-364

Mehler H (2007) Diffusion in solids. Fundamentals, methods, materials, diffusion-controlled processes. Springer-Verlag, Berlin, p 651

Mekki A, Holland D, McConville CF, Salim M (1996) An XPS study of iron sodium silicate glass surfaces. Journal of Non-Crystalline Solids 208:267-276

Meshkhidze N, Chameides WL, Nenes A, Chen G (2003) Iron mobilization in mineral dust: Can anthropogenic SO_2 emissions affect ocean productivity? Geophysical Research Letters 30(21):doi:10.1029/2003GL018035

Michel AE, Usher CR, Grassian VH (2003) Reactive uptake of ozone on mineral oxides and mineral dusts. Atmospheric Environment 37(23):3201-3211

Miller CF, Hong L (1966) Operation Ceniza-Arena: The retention of fallout particles from Volcan Irazu (Costa Rica) by plants and people. Part 1. In: Stanford Research Institute, p 374

Moriizumi M, Nakashima S, Okumura S, Yamanoi Y (2009) Color-change processes of a plinian pumice and experimental constraints of color-change kinetics in air of an obsidian. Bulletin of Volcanology 71:1-13

Muto H, Takizawa Y, Asada S (1994) Dioxins in dust fall and volcanic ash samples from the active volcanos Fugendake and Sakurajima. Organohalogen Compounds 20:359-362

Mysen BO, Richet P (2005) Natural Melts. In: Silicate Glasses and Melts. Properties and Structure. Elsevier, London, pp 503-524

Mysen BO, Richet P (2005) Silicate Glasses and Melts. Elsevier, London, p 544

Nakada S (2000) Hazards from pyroclastic flows and surges. In: Sigurdsson H, Houghton B, McNutt S, Rymer H, Stix J (eds) Encyclopedia of Volcanoes. Academic Press, London, pp 945-956

Newhall CG, Self S (1982) The volcanic explosivity index (VEI): An estimate of explosive magnitude for historical volcanism. Journal of Volcanology and Geothermal Research 87(C2):1231-1238

Nowok JW, Hurley JP, Benson SA (1995) Sulfation propensity of coal ashes and instability of calcium and magnesium sulfates at high temperatures. In: Carvalho MG, Fiveland WA, Lockwood FC (eds) Combustion Technologies for a Clean Environment. Selected Papers from the Proceedings of the Third International Conference. Taylor & Francis, New York, pp 333-344

Okui M, Sawada H, Marumo F (1998) Structure refinement of a nonstoichiometric pyroxene synthesized under ambient pressure. Physics and Chemistry of Minerals 25:318-322

Oppenheimer C (2002) Limited global change due to the largest known Quaternary eruption, Toba ≈74 kyr BP? Quartenary Science Reviews 21(14-15):1593-1609

Oppenheimer C, Francis P, Stix J (1998) Depletion rates of sulfur dioxide in tropospheric volcanic plumes. Geophysical Research Letters 25(14):2671-2674

Óskarsson N (1980) The interaction between volcanic gases and tephra: fluorine adhering to tephra of the 1970 Hekla eruption. Journal of Volcanology and Geothermal Research 8:251-266

Parikh NM (2006) Effect of atmosphere on surface tension of glass. Journal of the American Ceramic Society 41(1):18-22

Partanen J, Backman P, Backman R, Hupa M (2005) Absorption of HCl by limestone in hot flue gases. Part III: simultaneous absorption with SO2. Fuel 84(12-13):1685

Paul A (1982) Chemistry of Glasses. Chapman and Hall, London, p 367

Percy KE, Baker EA (1988) Effects of simulated acid rain on leaf wettability, rain retention and uptake of some inorganic ions. New Phytologist 108(1):75–82

Percy KE, Baker EA (1990) Effects of simulated acid rain on epicuticular wax production, morphology, chemical composition and on cuticular membrane thickness in two clones of Sitka spruce (Picea sitchensis (Bong.) Carr.). New Phytologist 116(1):79–87.

Peters LN, Witherspoon JP (1972) Retention of 44-88 μ simulated fallout particles by grasses. Health Physics 22:261-266

Prencipe M, Pascal F, Zicovich-Wilson CM, Saunders VR, Orlando R, Dovesi R (2004) The vibrational spectrum of calcite (CaCO3): an ab initio quantum-mechanical calculation note: theoretically derived structure. Physics and Chemistry of Minerals 31:559-564

Pye KT, H. (2009) Aeolian sand and sand dunes. Springer-Verlag, Berlin, p 458

Rampino MR, Ambrose SH (2000) Volcanic winter in the Garden of Eden: The Toba supereruption and the late Pleistocene human population crash. Geological Society of America Special Papers 345:71-82

Rampino MR, Self S (1982) Historic eruptions of Tambora (1815), Krakatau (1883), and Agung (1963), their stratospheric aerosols, and climatic impact. Quartenary Research 18(2):127-143

Reese ME, Sanchez J, McCormick AV (1993) Preparation of homogeneous aluminosilicate gels by sol/gel techniques. In: MRS Meeting, Fall, 1991.

Reimer L (1998) Scanning Electron Microscopy: Physics of Image Formation and Microanalysis. Springer-Verlag, Berlin, p 527

Rigg GB (1914) The effects of the Katmai eruption on marine vegetation. Science 40(1032):509-513

Risacher F, Alonso H (2001) Geochemistry of ash leachates from the 1993 Lascar eruption, Northern Chile. Implication for recycling of ancient evaporites. Journal of volcanology and geothermal research 109:319-337

Rodríguez LA, Watson I, M., Edmonds M, Ryane G, Hards V, Oppenheimer C, Bluth GJS (2008) SO_2 loss rates in the plume emitted by Soufrière Hills volcano, Montserrat. Journal of Volcanology and Geothermal Research 173(1-2):135-147

Rogers N, Hawkesworth C (2000) Composition of magmas. In: Sigurdsson H, Houghton B, McNutt S, Rymer H, Stix J (eds) Encyclopedia of Volcanoes. Academic Press, London, pp 115-131

Rose WI (1977) Scavenging of volcanic aerosol by ash: atmospheric and volcanological implications. Geology 5:621-624

Rose WI, Bluth GJS, Ernst GGJ (2000) Integrating retrievals of volcanic cloud characteristics from satellite remote sensors: A summary. Philosophical Transactions: Mathematical, Physical and Engineering Sciences 358(1770):1585-1606

Rose WI, Bluth GJS, Schneider DJ, Ernst GGJ, Riley CM, Henderson LJ, McGimsey RG (2001) Observations of volcanic clouds in their first few days of atmospheric residence: The 1992 eruptions of Crater Peak, Mount Spurr Volcano, Alaska. The Journal of Geology 109:677-694

Rose WI, Durant AJ (2009) Fine ash content of explosive eruptions. Journal of Volcanology and Geothermal Research 186(1-2):32-39

Rosen CJ, Eliason R (2005) Nutrient Management for Commercial Fruit & Vegetable Crops in Minnesota. In: Department of Soil, Water and Climate, University of Minnesota, Minneapolis

Rossi MJ (2003) Heterogeneous reactions on salts. Chemical Reviews 103(12):4823-4882

Rouxhet PG, Genet MJ (1991) Chemical composition of the microbial cell surface by x-ray photoelectron spectroscopy. Microbial Cell Surface Analysis 173(220):173-234

Rubeška I, Moldan B (1971) Atomic Absorption Spectrophotometry. CRC Press, London, p 189

Russ JC (1984) Fundamentals of Energy Dispersive X-ray Analysis. Butterworths, London, p 308

Sarmiento JL (1993) CO_2 stalled. Nature 365:697-698

Scaillet B, Clemente B, Evans WB, Pichavant M (1998) Redox control of sulfur degassing in silicic magmas. Journal of Geophysical Research 103(B10):23937-23949

Schaeffer HA (1984) Diffusion-controlled processes in glass forming melts. Journal of Non-Crystalline Solids 67:19-33

Schenk PW, Steudel R (1968) Oxides of sulphur. In: Nickless G (ed) Inorganic Sulphur Chemistry. Elsevier Publishing Company, London, pp 369-415

Scherbatskoy T, Tyree MT (1990) Kinetics of exchange of ions between artificial precipitation and maple leaf surfaces. New Phytologist 114:703-712

Schlotz R, Uhlig S (2000) Fundamental Principles. Bruker AXS GmbH, Karlruhe, p 62

Schmauß-Schreiner D (2007) Experimental studies on the adsorption of SO_2 on volcanic ashes. In: Fakultät für Chemie/Biologie/Geowissenschaften. Universität Bayreuth, Bayreuth, p 112

Scholze H (1990) Glass. Nature, Structure, and Properties. Springer-Verlag, London, p 454

Schulte PJ, Teskey RO, Hinckley TM, Stevens RG, Leslie DA (1985) The effect of tephra deposition and planting treatment on soil oxygen levels and water relations of newly planted seedlings. Forest Science 31(1):109-116

Seah MP, Dench WA (1979) Quantitative electron spectroscopy of surfaces. Surface and Interface Analysis 1(1):2-11

Self S (2006) The effects and consequences of very large explosive volcanic eruptions. Philosophical Transactions of the Royal Society, A. 364:2073-2097

Seymour VA, Hinckley TM, Morikawa Y, Franklin JF (1983) Foliage damage in coniferous trees following volcanic ashfall from Mt. St. Helens. Oecologia 59:339-343

Shepherd T, Wynne Griffiths D (2006) The effects of stress on plant cuticular waxes. New Phytologist 171:469-499

Shinohara H (2008) Excess degassing from volcanoes and its role on eruptive and intrusive activity. Reviews of Geophysics 46:doi:10.1029/2007RG000244

Shipley S, Sarna-Wojciki AM (1983) Distribution, thickness, and mass of late Pleistocene and Holocene tephra from major volcanoes in the northwestern United States: a preliminary assessment of hazards from volcanic ejecta to nuclear reactors in the Pacific Northwest. United States Geological Survey Miscellaneous Field Studies Map MF-1435

Shoji S, Nanzyo M, Dahlgren RA (2003) Volcanic ash soils. Genesis, properties and utilization., p 288

Siegel BZ, Siegel SM (1982) Mercury Content of Equisetum Plants Around Mount St. Helens One Year After the Major Eruption. Science 216(4543):292-293

Sigurdsson H (2000) Introduction. In: Sigurdsson H, Houghton B, McNutt S, Rymer H, Stix J (eds) Encyclopedia of Volcanoes. Academic Press, San Diego, pp 1-13

Simons GA, Garman AR, Boni AA (1986) The kinetic rate of SO_2 sorption by CaO. American Institute of Chemical Engineers Journal 33(2):211-217

Skille JM, Falter CM, Kendra WR, Schuchard KM (1983) The Fate, Distribution and Limnological Effects of Volcanic Tephra in the St. Joe and Coeur D'Alene River Deltas of Lake Coeur D'Alene, Idaho. In: Idaho Water and Energy Resources Research Institute Completion Report., Moscow, p 156

Small H (1989) Ion Chromatography. Plenum Press, New York, p 276

Smedskjaer MM, Yue YZ (2009) Inward cationic diffusion in glass. Journal of Non-Crystalline Solids 355(14-15):908-912

Smirnov MY, Kalinkin AV, Pashis AV, Sorokin AM, Noskov AS, Bukhtiyarov VI, Kharas KC, Rodkin MA (2003) Comparative XPS study of Al_2O_3 and CeO_2 sulfation in reactions with SO_2, $SO_2 + O_2$, $SO_2 + H_2O$, and $SO_2 + O_2 + H_2O$. Kinetics and Catalysis 44(4):575-582

Smith DB, Zielinski RA, Taylor HE, Sawyer MB (1983) Leaching characteristics of ash from the May 18, 1980, eruption of Mount St. Helens volcano, Washington. Bulletin of Volcanology 46(2):103-124

Smith DR, Cooper RF (2000) Dynamic oxidation of a Fe^{2+}-bearing calcium-magnesium-aluminosilicate glass: the effect of molecular structure on chemical diffusion and reaction morphology. Journal of Non-Crystalline Solids 278:145-163

Smith WH, Staskawicz BJ (1977) Removal of atmospheric particles by leaves and twigs of urban trees: some preliminary observations and assessment of research needs. Environmental Management 1(4):317-330

Sneva F (1982) Mt. St. Helens ash: considerations on its fallout on rangelands. In: Special Report no. 650. Oregon State University Agricultural Station, Corvallis, OR, pp 1-29

Spadaro FR, Lefèvre R, Ausset P (2002) Experimental rapid alteration of basaltic glass: Implications for the origins of atmospheric particulates. Geology 30(8):671-674

Sparks RS, Bursik MI, Carey SN, Gilbert JS, Glaze LS, Sigurdsson S, Woods AW (1997) Volcanic Plumes. Wiley & Sons, London

Spera FJ (2000) Physical properties of magma. In: Sigurdsson H, Houghton B, McNutt S, Rymer H, Stix J (eds) Encyclopedia of Volcanoes. Academic Press, London, pp 171-190

Spirakis CS (1989) Possible effect of readily available iron in volcanic ash on the carbon to sulfur ratio in lower Paleozoic normal marine sediments and implications for atmospheric oxygen. Geology 17(7):599-601

Stöcker M (1996) X-Ray photoelectron spectroscopy on zeolites and related materials. Microporous Materials 6(5-6):235-257

Stoiber RE (1995) Volcanic gases from subaerial volcanoes on Earth. In: Ahrens T (ed) Global Earth Physics. A handbook of physical constants. American Geophysical Union, Washington, pp 308-319

Stracquadanio M, Dinelli E, Trombini C (2003) Role of volcanic dust in the atmospheric transport and deposition of polycyclic aromatic hydrocarbons and mercury. Journal Of Environmental Monitoring 5(6):984-988

Stuart Chapin F (1980) The mineral nutrition of wild plants. Annual Reviews of Ecology and Systematics 11:233-260

Sugama T, KuKacka LE, Carciello N, Hocker NJ (1989) Study of interactions at water-soluble polymer/$Ca(OH)_2$ or gibbsite interfaces by XPS. Cement and Concrete Research 19(6):857-866

Taran YA, Bernard A, Gavilanes JC, Luhezheva E, Cortés A, Armienta MA (2001) Chemistry and mineralogy of high-temperature gas discharges from Colima volcano, Mexico. Implications for magmatic gas–atmosphere interaction. Journal of Volcanology and Geothermal Research 108(1-4):245-264

Taylor PS, Stoiber RE (1973) Soluble material on ash from active Central American volcanoes. Geological Society of America Bulletin 84:1031-1042

Tejedor M, Jiménez C, Díaz F (2003) Volcanic materials as mulches for water conservation. Geoderma 117:283-295

Telford R, Barker P, Metcalfe S, Newton A (2004) Lacustrine responses to tephra deposition: examples from Mexico. Quartenary Science Reviews 23:2337-2353

Textor C, Graf H-F, Herzog M (2003) Injection of gases into the stratosphere by explosive volcanic eruptions. Journal of Geophysical Research 108(D19)(4606):doi:10.1029/2002JD002987, 002003

Textor C, Graf H-F, Timmreck C, Robock A (2004) Emissions from volcanoes. In: Granier C, Artaxo P, Reeves CE (eds) Emissions of Atmospheric Trace Compounds. Springer, Dordrecht, pp 269-304

Thorarinsson S (1979) On the damage caused by volcanic eruptions with special reference to tephra and gases. In: Sheets PD, Grayson DK (eds) Volcanic activity and human ecology. Academic Press, pp 125-158

Turner NH, Murday JS, Ramaker DE (1980) Quantitative determination of surface composition of sulfur bearing anion mixtures by Auger electron spectroscopy. Analytical Chemistry 52(1):84-92

Turner NH, Schreifels JA (1996) Surface analysis: x-ray photoelectron spectroscopy and auger electron specstroscopy. Analytical chemistry 68(12):309-332

Ullerstam M, Vogt R, Langer S, Ljungström E (2002) The kinetics and mechanism of SO_2 oxidation by O_3 on mineral dust. Physical Chemistry Chemical Physics 4:4694 - 4699

Usher CR, Michel AE, Grassian VH (2003) Reactions on Mineral Dust. Chem. Rev. 103(12):4883-4940

Van Doveren H, Verhoeven JAT (1980) XPS spectra of Ca, Sr, Ba and their oxides. Journal of Electron Spectroscopy and Related Phenomena 21:265-273

Varekamp JC, Luhr JF, Prestegaard KL (1984) The 1982 eruptions of El Chichón volcano (Chiapas, Mexico): Character of the eruptions, ash-fall deposits and gas phase. Journal of Volcanology and Geothermal Research 23:39-68

Veneklaas EJ (1990) Nutrient fluxes in bulk precipitation and throughfall in two montane tropical rain forests, Colombia. Journal of Ecology 78:974-992

Venezia AM (2002) X-ray photoelectron spectroscopy (XPS) for catalysts characterization. Catalysis Today 77(4):359-370

Volf MB (1984) Chemical Approach To Glass. Elsevier, Oxford, p 594

Wagner CD (1975) Chemical shifts of Auger lines, and the Auger parameter. Faraday Discussions of the Chemical Society 60:291-300

Wagner CD, Passoja DE, Hillery HF, Kinisky TG, Six HA, Jansen WT (1982) Auger and photoelectron line energy relationships in aluminum–oxygen and silicon–oxygen compounds. Journal of Vacuum Science Technology 21(4):933-944

Wallace PJ, Dufek J, Anderson AT, Zhang Y (2002) Cooling rates of Plinian-fall and pyroclastic-flow deposits in the Bishop Tuff: inferences from water speciation in quartz-hosted glass inclusions. Bulletin of Volcanology 65:105-123

Wallace PJ, Gerlach TM (1994) Magmatic Vapor Source for Sulfur Dioxide Released During Volcanic Eruptions: Evidence from Mount Pinatubo. Science 265(5171):497-499

Walton AG, Whitman DR (1964) Calculations of the surface energy of some orthorhombic sulfates. Journal Of Chemical Physics 40(9):2722-2725

Warren BE, Biscoe J (1937) X-Ray Diffraction Studies of Silica and Soda-Silica Glass. In: Thirty Ninth Annual Meeting, American Chemical Society. New York, N.Y.

Warren G (1982) Optical Properties of Snow. Reviews of Geophysics and Space Physics 20(1):67-89

Wasastjerna JA (1927) The crystal structure of anhydrite, $CaSO_4$. Societas Scientiarum Fennica. Commentationes Physicomathematicae II 2:1-46

Watson A (1997) Volcanic Fe, CO_2, ocean productivity and climate. Nature 385:587-588

Weinstein LH, Davison A (2004) Fluorides in the Environment: Effects on Plants and Animals. CABI Publishing, Oxon

Weiss H, Braeu MF (2009) How much water does calcined gypsum contain? Angewandte Chemie International Edition 48:3250-3524

Welz B (1985) Atomic Absorption Spectrophotometry. VCH, Weinheim and Deerfield Beach, p 506

Wieczorek-Ciurowa K (1996) Versatility of the application of thermal analysis to the simulation of gas desulphurisation. Thermochimica Acta 272(20):233-241

Wiesner MG, Wang Y, Zheng L (1995) Fallout of volcanic ash to the deep South China Sea induced by the 1991 eruption of Mount Pinatubo (Philippines). Geology 23(10):885-888

Williams DB, Barry Carter C (2009) Transmission Electron Microscopy. A textbook for Materials Science. Springer Science, New York, p 223

Wilson L, Sparks RSJ, Huang TC, Watkins ND (1978) The control of volcanic column heights by eruption energetics and dynamics. Journal of Geophysical Research 83(B4):1829-1836

Witham CS, Oppenheimer C, Horwell CJ (2005) Volcanic ash-leachates: a review and recommendations for sampling methods. Journal of Volcanology and Geothermal Research 141:299-326

Witherspoon JP, Taylor FGJ (1969) Retention of a fallout simulant containing 134Cs by Pine and Oak trees. Health Physics 17(6):825-829

Wolejko L, Ito K (1986) Mires of Japan in relation to mire zones, volcanic activity and water chemistry. Japanese Journal of Ecology 35(5):575-586

Wolff-Boenisch D, Gislason SR, Oelkers EH, Putins CV (2004) The dissolution of natural glasses as a function of their composition at pH 4 and 10.6, and temperatures from 25 to 74°C. Geochimca et Cosmochimica Acta 68(23):4843-4858

Woods DC, Bursik MI (1991) Particle fallout, thermal disequilibrium and volcanic plumes. Bulletin of Volcanology 53(7):559-570

Worcester DC (1912) Taal Volcano and its recent destructive eruption. National Geographic Magazine 23(4):313–367

Yamaguchi DK, Hoblitt RP (1995) Tree-ring dating of pre-1980 volcanic flowage deposits at Mount St. Helens, Washington. Geological Society of America Bulletin 107(9):1077-1093

Zimanowski B, Wohletz K, Dellino P, Büttner R (2003) The volcanic ash problem. Journal of Volcanology and Geothermal Research 122:1-5

Ziolek M, Kujawa J, Saur O, Aboulayt A, Lavalley JC (1996) Influence of sulfur dioxide adsorption on the surface properties of metal oxides. Journal of Molecular Catalysis A: Chemical 112:125-132

Zobel DB, Antos JA (1987) Composition of rhizomes of forest herbaceous plants in relation to morphology, ecology and burial by tephra. Botanical Gazette 148(4):490-500

Zobel DB, Antos JA (1992) Survival of plants buried for eight growing seasons by volcanic tephra. Ecology 73(2):698-701